Technische Universität München

Technische Universität München
Max-Planck-Institut für extraterrestrische Physik

Testing the standard GRB afterglow model with the *snapshot method* using multi-epoch multi-wavelength data.

Karla Patricia Varela Cardozo

Vollständiger Abdruck der von der Fakultät für Physik der Technischen Universität München zur Erlangung des akademischen Grades eines

Doktors der Naturwissenschaften

genehmigten Dissertation.

Vorsitzender:	Univ.-Prof. Dr. Alejandro Ibarra
Prüfer der Dissertation:	1. Priv.-Doz. Dr. Jochen Greiner
	2. Univ.-Prof. Dr. Lothar Oberauer

Die Dissertation wurde am 13.04.2017 bei der Technischen Universität München eingereicht und durch die Fakultät für Physik am 30.05.2017 angenommen.

ABSTRACT

Gamma-ray Bursts (GRBs) are observed as high-energy γ-rays with an isotropic energy of about $10^{49} - 10^{54}$ erg released in a few seconds. This emission is followed by a long-lasting afterglow detected at longer wavelengths, from radio to X-rays. Although still under debate, the most-widely accepted model for the production of the GRB prompt and afterglow phase is the relativistic fireball model. It proposes an ultra-relativistic jet composed by e^+e^- pairs, photons and baryons. The GRB emission is then associated to internal shocks within the jet. The afterglow emission is associated to the synchrotron radiation from the Fermi accelerated electrons in external shocks between the jet and the external medium.

There are many open questions regarding the physical processes leading to the observed GRB emission and the details of the fireball model. These processes include the dynamics of the outflow, and the mechanisms responsible for particle acceleration, magnetic field (B) generation and radiation processes. There are also questions about the progenitor and central engine, and about the external density profile. Previous studies aiming to solve some of these questions often had to introduce further assumptions to the standard model to explain the data. However, these assumptions introduce degeneracies in the parameters and do not allow an independent test of the model.

I present the data for four GRBs that have excellent simultaneous multi-epoch multi-wavelength coverage.These data sets allow me to test the standard afterglow model through a combined temporal and spectral analysis called the *snapshot method*. I analyse the following questions: 1) What is the evolution of the break frequencies and the afterglow parameters? 2) Can I set constraints on the CBM density type? 3) Is it possible to differentiate among the proposed energy injection models? 4) How collimated are the outflows? 5) Is it possible to favour a single mechanism of B field production. 6) Is synchrotron emission the only relevant radiation process for the cooling of the electrons? s

I present a detailed analysis of the temporal evolution of the break frequencies and the afterglow parameters, and I find that they follows the expected theoretical values. I derive two important results in the context of the standard afterglow model: first, I show that the evolution of B is in agreement with the prediction of the shock amplification of the circumburst medium magnetic field mechanism. This results suggests that an analysis of the evolution of B gives valuable information on the magnetic field production mechanisms, that can not be obtained from the measurement of its magnitude. Second, the four GRBs are all in agreement with a stellar wind-like density profile, as expected in the collapsar model. Previous studies have shown that the density profile is usually in agreement with an ISM profile. However, I show that the inclusion of radio and submm data is a key factor to determine the density profile without ambiguity.

VORWORT

Gammastrahlenausbrüche (Englisch: Gamma-Ray Burst, GRB) werden als hochenergetische Gammastrahlung beobachtet, deren isotropisches Energieäquivalent von etwa 10^{49} - 10^{54} erg in nur wenigen Sekunden emittiert wird. Dieser Gammaemission folgt ein lang anhaltendes Nachglühen, welches bei längeren Wellenlängen, von Radiowellen bis Röntgenstrahlung, gemessen wird. Das relativistische Feuerballmodell, das die anfängliche Gammastrahlung und das Nachglühen beschreibt, ist trotz anhaltender Diskussionen die heutzutage am weitesten akzeptierte Theorie. Das Modell beschreibt einen ultra-relativistischen gerichteten Materiefluss (einen Jet), der aus e^+-e^- Paaren, Photonen und Baryonen besteht. Die Gammaemission wird durch interne Schocks im Materiefluss erzeugt. Das Nachglühen ist Synchrotron-Strahlung von Fermi-beschleunigten Elektronen in externen Schocks, die entstehen, wenn der Jet auf das externe Medium trifft.

Sowohl die physikalischen Prozesse, die zur beobachteten GRB Emission führen, als auch grundlegende Details des Feuerballmodells werfen noch viele Fragen auf. Diese beinhalten zum einen die Dynamik des Flusses und zum anderen die Mechanismen, die zur Beschleunigung der Teilchen, zur Erzeugung des magnetische Felds (B), und zu den unterschiedlichen Strahlungsprozessen führen. Auch viele Fragen zum Vorläuferobjekt und zum Dichteprofil des externen Mediums sind nach wie vor unbeantwortet. In vorausgegangenen Studien mussten zusätzliche Annahmen zum Standardmodell gemacht werden, um die Beobachtungen zu erklären. Diese Annahmen führen jedoch zur Entartung der Parameter und erlauben somit keinen unabhängigen Test des Modells.

In dieser Arbeit präsentiere ich Daten für vier GRBs, die mehrere zeitliche Epochen mit gleichzeitigen Breitband-Beobachtungen abdecken. Dieser Datensatz erlaubt es mir, das Feuerballmodell mit einer Kombination aus Zeit- und Spektralanalyse zu testen. Man nennt dies "Schnappschussmethode". Damit möchte ich die folgenden Fragen beantworten: 1) Wie verändern sich die charakteristischen Frequenzen des Spektrums und die Parameter des Nachglühens? 2) Kann das radiale Dichteprofil des Mediums, das den GRB umgibt, genauer beschrieben werden? 3) Ist es möglich, zwischen den verschieden Theorien zur Einspeisung von Energie in den Jet zu unterscheiden? 4) Wie stark ist der Jet kollimiert? 5) Ist es möglich, den vorherrschenden Mechanismus zur Erzeugung des Magnetfeldes zu bestimmen? 6) Ist Synchrotronemission der einzige relevante Prozess, um die Elektronen zu kühlen?

Ich präsentiere eine detaillierte Analyse der zeitlichen Entwicklung der charakteristischen Frequenzen im Synchrotronspektrum und der Nachglüh-Parameter. Dabei stelle ich fest, dass sie der theoretisch vorhergesagten zeitlichen Evolution folgen. Ich leite zwei wichtige Ergebnisse für das Feuerballmodell ab: Erstens zeige ich, dass die Evolution des Magnetfelds B mit den Vorhersagen eines durch Schocks verstärkten magnetisches Felds im umgebenden Medium übereinstimmt. Dieses Ergebnis zeigt, dass eine Analyse der Entwicklung des magnetischen Felds wertvolle Informationen über den Mechanismus seiner Erzeugung gibt. Derartige Informationen können nicht von der Messung der Magnetfeldstärke allein abgeleitet werden. Zweitens stimmt das Dichteprofil des umgebenden Mediums um alle vier GRBs mit einem Wind-Profil überein, welches im Kollapsar-Modell erwartet wird. Bisherige Studien haben gezeigt, dass das Dichteprofil normalerweise mit einem ISM-Profil übereinstimmt. Ich zeige hiermit, dass Radio und Sub-mm Daten eine Schlüsselrolle bei der eindeutigen Bestimmung des Dichteprofiles spielen.

Contents

Chapter 1

Introduction

The Gamma-ray bursts (GRBs) were discovered by the military *Vela* satellites in 1967 (Klebesadel et al. 1973). GRBs are observed as high-energy γ-rays emitted in an energy range between 100 keV up to a MeV[1]. A total isotropic energy of about $10^{49} - 10^{54}$ erg is released in a short time interval (few seconds) (Kulkarni et al. 1999; Frail et al. 2001). GRBs can be used as a tool in different fields of astrophysics, e.g., study of the early universe or high-energy particle acceleration mechanisms. Because of this, many satellites and ground-based telescopes have been actively used in the follow-up of GRBs. The study of GRB physics represents a constant challenge. The GRB's irregular light curves and fast decaying nature (e.g., Fishman & Meegan 1995) make the a comparison between theory and observations a difficult task. After more than 5 decades there is still not a single model able to describe all the observed features of the GRBs. It is however a consensus that the best model is a cosmological model (e.g., Rees & Meszaros 1994) instead of a galactic one (e.g., galactic models, Schaefer & Cline 1985; Hartmann et al. 1990).

1.1 Overview

The first two decades of GRBs studies (Hurley 1989) were led by observations from different missions such as the *Konus* (Venera) experiment (Aptekar et al. 1995), *Ginga* (Swinbanks 1987) or *Solar Maximum Mission* (Bohlin et al. 1980). The observed variability of the light curves and high-energy emission component of the GRBs pointed towards a compact source as a possible progenitor. The observed isotropic distribution of the GRBs (Mazets et al. 1981) suggested an extragalactic origin (e.g., Hakkila et al. 1994; Briggs et al. 1996) instead of a galactic one (e.g., Atteia et al. 1987). The non-thermal nature of the spectrum was associated with a dominant synchrotron emission[2] and secondary radiation effects such as inverse-Compton radiation (e.g., Golenetskii et al. 1983; Fenimore et al. 1988). The spectrum is described by the Band Function (Cline et al. 1973; Band et al. 1993). This function is a combination of a power-law and an exponential law joined at a specific transition energy. The peak of the function is observed in the sub-MeV energy range. Finally, a temporal bimodal distribution of the GRBs was established. The distribution is based on T_{90}, i.e., the time it takes for 90% of the total fluence to be detected. GRBs are classified into long (LGRB, $T_{90} > 2$ s) and short (SGRB, $T_{90} < 2$ s) (Kouveliotou et al. 1993).

[1] GeV emission has been detected for a few burst by the *Fermi* satellite.

[2] David Yu, PhD Thesis 2016, TUM

In 1991 the *Compton Gamma-Ray Observatory* (CGRO, Fishman 1992) was launched. CGRO had 4 instruments on board: the *Energetic Gamma-Ray Experiment Telescope* EGRET had an improved sensitivity (>10 times) compared to other instruments operating in the same energy range (200 MeV - 10 GeV). This allowed the detection of the hardest GRBs and, for the first time a detection of GeV emission. The *Burst and Transient Experiment* BATSE (1 keV - 1 MeV) was used to detect, localise and measure the energy of the GRBs. BATSE observed more than 2700 GRBs that were used to produce the first homogenous and unbiased GRB sample. Due to the high quality of the data and high statistics of the sample, it was used to confirmed some of the main properties of GRBs previously suggested. The sample confirmed the high variability (Fig. 1.1) and the lack of periodicity of the GRB light curves.

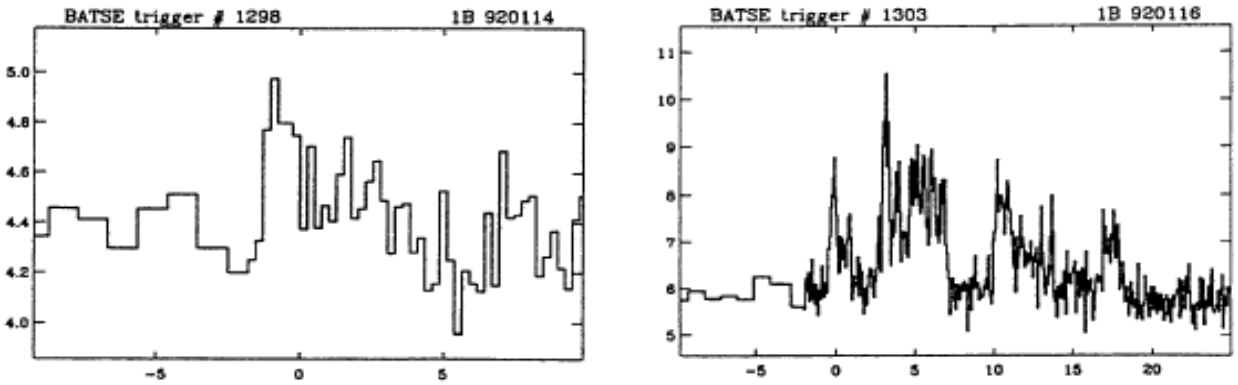

Figure 1.1: Light curves of 2 GRBs observed by BATSE (Fishman & Meegan 1995). The horizontal axes is in seconds and the vertical axes is in 10^3 counts/s.

The non-thermal nature of the GRB spectra was confirmed by a spectral study based on the BATSE sample and observations from EGRET, the *Comptel Telescope* and the *Oriented Scintillation Spectrometer* (OSSE). The spectrum was confirmed to be described by the band function (e.g., Fig. 1.2a) with its peak energy at around a few MeV, and it was observed to be harder towards high energies (Band et al. 1993). The bimodal distribution of the GRBs (Kouveliotou et al. 1993) was confirmed as seen in Fig. 1.2b.

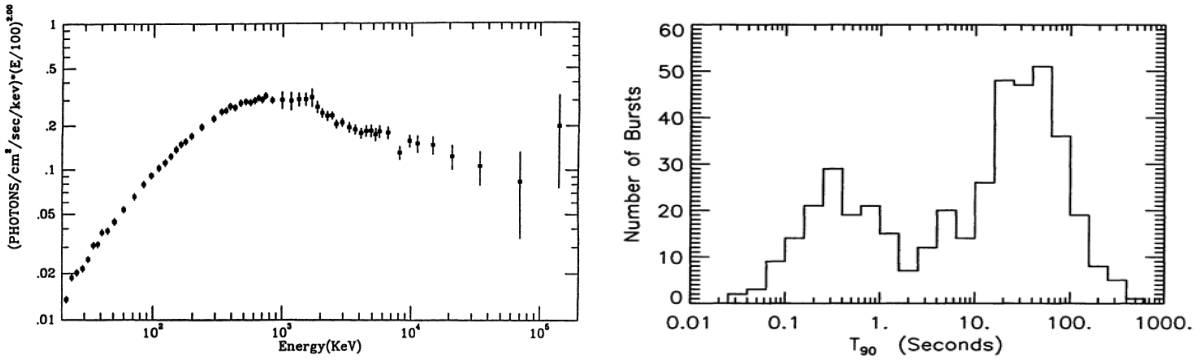

(a) Spectral energy distribution of GRB 910503 **(b)** Bimodal distribution of GRB based on T_{90}.

Figure 1.2: Left: GRB 910503 detected by CGRO. The spectrum is described by the Band function with the peak energy in the MeV range (Schaefer et al. 1994; Fishman & Meegan 1995). **Right**: Histogram with the bimodal distribution of GRBs based on the duration T_{90} (Kouveliotou et al. 1993).

The BATSE sample proved the isotropic angular distribution (Fig. 1.3, Meegan et al. 1992) and the in-homogeneity on the intensity distribution[3] (Fenimore et al. 1993; Mao & Mo 1998) of the GRBs. This was the first unambiguous proof against a galactic origin of the GRBs. It was supported by results from independent studies such as the first evidence of time delation (Nemiroff 1994; Wijers & Paczynski 1994; Davis et al. 1994). After the confirmation of the extragalactic origin (Usov & Chibisov 1975; van den Bergh 1983) further studies were based mainly on cosmological theories (e.g., Meszaros et al. 1993; Fenimore et al. 1993; Rees & Meszaros 1994).

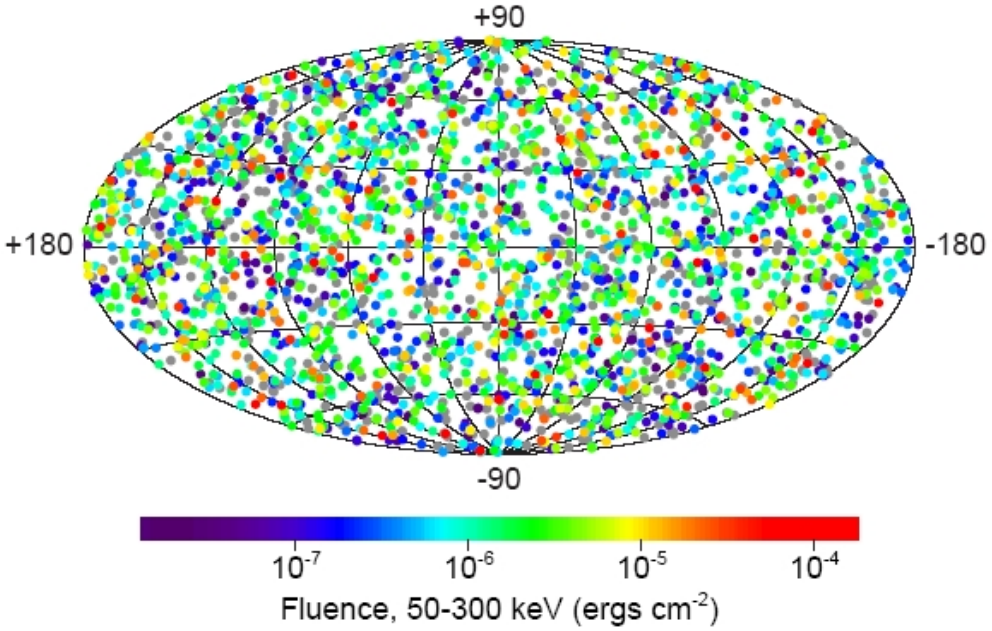

Figure 1.3: Spatial isotropic distribution of a 2704 GRBs detected by BATSE (Michael S. Briggs 2014).

CGRO opened a new era of GRB science after the confirmation of their cosmological origin. However, the mechanisms responsible for the gamma-ray emission had not been understood yet and there had been no detection of the fading multi-wavelength radiation (afterglow; e.g., Paczynski & Rhoads 1993; Mészáros & Rees 1997) that was predicted to follow the gamma-ray (prompt) emission. The first X-ray counterpart of a GRB (GRB 960720, Piro et al. 1996) was detected in July 20 1996, by the recently launched italian-dutch satellite *BeppoSAX* (Boella et al. 1997). The improved accuracy in the position of the source ($\sim$1 arcmin) was an important step to allow ground-based follow-up observations of the GRB afterglows. On February 27, 1998 BeppoSAX detected the X-ray counterpart of the GRB 970228 (Fig. 1.4a; Costa et al. 1997; van Paradijs et al. 1997), however, the observations were not deep enough to uniquely associate this host galaxy to the GRB. On May 8th 1997, the counterpart of GRB 970508 was observed in a multi-wavelength range (e.g., Frail et al. 1997; Djorgovski et al. 1997; Galama et al. 1998a; Bremer et al. 1998). A break in the light curve (LC), known as a jet break, was observed associated to the collimated nature of the outflow (Rhoads 1999; Sari et al. 1999). Furthermore, the determination of the redshift of the host galaxy was possible (z=0.835, Metzger et al. 1997) strengthening the theory of cosmological origin of the GRBs.

[3]Deviation of the relation between intensity (I) and number of sources (N) from the expected one in an Euclidean space ($N \propto I^{-3/2}$)

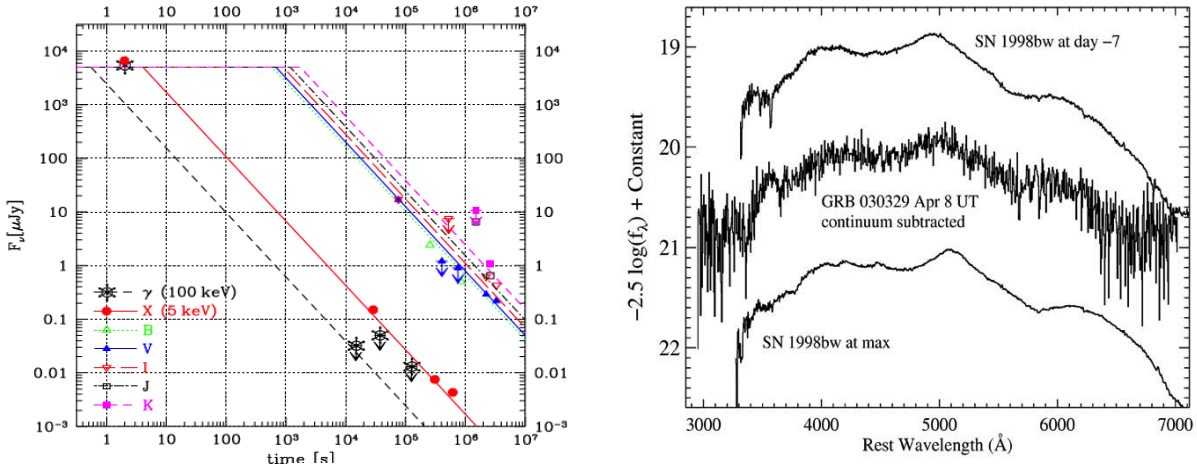

(a) LC of GRB 970228.

(b) Spectrum GRB 030329 and SN 1998bw.

Figure 1.4: Left: Light curve of GRB 979228 detected by BeppoSAX and observed later in the optical wavelength range (Wijers et al. 1997). **Right**: Optical afterglow spectrum of GRB 030329. The comparison with the spectrum of SN 1998bw shows the GRB-SN connection (Stanek et al. 2003).

So far, long GRBs have been associated with the deaths of a massive stars collapsing into black holes (BH), while short GRBs are associated with mergers of neutron stars (NS) and either other NS or BH. In both cases, long and short GRBs, the accretion disk around the final BH is thought to give rise to the ultra-relativistic collimated outflow (jet). The spectra of the long-GRBs and the afterglows are non-thermal spectra associated with synchrotron emission from Fermi accelerated electrons (Rees & Meszaros 1994; Nemiroff 1994). The predicted connection of the long-GRBs to core collapse supernovae (e.g., Woosley 1993) had the first evidence from the observations of the afterglow of GRB 980425 (Woosley 1993; Galama et al. 1998b) and the supernova SN1998bw. A stronger confirmation of this GRB-SN connection was obtained from observations of GRB 030329 with the High Energy Transient Explorer II - HETE II satellite (Eichler et al. 2010) and the supernova SN2003dh (Hjorth et al. 2003; Stanek et al. 2003). The follow-up of the afterglow of GRB 030329 with ground-based telescopes led to the measurement of its Lorentz factor Γ at late times confirming the ultra-relativistic nature of the outflows (e.g., Paczynski 1986).

In 2004 the *Swift* satellite (Gehrels et al. 2004) was launched with three instruments on board: the Burst Alert Telescope (BAT, Barthelmy et al. 2005), the X-ray Telescope (XRT) and the UV-Optical Telescope (UVOT, Roming et al. 2005). BAT detects the GRB and measures its position with an accuracy of 2 - 3 arcmin. Seconds after this detection *Swift* slews to the position of the GRB provided by BAT and starts the observations with the XRT and UVOT. These instruments obtain an accurate measurement of the afterglow energy and an enhanced position of the GRB with an accuracy of a few arcsec. The fast communication between the satellite and the ground-based stations allows the observations of the early light curve evolution in a multi-wavelength range. These early afterglow observations set the first basis for a different origin between the GRB prompt emission and the afterglow. The detailed structure of the new sample of X-ray light curves (Zhang et al. 2006) of GRB afterglows presents a late decay in agreement with theoretical predictions. They also have a break associated to a jet break and the collimated nature of the outflow and plateau phases (Nousek et al. 2006; Racusin et al. 2009). The detection of the afterglow of short

GRBs and their host galaxies made evident their less energetic nature and their association with lower redshifts and old stellar population. Other satellites (e.g., the Hubble space telescope HST[4], Spitzer[5], *Fermi* satellite), have been actively involved in the GRB research programs as well as different ground-based telescopes covering a wide range from radio to optical wavelengths. Great advances have been made in the GRB science field but there is still a long way to go in order to solve all the outstanding features that have been not understood yet.

1.2 Current state

In the standard afterglow model the afterglow emission is associated with an ultra-relativistic blast wave expanding into a cold external medium. The study of the physical processes in the shock region requires a proper understanding of: the generation of the magnetic field B, the kinetic isotropic energy $E_{\rm K,iso}$, and the energy content and distribution of the accelerated electrons in the shocked fluid. Three main parameters are introduced to overcome the unknown details of the underlying microphysical processes in the shock region: fraction of the total energy in the magnetic field ($\varepsilon_{\rm B}$), fraction of the total energy that goes into the accelerated electrons $\varepsilon_{\rm e}$ and the power-law index of the electron energy distribution p. These main parameters, known as *microphysical parameters*, together with the density of the external medium and the total energy in the ejecta, provide, in a simplified model, an overall description of the dynamical evolution and radiation processes leading to the GRB afterglow. The shape of the observed spectral energy distribution and the temporal evolution of the measured flux is determined by those five quantities. The spectral shape is described by a 4 segment power-law with 3 characteristic break frequencies: cooling $\nu_{\rm c}$, injection $\nu_{\rm m}$ and self-absorption $\nu_{\rm sa}$ frequencies. Therefore in order to determine all the five parameters, simultaneous broad-band observations covering the 3 breaks in the spectrum are required.

The standard afterglow model explains some of the main features observed in the afterglow light curves (e.g., normal decays, jet breaks, Racusin et al. 2009; Kann et al. 2010) but can not reproduce some other commonly observed features (e.g., plateau phases, flares, unexpected spectral evolution, Wijers & Galama 1999; Björnsson et al. 2004; Lazzati & Perna 2007). New modifications and additional components to the standard afterglow model have been suggested to explained these new features (e.g., refreshed shocks, reverse shocks, non-constant micro-physical parameters, Panaitescu 2005; Wijers & Galama 1999; Nardini et al. 2011; Filgas et al. 2011, 2012; Greiner et al. 2013). In order to test these new modifications, broadband observations are required. However only 70 afterglows out of over 1400 afterglow detections have been followed-up in a wavelength range from radio to X-rays. Furthermore, only 51 afterglows out of the 70 have redshift measurements and only 3 (GRB 000926 presented in Fig. 1.5, GRB 980703, GRB 030329, Panaitescu & Kumar 2002; Frail et al. 2003; Resmi et al. 2005) have broadband observations covering all the 3 break frequencies to determine the afterglow parameters.

When not all spectral breaks have been probed simultaneously, alternative analyses have been implemented, such as fixing the model parameters to certain values ($E_{\rm K,iso} = E^{\gamma}_{\rm iso}$, Dai & Lu 1999; Frail et al. 2001; Pandey et al. 2003) or linking the parameters with one another ($\varepsilon_{\rm B}$, $\varepsilon_{\rm e}$, Medvedev 2006; van Eerten & Wijers 2009). In these cases, the implications of the derived model parameters are conditional to the additional assumption(s). Thus there continues to exist a large uncertainty in

[4]http://hubblesite.org/the_telescope/hubble_essentials/

[5]http://www.spitzer.caltech.edu

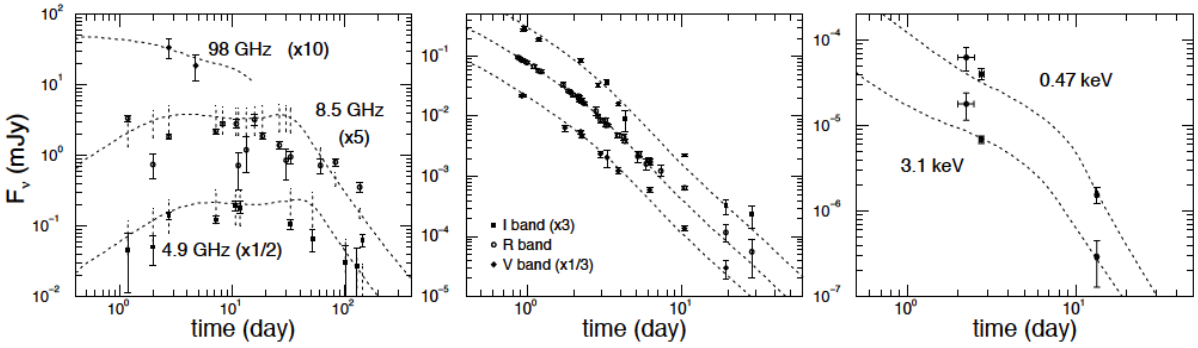

Figure 1.5: Light curves of GRB 000926 taken from (Panaitescu & Kumar 2002).

the detailed physical conditions that produce the afterglow emission. Here, I list the most relevant problems related to my work.

- Density profile: The relation between GRBs and SNe (collapsar progenitor model) was confirmed by observations of both GRB 030329 and SN2003dh (Stanek et al. 2003; Woosley & Heger 2003; Soderberg et al. 2006). In the collapsar model the central engine of long GRBs is associated to the collapse of a massive star that leaves a trace of stellar wind-like density profile, i.e., $\rho \sim r^{-k}$. However, observational data usually point to a constant density profile $k = 0$ (ISM) with normalisation values expanding over more than 5 orders of magnitude (Soderberg et al. 2006).

- Magnetic field B: The understanding of the production and amplification of the downstream magnetic field in the shock region is a key step to explain the acceleration mechanisms of the electrons and hence the observed spectrum. In the standard afterglow model, the main mechanism for the generation of the magnetic field in the shock region is shock amplification, by a factor of 4Γ, of the seed magnetic field B_0 in the circumburst medium (CBM). Besides this mechanism, there are two other plausible mechanisms that have been proposed: (1) a turbulent magnetohydrodynamic -MHD- processes (Medvedev & Loeb 1999) based on strongly magnetised sources. (2) A two-stream Weibel instability (Weibel 1959; Medvedev et al. 2005). This last mechanism is naturally expected during Fermi acceleration processes. The test of the mechanisms is based on the magnitude of ε_B. However, the wide range of values that have been measured for ε_B making it difficult to make a proper statement on the proposed mechanisms (Piran 2005).

- Energy efficiency: The efficiency of the conversion of the kinetic energy to γ-ray radiation is given by $\eta = E^{\gamma}_{\rm iso}/(E_{\rm K,iso}+E^{\gamma}_{\rm iso})$, with $E^{\gamma}_{\rm iso}$ being the isotropic energy emitted during the prompt emission. Theoretically, η should be lower than 10% (Kobayashi et al. 1997; Kumar 1999), however observations have shown extremely high efficiency requirements resulting from the measurement of $E_{\rm K,iso}$ going as far as $\eta \sim 100\%$ (Granot et al. 2006).

- Particle acceleration: Fermi acceleration is the proposed acceleration mechanism for the electrons during the external shock. The population of accelerated electrons is expected to have a particle energy distribution that follows a power-law behaviour with power-law index p. This index is known as the electron index and has to be > 2 due to energy conservation requirements in the shock front. There is no theoretical value for p, but statistical analyses suggest a value of $p \sim 2.3$ (see Chap. 2). However, there are some GRB afterglows with

$1 < p < 2$ (e.g., Dai & Cheng 2001; Panaitescu & Kumar 2002) and therefore an additional assumption on the model had to be imposed (i.e., upper cut on γ_m), rising questions on the particle acceleration mechanism (Dai & Cheng 2001; Bhattacharya 2001; Gao et al. 2013).

- Plateau phases and jet breaks: Analysis of the X-ray LC from a sample taken by the *Swift* /XRT shows that the afterglow evolution goes through a plateau phase followed by a break in the LC. The plateau phases are generally associated with an energy injection mechanism, however the mechanism responsible for the prolonged energy injection is still a matter of debate (Zhang et al. 2006; Racusin et al. 2009). Solutions such as stratified ejecta composed of shells with different Lorentz factors where the faster ones are catching up with the slower ones, or a millisecond magnetar model where the outflow is dominated by a Poynting flux, have been proposed in the energy injection scenario, but they still have to be tested with broadband observations.

I have performed a spectral energy distribution (SED) and a temporal analysis on multiwavelength data to measure the individual parameters of afterglow. These measurements allow first to test some of the main features of the standard afterglow model, and second to give some insight into the possible additional components that are required to be added to the model in order to explain the whole set of observations. The analysis is performed on 4 GRBs that have more than two simultaneous X-ray to radio observations, and therefore on top of measuring the parameters at a single point in time, enable the test of the evolution (or lack of it) of these parameters and the break frequencies. Although there are several resources in the literature with details on the standard afterglow model, there is no full description of a set of analytical equations that include all the basic features of the standard model and the additional components that have been proposed along the years. A detailed description of the derivations to construct a more complete analytical set of equations ready to be used in the analysis of the observational data is given in Chap. 2. A set of computational tools to reduce and analyse the data together with the set of analytical equations was implemented to analyse some of the proposed questions of the thesis. Based on the list of open questions presented before, here are the questions that were studied in detail in this thesis.

1. Is it possible to differentiate between the proposed scenarios for the magnetic field production based on the measurement of ε_B?

2. Is the external medium density profile ISM- or stellar wind-like ? What is the density magnitude? How is this related to the progenitor star? What can we say from the density profile in relation to the GRB-SN connection?

3. The main radiation process is synchrotron radiation, but how important are other radiation processes such as synchrotron-self Compton radiation during the afterglow emission?

4. Can the observed X-ray plateau phases be explained as a continuous energy injection from the source into the outflow? Is it possible from the actual observations to discern between the different proposed mechanisms that may provide a long-lasting source of energy, and, if so, how does this set some constraints on the progenitor star?

5. The outflow is expected to be a jetted outflow: is this observed? What is the collimation angle?

6. The main acceleration process in the shock region is expected to be Fermi acceleration, however some deviations from the theoretical predictions have been observed. How can this be explained?

Chapter 2

Afterglow theory

In the standard afterglow model the observed γ-ray radiation is associated to an ultra-relativistic collimated outflow. The first indication of the need of an ultra-relativistic outflow comes from the "compactness problem". This problem makes reference to the large amount of energy and small size of the source required in the framework of a non-relativistic regime. An outflow with Lorentz factor $\Gamma > 100$ can solve this problem. However, Γ would be 2 orders of magnitude larger than known relativistic sources so far. This is solved in the relativistic fireball model by introducing an ultra-relativistic motion for both, the source and the outflow (Goodman 1986; Paczynski 1986). The relativistic fireball is composed of electrons, positrons, photons and baryons. The evolution of the fireball undergoes two main phases: a radiation and a matter dominated phase. In the radiation dominated phase the temperature of the fireball is > 20 keV allowing pair production. Because the source is optically thick the radiation pressure increases resulting in an expansion of the fireball. When the temperature drops below 20 keV pair production stops and the fireball becomes matter dominated. Baryons are accelerated to relativistic velocities until reaching a coasting stage (constant velocity). During this stage the energy can be either radiated away (radiative evolution) or most of the energy can be converted into kinetic energy (adiabatic evolution)[1].

The dissipation of the energy in the outflow takes place during the prompt (i.e., GRB) and, afterglow emissions Fig. 2.1. The prompt emission is associated to internal shocks between layers with different Lorentz factors (Rees & Meszaros 1992; Meszaros & Rees 1993). The afterglow emission is associated to the synchrotron radiation from Fermi accelerated electrons in the external shocks (between the outflow and the CNM). The synchrotron emission has been proven to be a dominant process in the afterglow emission, however, additional components to the model are required to explain all data sets (e.g., Price et al. 2002). For example, SSC radiation, continuous energy injection into the outflow and dynamical and geometrical effects of the outflow. The progenitor and central engine are still a main topic of debate. Even though, long GRBs are repeatedly associated with the collapse of massive stars and short GRBs with mergers of neutron stars and black holes, no convincing and definite evidence has been obtained yet.

[1] A fraction of the energy is radiated away in the form of gravitational waves and neutrinos.

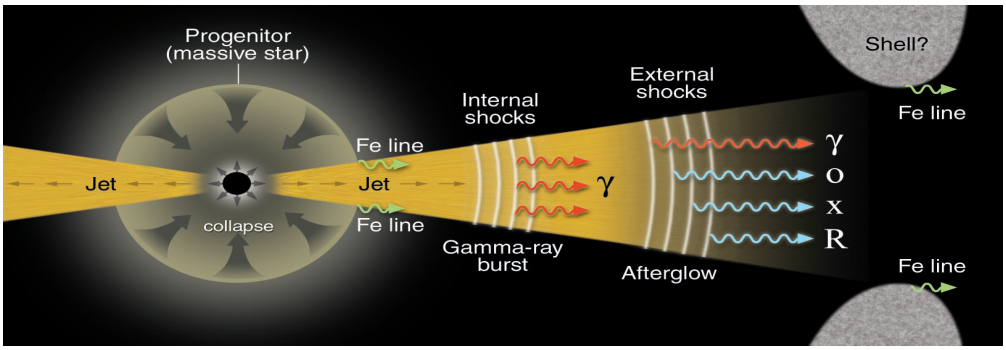

Figure 2.1: Schematic of the internal and external shocks system (Mészáros 2001).

2.1 Relativistic blast wave dynamics

In the standard GRB afterglow model the interaction between the ultra-relativistic outflow and the external medium produces a dual shock system (Piran 2004). The system is composed by a reverse shock (RS) propagating into the ejecta itself and, a forward shock (FS) propagating into the circumburst medium (CBM). The shock system has 4 regions (Fig. 2.2) that are described by the following thermodynamical quantities: particle density $n_{\rm i}$, pressure $p_{\rm i}$ and energy density $e_{\rm i}$ (Sari & Piran 1995). The un-shocked regions (1, 4) are cold fluids with energy densities $e_1 = e_4 = 0$ and, $\gamma_4 \approx \Gamma \gg 1$. The shocked regions (2,3) have the same pressure and therefore $e_2 = e_3 = e$. Due to the shock compression the energy density in the shocked region is $e \approx 4\Gamma n_1 m_p c^2$, with m_p the proton mass and c the speed of light in vacuum. However, the density in the shocked shell material region is lower than the one in the shocked CBM due to the difference in temperature, i.e., $T_{\rm FS} < T_{\rm RS}$. This difference implies a lower peak frequency for the emission from the RS region than the one from the FS region.

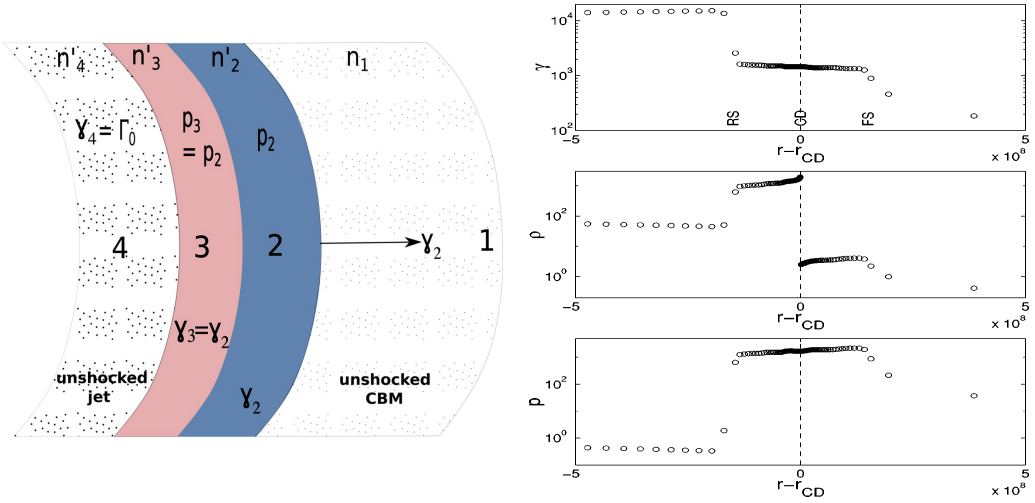

(a) Schematic of the dual shock system. **(b)** Thermodynamical quantities.

Figure 2.2: Left: *Region 1*: unshocked CBM. *Region 2*: shocked CBM (FS). *Region 3*: shocked shell inside the outflow (RS). *Region 4*: unshocked shell (Kumar & Zhang 2014). **Right**: Thermodynamical quantities in the 4 regions system. Mass density ρ, pressure p and the Lorentz factor of each region γ (Piran 2004).

The RS can have an important contribution to the afterglow emission and can affect the dynamics of the outflow (Sec. 2.1.1). However, once the RS crosses the shell and, assuming that all the energy is instantaneously injected, the blast wave enters a self-similar phase (Blandford & McKee 1976) and RS is not important anymore. Assuming an adiabatic evolution this phase self-similar is described by

$$\rho = A r^{-k}, \quad k<4 \quad , \tag{2.1}$$

$$e = 2\Gamma^2 \rho_{ext} c^2 \chi^{-\frac{17-4k}{3(4-k)}} \quad , \tag{2.2}$$

$$n = 2^{\frac{3}{2}} \Gamma n_{ext} \chi^{-\frac{10-3k}{3(4-k)}} \quad , \tag{2.3}$$

$$\gamma = 2^{-\frac{1}{2}} \Gamma \chi^{-\frac{1}{2}} \quad , \tag{2.4}$$

for the mass ρ, energy e and particle n density, and the Lorentz factor of the shocked fluid γ, respectively. χ is the similarity variable. k defines the density profile of the CBM, i.e., $k=0$ homogeneous medium (ISM), $k=2$ stellar wind-like environment, and A is a normalisation factor (Chevalier 2000). This phase is usually referred as the FS emission.

The evolution of the FS observed along the line of sight is described by the Lorentz factor of the fluid γ_l (Eq. 2.6) and the radius r_l (Eq. 2.5) (Mészáros & Rees 1997; Granot & Sari 2002). In a simple analytical model, the emission from different sites on the blast wave can be important. This effect can be introduced by $r=\zeta r_{\rm L}$ and $\gamma=\zeta^{-1/2}\gamma_{\rm L}$, with ζ 0.78 and 0.56 for low- and high-frequencies[2], respectively. $Q_{\rm x}=Q\times 10^{\rm x}$ in CGS units[3].

$$r_l = N_{r_l} K_{r_l} \left[\frac{E_{52} t_{d_z}}{A_*}\right]^{\frac{1}{4-k}}, \quad N_{r_l} = \left[\frac{86400\times 10^{52}}{(5\times 10^{11})^{\frac{k}{2}} m_p^{\frac{2-k}{2}}}\right]^{\frac{1}{4-k}}, \quad K_{r_l} = \left[\frac{(17-4k)(4-k)}{4\pi c}\right]^{\frac{1}{4-k}} \tag{2.5}$$

$$\gamma_l = N_\gamma K_\gamma \left[\frac{E_{52}}{A_* t_{d_z}^{3-k}}\right]^{\frac{1}{2(4-k)}}, \quad ,N_\gamma = \left[\frac{10^{52}}{(5\times 10^{11})^{\frac{k}{2}} m_p^{\frac{2-k}{2}} 86400^{3-k}}\right]^{\frac{1}{2(4-k)}}, \quad K_\gamma = \left[\frac{17-4k}{4^{5-k}(4-k)^{3-k}\pi c^{5-k}}\right]^{\frac{1}{2(4-k)}} \quad . \tag{2.6}$$

2.1.1 Reverse shock

The RS[4] emission has two limiting regimes defined by the ratio $\eta_{\rm RS}$=n_4/n_1. A Newtonian regime when $\eta_{\rm RS}\gg\Gamma^2$ and a relativistic regime when $\eta_{\rm RS}\ll\Gamma^2$. Four main radii characterise the evolution of the RS: 1) $r_{\rm N}$: at which RS becomes relativistic, i.e., $\eta_{\rm RS}=\Gamma^2$. 2) r_Δ: radius where RS crosses the shell. 3) $r_{\rm dec}$ marks the deceleration phase. 4) $r_{\rm s}$ marks the start of the spreading phase.

Newtonian case (thin shell): $\eta_{\rm RS}>1$ and $r_\Delta<r_\Gamma<r_{\rm N}$. The RS is generally too weak to slow down the shell and to affect the dynamics of the outflow. However, if $r_{\rm s}<r_\Delta$ there is a time delay for RS to reach $r_{\rm N}$ and, therefore RS could become mildly relativistic. If this is the case the isotropic energies of both, the FS and the RS are comparable and the blast wave is no longer ultra-relativistic. New scalings to the self-similar solutions have to be introduced as $\gamma\sim r^{-g}$ and

[2]Numerical methods can include this effect integrating over θ.

[3]The stellar wind-like medium: $A=\dot{M}_{\rm W}/4\pi {\rm v_W}=5\times 10^{11}A_*$ g cm^{-1} (Chevalier & Li 2000). $\dot{M}_{\rm W}$ is the mass-loss rate and $\rm v_W$ is the wind velocity. The reference values are $\dot{M}_{\rm W}=10^{-5}M_\odot$ yr^{-1} and ${\rm v_W}=1000$ km s^{-1}. ISM: $A_*=n_0$. t is in days and is corrected by redshift z effect $t_{d_z}=t_{\rm d}/(1+{\rm z})$.

[4]The reverse shock emission is of special importance to characterise the properties of the GRB central engine and progenitor in cases where the forward shock is no longer ultra-relativistic, $\Gamma\sim 10$ (Kobayashi 2000).

$r \sim t^{1/1+2g}$, with $g = 2$ for ISM and $g = 1$ for a stellar wind-like density profile (Kobayashi 2000; Gao et al. 2013).

Relativistic case (thick shell): $\eta_{\rm RS} < 1$ and $r_{\rm N} < r_\Gamma < r_\Delta < r_{\rm s}$. In this case the contributions from both the FS and the RS are equally important. The spreading is irrelevant as it is expected to happen after the start of the deceleration phase where most of the energy have been converted into thermal energy. When the RS has crossed the shell $\gamma \sim t^{(2k-7)/4(4-k)}$ and $r \sim t^{1/(8-2k)}$. If the RS is strong enough an additional component at low frequencies is expected to rise in the spectral energy distribution.

2.1.2 Energy injection

If the energy is not injected "instantaneously" into the shock, there is a change in the dynamics of the outflow. Two different mechanisms are proposed to explained a prolonged energy injection phase:

Long-lived central engine: the luminosity of the central engine has a temporal dependence as $L(t) = L_0(t_{\rm obs}/t_0)^{-q}$, with the injection parameter $q < 1$ ($q \geq 1$ represents the instantaneous energy injection) and L_0 the initial luminosity of the blast wave (Dai & Lu 1998a, 2000; van Eerten 2014). The total energy of the blast wave is $E = E_0 + E_{\rm inj}$. If $E_0 \gg E_{\rm inj}$ there is no change in the dynamics of the outflow, but if $E_0 \ll E_{\rm inj}$ the dynamics of the outflow are given by

$$E_{\rm inj} \propto t_{d_z}^{1-q}, \quad r_{\rm inj} \propto t_{d_z}^{\frac{2-q}{4-k}}, \quad \gamma_{\rm inj} \propto t_{d_z}^{\frac{k-q-2}{2(4-k)}} \quad \text{for} \quad \mathrm{q} < 1. \tag{2.7}$$

This change in the dynamics can be written in terms of γ (Eq. 2.6) and r (Eq. 2.5) as

$$\gamma_{\rm inj} \;=\; \gamma\, N_{\gamma_{\rm inj}}\, t_{d_z}^{\frac{1-q}{2(4-k)}}, \quad N_{\gamma_{\rm inj}} = 86400^{\frac{1-q}{2(4-k)}}\,(1-q)^{-1}, \tag{2.8}$$

$$r_{\rm inj} \;=\; r\, N_{r_{\rm inj}}\, t_{d_z}^{\frac{1-q}{4-k}}, \quad N_{r_{\rm inj}} = 86400^{\frac{1-q}{4-k}}\,(1-q)^{-1}. \tag{2.9}$$

The exact type of progenitor and central engine are not known yet. A strong candidate in this scenario is a millisecond magnetar which has q = 0.

Stratification of the mass ejecta: In this case the outflow is composed by shells moving with different velocities, γ_s, and a distribution given by $M(>\gamma) \propto \gamma^{-\rm s}$ (Rees & Mészáros 1998), with s>1. The dynamics of the outflow during this phase are given by

$$E^s_{\rm inj} \propto \gamma^{-s+1}, \quad r^s_{\rm inj} \propto t_{d_z}^{\frac{s+1}{7+s-2k}}, \quad \gamma^s_{\rm inj} \propto t_{d_z}^{\frac{k-3}{7+s-2k}}. \tag{2.10}$$

The radius and the Lorentz factor in the energy injection phase can be written in terms of γ (Eq. 2.6) and r (Eq. 2.5) as

$$\begin{aligned} \gamma^s_{\rm inj} &= \gamma\, N^s_{\gamma_{\rm inj}}\, t_{d_z}^{\frac{(3-k)(s-1)}{2(4-k)(7+s-2k)}}, \quad N^s_{\gamma_{\rm inj}} = 86400^{\frac{(3-k)(s-1)}{2(4-k)(7+s-2k)}}, \\ r^s_{\rm inj} &= r\, N^s_{r_{\rm inj}}\, t_{d_z}^{\frac{(3-k)(s-1)}{(4-k)(7+s-2k)}}, \quad N^s_{r_{\rm inj}} = 86400^{\frac{2(3-k)(s-1)}{(4-k)(7+s-2k)}}. \end{aligned} \tag{2.11}$$

This scenario complete agreement with the collapsar model and with a short-lived central engine.

Assuming that the energy injection in any of the two proposed scenarios has the same evolution, a relation between the injection parameters s and q can be establish as (Zhang et al. 2006)

$$s = \frac{3k - 10 + 7q - 2kq}{k - 2 - q}, \quad q = \frac{3k - 10 + 2s - ks}{2k - 7 - s}. \tag{2.12}$$

2.1.3 Jet break

The relativistic outflow can be treated as an isotropic outflow as long as $\gamma > 1/\theta_0$, with θ_0 the initial half-opening angle. However, when $\gamma^{-1} \sim \theta_0$, the jet nature of the outflow becomes evident to the observer and corrections on the dynamics of the afterglow have to be included. The jet-break is observed as an achromatic change in the temporal slopes. The time of the break is given by (Granot et al. 2005)

$$t_{\rm j}(E) = \frac{(1+z)}{4\,c}\left[\frac{(3-k)\,E_{\rm jet}}{2\,\pi\,A\,c^2}\right]^{1/(3-k)}, \tag{2.13}$$

where $E_{\rm jet}$ is the true energy of the outflow related to $E_{\rm K,iso}$ as $E_{\rm jet} \approx f_{\rm b} E_{\rm K,iso}$, with $f_{\rm b} = 1 - \cos\theta \approx {\theta_0}^2/2$.

There are two limiting scenarios to study the effects and causes of the jet break:
Geometrical "edge" effect: The jet break is due to geometrical effects, i.e., when the edge of the outflow becomes evident, rather than to the change in the dynamics of the outflow. The jet keeps expanding within the initial opening angle θ_0 until it becomes non-relativistic at $t(E_{\rm K,iso})$. This time has a delay by a factor of ${\theta_0}^{-2/(3-k)}$ compared with the case when lateral expansion of the outflow is assumed. In this case, because no change in the dynamics is observed yet, the self-similar solutions are still valid. A correction to the peak flux to compensate for the difference when compared to the isotropic case must be included (Granot et al. 2005).
Sideways expansion: In this case a sideways expansion of the jet starts as soon as $\theta_0 \sim \gamma^{-1}$ at $t(E_{\rm jet})$ (Rhoads 1999). Results from simulations suggest that most of the energy in the jet remains within θ_0 until the outflow reaches a sub-relativistic phase (e.g., van Eerten & MacFadyen 2012). The change in the dynamics is treated, in semi-analytical models, as an exponential behaviour. The evolution of $\gamma \approx {\theta_0}^{-1}\exp(-r/r_{\rm j})$ with $r_{\rm j} = ct(E_{\rm jet})$ (Granot & Piran 2012).

2.1.4 Particle acceleration and microphysics

An external shock is produced during the interaction between the outflow and the external medium. The magnetic field strength in the shocked region holds a fraction $\varepsilon_{\rm B}$ of the internal energy as $B^2/8\pi = \varepsilon_{\rm B} e$ and $B = \left(32\pi m_{\rm p} c^2\right)^{1/2} {\varepsilon_{\rm B}}^{1/2} {n}^{1/2} \gamma$. The magnetic field is randomise and the particles are reflected due to magnetic field inhomogeneities back and forth between the shocked and the un-shocked regions changing the velocity vectors of the particles (Waxman & Draine 2000). This change in B and velocity, combined with the fact that the mean free path for collisions between the particles is larger than the typical size of the system (width of the shell) result in electrons undergoing Fermi acceleration. The energy distribution of the non-thermal population of accelerated electrons is described by (Panaitescu & Kumar 2000)

$$\frac{dn_e}{d\gamma_e} \propto \gamma_e^{-p}, \quad \text{for} \quad \gamma_{\rm m} < \gamma_{\rm e}, \tag{2.14}$$

with p the e^- index, $\gamma_{\rm e}$ the Lorentz factor of the accelerated electrons and $\gamma_{\rm m}$ the injection factor. The electron energy distribution defines the general shape of the observed spectrum. The boundary condition at the shock front for energy and mass conservation are

$$\int_{\gamma_m}^{\gamma_M} \frac{dn_e}{d\gamma_e} d\gamma_e = 4\gamma n \quad , \tag{2.15}$$

$$\int_{\gamma_m}^{\gamma_M} (\gamma_e m_e c^2) \frac{dn_e}{d\gamma_e} d\gamma_e = 4\gamma^2 n m_p c^2 \varepsilon_e \quad , \tag{2.16}$$

respectively, with $\gamma_{\rm M}$ an upper limit on the energy of the accelerated electrons that have a fraction $\varepsilon_{\rm e}$ ($= e_e/e$) ($\bar{\varepsilon}_{\rm e} = |p-2|/(p-1)\varepsilon_{\rm e}$) of the available internal energy[5] From the boundary conditions, a general expression is derived for the injection Lorentz factor $\gamma_{\rm m}$ as

$$\gamma_m = \frac{m_p}{m_e} \begin{cases} \bar{\varepsilon}_e \, \gamma, & \text{for p} > 2\,, \\ \left(\bar{\varepsilon}_e \, \gamma \, \gamma_M^{p-2}\right)^{\frac{1}{p-1}}, & \text{for } 1 < \text{p} < 2\,. \end{cases} \tag{2.17}$$

As introduced in Sec. 1.2, the essential quantities to understand the physics of the GRB afterglows are: the *microphysical parameters* $\varepsilon_{\rm e}$, $\varepsilon_{\rm B}$ and p and, the *dynamical parameters* $E_{\rm K,iso}$ which is the kinetic isotropic in the outflow during the afterglow phase and A that is the density normalisation (A_* for k = 2 and n_0 for ISM).

2.2 Radiation processes

The Lorentz factor of the accelerated electrons $\gamma_{\rm e}$evolves during the acceleration and emission processes (Rybicki & Lightman 1979) as

$$\frac{d\gamma_e}{dt'} = -\frac{\sigma_T \, B^2 \, (1+Y)}{6 \, \pi \, m_e \, c} \gamma_e^2 + \frac{\gamma_e}{3 \, n} \frac{dn}{dt'}. \tag{2.18}$$

with Y the Compton parameter introduced as a correction due to SSC radiation, m_e the electron mass and σ_T the Thompson cross section (Panaitescu & Kumar 2000). The first term in Eq. 2.18 represents the radiative losses, i.e., global cooling, while the second term represent the adiabatic losses, i.e., local cooling. Radiative losses are associated to a dominant synchrotron emission and other cooling processes such as SSC radiation. Neglecting adiabatic losses, the characteristic Lorentz factor for the cooling of the electron $\gamma_{\rm c}$ can be derived as

$$\gamma_c = \frac{6\pi m_e c}{\sigma_T} \frac{1}{(1+Y) B^2 \gamma t_z}. \tag{2.19}$$

Three important time scales can be defined: the acceleration time, the radiation time and a timescale equivalent to the remanent age as

$$t_{acc} = \frac{2 \, \pi \, r_L}{c} = \frac{2 \, \pi \, m_e \, c^2}{q_e \, B \, \gamma}, \tag{2.20}$$

$$t_{rad} = \frac{\gamma_e \, m_e \, c^2}{P_e} = \frac{6 \, \pi \, m_e \, c}{(1+Y) \, \sigma_T \, \gamma \, \gamma_e \, B^2}, \tag{2.21}$$

$$t_{rem} = \frac{1}{c} \int \frac{dr}{\gamma^2}, \tag{2.22}$$

[5] $\gamma_{\rm M}$ is important to avoid an energy divergence in case the an electron index $1 < p < 2$. The exact mathematical expression for this upper limit may vary depending on the assumptions.

respectively. Where r_L is the Larmor radius, P_e is the radiated power per electron with energy γ_e and q_e is the electron charge. $\gamma_{\rm M}$is derived at the time when $t_{acc} = t_{rad}$ (Bhattacharya 2001; Dai & Cheng 2001) as

$$\gamma_M \;=\; \left(\frac{3\,q_e\,(1+Y)\,B}{\phi\;\sigma_T}\right)^{\frac{1}{2}}, \tag{2.23}$$

with ϕ the ratio between the acceleration the gyration times. $\gamma_{\rm M}$ becomes more important as the values for $p \to 1$ or for $\phi > 1000$, otherwise $\gamma_{\rm M}$lies above the soft X-ray domain. For simplicity of the model and the available data ϕ is set to 1.

Synchrotron self-Compton radiation

Synchrotron self-Compton radiation (SSC) is expected to be a dominant component to the electron cooling during the early stages of the evolution. The strength of SSC depends only on the underlying physics of the blast wave (Sari & Esin 2001). It is defined as the ratio of the luminosities due SSC and synchrotron radiation, i.e., $L_{\rm IC}/L_{\rm syn} = U_{\rm rad}/U_{\rm B}$. $\eta_{\rm IC}$ is the fraction of the electron energy that is radiated away during the afterglow emission defined as

$$\eta_{\rm IC} = \begin{cases} 1 & , \quad \text{if} \quad \gamma_{\rm m} > \gamma_{\rm c}\,, \\ \left(\frac{\gamma_c}{\gamma_m}\right)^{2-p} = \left(\frac{\nu_c}{\nu_m}\right)^{\frac{2-p}{2}} & , \quad \text{if} \quad \gamma_{\rm m} < \gamma_{\rm c}\,. \end{cases} \tag{2.24}$$

If $\eta_{\rm IC}(\varepsilon_{\rm e}/\varepsilon_{\rm B}) \ll 1$ SSC radiation is negligible, otherwise the SSC component is important and must be included through out the analysis. A general expression for the Compton factor Y is given by

$$Y = \left(\eta_{\rm IC}\,\frac{\bar{\varepsilon}_e}{\varepsilon_B}\,\frac{p-1}{|p-2|}\right)^{\frac{1}{2}}, \quad \text{for} \quad \eta_{\rm IC}\,\frac{\bar{\varepsilon}_{\rm e}}{\varepsilon_{\rm B}} \gg 1\,. \tag{2.25}$$

The main effect of the SSC is reflected in the initial position of the main break frequencies of the synchrotron spectrum. When it is strong enough it is directly observed as a change in the temporal slope of the X-ray data and in the spectral energy distribution (SED) slope above $\nu_{\rm c}$. A test to check whether the synchrotron emission is the only dominant component in the observed emission or, if there are other important contributing effects can be done using the C parameter (Sari & Esin 2001). This parameter is derived based only on the observables, i.e., break frequencies (Sec. 2.2.1) and is given by

$$C \equiv \begin{cases} S : N_S\, d_{L_{28}}^{-2} t_d^4 (1+z)^4 \eta_{IC} F_m^{-1} \nu_c^{\frac{3}{2}} \nu_m^{\frac{13}{6}} \nu_{sa}^{\frac{10}{3}} = \frac{Y}{(Y+1)^2}, \\ F : N_F\, d_{L_{28}}^{-2} t_d^4 (1+z)^4 \eta_{IC} F_m^{-1} \nu_c^{\frac{19}{6}} \nu_m^{\frac{1}{2}} \nu_{sa}^{\frac{10}{3}} = \frac{Y}{(Y+1)^2}, \end{cases} \tag{2.26}$$

where S stands for slow cooling and F for fast cooling. N_i are the normalisation constants that depend on the normalisation of the break frequencies and the peak flux $F_{\rm m}$. The Eq. 2.26 only have a real solution if C<1/4 and is of the form

$$C \ll \frac{1}{4} : \begin{cases} Y = \frac{1-2C-(1-4C)^{\frac{1}{2}}}{2C} \approx C \ll 1 & , \\ Y = \frac{1-2C+(1-4C)^{\frac{1}{2}}}{2C} \approx \frac{1}{C} \gg 1 & . \end{cases} \tag{2.27}$$

If C < 1/4 SSC component can be either dominant or not. If C > 1/4 there must be an important contribution from another process to the cooling of the electrons. This contribution can be SSC and/or any other mechanisms.

2.2.1 Synchrotron spectrum

The typical observed afterglow spectrum is composed by a set of power-law segments joined at some specific frequencies. These frequencies are known as the characteristics break frequencies and are derived based on the standard definition of the general synchrotron frequency

$$\nu_{syn}(\gamma_e) = K_\nu \, \gamma B \, \gamma_e^2 \, (1+z)^{-1}, \quad K_\nu = \frac{3\, q_e \sin\alpha}{4\pi m_e c} \quad , \tag{2.28}$$

for an electron with Lorentz factor γ_e. The radiated power per electron with energy γ_e due to synchrotron radiation is given by

$$P(\gamma_e) = K_P \, \gamma^2 \, B^2 \, \gamma_e^2 \, , \quad K_P = \frac{4\sigma_T c}{3\,8\pi} \, , \tag{2.29}$$

with the maximum power emitted at a frequency $\nu(\gamma_e)$

$$P_m = \frac{P(\gamma_e)}{\nu(\gamma_e)} \, , \tag{2.30}$$

and the peak flux F_m of the observed synchrotron spectrum given by

$$F_m = \frac{1}{4\pi \cdot 10^{56}} \, N_e(r) \, P_m \, d_{L_{28}}^{-2} \, , \tag{2.31}$$

where d_L is the luminosity distance and $N_e(r)$ is the number of electrons in a volume with radius r.

The synchrotron spectrum is defined by F_m together with three characteristic break frequencies: the cooling frequency $\nu_c = \nu(\gamma_c)$, the injection frequency $\nu_m = \nu\,(\gamma_m)$ and the self-absorption break frequency ν_{sa} . Based on the relative position of the break frequencies, different spectral regimes are defined. First, fast ($\nu_c < \nu_m$) and slow ($\nu_c > \nu_m$) cooling regimes. In the fast cooling regime the bulk of the electrons have energies above γ_c, being able to cool down fast and efficiently, i.e., within the dynamical time of the system. The time duration of the fast cooling regime depends on the CBM profile. A few hundred of seconds for an ISM density profile and, a few thousand of seconds for a stellar wind-like density profile. In the slow cooling regime most of the electrons have Lorentz factor γ_m . Therefore only a small fraction of the electron ($\gamma_e > \gamma_c$) is affected by the cooling effects.

When ν_{sa} is taken into account, there is a subdivision of both, the fast and slow cooling regimes. Following Granot & Sari (2002) five spectral regimes can describe the whole evolution of the GRB afterglow. The shape of the five different spectral energy distribution regimes is given by

$$F_\nu^{[1]} = F_m^{[1]} \begin{cases} \left(\frac{\nu}{\nu_{sa_1}}\right)^2 \left(\frac{\nu_{sa_1}}{\nu_m}\right)^{\frac{1}{3}}, & [B] : \nu < \nu_{sa_1} \quad , \\ \left(\frac{\nu}{\nu_m}\right)^{\frac{1}{3}}, & [D] : \nu_{sa_1} < \nu < \nu_m \quad , \\ \left(\frac{\nu}{\nu_m}\right)^{\frac{1-p}{2}}, & [G] : \nu_m < \nu < \nu_c \quad , \\ \left(\frac{\nu}{\nu_c}\right)^{\frac{-p}{2}} \left(\frac{\nu_c}{\nu_m}\right)^{\frac{1-p}{2}}, & [H] : \nu_c < \nu \quad , \end{cases} \tag{2.32}$$

$$F_\nu^{[2]} = F_m^{[2]} \begin{cases} \left(\frac{\nu}{\nu_m}\right)^2 \left(\frac{\nu_m}{\nu_{sa_2}}\right)^{\frac{5}{2}}, & [B] : \nu < \nu_m \quad , \\ \left(\frac{\nu}{\nu_{sa_2}}\right)^{\frac{5}{2}}, & [A] : \nu_m < \nu < \nu_{sa_2} \quad , \\ \left(\frac{\nu}{\nu_{sa_2}}\right)^{\frac{1-p}{2}}, & [G] : \nu_{sa_2} < \nu < \nu_c \quad , \\ \left(\frac{\nu}{\nu_c}\right)^{\frac{-p}{2}} \left(\frac{\nu_c}{\nu_{sa_2}}\right)^{\frac{1-p}{2}}, & [H] : \nu_c < \nu \quad , \end{cases} \tag{2.33}$$

$$F_\nu^{[3]} = F_m^{[3]} \begin{cases} \left(\frac{\nu}{\nu_m}\right)^2 \left(\frac{\nu_m}{\nu_{sa_3}}\right)^{\frac{5}{2}}, & [B] : \nu < \nu_m \quad , \\ \left(\frac{\nu}{\nu_{sa_3}}\right)^{\frac{5}{2}}, & [A] : \nu_m < \nu < \nu_{sa_3} \quad , \\ \left(\frac{\nu}{\nu_{sa_3}}\right)^{\frac{-p}{2}}, & [H] : \nu_{sa_3} < \nu \quad , \end{cases} \tag{2.34}$$

$$F_\nu^{[4]} = F_m^{[4]} \begin{cases} \left(\frac{\nu}{\nu_{ac}}\right)^2 \left(\frac{\nu_{ac}}{\nu_{sa_4}}\right)^{\frac{11}{8}}, & [B] : \nu < \nu_{ac} \quad , \\ \left(\frac{\nu}{\nu_{sa_4}}\right)^{\frac{11}{8}}, & [C] : \nu_{ac} < \nu < \nu_{sa_4} \quad , \\ \left(\frac{\nu}{\nu_{sa_4}}\right)^{-\frac{1}{2}}, & [F] : \nu_{sa_4} < \nu < \nu_m \quad , \\ \left(\frac{\nu}{\nu_m}\right)^{\frac{-p}{2}} \left(\frac{\nu_{sa_4}}{\nu_m}\right)^{\frac{1}{2}}, & [H] : \nu_m < \nu \quad , \end{cases} \tag{2.35}$$

$$F_\nu^{[5]} = F_m^{[5]} \begin{cases} \left(\frac{\nu}{\nu_{ac}}\right)^2 \left(\frac{\nu_{ac}}{\nu_{sa_5}}\right)^{\frac{11}{8}} \left(\frac{\nu_{sa_5}}{\nu_c}\right)^{\frac{1}{3}} & [B] : \nu < \nu_{ac} \quad , \\ \left(\frac{\nu}{\nu_{sa_5}}\right)^{\frac{11}{8}} \left(\frac{\nu_{sa_5}}{\nu_c}\right)^{\frac{1}{3}}, & [C] : \nu_{ac} < \nu < \nu_{sa_5} \quad , \\ \left(\frac{\nu}{\nu_c}\right)^{\frac{1}{3}}, & [E] : \nu_{sa_5} < \nu < \nu_c \quad , \\ \left(\frac{\nu}{\nu_c}\right)^{\frac{-1}{2}}, & [F] : \nu_c < \nu < \nu_m \quad , \\ \left(\frac{\nu}{\nu_m}\right)^{\frac{-p}{2}} \left(\frac{\nu_c}{\nu_m}\right)^{\frac{1}{2}}, & [H] : \nu_m < \nu \quad , \end{cases} \tag{2.36}$$

where the lower index refers to the spectrum number and, the labels from [A] to [H] refers to the specific power-law segment on the spectrum (Fig. 2.3). Expressions for $F_{\rm m}$[6] in the optically thick region and $\nu_{\rm sa}$ and $\nu_{\rm ac}$ are discussed in more detail later in the chapter.

Cooling break

$\nu_{\rm c}$ is given by $\nu(\gamma_{\rm c})$, corresponding to the breaks (3) and (11) in Fig. 2.3. It can written in terms of the afterglow parameters as

$$\nu_c \sim \varepsilon_B^{\frac{-3}{2}} A_*^{\frac{-4}{(4-k)}} (E_{52}\, t_d)^{\frac{3k-4}{2(4-k)}} (1+z)^{\frac{(4+k)}{2(4-k)}} (1+Y)^{-2}. \tag{2.37}$$

When the energy injection contribution is included, a temporal evolution of $\nu_{\rm c}$ is modifies as

$$\nu_{c_{\rm inj}} \sim \nu_c\, t_{d_z}^{\frac{(3k-4)(1-q)}{2(4-k)}}. \tag{2.38}$$

Finally, when $Y \gg 1$ the SSC component is included and $\nu_{\rm c}$ is of the form

$$\nu_c^{IC} \sim \eta_{IC}^{-2}\, \varepsilon_B^{-\frac{1}{2}}\, \bar{\varepsilon}_e^{-1} A_*^{\frac{-4}{(4-k)}} (E_{52}\, t_d)^{\frac{3k-4}{2(4-k)}} (1+z)^{\frac{(4+k)}{2(4-k)}}, \tag{2.39}$$

$$\nu_{c_{inj}}^{IC} \sim \nu_c^{IC}\, t_{d_z}^{\frac{(3k-4)(1-q)}{2(4-k)}}. \tag{2.40}$$

without and with energy injection component, respectively.

Injection break

$\nu_{\rm m}$ is given by $\nu(\gamma_{\rm m})$, corresponding to the breaks (2), (4) and (9) in Fig. 2.3. If $p > 2$ then $\gamma_{\rm m} \sim \gamma$, but if $1 < p < 2$ this proportionality changes and so does the temporal evolution of the break frequencies and peak flux. Due to the lack of consensus on the definition of $\gamma_{\rm M}$, I present

[6]Eq. 2.31 applies for $F_{\rm m}$ in Eq. 2.32 and Eq. 2.36. For the remaining three spectra the peak flux is modified.

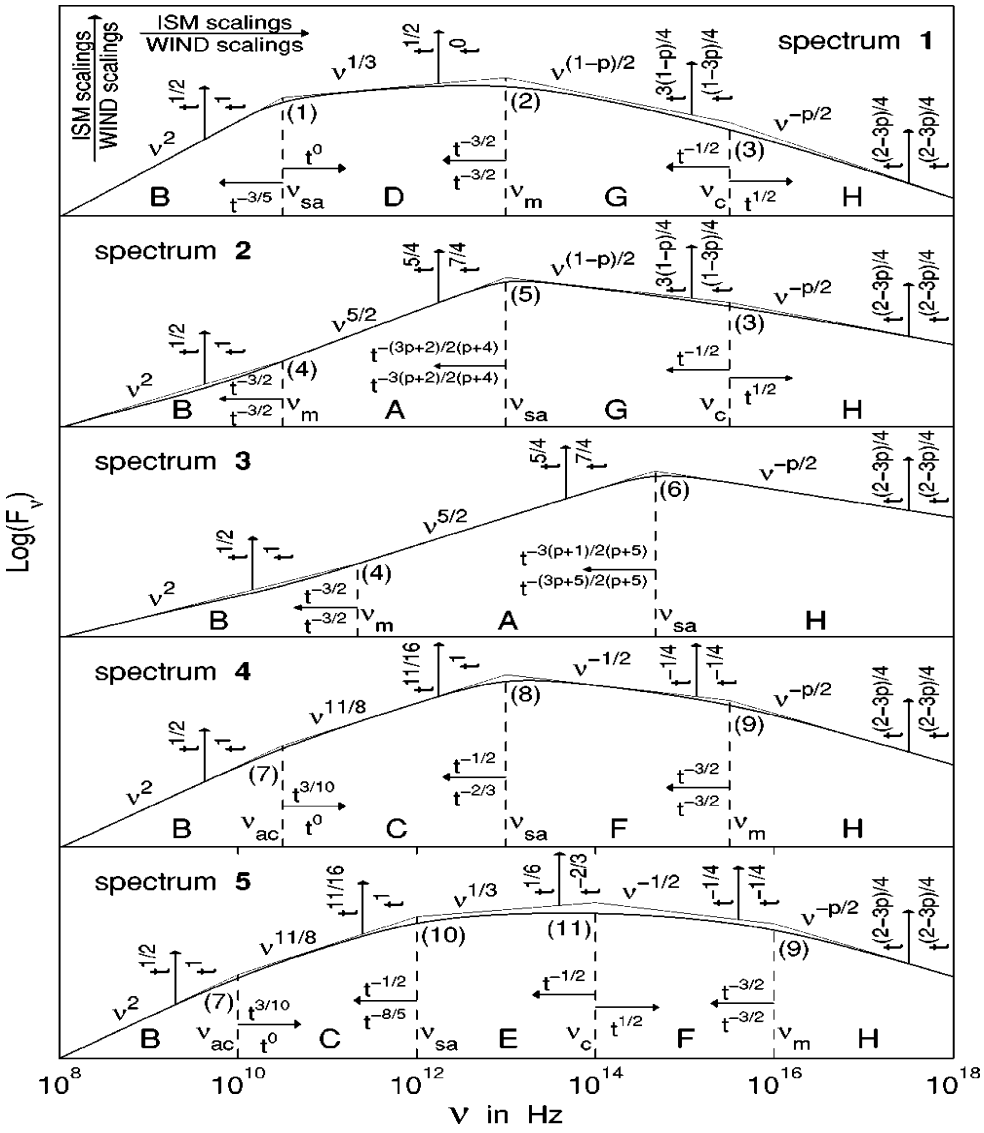

Figure 2.3: Schematic representation of the observed synchrotron spectra at five different stages during the afterglow evolution. Each spectra is described by Eqs. 2.32, 2.33, 2.34, 2.35 and 2.36, from top to bottom, respectively. Taken from Granot & Sari (2002)

two approaches: DC[7] (Dai & Cheng 2001) where $\gamma_{\rm M}$ is defined by Eq. 2.23 and, GS where $\gamma_{\rm m}$ is assumed to keep the proportionality to γ (i.e., $p \sim 2$) and the equations presented in Granot & Sari (2002) for the break frequencies and the peak flux are still valid. $\nu_{\rm m}$ is then given by

$$\nu_m \sim \begin{cases} \varepsilon_B^{\frac{1}{2}}\,\bar{\varepsilon}_e^{2}\,E_{52}^{\frac{1}{2}}\,t_d^{\frac{-3}{2}}\,(1+z)^{\frac{1}{2}} & ,\ \text{for}\quad \mathrm{p}>2\,, \\ \left[\dfrac{\bar{\varepsilon}_e^{4(4-k)}\,\varepsilon_B^{4-k}\,t_d^{p(k-3)+k-6}\,E_{52}^{4+k(p-2)-p}\,A_*^{p-2}}{(1+Y)^{2(2-p)(4-k)}\,(1+z)^{14+k(p-3)-5p}}\right]^{\frac{1}{2(4-k)(p-1)}} & ,\ \text{for}\quad 1<\mathrm{p}<2\,. \end{cases} \tag{2.41}$$

[7] I derive independently all the equations for the regime where $1 < \mathrm{p} < 2$. The formalism is described in detail along the chapter and is similar to GS with $\gamma_{\rm M}$ introduced. SSC and energy injection components in this regime are analysed in the fast and slow cooling regime. The euqationss were derived for a general density profile with slope k.

The temporal evolution of $\nu_{\rm m}$ when the energy injection phase is ongoing is given by

$$\nu_{m_{\rm inj}} \sim \begin{cases} \nu_m \cdot t_{d_z}^{\frac{1-q}{2}} & , \text{for} \quad \mathrm{p} > 2\,, \\ \nu_m \cdot t_{d_z}^{\frac{(k-p-2)(1-q)}{2(4-k)(1-p)}} & , \text{for} \quad 1 < \mathrm{p} < 2\,. \end{cases} \tag{2.42}$$

Finally, only when $1 < p < 2$ $\gamma_{\rm M}$ depends on the mechanisms responsible for the electron cooling and, therefore SSC radiation becomes important. The general expression for $\nu_{\rm m}$ with SSC effect included for $1 < p < 2$, without and with energy injection contribution included, is given by

$$\nu_m^{IC} \sim \eta_{IC}^{\frac{p-2}{p-1}} \bar{\varepsilon}_e^{\frac{2+p}{2(p-1)}} \varepsilon_B^{\frac{3-p}{2(p-1)}} t_d^{\frac{p(k-3)+k-6}{2(4-k)(p-1)}} E_{52}^{\frac{4+k(p-2)-p}{2(4-k)(p-1)}} A_*^{\frac{p-2}{2(4-k)(p-1)}} (1+z)^{\frac{5p-14-k(p-3)}{2(4-k)(p-1)}}\,, \tag{2.43}$$

$$\nu_{m_{inj}}^{IC} \sim \nu_m^{IC} t_{d_z}^{\frac{(k-p-2)(1-q)}{2(4-k)(1-p)}}\,. \tag{2.44}$$

Optically thick emission region

The emission region can be thin or thick during the afterglow emission. The optical depth (τ) to electron scattering is only important if the mission region is optically thick. When $\tau > 1$ there is an important change in the observed flux density and in the evolution of $\nu_{\rm sa}$ and $\nu_{\rm ac}$. In this optically thick case, i.e., $\nu_{\rm sa} > \nu$, the location in the system of the emitting electrons is important. In the optically thin emission all the electron will escape the system regardless their distribution (homogeneous or inhomogeneous), while in the optically thick part of the spectrum they will not. Following Rybicki & Lightman (1979) and Panaitescu & Kumar (2000), an expression for the optical thickness in terms of ν, $\nu_{\rm m}$, $\nu_{\rm c}$ is derived by equating the synchrotron emission (optically thin) and the blackbody emission (optically thick). τ is given by

$$\tau_\nu = \begin{cases} \tau_p \times \left(\frac{\nu}{\nu_p}\right)^{-\frac{5}{3}}, & \nu < \nu_p \\ \tau_p \times \left(\frac{\nu}{\nu_p}\right)^{-\frac{q+4}{2}}, & \nu_p < \nu < \nu_o \end{cases} \tag{2.45}$$

where γ_p =min($\gamma_{\rm m}$,$\gamma_{\rm c}$), ν_p =min($\nu_{\rm m}$,$\nu_{\rm c}$), ν_o =max($\nu_{\rm m}$, $\nu_{\rm c}$) and, $q = 2$ or 0 for the fast and the slow cooling regimes, respectively. τ_p is define by

$$\tau_p(\gamma_p) = \tau_{gen}\,\gamma_p^{-5}\,, \quad \text{with} \quad \tau_{\rm gen} = 5\,\mathrm{q_e}(3-\mathrm{k})^{-1}\,\mathrm{n\,r\,B}^{-1}\,. \tag{2.46}$$

There are two scenarios for τ_p. The fast cooling regime where τ_p is evaluated at $\gamma_{\rm c}$ as

$$\tau_c(\gamma_c) = \tau_{gen} \cdot \gamma_c^{-5}\,, \tag{2.47}$$

and the slow cooling regime where τ_p is evaluated at γ_m as

$$\tau_m(\gamma_m) = \tau_{gen}\,\gamma_m^{-5}. \tag{2.48}$$

In the optically thick emission region two layers are identified. A thick layer of electrons that have cooled down to $\gamma_{\rm m}/2$ and, a thin layer of uncooled electrons, right behind the shell. The transition between the two layers is observed as a break in the afterglow spectrum. At this break, two power-law segments are joined. A segment corresponding to a standard blackbody spectrum ($F_\nu \propto \nu^2$) and a segment with a blackbody spectrum that has an effective temperature that depends on the frequency ($F_\nu \propto \nu^{11/18}$). The transition between the absorption due to uncooled electrons

to the absorption due to cooled electrons occurs at $\nu_{\rm ac}$. This break is difficult to observe and is usually not included in the afterglow analysis. However, $\nu_{\rm ac}$ add an important contribution to the flux density at low frequencies, with its main relevance in the analysis of early radio observations (Granot et al. 2000). Setting $\tau_\nu = 1$ in Eq. 2.45 an expression for $\nu_{\rm sa}$ can be derived. The specific expressions for $\nu_{\rm sa}$ and $\nu_{\rm ac}$ are given for each one of the five spectral regimes are given by

$$\nu_{\rm sa} = \begin{cases} \nu_c\, \tau_c^{\frac{3}{5}} & \text{for} \quad \text{break 10}\,, \\ \nu_c\, \tau_c^{\frac{1}{3}} & \text{for} \quad \text{break 8}\,, \\ \left[\nu_{sa_5}^{\frac{10}{3}}\, \nu_c^{\frac{8}{3}}\, \nu_m^{p-1} \right]^{\frac{1}{p+5}} & \text{for} \quad \text{break 6}\,, \\ \nu_m\, \tau_m^{\frac{2}{p+4}} & \text{for} \quad \text{break 5}\,, \\ \nu_m\, \tau_m^{\frac{3}{5}} & \text{for} \quad \text{break 1}\,, \end{cases} \tag{2.49}$$

$$\nu_{\rm ac} = \nu_{sa_5}\, \nu_c^{\frac{4}{5}}\, \nu_m^{-\frac{4}{5}}\,, \tag{2.50}$$

In order to include the energy injection or the SSC component the proper expression for $\nu_{\rm c}$, $\nu_{\rm m}$, τ_c and τ_m have to be used, as well as the cases for p>2 or 1<p<2.

Peak Flux

The peak flux, $F_{\rm m}$, can be written in terms of the maximum power $P_{\rm max}$ as in Eq. 2.31 (for breaks 2 and 11 in Fig. 2.3). The peal flux is not affected by the especific mechanism for the electron cooling, but it is affected by a prolonged energy injection. This energy injection component modified the $F_{\rm m}$ termporal evolution as

$$F_{m_{inj}} \quad \sim \quad F_m\, t_{d_z}^{\frac{(q-1)(3k-8)}{2(4-k)}}\,. \tag{2.51}$$

When the frequency at which the peak flux occurs is in the self-absorbed region, the absorption effects affect $F_{\rm m}$. The correction factor for the spectra (2), (3) and (4) where this absorption effects are important are given by

$$F_{\rm m} = \begin{cases} F_{m_{(\rm break8)}} = F_m\, \tau_c^{-\frac{1}{6}} & \text{for} \quad \text{Spec. 4, break 8}\,, \\ F_{m_{(\rm break3)}} = F_m\, \nu_{sa} & \text{for} \quad \text{Spec. 3, break 3}\,, \\ F_{m_{(\rm break5)}} = F_m\, \tau_m^{\frac{1-p}{p+4}} & \text{for} \quad \text{Spec. 2, break 5}\,. \end{cases} \tag{2.52}$$

2.2.2 Closure relations

The flux of the afterglow is described by $F \sim \nu^{-\beta} t^{-\alpha}$. For a specific model and synchrotron spectrum, there is a unique set of relations between α and β that constrained the cooling regime, the circumburst environment, the jet geometry and the electron energy distribution index p (Rees & Meszaros 1994; Wijers et al. 1997; Sari et al. 1998; Dai & Cheng 2001; Zhang & Mészáros. 2004), this set of relations is called "closure relations". Here I present the closure relations for the standard model in the case of a deceleration blast wave for an ISM or wind-like density profiles, $p > 2$ and $1 < p < 2$, including energy injection relations for $p > 2$ and a jet break for both cases: a spreading phase and a non-spreading phase. The table is taken from (Racusin et al. 2009). For details on

the closure relations under other spectral regimes and including reverse shock and forward shock emission for a thin and thick shell, as well as a detailed analysis on the relations for the jet break behaviour, they are presented in 20 Tables in Gao et al. (2013) as well as in other reviews e.g., Piran (2004), Mészáros (2006).

			a	b	c
			No Energy Injection		Energy Injection
		β	$\alpha(\beta)$ $(p > 2)$	$\alpha(\beta)$ $(1 < p < 2)$	$\alpha(\beta)$ $(p > 2)$
			ISM, Slow Cooling		
1	$\nu_m < \nu < \nu_c$	$\frac{p-1}{2}$	$\alpha = \frac{3\beta}{2}$	$\alpha = \frac{3(2\beta+3)}{16}$	$\alpha = (q-1) + \frac{(2+q)\beta}{2}$
2	$\nu > \nu_c$	$\frac{p}{2}$	$\alpha = \frac{3\beta-1}{2}$	$\alpha = \frac{3\beta+5}{8}$	$\alpha = \frac{q-2}{2} + \frac{(2+q)\beta}{2}$
			ISM, Fast Cooling		
3	$\nu_c < \nu < \nu_m$	$\frac{1}{2}$	$\alpha = \frac{\beta}{2}$	$\alpha = \frac{\beta}{2}$	$\alpha = (q-1) + \frac{(2-q)\beta}{2}$
4	$\nu > \nu_m$	$\frac{p}{2}$	$\alpha = \frac{3\beta-1}{2}$	$\alpha = \frac{3\beta+5}{8}$	$\alpha = \frac{q-2}{2} + \frac{(2+q)\beta}{2}$
			Wind, Slow Cooling		
5	$\nu_m < \nu < \nu_c$	$\frac{p-1}{2}$	$\alpha = \frac{3\beta+1}{2}$	$\alpha = \frac{2\beta+9}{8}$	$\alpha = \frac{q}{2} + \frac{(2+q)\beta}{2}$
6	$\nu > \nu_c$	$\frac{p}{2}$	$\alpha = \frac{3\beta-1}{2}$	$\alpha = \frac{\beta+3}{4}$	$\alpha = \frac{q-2}{2} + \frac{(2+q)\beta}{2}$
			Wind, Fast Cooling		
7	$\nu_c < \nu < \nu_m$	$\frac{1}{2}$	$\alpha = \frac{1-\beta}{2}$	$\alpha = \frac{1-\beta}{2}$	$\alpha = \frac{q}{2} - \frac{(2-q)\beta}{2}$
8	$\nu > \nu_m$	$\frac{p}{2}$	$\alpha = \frac{3\beta-1}{2}$	$\alpha = \frac{\beta+3}{4}$	$\alpha = \frac{q-2}{2} + \frac{(2+q)\beta}{2}$
			Uniform Jet (spreading), Slow Cooling		
9	$\nu_m < \nu < \nu_c$	$\frac{p-1}{2}$	$\alpha = 2\beta + 1$	$\alpha = \frac{2\beta+7}{4}$	$\alpha = 2\beta + 1 - \frac{2(1-q)(\beta+2)}{3}$
10	$\nu > \nu_c$	$\frac{p}{2}$	$\alpha = 2\beta$	$\alpha = \frac{\beta+3}{2}$	$\alpha = 2\beta - \frac{2(1-q)(\beta+1)}{3}$
			ISM, Uniform Jet (nonspreading)		
11	$\nu_m < \nu < \nu_c$	$\frac{p-1}{2}$	$\alpha = \frac{6\beta+3}{4}$	$\alpha = \frac{6\beta+21}{16}$	$\alpha = \frac{6\beta+3}{4} - \frac{(1-q)(2\beta+5)}{4}$
12	$\nu > \nu_c$	$\frac{p}{2}$	$\alpha = \frac{6\beta+1}{4}$	$\alpha = \frac{3\beta+11}{8}$	$\alpha = \frac{6\beta+1}{4} - \frac{(1-q)(2\beta+3)}{4}$
			Wind, Uniform Jet (nonspreading)		
13	$\nu_m < \nu < \nu_c$	$\frac{p-1}{2}$	$\alpha = \frac{3\beta+2}{2}$	$\alpha = \frac{2\beta+13}{8}$	$\alpha = \frac{3\beta+2}{2} - \frac{(1-q)(\beta+2)}{2}$
14	$\nu > \nu_c$	$\frac{p}{2}$	$\alpha = \frac{3\beta}{2}$	$\alpha = \frac{\beta+5}{4}$	$\alpha = \frac{3\beta}{2} - \frac{(1-q)(\beta+2)}{2}$
			ISM, Structured Jet		
15	$\nu_m < \nu < \nu_c$	$\frac{p-1}{2}$	$\alpha = \frac{3k+12\beta}{8-k}$		
16	$\nu > \nu_c$	$\frac{p}{2}$	$\alpha = \frac{12\beta+2k-4}{8-k}$		
			Wind, Structured Jet		
17	$\nu_m < \nu < \nu_c$	$\frac{p-1}{2}$	$\alpha = \frac{6\beta+k\beta+2}{4-k}$		
18	$\nu > \nu_c$	$\frac{p}{2}$	$\alpha = \frac{6\beta+k-k\beta-2}{4-k}$		

Figure 2.4: Table of closure relations taken from Racusin et al. (2009).

Chapter 3

Instrumentation and data analysis

3.1 *Swift*

The *Swift* satellite (Gehrels et al. 2004) was launched on November 20 2014 being part of NASA's medium explorer MIDEX program with its main science goal focussing on the study of gamma-ray bursts (GRBs). It is a multi-wavelength observatory with onboard instruments working in the wavelengths from ultraviolet to γ-rays that provides temporal and spectral information of the event. It has discovered more than 1400 bursts during its 12 years in orbit and it continues to detect an average of 100 bursts/year. Three main instruments onboard of the *Swift* satellite work together in the observations of the GRB events and other transients that are detected. The observations start with the Burst Alert Telescope BAT that detects the transient with an accuracy of 3 arcmin in position. *Swift* slews to the event within seconds and the X-ray Telescope XRT and the Ultraviolet/Optical Telescope start to observe. The observations by XRT and UVOT provide a better position of the burst with an accuracy of a few arcsec. The position of the burst is communicated to the ground based telescopes within 20 seconds after the detection of the GRB through a special designed notification system, called GRB Coordinate Network (GCN). This communication system allows a fast follow up of the events by ground based telescopes in a broadband range from radio to optical wavelengths.

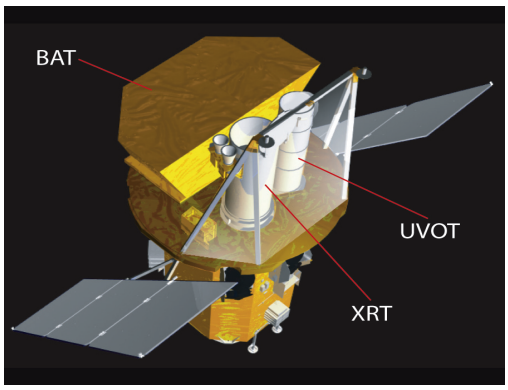

(a) *Swift* satellite.

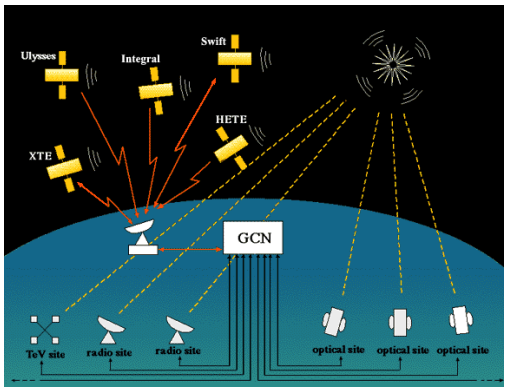

(b) GRB Coordinate Network GCN

Figure 3.1: Left: *Swift* satellite with three of its onboard instruments. The X-ray Telescope XRT, the Ultraviolet/Optical Telescope UVOT and the Burst Alert Telescope BAT (Gehrels et al. 2004). **Right:** Schematic of the GRB notification system. GRB Coordinate Network GCN.

Burst Alert Telescope - BAT (Barthelmy et al. 2005) is a γ-ray detector working in an energy range between 15-150 keV with a wide field of view of 1.4 sr (half coded). It is designed to detect and identify the GRB event with a detection rate of more about 100 bursts per year. It can calculate the position of the event with an accuracy of a few arcmin. However, it can also operate in a survey mode performing a hard X-ray survey. BAT is composed of a D-shaped coded aperture mask with an area of 2.7 m^2 made of more than 54000 lead tiles and a solid state detector made of more than 32000 CdZnTe detectors. The trigger algorithm is based on an excess in the count rate above the background counts with a detection algorithm based on the one developed for HETE-2. This complex count rate algorithm is complemented by an imaging phase to check whether the detection actually corresponds to a point source.

X-ray Telescope - XRT (Burrows et al. 2005) works in an spectral energy range from 0.2 to 10 keV and is designed to obtain images and spectra of the GRB afterglows. It uses the images to produce a position of the GRB with an accuracy of less than 5 arcsec within just 10 seconds. This fast and accurate localisation of the GRB allows the afterglow study by ground base telescopes in a multi-wavelength range. The telescope uses a grazing incidence Wolter 1 telescope with a charged-couple device (CCD) with an effective area of 110 cm^2, a field of view 23.6 x 23.6 arcmin and 18 arcsec resolution. Three readout modes are supported by the XRT: Imaging mode that allows to measure the position of bright sources but does not allow spectroscopy, a Windowed Timing (WT) mode that allows high resolution imaging and spectroscopy of the source during its brightest epoch but does not provide spatial information and, a Photon Counting (PC) mode that provides accurate spectral and spatial information of the source when its brightness has decrease to a range of about 2×10^{-14} to 9×10^{-10} erg cm^{-2} s^{-1}.

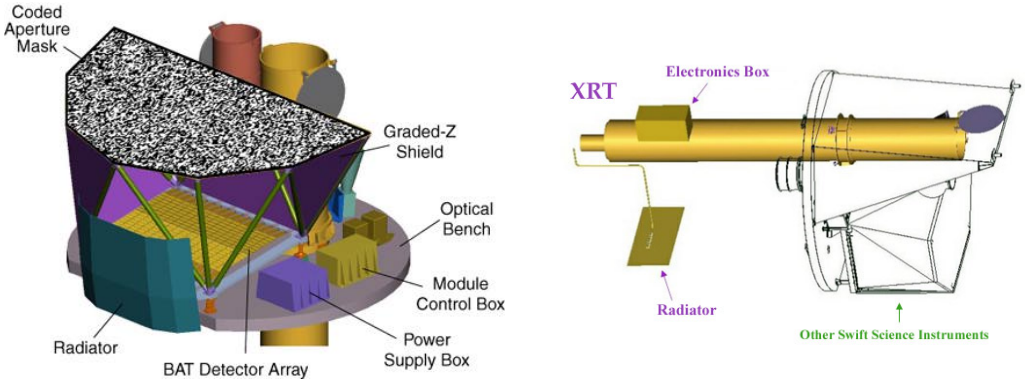

(a) Schematic BAT. **(b)** Schematic XRT.

Figure 3.2: Left: Schematic of the Burst Alert Telescope BAT. **Right:** Schematic of the X-ray Telescope.

Ultraviolet/Optical Telescope - UVOT (Roming et al. 2005) is designed for GRB studies uniquely as a rapid response observations is required to study the afterglow of the GRBs. It is a 30 cm modified Ritchey-Chrétien Telescopes with a CCD detector operating in photon counting mode. It has a field of view of 17 x 17 arcmin and works in a wavelength range between 170-650 nm. It produces positions of the afterglow with an accuracy of about 0.5 arcsec. Furthermore due to its seven filters it produces a SED of the afterglow that can be used for the redshift determination when the Ly_α cut-off is observed. UVOT can observe afterglows with a brightness of 22.3 mag in the white band in 1000 s compared to 20 mag that can be achieved by ground based telescopes. It has a brightness limit of 7.4 mag in the v band.

3.2 GROND

The Gamma-Ray burst Near-infrared Detector (Greiner et al. 2008) is a seven channel imager in the wavelength range from 400-2400 nm ($g'r'i'z'JHK_s$). It is mounted at the Max-Planck-Gesellshaft (MPG) 2.2 m telescope located at ESO La Silla observatory, Chile. It was designed as a GRB follow-up instrument being able to observed the GRB in the seven bands simultaneously. This simultaneous multi-wavelength observations allows the determination of the redshift based on the Ly$_\alpha$ break (Lamb & Reichart 2000) in the spectral energy distribution analysis. GROND allows a redshift determination up to 13, having observed burst with redshift z = 0.059 (Olivares et al. 2012) to z = 9.2 (Cucchiara et al. 2011). Although it was designed with the main purpose of GRB follow up it has been used to study different kind of transients, e.g., blazarz (Ghisellini et al. 2013), super luminous supernovae (Greiner et al. 2015).

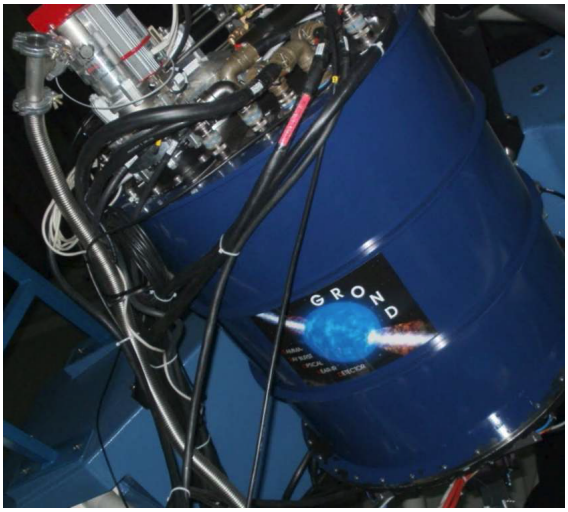

Figure 3.3: Gamma-Ray burst Near-infrared Detector (Greiner et al. 2008) mounted at the Max-Planck-Gesellschaft (MPG) 2.2 m telescope located at ESO La Silla observatory, Chile.

The design of GROND is based on four optical charged coupled devices CCDs and three near-infrared Rockwell HAWAII-1. A set of dichroic is used to split the incoming beam and make possible the simultaneous detection in all seven filters. The four optical detector matched the g', r', i', z' Sloan filters (Fukugita et al. 1996; Aihara et al. 2011) and cover a field of view of 5.4 x 5.4 arcmin^2 and the three NIR detectors matched the JHK_s bands of the extended Johnson system (Johnson & Morgan 1953) as in the two micron survey 2MASS (Skrutskie et al. 2006) covering a file of view of 10 x 10 arcmin^2. The readout of the optical detectors is performed by the Fast Imager Electronic Readout Assembly (FIERA Beletic et al. 1998) and of the NIR detector is performed by the Infrared Detector High Speed Array Control and Processing Electronics (IRACE Meyer et al. 1998). The output from the seven channels is a single FITS file for each one of the readout, i.e., one for the optical and one for the NIR readout. The fits file contains information about the exposure times, time of the observations, airmass, seeing among other science details.

Due to the fast decaying nature of the GRBs afterglows, GROND operates in Rapid Response Mode (RRM) anytime there is a new GRB trigger from *Swift* or any other satellite that has been communicated via the GCN system, ceasing all other observations currently taken place with any of the instruments in the telescope, i.e., Wide Field Imager (WFI Baade et al. 1999) and Fibre-fed Extended Range Optical Spectrograph (FEROS Kaufer et al. 1999). The automatic GROND

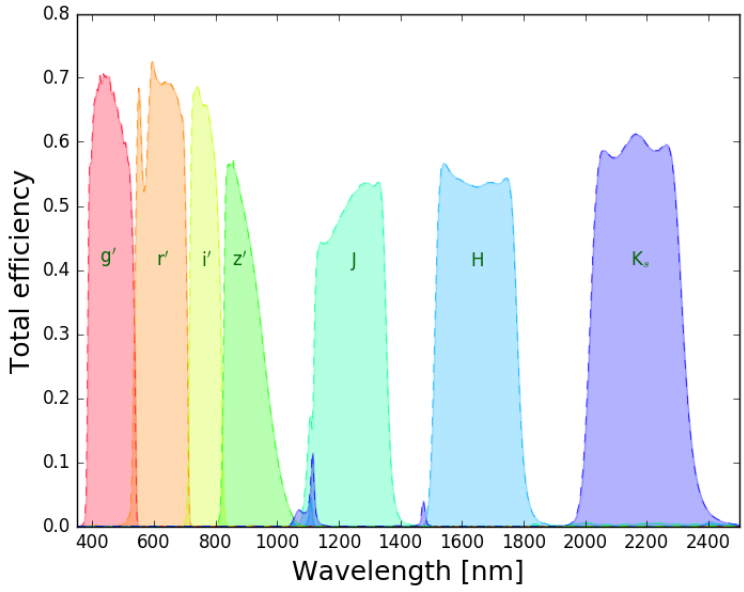

Figure 3.4: Total efficiency of each of the seven GROND bands.

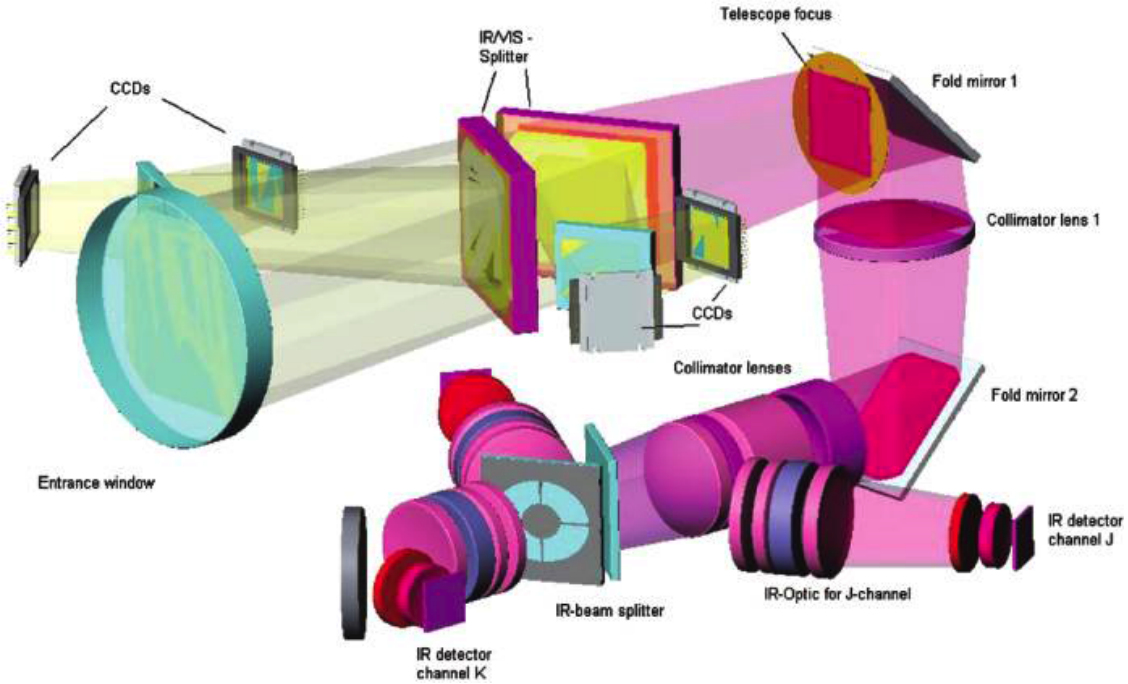

Figure 3.5: Schematic of the internal system of GROND. The splitting of the light beam that allows the simultaneous detection in seven bands is shown.

pipeline (GP Yoldaş et al. 2008) creates an observation block and executes the trigger anytime the GRB is visible from La Silla and there are no weather or technical restrictions. The observation blocks (OB Chavan et al. 2000) are based on the VLT software and ESO standards[1]. These OBs contain the basic information for the start of the observations such as the pointing of the telescope and the combination and length of the exposures in the different filters. The length of the OBs depends on the science objective, the brightness of the source at the moment of the observations

[1] https://www.eso.org/sci/software/pipelines/

and the field of the GRB. The OBs nomenclature in GROND is called after the exposure time in the NIR bands and the number of telescope dither positions (TDP), with the K channel having it own mirror dither position MDP to obtain 6 integrations in each TDP and reduced the final sky background. The shortest OB used for GRB observations is a 4m4td, this implies integrations of 10 second in the NIR bands and integrations of 35 or 66 seconds in the optical bands for the slow (46 s) or fast (4.4 s) readout modes, respectively. When the RRM trigger starts, the automatic pipeline generates a set of OBs that consequently increase the exposure time due to the fast decay of the optical emission. The typical OB construction that is mostly used in the follow-up of the GRB afterglows is 4m4td, 8m4td, 20m4td and 30m6td.

3.3 Data handling and analysis

3.3.1 Data reduction

***Swift* /XRT data**: The XRT light curve and spectral data are obtained from the *Swift* /XRT repository (Evans et al. 2007, 2009). The data set is already reduced and no manual reduction has to be carried out. The *Swift* /XRT repository allows the creation of time-average spectra for a given GRB in a given time window. The time slices that are created for each GRB can be defined by the user according to the studies that are going to be performed. The spectral data is re-grouped using the GRPPHA task from the GEAsoft packages in order to ensure a minimum number of counts per channel to allow the spectral analysis using χ^2 statistics.

GROND data: The GROND optical/NIR data are reduced using the GROND pipeline developed by Krühler et al. 2008. This pipeline is based on the standard astronomical tool Image Reduction and Analysis Facility tasks (IRAF, Tody 1993). The analysis has three main steps. It starts with the creation of the calibration frames to remove the dark and bias effects introduced by the detector electronics. Then skyflats images are created and used to correct the pixel-to-pixel sensitivity and the illumination variations along the image. After these initial corrections the FITS files containing the optical and NIR data are divided into individual files for each band. The sky is subtracted from the NIR images and the geometrical corrections for the different TDP positions are applied and all the TDPs are added into a single image per band. The individual TDP images can be saved and used as individual images for the astrometry and photometry process when the source is bright enough. Astrometry is performed using data from available public catalogues (e.g., USNO A-2, USNO B-1, SDSS, DENIS, NOMAD, 2MASS, GSC22) are chosen base on the band filter and the location of the GRB field. Finally the photometry is performed creating a point-spread function (PSF) of the bright stars in the field and using aperture photometry. The fluxes are corrected due to atmospheric effects using the airmass at the altitude at which the observations took place.

3.3.2 Light curve fitting

The study of the afterglow physics presented here relies on the analysis of the temporal and spectral evolution of the observed GRB afterglow. The observed flux of the afterglow depends on the time and frequency as $F \sim t^{-\alpha}\nu^{-\beta}$, with α and β being the temporal and spectral slopes. In order to derived these slopes a fitting of the light curve and spectral energy distribution (SED) is performed. The best fit values are determined based on χ^2 statistics. The light curves of the GRB afterglow are fitted using different routines written in Python (PhD thesis of Thomas Krühler, TUM). The models are based on a series of simple power-law segments that are joined by smooth breaks. The

simple model for the afterglow evolution is a sible power-law but it is modified by different effects such as flares, plateaus, supernovae bumps, underlying host galaxies, jet breaks. The main fitting profiles used in this thesis for the light curve fitting are:

$$F_\nu(t) = \begin{cases} F_0 \times \left(\frac{t}{t_0}\right)^{-\alpha} & , \\ F_1 \times \left[\left(\frac{t}{t_1}\right)^{-\alpha_1 \mathrm{sm}} + \left(\frac{t}{t_1}\right)^{-\alpha_2 \mathrm{sm}}\right]^{-1/\mathrm{sm}} + host & , \\ F_1 \times \left[F'_\nu(t_1)^{-\mathrm{sm}_3} + F'_\nu(t_2)^{-\mathrm{sm}_3} \times \left(\frac{t}{t_0}\right)^{-\alpha_3}\right]^{-1/\mathrm{sm}_3} + host & , \end{cases} \tag{3.1}$$

for a simple power-law, a broken power-law and a double broken power-law, respectively (Beuermann et al. 1999). F_i are the normalisation factors at the time t_i, $\mathrm{sm_i}$ is the smoothness of the break i, α_i are the slopes for each power-law segment and the *host* contribution when relevant. The analysis on the temporal evolution provides information on α and possible features like flares, breaks in the light curve, plateau phases and information on the host galaxy (e.g. optical/NIR magnitudes).

3.3.3 SED fitting

The SED fitting is performed using the X-ray Spectral-fitting program XSPEC v12.7.1 (Arnaud 1996). This tool is used in the individual SED fitting for the observations X-ray and is specially useful in the broad-band SED analysis as it can be extended to be use with any instrument at different wavelengths and with user defined models. In the standard afterglow model the afterglow is described mainly by a synchrotron spectrum composed by four power-law segments join at three smooth breaks (Granot & Sari 2002). The SED analysis follow two steps:

First an analysis of the optical/NIR and X-ray data is performed in order to derived the spectral slope β and the dust and gas attenuation effects along the line of sight due to both the local environment and the host galaxy. The dust reddening $E(\mathrm{B-V})$ affects primarily the wavelength range from UV to NIR. The extinction A_V is related to $E(\mathrm{B-V})$ as A_V=$E(\mathrm{B-V})\cdot R_V$. In the case of the Galactic reddening $A_\mathrm{v}^\mathrm{Gal}$ the values are based on previous measurements (Schlafly & Finkbeiner 2011) in several directions and a Milky Way extinction law with $R_V = 3.08$ for $A_\mathrm{v}^\mathrm{Gal}$. For the host galaxy templates based on the Small and Large Magellanic Cloud are used (Pei 1992) and the values for extinction $A_\mathrm{v}^\mathrm{host}$are derived from the observations. The gas absorption effects depends on the column gas along the line of sight of the source. The absorption factor is quantify based on the hydrogen column density and the photo-electric cross-section $\sigma(E)$ (Balucinska-Church & McCammon 1992). The gas absorption effects due to the Galactic environment $N_\mathrm{H}^\mathrm{Gal}$ are fixed while the effect due to the host galaxy $N_\mathrm{H}^\mathrm{host}$ are derived in the fit. Finally in terms of the input data, the time slice from the XRT repository are generally choose to overlap the optical/NIR measurements but due to statistical requirement on the counts per channel, the time interval expands over more than 1 decade usually. The time slices for the XRT SEDs are therefore renormalise in order to have the flux corresponding to the measured X-ray flux of the afterglow at the mid-time of the analysed epoch. The fit is generally performed separately for XRT and GROND data and then, a combined fit is performed (when possible) to obtain better constrains on the slope, on the gas and dust effects and, if existent, a measurement of the break between optical and X-rays.

The second step after the derivation of $A_\mathrm{v}^\mathrm{host}$, $N_\mathrm{H}^\mathrm{host}$ and β is the incorporation of submm and radio data to perform a broadband fit and measure all the three break frequencies. The only con-

straints introduced here are the $A_{\rm v}^{\rm host}$ and $N_{\rm H}^{\rm host}$ derived in the previous step. The slope β of the GROND and XRT bands is not fixed but allowed to vary only within a 3σ uncertainty interval. The smoothness of each break depends on the temporal slopes in the optical/NIR and the X-ray (Granot & Sari 2002). Here all the available multi-wavelength epochs are included and fitted simultaneously. The simultaneous fit assures a unique spectral slope β, dust and gas effect $A_{\rm v}^{\rm host}$ and $N_{\rm H}^{\rm host}$ due to the host environment and a smooth transition between different spectral regimes. The break frequencies are left free to vary in all the cases. Although the data are expected to be described by a SED with three breaks, it is possible that fewer breaks are needed if the evolution of the afterglow is in a phase were one or more of the breaks are outside of the observational range used. Therefore the different fit profiles described in Eq. 3.1 are tested (Eq. 3.1).

Chapter 4

Microphysics and dynamics of the Gamma-Ray Burst 121024A[1]

The aim of the study is to constrain the physics of gamma-ray bursts (GRBs) by analysing of the multi-wavelength afterglow data set of GRB 121024A, covering the full range from radio to X-rays. Using multi-epoch broad-band observations of the GRB 121024A afterglow, we measure the three characteristic break frequencies of the synchrotron spectrum. We use 6 epochs of combined XRT and GROND data to constrain the temporal slopes, the dust extinction, the X-ray absorption and the spectral slope with high accuracy. Two further epochs of combined data from XRT, GROND, APEX, CARMA and EVLA are used to set constraints on the break frequencies and therefore on the micro-physical and dynamical parameters. The XRT and GROND light curves show a simultaneous and achromatic break at around 49 ks. As a result, the crossing of the synchrotron cooling break is not suitable as an explanation for the break in the light curve. Two plausible scenarios are analysed. The jet break model has been suggested by previous analysis of the observed linear and circular polarisation, although it requires a hard electron spectrum, a very low cooling break frequency, a non-spreading jet and an extreme prompt emission efficiency. The energy injection model avoids these issues but introduces otherwise problematic values for the microphysics and environment density. Broad-band spectral analysis on a larger sample of GRBs will contribute to previous studies with the aim of a better understanding of the wide range in the microphysical and environmental parameters within GRB shock fronts that have been observed so far, and thus will provide more grounds to favour certain model interpretations.

4.1 Observations and data reduction

4.1.1 *Swift*

On 2012 October 24 at T_0 = 02:56:12 UT the *Swift* Burst Alert Telescope (BAT, Barthelmy et al. 2005) triggered and located GRB 121024A (Pagani et al. 2012). *Swift* slewed immediately to the burst and the observations with the X-Ray Telescope (XRT, Burrows et al. 2005) started 93 sec after the trigger. The observations were done in Windowed Timing (WT) mode during the first 242 s and then they were carried out in Photon Counting (PC) mode (Page et al. 2012). The initial flux in the 0.2-10 keV band was 1.1×10^{-9} erg cm^{-2} s^{-1}. The *Swift*/XRT light curve and spectral

[1](Varela et al. 2016)

data were obtained from the XRT repository (Evans et al. 2007, 2009). The afterglow was located RA, Dec (J2000) = 04:41:53.28, -12:17:26.8 with an uncertainty of 0.″8 (Pagani et al. 2012) by the *Swift* /UVOT, with a magnitude in the *b* band of 18.4±0.2 mag (Holland & Pagani 2012).

4.1.2 GROND

The Gamma-Ray burst Optical Near-infrared Detector - GROND (Greiner et al. 2008) mounted at the Max-Planck-Gesellschaft (MPG) 2.2m telescope located at ESO La Silla observatory, Chile, was designed as a GRB follow-up instrument. It provides simultaneous data in 7 bands in a wavelength range from 400-2400 nm ($g'r'i'z'JHK_{\rm s}$). GROND observations started 2.96 hours after the *Swift* trigger (Knust et al. 2012) and continued for the next 3.8 hours during the first night. The afterglow was detected in all 7 bands at the position RA, Dec (J2000) = 04:41:53.30, -12:17:26.5 with an uncertainty of 0.″4 in each coordinate (Fig. 4.1). After the observations during the first night, imaging of the field of GRB 121024A continued on the 2nd, 3rd, 4th, 16th and 17th night after the burst. The optical/NIR data were reduced using standard IRAF tasks (Tody 1993; Krühler et al. 2008). The data were corrected for Galactic foreground reddening $E(\mathrm{B}-\mathrm{V})$=0.09 mag (Schlafly & Finkbeiner 2011), corresponding to an extinction of $A_{\rm V}^{\rm Gal}$=0.27 mag for $R_{\rm V}=3.1$. The optical magnitudes were calibrated against secondary stars in the GRB field (Table 4.1). On 2013 December 8 a Sloan Digital Sky Survey (SDSS) field (Aihara et al. 2011) at RA, Dec (J2000) = 04:59:42.0, -04:54:00 and the field of GRB 121024A were consecutively observed during photometric conditions. The calibration of the secondary stars was done against the corrected zeropoints of the GRB field based on the SDSS field. The NIR magnitudes were calibrated against the Two Micron All-Sky Survey (2MASS, Skrutskie et al. 2006) catalogue stars in the field of the GRB.

Table 4.1: Secondary stars for photometric calibration. See Fig. 4.1

Star	RA, Dec J(2000)	$g'(\mathrm{mag_{AB}})$	$r'(\mathrm{mag_{AB}})$	$i'(\mathrm{mag_{AB}})$	$z'(\mathrm{mag_{AB}})$	$J(\mathrm{mag_{Vega}})$	$H(\mathrm{mag_{Vega}})$	$K_{\rm s}(\mathrm{mag_{Vega}})$
I	04:41:49.55, -12:16:47.2	19.96±0.05	18.75±0.05	18.21±0.06	17.92±0.06	16.73±0.06	15.96±0.07	15.88±0.08
II	04:41:52.36, -12:16:49.9	17.83±0.05	17.13±0.05	16.84±0.06	16.69±0.06	15.67±0.06	15.07±0.06	15.08±0.07
III	04:41:55.40, -12:16:30.3	20.73±0.06	19.45±0.05	18.91±0.06	18.68±0.06	17.45±0.07	16.66±0.07	–
IV	04:41:47.91, -12:16:15.2	20.74±0.06	19.23±0.05	18.44±0.06	18.04±0.06	16.79±0.06	16.07±0.06	15.96±0.06
V	04:41:46.29, -12:17:57.5	17.76±0.05	17.36±0.05	17.21±0.06	17.11±0.06	16.19±0.06	15.81±0.06	15.82±0.06
VI	04:41:52.83, -12:18:46.8	20.57±0.05	19.07±0.05	18.43±0.06	18.11±0.06	16.84±0.06	16.29±0.06	–

4.1.3 APEX

On 2012 October 24 we triggered an observation on the LABOCA bolometer camera (Siringo, G. et al. 2009)[2]. Two observations at a frequency of 345 GHz with a bandwidth of 60 GHz were performed. The first one started 19.8 ks after the GRB and the second one started 98.7 ks after the GRB. During both days, the observations were taken in mapping mode and in on-off mode (Schuller et al. 2010). The reduction of the data was done using the Bolometer Array analysis software (BoA, Schuller 2012). All the subscans (10 per scan) were used. A clipping of 2σ was used to remove any background effects. The focus calibration was done using Jupiter for the focus, N2071IR as a secondary calibrator and J0423-013 as a pointing source. There was no detection on either night, the upper limits are given in Table 4.2.

[2]Based on observations collected during Max-Planck Society time at the Atacama Pathfinder Experiment (APEX) under proposal m-090.f-0005-2012.

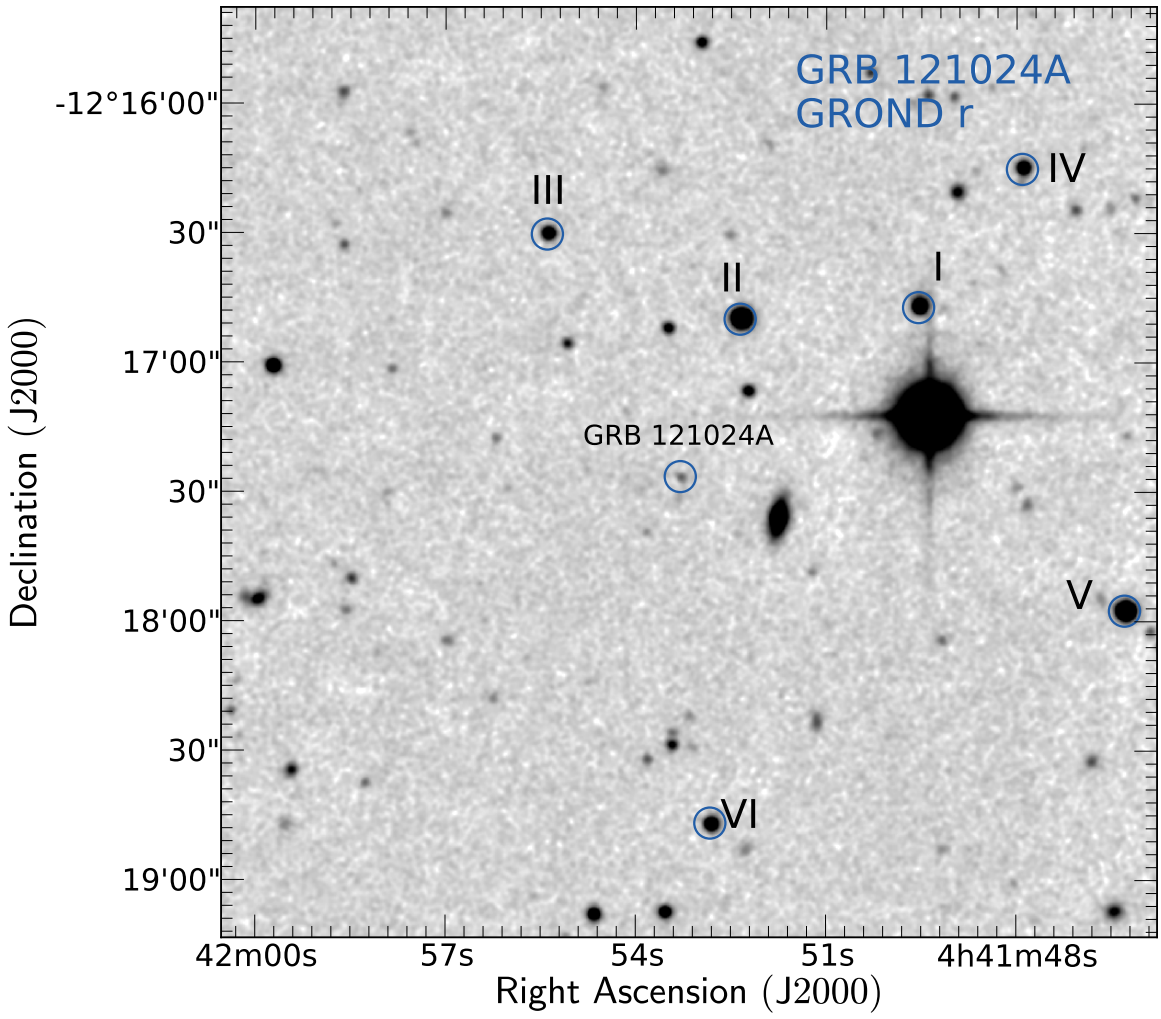

Figure 4.1: GROND r'-band finding chart. The secondary stars used for the calibration are labeled from I-VI and reported in Table 4.1. North is up and East to the left.

Table 4.2: 1σ Upper limits of the on-off measurements using the LABOCA instrument on APEX.

Date	On+off time [UTC]	UL-Flux [mJy/beam]	Mapping time [UTC]	UL-Flux [mJy/beam]
24-10-2012	08:22 - 09:20	3.6	09:30-10:27, 10:39-11:00	9.0
25-10-2012	06:16 - 06:38	10.4	08:52-09:29, 09:40-10:34, 10:41-10:51	12.0

4.1.4 Millimeter and radio observations

In addition to the X-ray, GROND and APEX data reported above, we also incorporated the following millimetre and radio observations reported in the literature in our SED analysis:

The Combined Array for Research in Millimetre-Wave Astronomy (CARMA) started observations of the field of GRB 121024A $\sim$ 120.9 ks after the BAT trigger at a mean frequency of $\sim$ 85 GHz (3mm) (Zauderer et al. 2012). A mm counterpart was detected with a flux of 1.0$\pm$0.3 mJy.

The Very Large Array (VLA) started observations of the field of GRB 121024A $\sim$ 109.0 ks after the trigger. A radio counterpart with flux of 0.10 ± 0.03 mJy was detected at a frequency of 22 GHz (Laskar et al. 2012).

4.2 Phenomenological data analysis

We start with a model-independent analysis of the data. The observed flux is described by $F \sim t^{-\alpha}\nu^{-\beta}$, with α and β the temporal and spectral slope, respectively. First, we analyse the temporal evolution of the GRB 121024A afterglow. Using the X-ray and optical/NIR light curves, we measure the temporal slope α and get information about particular features like flares, breaks in the light curve, flattening, or any behaviour different from that expected for a canonical afterglow light curve (LC) (Nousek et al. 2006; Zhang et al. 2006). Then, we analyse the SED from X-ray to optical/NIR wavelengths at six different epochs. We obtain the spectral slope β, and check if there is any spectral evolution. Given that absorption and dust extinction only affect the data at X-ray and optical wavelengths, we use this SED analysis to derive the host X-ray absorbing column density ($N_{\rm H}^{\rm host}$), commonly quoted as an equivalent neutral hydrogen column density, and the host visual dust extinction along the GRB line of sight ($A_{\rm v}^{\rm host}$).

4.2.1 Afterglow light curve fitting

The temporal evolution of the X-ray afterglow of GRB 121024A[3] shows an initial steep decay with a temporal slope α=3.6, followed by a small flare at $\sim$ 300 s. For the present work, we only use the data after 10^4 s, which is the start time of our GROND observations (Fig.4.2). We try fitting two models: First, a simple power-law with host contribution in the optical bands (*plh*) and slope decay α. Second, a smoothly broken power-law with constant host contribution (*brplh*) (Eq. 4.1) (Beuermann et al. 1999), with $\alpha_{\rm pre}$ and $\alpha_{\rm pos}$ being the power-law slopes before and after the break, respectively, *sm* is the smoothness and $t_{\rm b}$ the break time in the LC:

$$F_\nu(t) = C \times \left\{ \left(\frac{t}{t_{\rm b}}\right)^{-\alpha_{\rm pre}\,{\rm sm}} + \left(\frac{t}{t_{\rm b}}\right)^{-\alpha_{\rm post}\,{\rm sm}} \right\}^{-1/{\rm sm}} + host. \qquad (4.1)$$

The best fit to the X-ray light curve is a smoothly broken power-law with a statistical significance χ^2/d.o.f=51/44 (simple power-law: χ^2/d.o.f=87/47). The best fit parameters are an initial decay with $\alpha_{\rm pre}$=0.84$\pm$0.09 and break time $t_{\rm b}^{\rm xrt}$=32.5$\pm$16.1 ks with *sm*=5.0$\pm$2.6, followed by a steeper decay with $\alpha_{\rm pos}$=1.67$\pm$0.23.

The optical/NIR light curves (Table 4.3) are well fitted by both a *plh* and a *brplh* model. A *plh* model gives χ^2/d.o.f=140/112 and a decay slope α=1.07$\pm$0.02, while a *brplh* model gives χ^2/d.o.f=107/109 and best fitting parameters $\alpha_{\rm pre}$=0.71$\pm$0.03, $\alpha_{\rm pos}$=1.46$\pm$0.04, break time $t_{\rm b}^{\rm opt}$=31.4$\pm$9.4 ks, and *sm*=2.7$\pm$1.1. Colour evolution in the optical bands is detected in the last epoch of our observations, which we associate with the increased contribution from the host galaxy. An F-test between the two model gives a null hypothesis probability of 1.86×10^{-6}. Therefore, we conclude that the *brplh* profile describes the data in a better way. We use this profile for further analysis.

[3] http://www.swift.ac.uk/xrt_curves/536580

Both the X-ray and optical/NIR light curves are best fitted by a broken power-law with similar break times. We therefore tried a combined fit to both the XRT and GROND light curves to test whether the same model can describe both data sets, which would thus provide greater constraint to the best fit parameters. The best fit model provides a good fit (χ^2/d.o.f=157/141), with a pre-break temporal slope $\alpha_{\rm pre}$=0.86±0.05, post-break temporal slope $\alpha_{\rm pos}$=1.47±0.03, smoothness sm=1.7±0.3 and break time $t_{\rm b}$=49.8±5.1 ks.

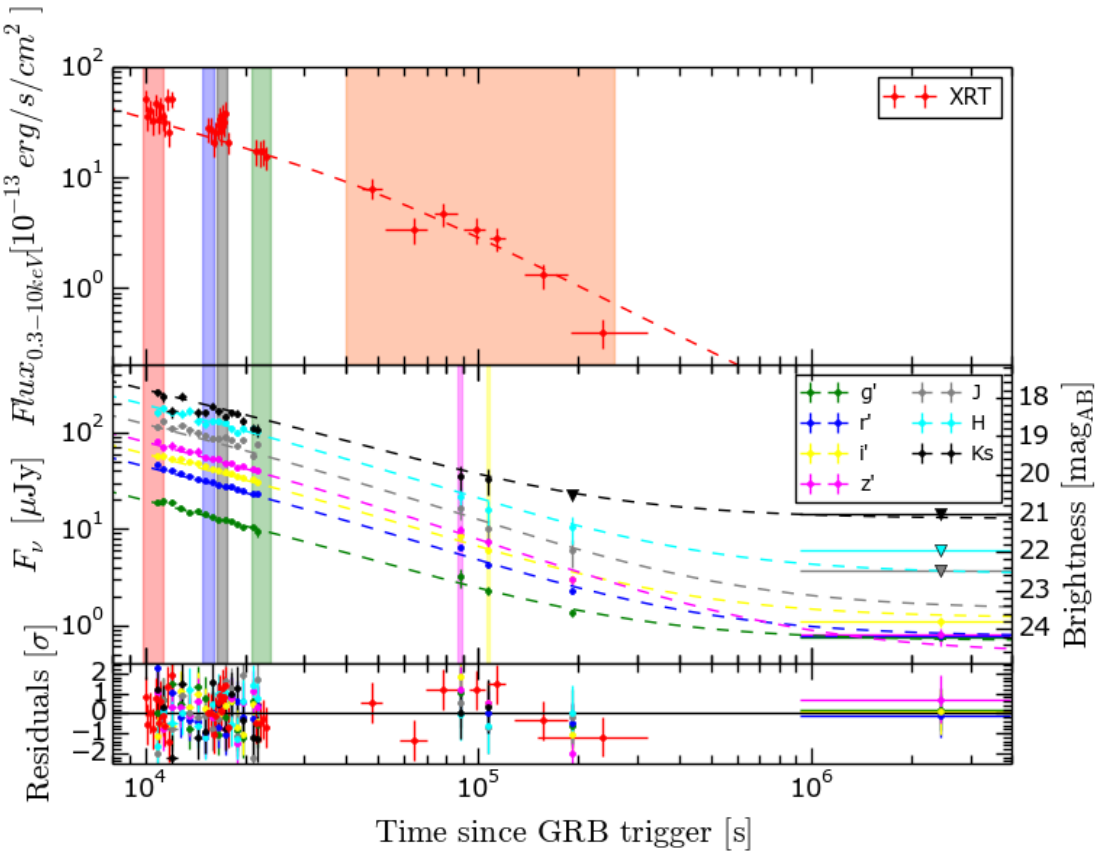

Figure 4.2: Light curve of the afterglow of GRB 121024A. **Top**: XRT light curve from the XRT repository. **Bottom**: GROND light curve in $g'r'i'z'JHK_{\rm s}$. The best fit for the combined light curve (optical/NIR and X-ray data) is a smoothly broken power-law with host contribution, shown with dashed lines. The epochs used for the spectral analysis are highlighted with the vertical bars. The break time $t_{\rm b}$=49.8±5.1 ks.

Table 4.3: Observed magnitudes of the GRB 121024A afterglow for the six highlighted epochs in Fig.4.2. The host contribution was subtracted. The magnitudes are not corrected for Galactic foreground extinction $A_{\rm V}^{Gal} = 0.27$ mag.

SED	mid-time [s]	$g'(\rm m_{AB})$	$r'(\rm m_{AB})$	$i'(\rm m_{AB})$	$z'(\rm m_{AB})$	$J(\rm m_{Vega})$	$H(\rm m_{Vega})$	$K_{\rm s}(\rm m_{Vega})$
I	11085	20.75±0.08	19.82±0.06	19.53±0.06	19.24±0.05	18.68±0.10	18.31±0.11	17.91±0.13
II	15497	21.12±0.05	20.20±0.05	19.84±0.05	19.63±0.04	19.05±0.10	18.67±0.10	18.34±0.12
III	17006	21.23±0.05	20.32±0.05	19.94±0.05	19.68±0.04	19.08±0.09	18.68±0.10	18.54±0.12
IV	21430	21.48±0.27	20.54±0.06	20.20±0.06	19.95±0.09	19.43±0.10	18.89±0.12	18.81±0.15
V	88010	22.89±0.24	22.03±0.09	21.74±0.10	21.49±0.14	21.01±0.26	20.76±0.31	20.41±0.31
VI	106998	23.41±0.12	22.54±0.08	22.13±0.09	21.85±0.13	21.61±0.31	21.18±0.33	20.61±0.34

4.2.2 Afterglow SED fitting

We analyse six different spectral epochs using XRT and GROND data, spanning the time interval $T_0 + 10$ ks to $T_0 + 240$ ks, four before the break time in the light curve and two after it (Fig. 4.3). The spectral analysis includes the effect of the dust and metal attenuation along the line of sight towards the source. For the last two SEDs, given the low signal-to-noise at X-ray energies, we extract the spectrum from the same time interval (40 ks - 240 ks), during which time there was no evidence of spectral evolution within the X-ray energy range. We then renormalise the spectra to correspond to the measured X-ray flux of the afterglow at the mid-time of the two corresponding SEDs (i.e., $t_{\rm SED}$V=88 ks and $t_{\rm SED}$VI=107 ks).

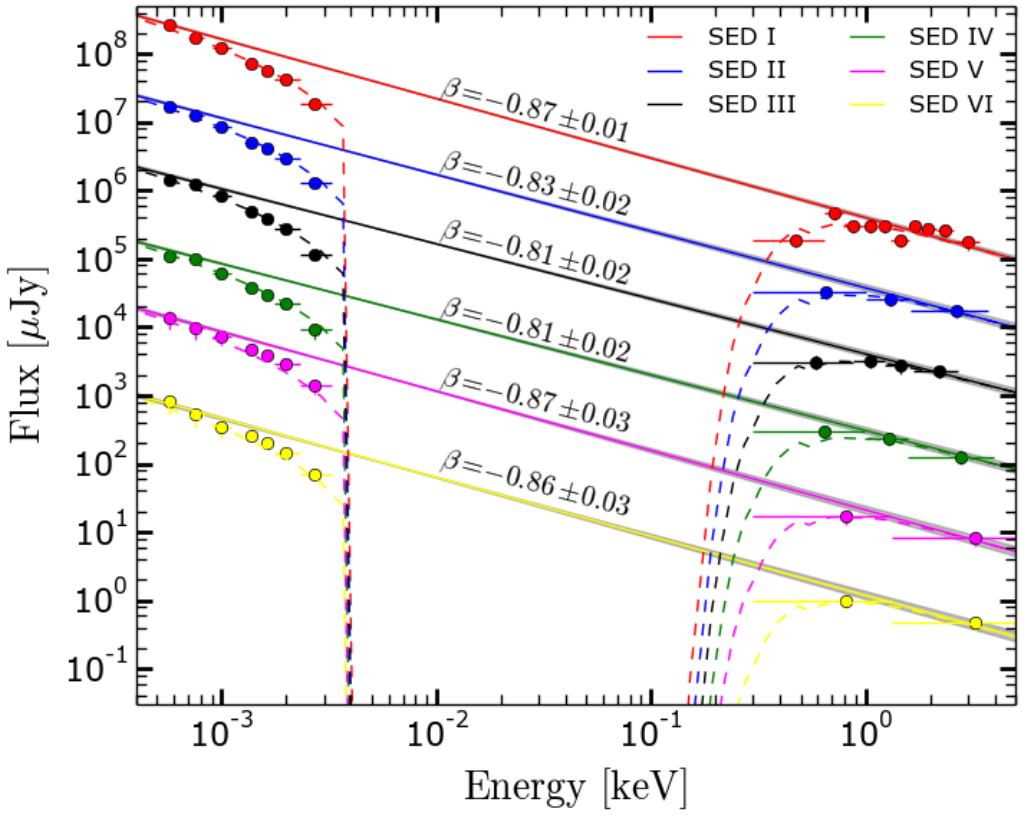

Figure 4.3: Spectral energy distribution for the 6 SEDs highlighted in Fig. 4.2. SEDs I - IV are from data before the observed break in the light curve. SEDs V & VI are from data taken after the break. The SEDs are scaled with an arbitrary factor for clarity in the plot. The values of β written above each line corresponds to the single power-law fit, where the slopes were left free to vary. The single power-law fit with a single tied slope has β=0.86±0.02.

The SED analysis for all the 6 SEDs is performed simultaneously. The Galactic reddening is fixed to $E(\mathrm{B-V})$=0.09 mag, corresponding to an extinction of $A_{\rm V}^{\rm Gal}$=0.27 mag (Schlafly & Finkbeiner 2011) for a Milky Way (MW) reddening law. The Galactic absorbing column density $N_{\rm H}^{\rm Gal}$=7.9 × 10^{20} cm^{-2} (Kalberla et al. 2005). The host magnitude was subtracted from the optical/NIR data and the g' band is not included in the fit because of the presence of a damped Lyα system along the line of sight towards the GRB (DLA, Friis et al. 2015). The values for the host extinction and absorption are tied between all the epochs and the spectral slopes are left free to vary. A single power-law fit has a goodness of fit χ^2/d.o.f=28/46 and all the spectral slopes values

(Fig. 4.3) are consistent within 1σ confirming the lack of spectral evolution. A broken power-law fit either puts the break outside the optical - X-ray frequency interval, or fails to improve the fit when the break is forced to lie within this interval. In the latter case, the best-fit models has a goodness of fit χ^2/d.o.f=32/40.

Given the lack of spectral evolution detected in our combined GROND/XRT light curve analysis out to 240 ks, we fit all six SEDs simultaneously with the same spectral model, with only the normalisation allowed to differ between epochs. The best fit results are given by a single power-law with a spectral slope β=0.86$\pm$0.02 and goodness of fit χ^2/d.o.f=48/51. The best-fit host dust extinction given by a Small Magellanic Cloud (SMC) reddening law (Pei 1992) is $A_{\rm V}^{\rm host}$=0.18$\pm$0.04 mag, and the host galaxy X-ray absorbing column is $N_{\rm H}^{\rm host}=0.30^{+0.46}_{-0.29}\times10^{22}$ cm^{-2}. The lack of spectral evolution together with the achromatic break observed in the light curve rule out the movement of the cooling break through the observed wavelength range.

We extend the SED analysis in the following section with two additional epochs containing simultaneous observations with XRT, GROND, APEX, CARMA and EVLA. The first SED at t=21.9 ks has GROND, XRT and APEX data. The additional APEX upper limit requires a break between the APEX and NIR energies (Fig. 4.4). Then, we have a second SED at t=109.0 ks, with two additional measurements: CARMA and EVLA data points. The CARMA data point requires a break between the millimetre and the NIR bands and the EVLA data point implies a break between the radio and the CARMA wavelength. Therefore at least two breaks in the broad-band spectrum of GRB 121024A are needed. These breaks are analysed in more detail in Sec. 4.3 in the context of the afterglow synchrotron spectrum model, where we use the constraints on β, $E(\rm B-V)$ and $N_{\rm H}^{\rm host}$ found in his section.

4.3 Physical parameters of the standard afterglow model

We now proceed with the derivation of the microphysical and dynamical parameters of the GRB afterglow, based on the standard afterglow model. In this model, the dominant emission is generally associated with synchrotron radiation from shock-accelerated electrons. These electrons are assumed to have a power-law energy distribution with slope p and minimum energy $\gamma_{\rm m}$. The observed synchrotron spectrum is characterised by three main break frequencies ($\nu_{\rm c}$,$\nu_{\rm m}$, $\nu_{\rm sa}$) and a peak flux. The synchrotron injection frequency $\nu_{\rm m}$ is defined by $\gamma_{\rm m}$. The cooling frequency $\nu_{\rm c}$ is defined by the critical value $\gamma_{\rm c}$, above which electrons radiate their energy on smaller timescales than the explosion timescale. The self-absorption frequency $\nu_{\rm sa}$ marks the frequency below which the optical depth to synchrotron-self absorption is >1. In this model, two main cooling regimes are defined by the relative position of the break frequencies: a fast cooling regime where $\nu_{\rm m}$>$\nu_{\rm c}$ and most of the electron are cooling fast, and a slow cooling regime where $\nu_{\rm m}<\nu_{\rm c}$ and most of the accelerated electrons are cooling slowly (Granot & Sari 2002).

The number of combinations of α and β is limited when a specific dynamical model and the synchrotron spectrum are given. This gives rise to a unique set of relations between α and β known as "closure relations" (Rees & Meszaros 1994; Wijers et al. 1997; Sari et al. 1998; Dai & Cheng 2001; Zhang & Mészáros. 2004). These relations constrain the cooling regime, the circumburst environment, the jet geometry and the electron energy distribution p. We follow two main steps to analyse the afterglow data:

1. Spectral regime: The derivation of the p value and identification of the external density profile depend on the power-law segment of the synchrotron spectrum containing the observing frequency. Using the closure relations (Racusin et al. 2009) together with the measured parameters for α and β, we find that the afterglow data can be described by two different spectral regimes (Table 4.4). In one case we have a spectral regime where $\nu_c<\nu_{K_s}$ (i.e., below the K_s band) and in the other case we have one where $\nu_c>\nu_{XRT}$ (i.e., above the XRT band).

2. Microphysical and dynamical parameters: We include the APEX, CARMA and EVLA data in our analysis and fit the data using a single, a double or a triple broken power-law model depending on each individual case (in the double and triple broken power-law fits, we only consider sharp breaks because the data at millimetre and radio frequencies is insufficient to constrain an additional free parameter i.e., smoothness). We use the standard formalism for a spherical blast wave propagating into an external cold medium during the slow cooling regime to derive all the micro-physical and dynamical parameters (Granot & Sari 2002; Dai & Cheng 2001; Leventis et al. 2012), and subsequently check for consistency with the slow/fast cooling transition times.

Both spectral regimes, i.e., $\nu_c<\nu_{K_s}$ and $\nu_c>\nu_{XRT}$, are explained and analysed in detailed in the following subsection. The former corresponds to the jet in the LC being associated with a jet break without energy injection, and the latter corresponds to the jet in the LC curve associated with either the end of energy injection into the outflow or with a jet break with an ongoing energy injection during the whole evolution of the afterglow (i.e., the ongoing energy injection is still visible until the last observations).

4.3.1 $\nu_c < \nu_{K_s}$: Jet break.

Using the closure relations for a decelerating spherical blast wave, we find that the measured temporal slope before the break in the light curve is consistent with $\nu_c<\nu_{K_s}$, for both ISM and wind environments. This implies p=1.73$\pm$0.03, as β=p/2. The only plausible scenario consistent with the measured α_{pos} and β corresponds to a non-spreading uniform jet propagating into a wind environment. We therefore associate the achromatic break observed in the light curve with a jet break (Rhoads 1999; Wiersema et al. 2014).

We proceed by including the post-break sub-mm and radio data in our analysis. The first broadband SED contains GROND, XRT and APEX data. The best fit to this is a broken power-law with both Galactic and host extinction and absorption, with χ^2/d.o.f=3.6/5 (Table 4.5). The measured value of ν_c=1.5 $\times$ 10^{12} Hz is a lower limit because the APEX measurement is an upper limit. The second broadband SED contains XRT, GROND, CARMA and EVLA detections. Two possible spectral sub-regimes in the slow cooling phase give a good fit to the data: The cooling regime where $\nu_{sa}<\nu_m<\nu_c$, and the one where $\nu_m<\nu_{sa}<\nu_c$. Due to the few data points at radio wavelengths, it is difficult to distinguish between these two cooling regimes. Therefore, we analyse both cases. In this special case, where $1 < p < 2$ (i.e., a hard electron spectrum), there is more energy-per-decade in high energy electrons (Bhattacharya 2001; Dai & Cheng 2001; Gao et al. 2013). This distribution has important implications for the analysis of the physics in the shock region, specifically requiring an additional high-energy cut-off in the electron population. We use two different approaches to overcome this issue.

Table 4.4: Closure relations*. β=0.86$\pm$0.02 was use in the analysis. When determining the energy injection parameter q, we use the measured $\alpha_{\rm pre}$=0.86$\pm$0.05 and $\alpha_{\rm pos}$=1.47$\pm$0.03. The equations used for q are for the case when $p > 2$, for both spectral regimes. More details in Racusin et al. 2009. [*] When $\nu_{\rm c}$<ν<$\nu_{\rm m}$ β=0.5 and it does not depend in p or α. We did not include this scenario as it is not compatible with our data at any time. [**] Details on the results and implications of the closure relations are discussed on the outlined section. [a] For $\nu_{\rm c}$>ν, p=2β. When β=0.86$\pm$0.02 we have p=1.73$\pm$0.03 (1<p< 2). [b] For $\nu_{\rm m}$<ν<$\nu_{\rm c}$. When β=0.86$\pm$0.02 we have p=2.73$\pm$0.03 (p>2).

		Instantaneous injection α (β)	Energy injection q (β, α)	Section**
		Radial outflow		
$\nu_{\rm c/m} < \nu^a$	ISM	$\frac{3\beta+5}{8}$ = **0.95 $\pm$ 0.01**	$\frac{2(1+\alpha-\beta)}{\beta+1}$ = 1.07 $\pm$ 0.05	4.3.1
	Wind	$\frac{\beta+3}{4}$ = **0.96 $\pm$ 0.01**	$\frac{2(1+\alpha-\beta)}{\beta+1}$ = 1.07 $\pm$ 0.05	
$\nu_{\rm m} < \nu < \nu_{\rm c}^b$	ISM	$\frac{3\beta}{2}$ = 1.29 $\pm$ 0.03	$\frac{2(1+\alpha-\beta)}{\beta+2}$ = **0.69 $\pm$ 0.04**	4.3.2
	Wind	$\frac{3\beta+1}{2}$ = 1.79 $\pm$ 0.03	$\frac{2(\alpha-\beta)}{\beta+1}$ = **-0.01 $\pm$ 0.05**	
		Uniform non-spreading jet		
$\nu_{\rm c/m} < \nu^a$	ISM	$\frac{3\beta+11}{8}$ = 1.70 $\pm$ 0.01	$\frac{2(1+2\alpha-2\beta)}{3+2\beta}$ = 0.95 $\pm$ 0.05	4.3.1
	Wind	$\frac{\beta+5}{4}$ = **1.47 $\pm$ 0.01**	$\frac{2(1+\alpha-\beta)}{2+\beta}$ = 1.13 $\pm$ 0.04	
$\nu_{\rm m} < \nu < \nu_{\rm c}^b$	ISM	$\frac{6\beta+3}{4}$ = 1.64 $\pm$ 0.01	$\frac{2(1+2\alpha-2\beta)}{5+2\beta}$ = **0.65 $\pm$ 0.03**	4.3.3
	Wind	$\frac{3\beta+2}{2}$ = 1.84 $\pm$ 0.01	$\frac{2(\alpha-\beta)}{2+\beta}$ = 0.43 $\pm$ 0.04	
		Uniform spreading jet		
$\nu_{\rm c/m} < \nu^a$	ISM/Wind	$\frac{\beta+3}{2}$ = 1.93 $\pm$ 0.01	$\frac{2+3\alpha-4\beta}{2(\beta+1)}$ = **0.79 $\pm$ 0.05**	4.3.3
$\nu_{\rm m} < \nu < \nu_{\rm c}^b$	ISM/Wind	$2\beta+1$ = 2.72 $\pm$ 0.04	$\frac{1+3\alpha-4\beta}{2(\beta+2)}$ = **0.35 $\pm$ 0.03**	4.3.3

Table 4.5: Results from SED fits for both a jet break model with $\nu_{\rm sa}$<$\nu_{\rm m}$ and $\nu_{\rm m}$<$\nu_{\rm sa}$, and for an energy injection model.

ν [Hz]	Time [ks]	Jet break $\nu_{\rm sa}$<$\nu_{\rm m}$	Jet break $\nu_{\rm m}$<$\nu_{\rm sa}$	Energy injection
$\nu_{\rm c}$	26	$>1.5\times10^{12}$	$>1.5\times10^{12}$	$>1.2\times10^{18}$
	109	$1.9^{+5.2}_{-0.4}\times10^{12}$	$3.9^{+3.2}_{-2.4}\times10^{12}$	$>1.2\times10^{18}$
$\nu_{\rm m}$	26	–	–	$<1.4\times10^{14}$
	109	$1.3^{+1.3}_{-0.3}\times10^{11}$	$<2.2\times10^{10}$	$5.1^{+1.9}_{-0.6}\times10^{11}$
$\nu_{\rm sa}$	26	–	–	–
	109	$8.3^{+1.7}_{-1.6}\times10^{10}$	$7.4^{+2.6}_{-0.7}\times10^{10}$	$7.4^{+0.2}_{-1.6}\times10^{10}$

Granot and Sari description: $\gamma_{\rm m} \propto \gamma$

The first approach is based on the assumption of a proportionality between $\gamma_{\rm m}$ and γ, where γ is the Lorentz factor of the shocked fluid. This implies that $\gamma_{\rm m}$ is proportional to local temperature, which is physically plausible since the non-thermal population is presumably accelerated out of a Maxwellian population. The upper cut-off in the electron distribution can be assumed to lie beyond the X-ray band and does not need to be accounted for explicitly. ε_e can no longer be interpreted as the fraction of energy in accelerated electrons. Instead, it becomes a scale factor between γ and

γ_m, according to γ_m=K$\times\gamma$ with K=$\bar{\varepsilon}_e \times m_p/m_e$ (Mészáros & Rees 1997). We follow the formalism used by Granot & Sari (2002), where they derive the flux equation using a full fluid profile for the blast wave (Blandford & McKee 1976) and take into account the line of sight effect and the cooling times of the individual electrons.

Based on the values for the break frequencies presented in Table 4.5 for both spectral regimes, $\nu_{sa}<\nu_m$ (Fig. 4.4a) and $\nu_m<\nu_{sa}$ (Fig. 4.4b), we derived the microphysical and dynamical parameters. The results are reported in Table 4.6 and they are used to calculate the transition times between the spectral regimes. First, the transition from fast to slow cooling. This corresponds to $t_{\nu_c=\nu_m} \sim 2.8\times10^4$ s and $t_{\nu_c=\nu_m} \sim 2.6\times10^3$ s for $\nu_{sa}<\nu_m$ and $\nu_m<\nu_{sa}$, respectively. In both cases, it is before the time of the analysed SED at t=109 ks, confirming the slow cooling assumption. Second, the transition from optically thin to optically thick, i.e., when ν_m goes below ν_{sa}. This occurs at $t_{\nu_{sa}=\nu_m} \sim 1.8\times10^5$ s when $\nu_{sa}<\nu_m$ and at $t_{\nu_{sa}=\nu_m} \sim 1.07\times10^5$ s when $\nu_m<\nu_{sa}$.

Dai and Cheng description : $\gamma_m \propto (\gamma\gamma_M^{(p-2)})^{(1/p-1)}$

Instead of assuming $\gamma_m \propto \gamma$, the effect of an upper cut-off $\gamma_M = [3e/\phi\sigma_T B]^{1/2}$ in the energy range of the accelerated particle population can be included in the minimal Lorentz factor such that $\gamma_m \propto (\gamma\gamma_M^{(p-2)})^{(1/p-1)}$ (Dai & Cheng 2001). This upper cut-off follows from equating acceleration and synchrotron cooling timescales. The advantages of this approach are that the extra cut-off is modelled explicitly, and that ε_e can still be interpreted as the fraction of energy in the accelerated electrons. However, it implies that the behaviour of the electron population at low energies is dictated by the few electrons that were accelerated more efficiently, which is not supported by any clear physical mechanism.

As in the GS description, here we calculate all the parameters for both regimes, when $\nu_{sa}<\nu_m$ and when $\nu_m<\nu_{sa}$, and report them in Table 4.6. The transition from the fast to slow cooling regime occurs at $t_{\nu_c=\nu_m} \sim 3.6\times10^4$ s for $\nu_{sa}<\nu_m$ and $t_{\nu_c=\nu_m} \sim 6.6\times10^2$ s for $\nu_m<\nu_{sa}$, consistent with the slow cooling assumption. The transition from optically thin to optically thick occurs at $t_{\nu_{sa}=\nu_m} \sim 9.8\times10^4$ s for $\nu_{sa}<\nu_m$ and at $t_{\nu_{sa}=\nu_m} \sim 1.2\times10^4$ s for $\nu_m<\nu_{sa}$.

4.3.2 $\nu_c>\nu_{XRT}$: Energy injection.

The closure relations (Table 4.4), and the possible spectral break positions resulting from fitting synchrotron spectra to the SED allow for an alternative scenario, where $\nu_c>\nu_{XRT}$ and p>2. In such a case, the break between the mm and NIR wavelength corresponds to ν_m and the break in the LC is associated with the end of the ongoing energy injection phase. Smooth energy injection into the ejecta can result from slower shells with a range of velocities catching up with each other, or from a long term engine luminosity. In the latter case, the energy injection parameter q is defined by $L = L_0(t/t_b)^{-q}$. Using the flux and frequency equations for radial flow from van Eerten & Wijers (2009) and Leventis et al. 2012, we derive the closure relation for a general density profile with an arbitrary k during the deceleration stage following energy injection ($k = \frac{4(2\alpha-3\beta)}{1+2\alpha-3\beta}$ for $\nu_m<\nu<\nu_c$). The best fit results for α_{pos} and β then imply k=1.05$\pm$0.23.

During the energy injection phase, a forward-reverse shock system is set up in the flow. Using the flux equation describing the energy injection phase from van Eerten (2014), we have a given

relation between α, β, k and q. If the emission is dominated by that from the forward shock (FS):

$$FS\ :\ q = \frac{8-2\alpha(-4+k)+2\beta(-4+k)-4k}{3k-8+\beta(k-4)}, \tag{4.2}$$

and the following relation if the reverse shock (RS) emission is dominant :

$$RS\ :\ q = \frac{4+8\alpha-2(1+\alpha+\beta)k}{(3+\beta)k-10}. \tag{4.3}$$

The values for $\alpha_{\rm pre}$ and β derived in Sec. 4.2.1 imply q=0.52±0.07 in the case of dominant FS emission and q=0.88±0.09 in the case of dominant RS emission. These q values (as well as the pre-break temporal slopes) are consistent with those determined for *Swift* samples (e.g., Racusin et al. 2009; Evans et al. 2009; Margutti et al. 2013). If we fix k=2, we obtain $q \simeq 0$ for both RS and FS, consistent with predictions for a magnetar model (Dai & Lu 1998b; Zhang & Mészáros. 2004). In the case of an ISM density profile, q=0.69±0.04 for FS emission and q=1.09±0.03 for RS emission. RS emission can therefore not be dominant as $q > 1$ implies that the energy injection decays too rapidly to sustain a plateau.

After the energy injection phase, only a decelerating forward shock remains and a standard afterglow emission model can be applied. We therefore proceed with the analysis of the final SED at $t = 109s$, which contains EVLA, CARMA, GROND and XRT data. The best fit profile is a sharp double broken power-law with χ^2/d.o.f=8.50/8 (Fig. 4.4c). The critical values reported in Table 4.5 are used to derive the micro-physical parameters after the energy injection phase (Table 4.6). In this scenario, $\nu_{\rm c}$ cannot be measured and we can only place a lower limit. The k value lies just between the expected values for ISM and wind environments, and therefore we determine the values for both wind and ISM environments using Granot & Sari (2002) and for $k = 1.05$ using van Eerten & Wijers (2009) and Leventis et al. (2012).

4.3.3 $\nu_{\rm c}$>$\nu_{\rm XRT}$: Energy injection and jet break.

Now, we analyse the afterglow parameters assuming prolonged energy injection at all times, both before and after the break in the LC, and the break in the LC is associated to a jet break. As shown in Sec. 4.3.2 RS emission is not dominant before the break and therefore we assume only a dominant FS emission. In order to avoid too many free parameters, we restrict the study to ISM and wind density profiles. The analysis for these two medium profiles for the ongoing energy injection phase before the break in the LC is presented in the previous section (4.3.2). Here, we use $\alpha_{\rm pos}$ to derive the q values after the break and, assuming q does not evolve, we compare these post break values with the pre-break values to check if it is possible to have ongoing energy injection together with a jet break. We analyse two cases for the post jet break evolution: a sideways spreading jet and a non-spreading jet. For the former case q=0.35±0.03, inconsistent with the q value before the jet break. Besides this inconsistency, if the energy is continuously injected within θ_0, while the front of the jet begins to spread, the homogeneous shell approximation leading to the closure relations used here is no longer valid. On balance the bulk of the energy will remain confined to θ_0 (see discussion in van Eerten 2014) and then the non-spreading jet approximation is favoured. The non-spreading case gives q=0.65±0.03 for an ISM density profile and q=0.43±0.03. Therefore, only the ISM density profile is consistent with the pre-break q value and the prolonged energy injection would only be possible if the observed jet break is due to geometrical effects only.

We analyse our last two SEDs including radio, submm, NIR, optical and X-ray data. We use the flux and break frequencies equations for energy injection presented in van Eerten (2014) together with equations for ν_{sa} (van Eerten in prep.) to obtain the model parameter values presented in Table 4.6. As in the previous case, where energy injection was only operating before the break in the light curve, some unphysical values for the parameters are found. The main problems are ε_e>7.6, when it should not be greater than unity, and the value for the density $\sim 10^7$ cm^{-3}, instead of being of order unity as expected.

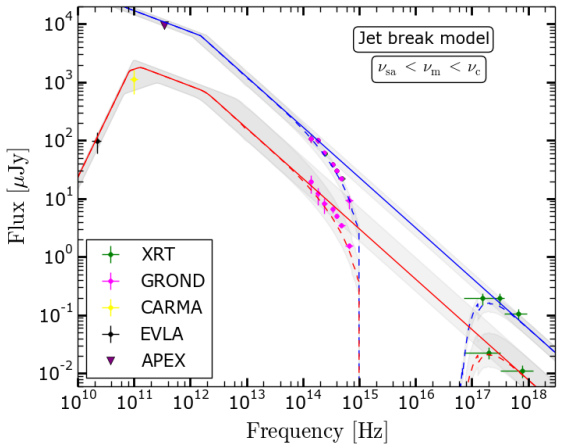

(a) Jet break: ν_{sa}<ν_m<ν_c

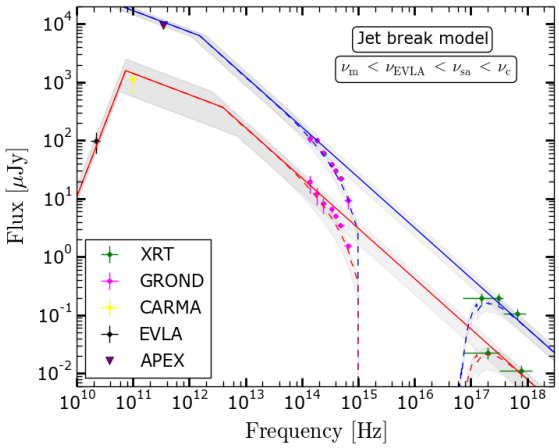

(b) Jet break: ν_m<ν_{sa}<ν_c

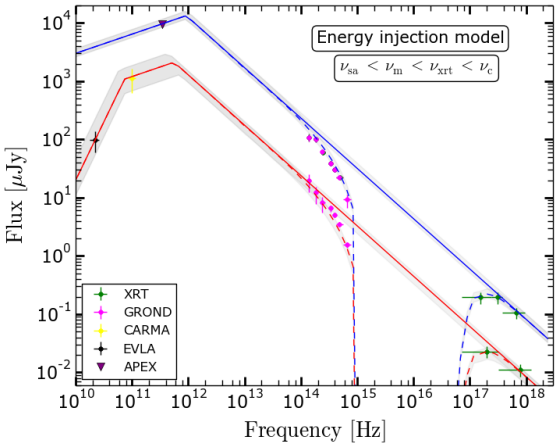

(c) Energy injection

Figure 4.4: The broadband SEDs of the afterglow of GRB 121024A from the radio to the X-ray regime for the three models described in Sec. 4.3. Blue line: SED at t=21.9 ks. Red line: SED at t=109.0 ks. The dashed lines represent the absorbed model and the solid lines represent the unabsorbed model. The grey-shaded regions corresponds to the 1σ limits of the model.

Table 4.6: γ_m, $\bar{\varepsilon}_e$, ε_B, $E_{K,iso}$, n and θ_0 for the models described in Sec. 4.3.1, 4.3.1, 4.3.2 and 4.3.3. $\bar{\varepsilon}_e$=$\varepsilon_e\times(|p-2|)/(p-1)$ and $E_{K,iso,52}$=$E_{K,iso}/10^{52}$. The half-opening angle is derived using Eq.(4) from Granot et al. (2005). $n = Ar^{-2}$ with $A = \dot{M}/4\pi v_w = 5\times10^{11} A_*$ g cm^{-1} (Chevalier & Li 2000). For $k=2$ we report the density in terms of A_*. For k=0 and k=1.05 we report the number density n_0 in units of cm^{-3}. In the special case of k=1.05 we use a reference distance of $r = 10^{17}$ cm.

	γ_m	$\bar{\varepsilon}_e$	ε_B	A_*, n_0	θ_0 [rad]	$E_{iso,52}$[erg]	η
		Jet break,	GS description,	p=1.73±0.03,	$\nu_c<\nu_{K_s}$		
$\nu_{sa}<\nu_m$	$102.7^{+139.6}_{-54.2}$	$2.09^{+2.86}_{-1.05}\cdot10^{-2}$	$2.11^{+2.49}_{-0.91}\cdot10^{-2}$	$1.41^{+4.01}_{-1.47}$	$0.32^{+0.07}_{-0.02}$	$0.15^{+0.07}_{-0.03}$	98^{+2}_{-3}%
$\nu_m<\nu_{sa}$	<11.2	$<9.31\cdot10^{-4}$	$<7.87\cdot10^{-2}$	>0.78	>0.13	>2.94	<74%
		Jet break,	DC description,	p=1.73±0.03,	$\nu_c<\nu_{K_s}$		
$\nu_{sa}<\nu_m$	$115.9^{+42.7}_{-31.2}$	$0.80^{+0.20}_{-0.62}$	$7.46^{+1.33}_{-6.37}\cdot10^{-3}$	$2.07^{+3.46}_{-1.38}$	$3.75^{+18.33}_{-0.62}\cdot10^{-2}$	$1.25^{+0.75}_{-0.75}\cdot10^{-2}$	99^{+1}_{-8}%
$\nu_m<\nu_{sa}$	<18.6	<0.11	<0.18	>0.26	$>1.12\cdot10^{-2}$	>0.19	<98%
		Energy Injection until t_b in the LC,		p=2.73±0.03,	$\nu_c>\nu_{XRT}$		
k=2	$>2.01\cdot10^3$	>1.10	$<6.64\cdot10^{-10}$	$>1.23\cdot10^3$	>0.85	>2.36	<78%
k=1.05	$>1.4\cdot10^3$	>0.76	$<2.1\cdot10^{-9}$	$>4.3\cdot10^5$	>0.8	>3.4	<71%
k=0	$>1.11\cdot10^3$	>0.75	$<2.25\cdot10^{-9}$	$>1.21\cdot10^7$	>0.77	>3.67	<69%
		Energy Injection scenario with jet break,		p=2.73±0.03,	$\nu_c>\nu_{XRT}$		
k =0	$>1.6\cdot10^4$	>7.6	$<3.9\cdot10^{-8}$	$>1.29\cdot10^7$	$>1.21\cdot10^{-2}$	>0.16	<98%

4.4 Discussion

In the previous sections we have presented a detailed analysis of the afterglow observations and derived values for the microphysical and dynamical parameters. Here we make a comparison between the derived values in the different scenarios. We discuss the positive and negative aspects of each model in the framework of the standard afterglow model.

4.4.1 Jet break without energy injection

This scenario requires three main features: First, the cooling break must be at around a few times 10^{12} Hz at 109 ks. Although such a small value for ν_c has been seen before (i.e., GRB 060418, Cenko et al. 2010), in more than 95% of a combined GROND-XRT sample, ν_c was detected above the optical frequencies (Greiner et al. 2011). Second, the closure relations require that the jet does not spread out sideways following the break time. The jet has to remain in this non-spreading state at least until $\sim$ 1 day after the jet break as no spectral evolution is detected so far in the observations. This behaviour is at odds with findings from theoretical (Granot & Piran 2012) and numerical (van Eerten et al. 2010; De Colle et al. 2012; van Eerten & MacFadyen 2012) studies of afterglow jets. Third, a very hard electron spectrum ($p < 2$) with $p = 1.73$ is required and further assumptions about the minimal Lorentz factor are required. Although this is significantly lower than the value of 2.3 expected from Fermi acceleration theory (e.g., Kirk et al. 2000; Achterberg et al. 2001), it is within the average range of values 1.5-3.0 observed in previous GRB afterglow studies(Curran et al. 2010). Two different spectral sub-regimes were presented in Sec. 4.3.1, either with $\nu_{sa}<\nu_m$ or with $\nu_m<\nu_{sa}$, and both sub-regimes where analysed using two approaches to the treatment of the hard electron spectrum.

Granot and Sari description

Here the main assumption is $\gamma_m \sim \gamma$. For both spectral sub-regimes, the derived values for ε_B (Table 4.6) are in the same range as previous measurements reported in the literature and the values of θ_0 are consistent with a collimated outflow (0.1-0.3 rad). The values for the circumburst density are therefore in agreement with the collapsar model and a Wolf-Rayet star as possible progenitor, with mass loss rates of $\sim 1.4 \times 10^{-5}\, M_\odot \mathrm{yr}^{-1}$ when $\nu_{sa}<\nu_m$ and $>7.8\times10^{-6}\, M_\odot \mathrm{yr}^{-1}$ when $\nu_m<\nu_{sa}$, for a wind velocity v=1000 km s^{-1} (Chevalier & Li 1999, 2000). The efficiency[4] requirements are extremely high. For $\nu_{sa}<\nu_m$ the measured $E_{K,iso}$ implies an efficiency of $\eta \sim 98\%$ and for $\nu_m<\nu_{sa}$ the efficiency is $\eta < 74\%$. Both of these efficiency values are much larger than expected in the standard fireball shock model for which an efficiency of $\eta < 10\%$ is predicted (Kobayashi et al. 1997; Daigne & Mochkovitch 1998; Kumar 1999; Granot et al. 2006; Cenko et al. 2011).

As a final verification of this model, we apply a condition from Granot & Sari (2002) on the evolution of the afterglow spectrum in a wind environment for a given set of microphysical and environmental parameters. This states that: If $A_* \bar{\varepsilon}_e^{-1} E_{iso,52}^{-3/7} \varepsilon_B^{2/7} > 100$ the afterglow spectrum evolves from fast to slow cooling, where in the slow cooling phase, initially $\nu_{sa}<\nu_m<\nu_c$, but eventually $\nu_m<\nu_{sa}<\nu_c$. If $A_* \bar{\varepsilon}_e^{-1} E_{iso,52}^{-3/7} \varepsilon_B^{2/7} < 100$ the afterglow spectrum only goes through one spectral regime in the slow cooling phase where $\nu_{sa}<\nu_m<\nu_c$. In this latter scenario we are never in the regime where $\nu_{sa}<\nu_m$ during the slow cooling phase. In our jet break model where the spectral regime is $\nu_{sa}<\nu_m$, we therefore require that the derived micro-physical and dynamical parameters give $A_* \bar{\varepsilon}_e^{-1} E_{iso,52}^{-3/7} \varepsilon_B^{2/7} > 100$. However, we find that our best fit values presented in Table 4.6 for $\nu_{sa}<\nu_m$ gives 52, inconsistent with the condition stated above, and therefore this regime can be ruled out. The favoured regime is then a slow cooling phase where $\nu_m<\nu_{sa}$, where our best-fit parameters give the value 257.

Dai and Cheng description

Here the assumption is based on the upper cut-off γ_M that is applied to γ_m. This upper cut-off introduces new dependences of the break frequencies and the peak flux on the parameters. In this case, the sub-regime where $\nu_{sa}<\nu_m$ is ruled out because in such a case, the time that ν_m would cross ν_{sa} is $\sim$ 81 ks, which is before the epoch of the SED (109 ks) used in the analysis. In the second sub-regime, where $\nu_m<\nu_{sa}$, θ_0 is consistent with a collimated outflow and A_* is in the range of expected values for a wind environment and corresponds to a mass loss rate of $> 2.6 \times 10^{-6}$ $M_\odot \mathrm{yr}^{-1}$ for a wind velocity v=1000 km s^{-1} (Chevalier & Li 1999, 2000), consistent with a Wolf Rayet star as a possible progenitor. The efficiency η<98%, even though it is just an upper limit is extremely high.

4.4.2 Energy injection

According to the shape of the spectrum and the closure relations, it is also possible to have $\nu_c>\nu_{XRT}$, implying an energy injection model. In the energy injection scenario, both with and

[4]Efficiency of the conversion of the kinetic energy in the outflow to gamma-rays during the prompt emission $\eta=E_{iso}^{\gamma}/(E_{iso}^{\gamma}+E_{K,iso})$. E_{iso}^{γ} is the isotropic energy released in the prompt gamma-ray emission. In this case $E_{iso}^{\gamma}=8.4^{+2.6}_{-2.2} \times 10^{52}$ erg (Butler & Kocevski 2007) (http://butler.lab.asu.edu/Swift/index.html). It is calculated using $E_{iso}^{\gamma}=4\pi d_L^2 F/(1+z)$, where F is the fluence in the gamma-ray band. BAT: from 15-150 keV in the observer-frame. $E_{K,iso}$: energy range $1-10^4$ keV in the rest frame.

without a jet break, our best-fit values for q are consistent with $q \sim 0.5$, corresponding to smooth energy injection which has been observed in several other cases (e.g., Zhang et al. 2006), and the hard electron spectrum is not required anymore since we now have p=2β+1=2.73. However, further problems with the other afterglow parameters are found.

The energy injection scenario together with a jet break in an ISM external medium and without a jet break in a wind-like (k=2) external medium can be ruled out because ε_e>1, therefore, such scenario is not physically meaningful. There are two further scenarios to be analysed then: the energy injection scenario without a jet break in an ISM medium and with a general density profile with slow k=1.05. The analysis below is focuses on these two cases.

In relation to the micro-physical parameters, the derived values for ε_B differ from previous observations but are in agreement with theoretical predictions. In the former case ε_B is more than four orders of magnitude ($< 10^{-9}$) smaller than the average measured values from previous studies (e.g., Panaitescu & Kumar 2002; Yost et al. 2003; Panaitescu 2005; Cenko et al. 2010). In the latter case, the value ε_B<10^{-9} for an ISM density profile is consistent with expected values from shock compression of the seed magnetic field ($B_0 \sim \mu$G) in the surrounding medium (Kumar & Barniol Duran 2009; Santana et al. 2014) and no further amplification or additional magnetic field would be required in the shock region. On the other hand, the derived value for $\bar{\varepsilon}_e$<0.75 consistent with theory as ε_e<1 but larger than the average of observations where $\varepsilon_e \sim 0.2$ (Santana et al. 2014).

Furthermore, in the case where $\varepsilon_B \ll \varepsilon_e$, as implied by our analysis, we would expect there to be a contribution to the cooling of electrons from inverse Compton (IC) scattering processes (Panaitescu & Kumar 2000; Sari & Esin 2001). The IC emission will mainly affect the cooling frequency in the slow cooling regime. The final value of ν_c is expected to be lower than the value with synchrotron cooling only. The IC contribution to the total observed afterglow emission can be included using the Compton parameter defined as Y=$\eta_{IC}\varepsilon_e/\varepsilon_B$, where $\eta_{IC}=(\gamma_c/\gamma_m)^{2-p}$ for the slow cooling regime (for more details see **?**). With this parameter the cooling frequency will be lowered by a factor of $(1+Y)^2$. A constraint C can be derived to test whether the IC contribution is important during the evolution of the observed emission from the afterglow or it it can be neglected (see Eq. 4.9 of Sari & Esin 2001). This constraint depends only on the observational quantities (break frequencies and peak flux) of the afterglow, and is independent of the theoretical afterglow parameters. It can be expressed in terms of Y as C=Y/(1+Y)^2 and it has a consistent solution for Y only if C<1/4. Using our measurements we find C$\sim 10^6$ for ISM. This result indicates that the IC component is not a relevant contribution for this afterglow, contrary to the theoretical expectation when $\varepsilon_B/\varepsilon_e \ll 1$ and the energy injection scenario will be not favoured.

The lower limits derived for the density are 2 (k=1.1) and 4 (k=0) orders of magnitude larger than previous density measurements for bursts with similar isotropic energies ($E_{K,iso} \sim 10^{52}$ erg) between 10^{-2} and 10^3 for constant density circumburst profiles (n) (e.g., see Fig. 11 in Cenko et al. 2011). The values for θ_0 in the case of no jet break indicate a spherical outflow, opposite to the collimated outflow usually expected and assumed in the standard afterglow theory. Finally, the energy lower limit is $\sim 3 \times 10^{52}$ erg implying an efficiency of $\eta < 70\%$.

4.4.3 Origin of the light curve break

From the available data, it is difficult to make a clear case for a preferred model for this GRB afterglow. Each of the studied models has specific problems that are difficult to explain with a simple afterglow model and would probably be better understood with a more complex and detailed model of the afterglow emission, especially at early times (e.g., Waxman & Mészáros 2003; Morsony et al. 2007). However, we are able to rule out some of the possible models. For instance, the jet break model where the spectral regime is ν_m<ν_{sa} is ruled out. In the case of GS description, it is ruled out because the spectral evolution will never cross that regime in the slow cooling phase (Sec. 4.4.1). In the case of DC it is ruled out because the time when ν_m crosses ν_{sa} is before the time of the studied SED (t=109 ks) (Sec. 4.4.1). In a similar way we can rule out the energy injection model with a wind density profile k=2, and the energy injection model with a jet break for k=0, as $\bar{\epsilon}_e$ has to be larger than one which is not physically meaningful. The energy injection model without jet break for k=1.1 and ISM density profiles can not be ruled out. However, in this model the extremely high density requirements are far from theoretically expected values and previous measurements. Moreover, the resulting spherical outflow geometry, implied by the derived value for the half-opening angle, would require a very energetic explosion.

For more than 40% of the X-ray afterglows an initial plateau lasting about $10^3 - 10^4$ s is observed (Lazzati & Perna 2007; Margutti et al. 2013) and has been associated with a continuous energy injection during the afterglow evolution (Nousek et al. 2006; van Eerten 2014). We compare the X-ray luminosity (0.3-30 keV) (L_f) and the break time in the rest frame (t_f^{RF}) to the relation observed in other GRBs (Dainotti et al. 2008). Fig. 4.5 shows the relation between L_f and t_f^{RF} observed in a sample of 62 long GRBs studied by Margutti et al. (2013). We include GRB 121024A for both: an energy injection phase that ends at the time of the break in the LC (red star) and an ongoing injection phase until the end of the observations at t=240 ks, both taking the end time luminosity directly (green star), and correcting for the change in the slope introduced at the break (grey star). Energy injection follows the correlation very well, supporting the scenario with energy injection up to the break in the LC. Continued energy injection is disfavoured in view of the correlation. Note that assuming energy injection to extend beyond the final data point at 240 ks will only further shift the grey and green stars farther away from the correlation.

We consider the jet break model where ν_m<ν_{sa} to be the preferred scenario. In this model, all the micro-physical and dynamical parameters are within the range of previous measurements and within the expected values from the standard afterglow model. The low values for the energy are just lower limits and therefore they are not a strong argument against this model. The main problem is related to the hard electron spectrum that requires additional assumptions on the acceleration process of the electrons in the shock region. However, this is certainly not the first GRB for which such a shallow electron spectrum was derived, and viable ways to handle this scenario have been put forward, two of which we investigated, and found to give reasonable and physically meaningful results. The derived hard electron spectrum need not be a reason to reject a model, and more likely reflects our poor understanding of acceleration processes under extreme conditions. Finally, the linear polarisation observations reported by Wiersema et al. (2014) would be in agreement with a jet break model where the linear polarisation would be a direct result from the jet break. However, there are still no studies reported in the literature analysing whether it would be possible to obtain this type of polarisation from an energy injection model.

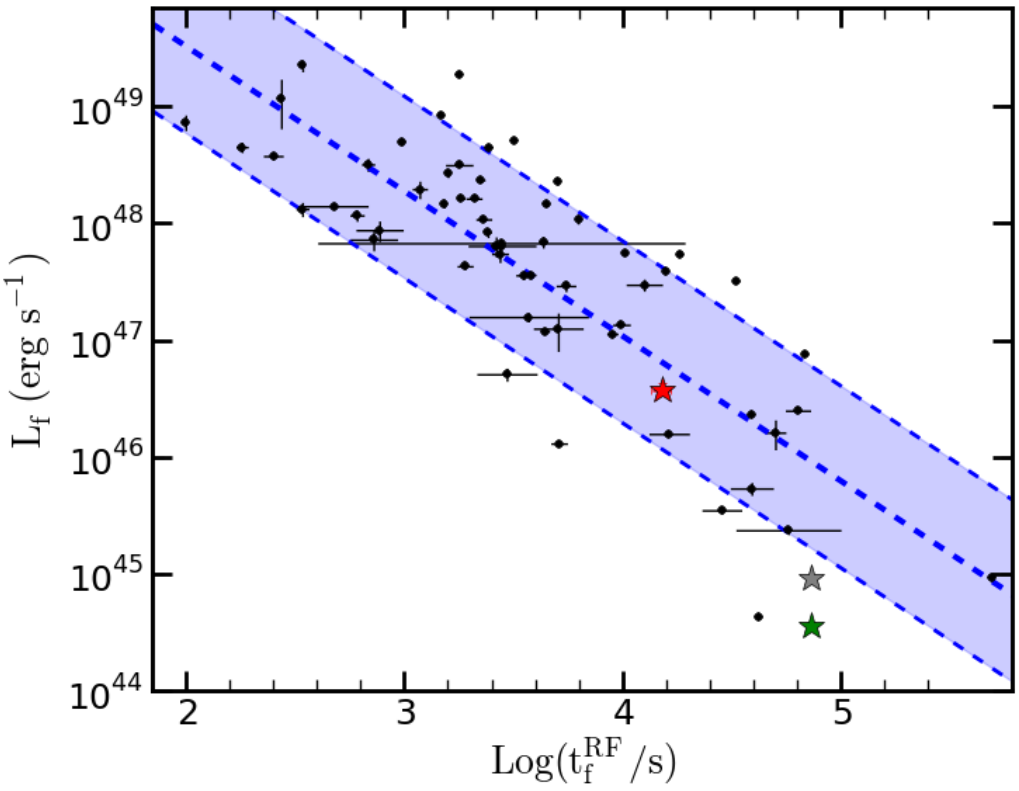

Figure 4.5: 0.3-30 keV luminosity at the end of the energy injection phase (Dainotti et al. 2008). The black dots are taken from Margutti et al. (2013). The stars corresponds to the GRB 121024A afterglow: the red one when the end of the plateau phase lies at 49.8 ks, the green star corresponds to the ongoing energy injection phase before and after the break in the LC at t = 240 ks, and the grey star corresponds to the luminosity corrected due to the jet break effect. The dashed line in the middle corresponds to the best fit and the shaded region is the 1σ error of the fit.

4.5 Summary and conclusions

We analysed the afterglow of GRB 121024A and showed how the multi-wavelength data give us a unique opportunity to set constraints on the micro-physics in the shock region and on the dynamics of the jet. The combined GROND and XRT data allowed us to determine the spectral slope β in this energy regime with high accuracy and therefore we are able to measure the electron index p We model our complete set of observations using two different physical interpretations: a jet break model and an energy injection model. The energy injection model requires $\eta < 77\%$, 71% and 69% for k = 2,1.1 and 0, respectively, and is not in contradiction with Fermi acceleration predictions for the electron index p. However it does face some problems with the derived microphysical parameters in the case of a wind density profile, and the density values are extremely high in all three of the density profiles studied.

The jet break model requires a hard electron spectrum, and in this case there is a strong dependence of the micro-physical and dynamical parameters on p. This arises from the change in the minimal Lorentz factor when an upper cut is imposed. The difference between γ_m for p>2 and for p<2 is about a factor of 60 ($p = 1.73$). However, the derived microphysical and dynamical parameters are all consistent with previous measurements and with expected values from theoretical

analysis. There is a problem with the efficiency requirements, which in the case of $\nu_{sa}<\nu_m$, can be as high as $\eta \sim 98\%$ in both GS and DC descriptions, and in the case where $\nu_m<\nu_{sa}$ the efficiency has an upper limit of $\eta < 71\%$ in the GS description and $\eta < 97\%$ in the DC description.

The results presented here on GRB 121024A show that broadband afterglow data from the X-ray to the radio allow for a detailed analysis of the characteristic properties of the GRB afterglow synchrotron emission spectrum. As studies of other GRBs have also shown, such datasets are invaluable to determine the range of microphysical and dynamical parameters within GRB shock-fronts with better statistics and avoiding adding additional assumptions to the analysis. Through our extensive data coverage of GRB 121024A we have been able to constrain the position of all synchrotron breaks, which in turn has allowed us to measure, or put constraints on, all the micro-physical and dynamical parameters of GRB afterglow.

Chapter 5

GRB 100418A

The afterglow of GRB 100418A was extensively followed-up by ground based telescopes over a wide energy range (from radio to X-ray wavelengths) over several days and weeks. The redshift determination from VLT/X-shooter was z=0.625. After the afterglow of GRB 030309, this afterglow is the brightest afterglow in the submm wavelength range that has been detected. The observations provide an excellent data set to test some of the basic assumptions and predictions of the standard afterglow model. We were able to test additional components to the basic standard model, such as energy injection, jet breaks and inverse Compton scattering. The XRT and optical observations have a plateau phase up to 76 ks that is associated with an energy injection phase. The measured value of the energy injection parameter is q=0.23$\pm$0.04, which can originate from either a magnetar model or an outflow composed by stratified shells due to the difference in Lorentz factors. The end of the energy injection coincides with the start of a geometrical jet break. After the energy injection phase, eight epochs, using multi-wavelength broadband observations were analysed. There is evidence of a late transition from fast to slow cooling regime. The external medium density is a stellar wind-like density profile. This density profile supports the association of long GRBs with the death of massive stars and the predicted and observed GRB-SN connection. A study of the evolution of all of the three break frequencies during the eight epochs was performed and the fitting results are in agreement with the theoretical predictions. The microphysical and dynamical parameters were derived from the measurement of the break frequencies and the peak flux. The results show a constant evolution of the parameters in time. As a general conclusion, the evolution of the breaks, the best fit parameters confirm that the basic assumptions of the standard afterglow are appropriate to described the observations if additional components to the model, such as energy injection, are included. The contribution of inverse Compton scattering was also tested and it is shown that it is not compatible with the observations during the fast cooling regime but it is compatible with the observation during the slow cooling regime.

5.1 Observations and data reduction

5.1.1 *Swift*

The *Swift* Burst Alert Telescope triggered and located GRB 100418A on 2010 April 18 at T_0 = 21:10:08 UT (Marshall et al. 2010). *Swift* slewed immediately to the position of the burst with the observations starting 79.1 s after the trigger with the X-ray Telescope. The afterglow was located at RA, Dec (J2000) = 17:05:27.24, 11:27:42.7 with an uncertainty of $3\farcs1$. The observations started in Windowed Timing (WT) mode until T_0+174 seconds followed by Photon Counting (PC) mode

observations up to T_0+3 Ms (Marshall et al. 2011). The *Swift* /XRT light curve and spectral data in the energy range from 0.3 - 10 keV were obtained from the XRT repository (Evans et al. 2007, 2009). The Ultraviolet/Optical Telescope (UVOT Roming et al. 2005) observed the afterglow source in the same time interval as *Swift*/XRT. The preliminary analysis of collected data with the white filter in the first 150 seconds located the source at RA, Dec (J2000)=17:05:26.96, 11:27:41.9 with an uncertainty of $1\farcs0$ (Marshall et al. 2010). The observations show an initial plateau phase followed by a normal decay phase after T_0+50 ks, with a host of magnitude 22.7 in the white band (Marshall & Holland 2010).

5.1.2 GROND

Optical/NIR observations in a wavelength range from 400-2400 nm ($g'r'i'z'JHK_s$) using GROND were performed on the afterglow source reported by Marshall et al. (2010). The observations started on April 19 2010 at 4:50 UT (Filgas et al. 2010) and continued for the next 6 hours during the first night. The afterglow was detected in all 7 bands at the position RA, Dec (J2000) = 17:05:27.09, 11:27:42.3 with an uncertainty of $0\farcs4$ in each coordinate (Fig. 5.1). The observations of the field of GRB 100418A continued on the 2nd, 3rd, 4rd, 6th and 23rd night after the burst. The optical/NIR data were reduced using standard IRAF tasks (Tody 1993; Krühler et al. 2008). The data were corrected for Galactic foreground reddening $E(\mathrm{B}-\mathrm{V})=0.07$ mag (Schlafly & Finkbeiner 2011), corresponding to an extinction of $A_\mathrm{V}=0.22$ mag for $R_\mathrm{v}=3.08$. The optical magnitudes were calibrated against Sloan Digital Sky Survey SDSS (Aihara et al. 2011) stars in the GRB field. The NIR magnitudes were calibrated against the Two Micron All-Sky Survey (2MASS, Skrutskie et al. 2006) catalogue stars in the field of the GRB.

Table 5.1: Secondary stars for photometric calibration. Fig. 5.1

Star	RA, Dec J(2000)	$g'(\mathrm{mag_{AB}})$	$r'(\mathrm{mag_{AB}})$	$i'(\mathrm{mag_{AB}})$	$z'(\mathrm{mag_{AB}})$	$J(\mathrm{mag_{Vega}})$	$H(\mathrm{mag_{Vega}})$	$K_\mathrm{s}(\mathrm{mag_{Vega}})$
I	17:05:29.60 +11:27:05.9	17.43±0.05	17.05±0.05	17.01±0.05	16.98±0.06	15.83±0.09	15.59±0.10	—
II	17:05:29.06 +11:27:44.8	18.24±0.05	16.99±0.05	16.60±0.05	16.39±0.06	14.93±0.09	14.26±0.08	16.27±0.39
III	17:05:26.42 +11:27:32.5	18.24±0.05	17.68±0.05	17.57±0.06	17.49±0.07	16.27±0.07	15.89±0.10	—
IV	17:05:28.59 +11:28:02.9	19.05±0.06	17.72±0.06	17.26±0.06	17.02±0.06	15.51±0.09	14.89±0.08	17.10±0.57
V	17:05:27.61 +11:27:40.8	18.89±0.06	18.48±0.07	18.42±0.07	18.38±0.07	17.18±0.09	15.71±0.08	15.34±0.14

5.1.3 Submillimeter

The optical counterpart of GRB 100418A was followed-up in the submm wavelength range using the Submillimeter Array SMA and the Plateau de Bure interferometer PdBI over several days.
SMA: observations of the afterglow of GRB 100418A started on April 19th 2010 at 13:00 UT, 16 hours after the trigger (Martin et al. 2010). The observations were performed at a mid frequency of 340 GHz with an initial detection of the counterpart with a flux of 13.40±1.60 mJy (de Ugarte Postigo et al. 2012). Follow-up observations were performed during the following 4 nights until the source was not detected anymore (see Table 5.2) down to a 3σ upper limit of < 4.2 mJy.
PdBI: observations started on April 19th 2010, 1.26 days after the trigger, and continued for 2 months until the source was not detected anymore after 69 days down to a 3σ upper limit of $<$ 0.57 mJy (de Ugarte Postigo et al. 2012). The observations were performed in three different bands: 86.7 GHz, 103.0 GHz and 106.0 GHz with an initial detection at 103.0 GHz with a flux of 6.57±0.07 (see Table 5.2).

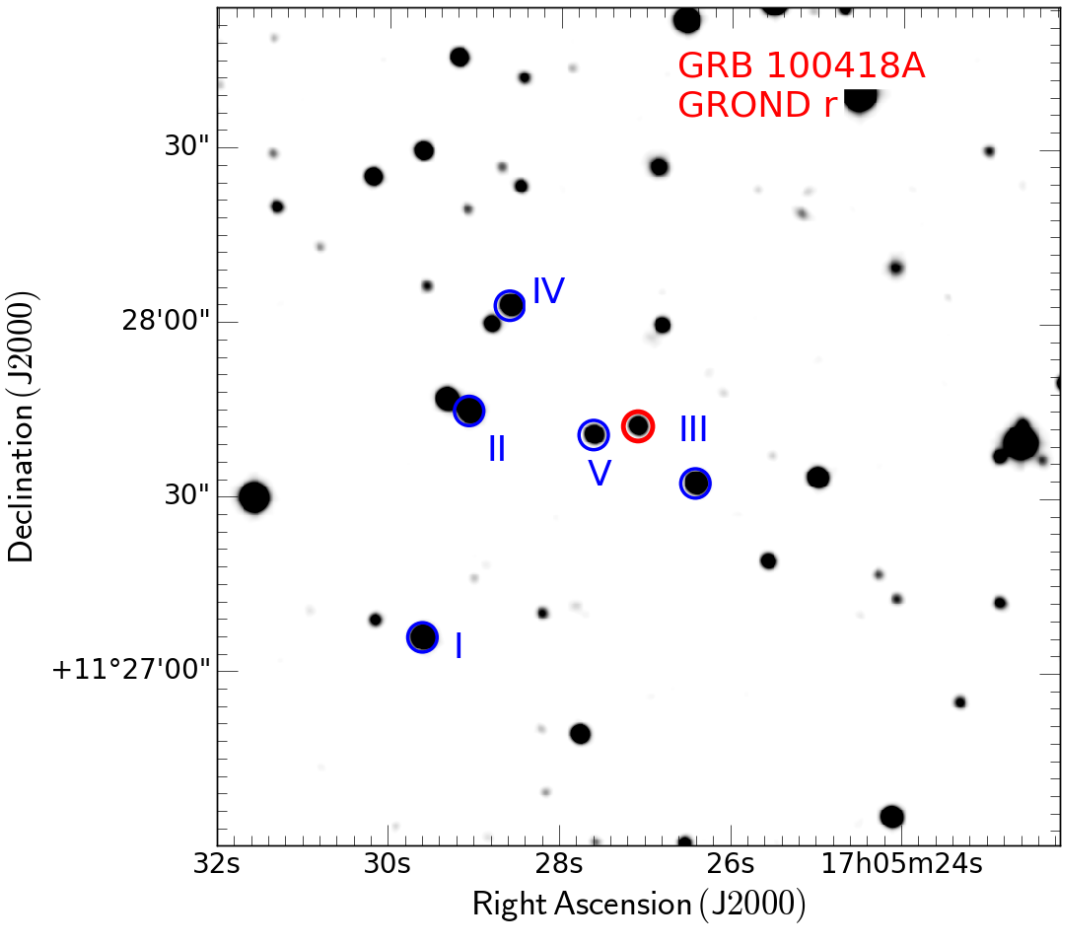

Figure 5.1: GROND r'-band finding chart. The secondary stars are reported in Table 5.1 and are labeled from I-V. North is up and East to the left.

5.1.4 Radio

Radio observations were also performed on the source. The Very Large Array VLA, the Australian Telescope Compact Array ATCA and the Westerbork Synthesis Radio Telescope WSRT were used to monitor the source during 2 years.

On April 20th ATCA follow-up observation began of the afterglow. The afterglow was followed up for three epochs on the 2nd, 38th and 67th day after the trigger in two different bands 5.5 GHz and 9.0 GHz (see Table 5.2). The observations show a constant flux for both frequencies with an average flux of 900 μJy in the 5.5 GHz band and 1250 μJy in the 9.0 GHz band. On the same day of the start of the observations with ATCA, WSRT observed the field of the afterglow for $\sim$ 8 hours and detected a radio counterpart with a flux density of 369$\pm$29 μJy at a frequency of 4.8 GHz (van der Horst et al. 2010).

The source was monitored at 8.46 GHz frequencies using the VLA (Moin et al. 2013) between 2 and 157 days after the trigger. The flux increased during the first days until about the 38th days and then if starter to decrease. It was also followed-up at frequencies of 4.95 GHz, 4.9 GHz and 7.9 GHz (see Table 5.2).

Table 5.2: Submm and radio fluxes. The epochs corresponds to the eight highlighted epochs in Fig. 5.4. (Chandra & Frail 2012; de Ugarte Postigo et al. 2012; Moin et al. 2013)

SED	mid-time [ks]	SMA [mJy] 345 GHz	PdBI [mJy] 103/106 GHz	PdBI [mJy] 86.7 GHz	ATCA [mJy] 9 GHz	VLA [mJy] 8.46 GHz	ATCA [mJy] 5.5 GHz
I	173	5.10 ±0.90	–	–	1.27±0.09	–	0.86±0.12
II	259	5.40 ±1.10	3.43±1.00	–	–	0.46±0.02	–
III	450	4.20 UL	–	3.70±0.07	–	0.29±0.02	–
IV	1065	–	1.13±0.12	–	–	0.52±0.02	–
V	1555	–	–	1.14±0.05	–	0.54±0.02	–
VI	2246	–	–	1.18±0.09	–	0.85±0.03	–
VII	3283	–	0.61±0.13	–	1.39±0.18	1.02 ±0.06	0.90±0.08
VIII	5788	–	–	0.55±0.18	1.60±0.20	0.82 ±0.06	1.27±0.12

5.2 Phenomenological data analysis

5.2.1 Afterglow light curve fitting

The X-ray temporal evolution for the afterglow of GRB 100418A is well described by a double broken power-law with smooth breaks Eq. 3.1. It starts with an initial steep decay up to 700 s. This phase was initially covered by observations in WT mode up to 200 s and then it was followed by observations in the PC mode. This steep decay is commonly observed in the canonical light curve in X-rays and it is associated to the curvature effect of the high latitude emission (Zhang et al. 2006). This is followed by a slowly increasing, almost flat phase which is consistent with the previously observed plateau phases up to about 80 ks. This plateau phase may be associated to an ongoing energy injection phase (Marshall et al. 2011). Finally, it has a late decay associated to a normal decay phase during the afterglow emission where the break time is associated to be the end of the ongoing energy injection. It could also be associated not only to the end of the energy injection but to a jet break. The data are best described by an initial steep decay with $\alpha_{\rm pre}$=4.16±0.08 up to $t_{\rm b_1}$=622±78 s with smoothness sm_1=1.0±1.2. A plateau phase with slope $\alpha_{\rm EI}$=-0.21±0.12 up to $t_{\rm b_2}$=82.3±29.1 ks with smoothness sm_2=1.1±6.6 and a final decay phase with $\alpha_{\rm pos}$=1.61±0.19. The goodness of the fit is χ^2/d.o.f=69.9/59. These results are fully consistent with the ones reported by Marshall et al. (2011), with the main differences arising from the smoothness factor that is only included here to account for the soft transition that is expected in the afterglow process (Fig. 5.2).

The optical/NIR light curves (Table 5.3) in all 7 bands ($g'r'i'z'JHK_s$) have an initial plateau phase followed by a decay phase. The best fit describing the observations is a smooth broken power-law with host contribution Eq. 3.1. The best fit parameters are $\alpha_{\rm pre}$= 0.32±0.04, $\alpha_{\rm pos}$=1.41±0.04, $t_{\rm b}$=73.6±2.5 ks, sm=15.0±10.8, with a goodness of the fit χ^2/d.o.f=180.7/184. The observations from UVOT in the *white* band (Siegel & Marshall 2010) and the observations in the Rc band (Bikmaev et al. 2010; Hattori & Aoki 2010) show a fast increase in flux between 2000 s and 7000 s, this increase in flux could be the result of a flare on top of the plateau phase (Marshall et al. 2011) or a refreshed shock. However, it is not coverer by either XRT or GROND observations, and therefore it is difficult to determine the real effect of the flare on the plateau phase evolution. Even more, the difference in the increment on flux between the observations in the R_c and the *white* band could be instrument related. Even though, after this time of the flare, the observations are consistent with GROND and XRT and therefore the possible flare contribution is not taken into account in the study.

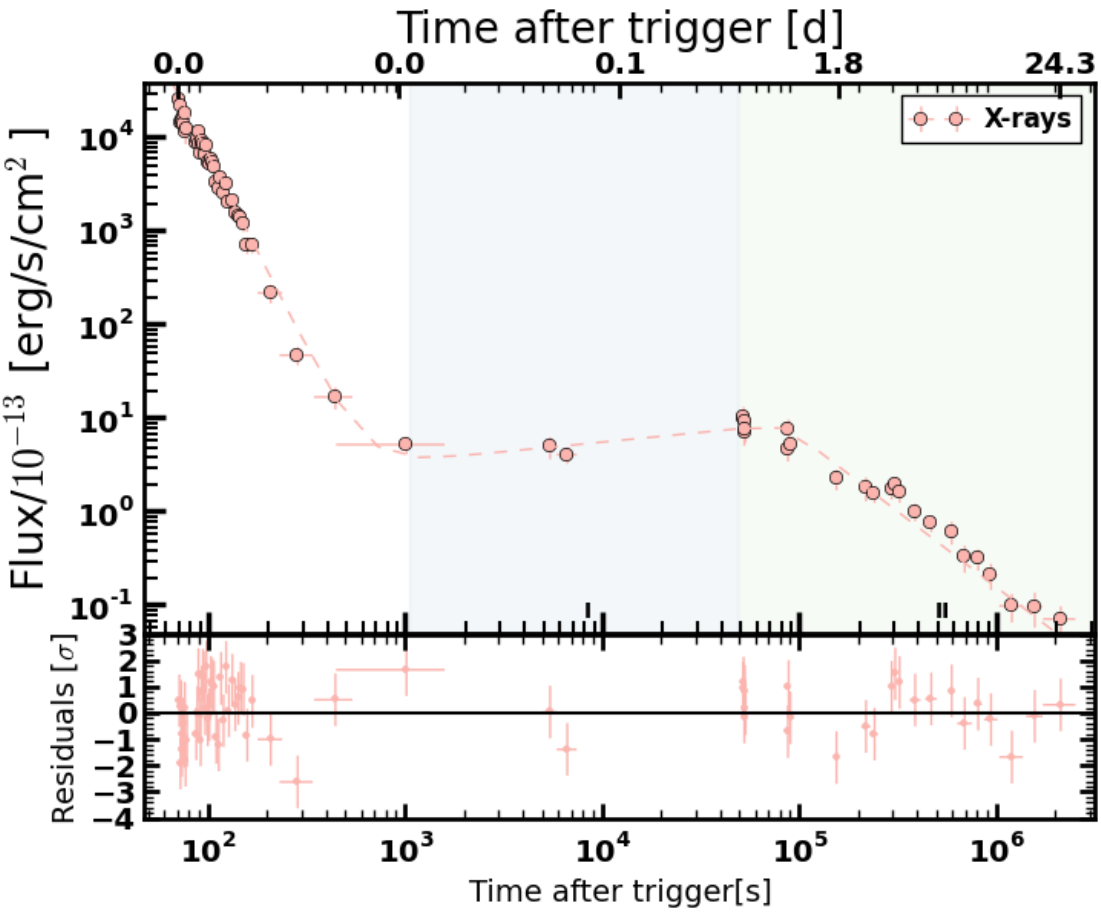

Figure 5.2: X-ray light curve of GRB 100418A from the XRT repository. The best fit is a smoothly double broken power-law shown in dashed lines. The analysed epochs are shown in the plot by vertical shaded regions with different colours. The white region corresponds to the steep decay phase observed in WT+PC mode. The blue highlighted region corresponds to the plateau phase and the light green highlighted region correspond to the post-energy injection phase after a jet break.

Table 5.3: Observed magnitudes of the GRB 100418A afterglow for the seven highlighted epochs in light blue and light red in Fig. 5.3. Two epochs during the energy injection phase and five epochs after the break in the light curve. The host contribution was subtracted for each band. The Galactic foreground extinction is $A_{\rm v}^{\rm Gal} = 0.22$ mag.

SED	mid-time [ks]	$g'(\mathrm{m_{AB}})$	$r'(\mathrm{m_{AB}})$	$i'(\mathrm{m_{AB}})$	$z'(\mathrm{m_{AB}})$	$J(\mathrm{m_{Vega}})$	$H(\mathrm{m_{Vega}})$	$K_{\rm s}(\mathrm{m_{Vega}})$
I*	27.7	18.99±0.05	18.64±0.05	18.33±0.07	18.08±0.07	17.63±0.07	17.26±0.08	17.18±0.14
II*	40.2	19.11±0.05	18.48±0.07	18.77±0.06	18.24±0.07	17.81±0.09	17.49±0.10	17.15±0.12
I	130.9	20.20±0.06	19.87±0.06	19.56±0.07	19.36±0.07	18.93±0.09	18.66±0.12	18.34±0.11
II	202.1	20.92±0.06	20.60±0.06	20.27±0.06	20.01±0.07	19.66±0.09	19.51±0.11	19.12±0.16
III	217.8	21.07±0.07	20.73±0.07	20.36±0.06	20.22±0.08	19.85±0.10	19.55±0.13	19.22±0.18
IV	296.8	21.34±0.06	21.13±0.07	20.72±0.07	20.59±0.07	20.07±0.11	19.91±0.16	19.72±0.14
V	476.4	21.96±0.05	21.60±0.04	21.36±0.06	21.09±0.08	20.53±0.17	20.18±0.16	19.98 UL
h	–	22.82±0.06	22.36±0.06	22.25±0.07	22.14±0.07	21.95±0.08	21.70±0.18	21.68±0.25

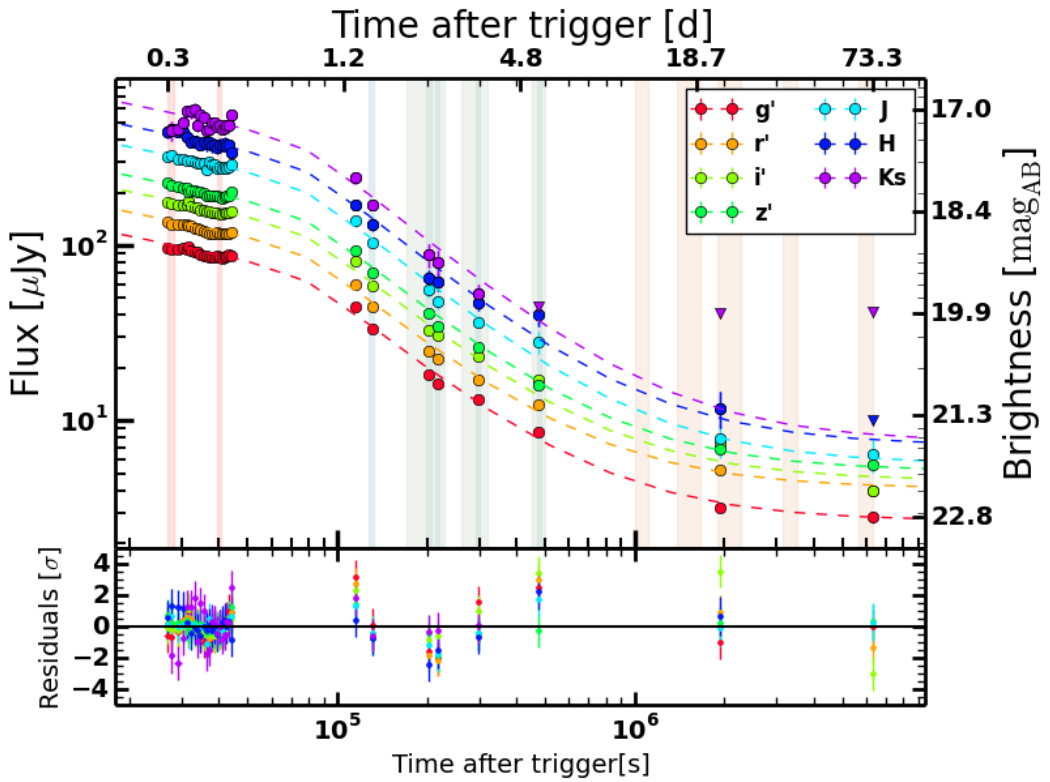

Figure 5.3: GROND light curve $g'r'i'z'JHK_s$ of the afterglow of GRB 100418A. The best fit of the combined optical/NIR and X-ray data is a smooth broken power-law with host contribution shown in dash lines. The epochs used for the spectral analysis are highlighted with the vertical bars. The first two epochs highlighted in light red corresponds to the energy injection phase (see Sec. 5.4.2). The 4 epochs in light blue and light green correspond to the fast cooling regime and the last five epochs in orange correspond to the slow cooling regime. The red and blue epochs are used in the first SED analysis using GROND and XRT data (Sec. 4.2.2). The green and orange epochs corresponds to the SED analysis that includes radio data (Sec. 4.3).

As discussed above, the XRT and GROND data are both described well by a smooth broken power-law with consistent best-fit parameters. In order to have a better constraint on the break time, a combined fit of both the XRT and GROND data is performed. The main difference between the combined and the individual data sets are the values of the pre-break slopes. As observed in the individual fits, the optical bands are slowly decreasing and the X-ray band is slowly increasing. However within a 3σ uncertainty range they are consistent with a flat slope. The difference might be associated to either a different contribution from a flare or refreshed shock to the different bands. If data before 10 ks in X-rays is not included in the fit, the best fit is then completely consistent with GROND observations. I performed three different fits (all of them with the break time linked): linking both the pre- and post- break slopes of XRT and GROND (χ^2/d.o.f=302.4/260), linking only the post-break slopes (χ^2/d.o.f=269.6/259) and leaving both slopes free to vary (χ^2/d.o.f=266.2/258). The post break slopes are consistent to be the same for both XRT and GROND when they are free to vary. The pre-break slopes are consisted with the individual fits of XRT and GROND when they are not linked to each other and, they have an average value of 0 when they are linked. An F-test was applied to check for the best fitting profile, as a result, with an F value of 31.5 and probability of order 10^{-8} the best fit is the model where only the post-break slopes to be linked. The best fitting parameters are $\alpha_{\rm pre}^{\rm XRT}$=0.11$\pm$0.05 and $\alpha_{\rm pre}^{\rm opt}$=0.36$\pm$0.04, $t_{\rm b}$=76.4$\pm$2.7 ks, sm=6.9$\pm$1.3 and $\alpha_{\rm pos}$=1.46$\pm$0.04.

The observations with SMA at 340 GHz are described by an initial decay phase with $\alpha_{\rm pre}^{\rm opt} \sim 1.61$ up to $t_{\rm b} \sim 126$ ks, followed by a plateau phase of $\alpha_{\rm pos}^{\rm opt} \sim 0.15$. Further observations were performed with PdBI at 106 GHz and 103 GHz. There are three epochs that are described by a power-law with a decaying slope of $\alpha \sim 0.75$. The PdBI observations are described by an initial slope with $\alpha \sim 2.1$ up to $t_{\rm b_1} \sim 8.2 \times 10^5$ s followed by a plateau phase with $\alpha \sim 0.23$ up to $t_{\rm b_2} \sim 3.1 \times 10^6$ s and a final decay phase with $\alpha \sim 1.5$. The observations with ATCA at 9.0 GHz and 5.5 GHz show a constant flux from 10^5 to 10^6 seconds, however, it is possible that the first observations are affected by interstellar scintillation effects and therefore the actual flux might be lower. This is supported by the VLA observations at 8.46 GHz. The temporal evolution of the data obtained with VLA shows an initial decrease in flux between the first two epochs, followed by an increase in the flux with $\alpha \sim -1.8$ up to $t_{\rm b} \sim 4 \times 10^6$ s and then a decay phase with $\alpha \sim 2.1$. The scintillation effects on the observations are included as an additional error on the individual observations. The evolution of VLA is, however, increasing faster than the expectations (Fig. 5.4).

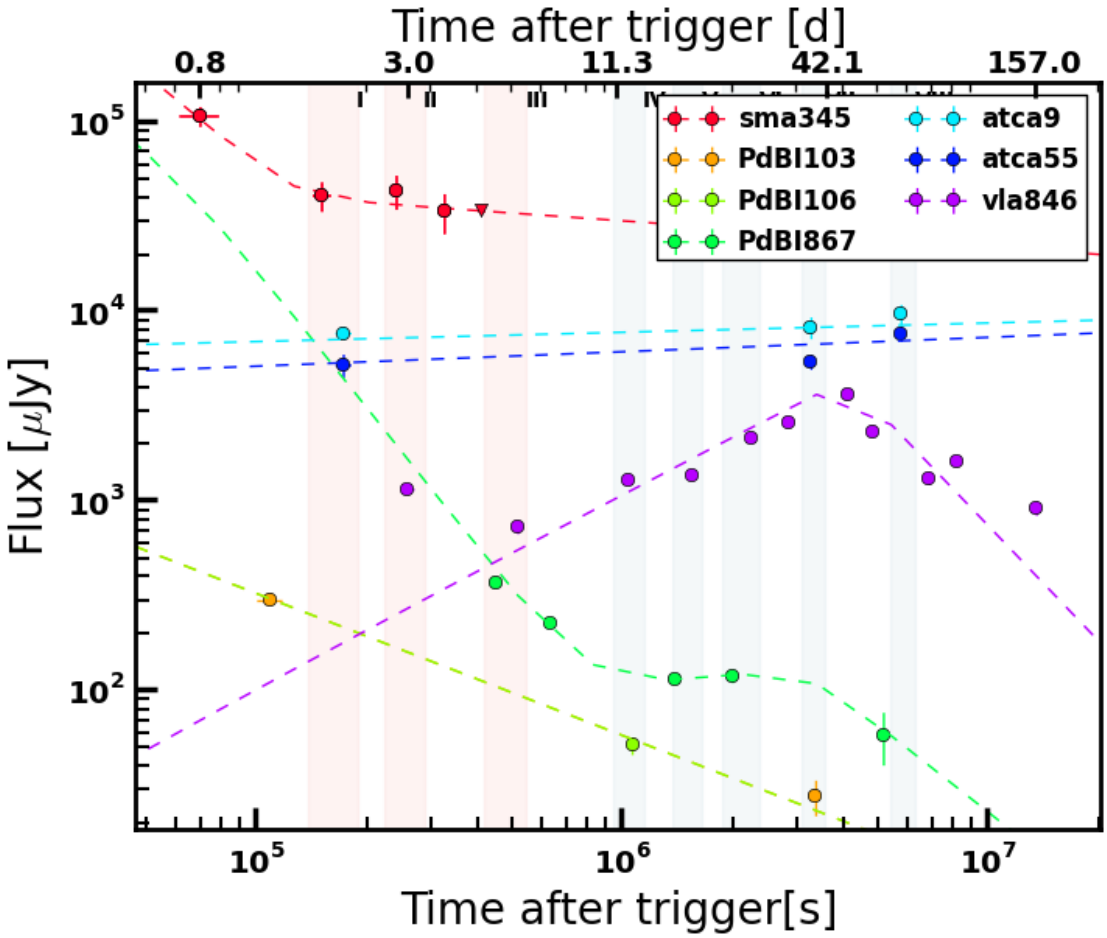

Figure 5.4: Submm and radio light curves. The best fit for each one of the bands is presented by dashed lines. The eight highlighted vertical regions correspond to the epochs used in the SED analysis using multi wavelength data. The orange regions corresponds to the fast cooling regime and the blue regions corresponds to the slow cooling regime. The light curves are scaled to a arbitrary factor for clarity of the plot.

5.2.2 Afterglow SED fitting

I used seven epochs with combined XRT and GROND data for the SED analysis (see Chap. 3). Two epochs during the plateau phase and five epochs after the break in the light curve. In the case of the optical data, they were previously corrected for the Galactic reddening $E(\mathrm{B}-\mathrm{V})$=0.07 mag, corresponding to an extinction of $A_{\mathrm{v}}^{\mathrm{Gal}}$=0.22 mag (Schlafly & Finkbeiner 2011) for a Milky Way (MW) reddening law and the host magnitude was subtracted from the optical/NIR data. The values for the dust extinction and gas absorption from the host are linked between all the epochs.

The first analysis starts with the two epochs during the plateau phase. Initially, the SED slopes are left free to vary, however, the fit consistently have the same slope in all cases. To have a more accurate measurement of the SED slope β, the dust and gas extinction due to the host galaxy, we linked the slopes of the SEDs (Fig. 5.5a). Because there is no simultaneous coverage of the plateau phase with GROND and XRT instruments, the SED fitting is done separately during this epoch. The best fit to the data is a power-law fit with no SED evolution observed. The fit for the two SEDs at t=27.7 ks and t=40.2 ks using GROND data has a goodness of fit χ^2/d.o.f=5.66/10 with a spectral index $\beta = 1.12^{+0.10}_{-0.18}$ and host dust extinction given by a Small Magellanic Cloud (SMC) reddening law (Pei 1992) $A_{\mathrm{v}}^{\mathrm{host}} = 0.06^{+0.19}_{-0.06}$ mag. In the case of the X-ray SEDs, the observations during the three analysed epochs are well described by a power-law with β=0.94±0.12, $N_{\mathrm{H}}^{\mathrm{host}} = 0.03^{+0.01}_{-0.03}$ cm^{-2} and a goodness of the fit of χ^2/d.o.f= 7.4/9 [1].

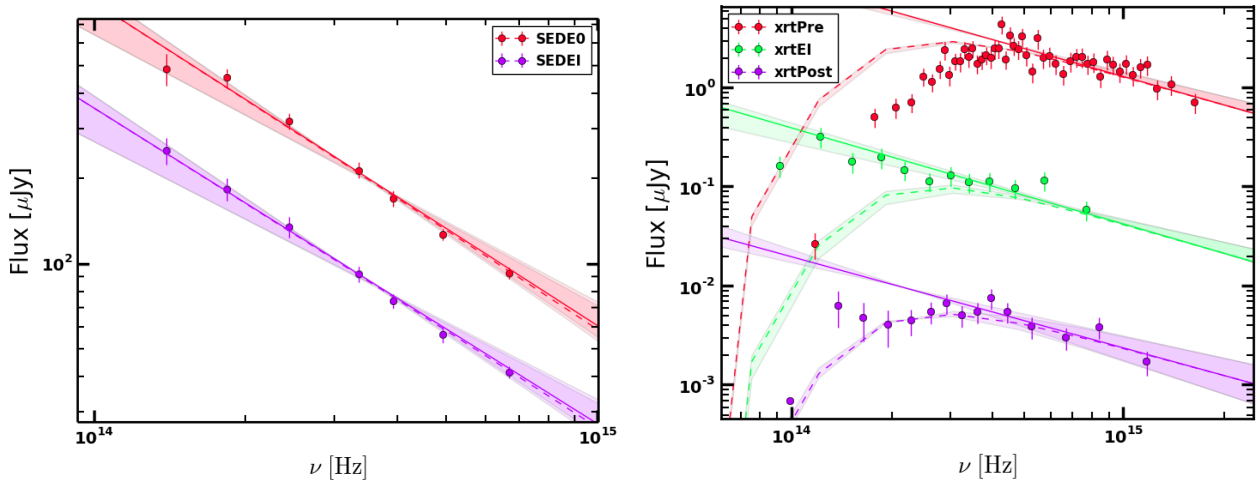

(a) GROND SED **(b)** XRT spectra

Figure 5.5: Left: GROND SED at t=27.7 ks and t=40.2 ks during the plateau phase. The plot shows the free slope fit with $\beta = 1.14^{+0.08}_{-0.19}$ for the epoch at t=27.7 ks and $\beta = 1.11^{+0.08}_{-0.20}$ for the epoch at t=40.2 ks (red regions in Fig. 5.3). The slopes are consistent with the results from the fit when the slopes are linked with $\beta = 1.12^{+0.10}_{-0.18}$. **Right**: XRT spectra for the three analysed epochs. xrtPre corresponds to the white region in Fig. 5.3. The spectra xrtEI corresponds to the plateau phase observed in Fig. 5.3 in light blue. The xrtPost corresponds to the normal decay phase as observed in the light-green region in Fig. 5.3. The SED slope for the three epochs is consistent with being $\beta = 0.94 \pm 0.12$ (Fig. 5.2).

[1] The gas column density has an apparent evolution through out the observations before and during the energy injection phase. For the present work the relevant $N_{\mathrm{H}}^{\mathrm{host}}$ is the one after the energy injection phase ends.

An analysis of the spectral evolution after the end of the plateau phase is performed. The individual analysis of the XRT and GROND data shows, as in the plateau phase case, that they have the same spectral slopes and can be described by a power-law. The XRT SED epoch between t=100 ks to t=300 ks is described by a spectral slope $\beta = 0.98^{+0.24}_{-0.20}$ with a goodness of the fit of χ^2/d.o.f= 8.98/12 and $N_{\rm H}^{\rm host} = 0.42^{+0.22}_{-0.08} \times 10^{22}$ cm^{-2}. The five GROND epochs have a spectral slope $\beta = 1.01^{+0.11}_{-0.12}$. All the slopes are linked between the five SEDs, this is completely consistent with the fit if the slopes are left unlinked and, therefore it is evident that there is no spectral evolution. This lack of evolution is an indication of the plateau phase being associated with an energy injection phase or to a jet break rather than a crossing of a break frequency through the observing bands (Sec. 5.5). To obtain a better constraint on the spectral slopes and the dust and metal attenuation effects, a combined fit between XRT and GROND data is done (Fig. 5.6). The best fit results are a power-law with a spectral slope β=1.11$\pm$0.02. The host dust extinction is given by a Small Magellanic Cloud (SMC) reddening law (Pei 1992) with a value $A_{\rm v}^{\rm host} = 0.01^{+0.03}_{-0.01}$ mag. The gas column density is $N_{\rm H}^{\rm host} = 0.57^{+0.09}_{-0.08} \times 10^{22}$ cm^{-2} and goodness of the fit is χ^2/d.o.f=84.71/101. A broken power-law is discarded not only by the fact that GROND and XRT data have the same spectral and temporal slopes, but by a test fit using a broken power-law model.

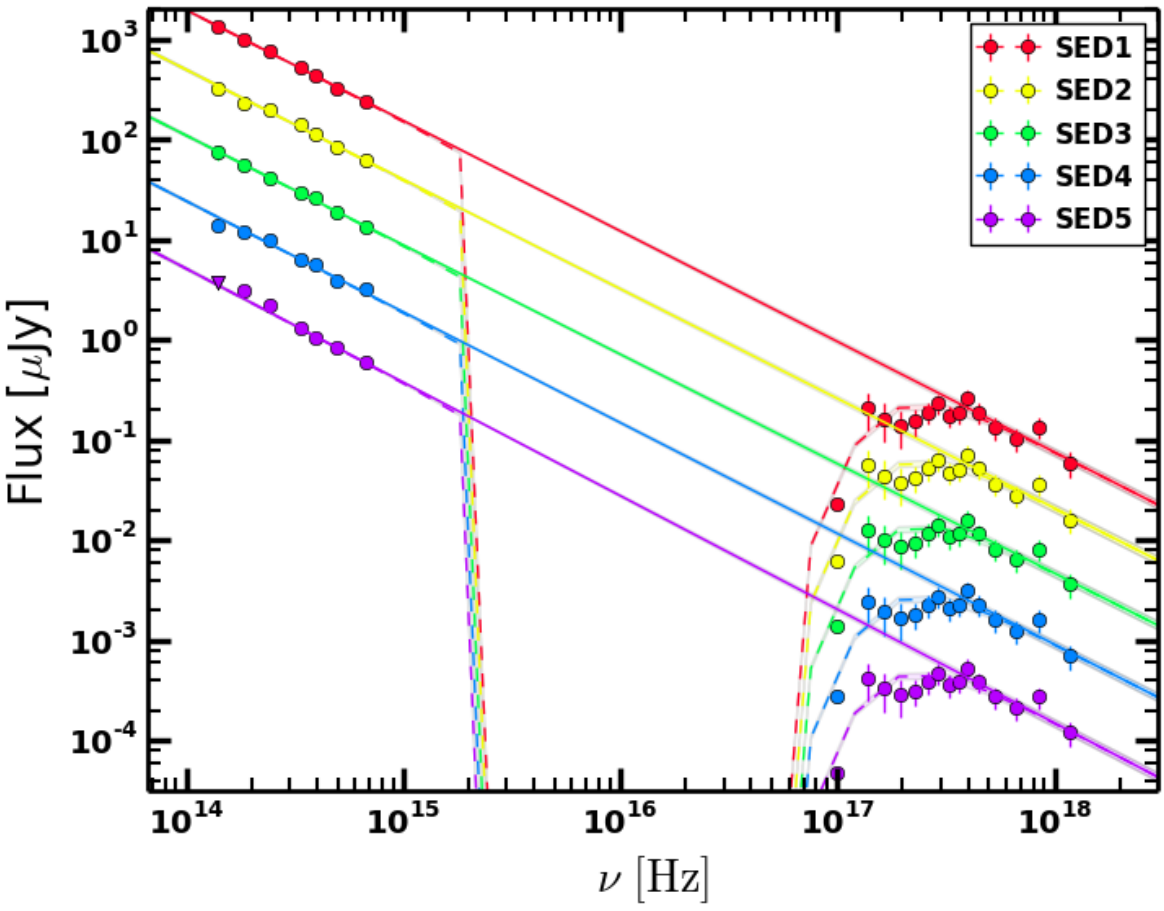

Figure 5.6: SED analysis of the afterglow of GRB 100418A using GROND and XRT data. Five epochs at SED1 (t=130.9 ks), SED2 (t=202.1 ks), SED3 (t=217.8 ks), SED4 (t=296.8 ks) and SED5 (t=476.4 ks) are presented. Each SED is scaled to an arbitrary factor for the clarity of the plot. Detailed magnitudes are given in Table 5.3. SED slope is β=1.11$\pm$0.02.

As seen in Fig. 5.7a and Fig. 5.7b, the spectral slopes, $A_{\rm v}^{\rm host}$ and $N_{\rm H}^{\rm host}$ are well constrained and their dependencies are not strong. Therefore the constrains obtained for this values are going to be used as base values for the analysis in the following sections. The submm and radio data is now included in the SED analysis (Fig. 5.8). A spectrum with three breaks is necessary to described the observations. The spectrum is analyse in the context of the afterglow synchrotron models, with synchrotron emission as the dominant emission during the afterglow phase (Chap. 2).

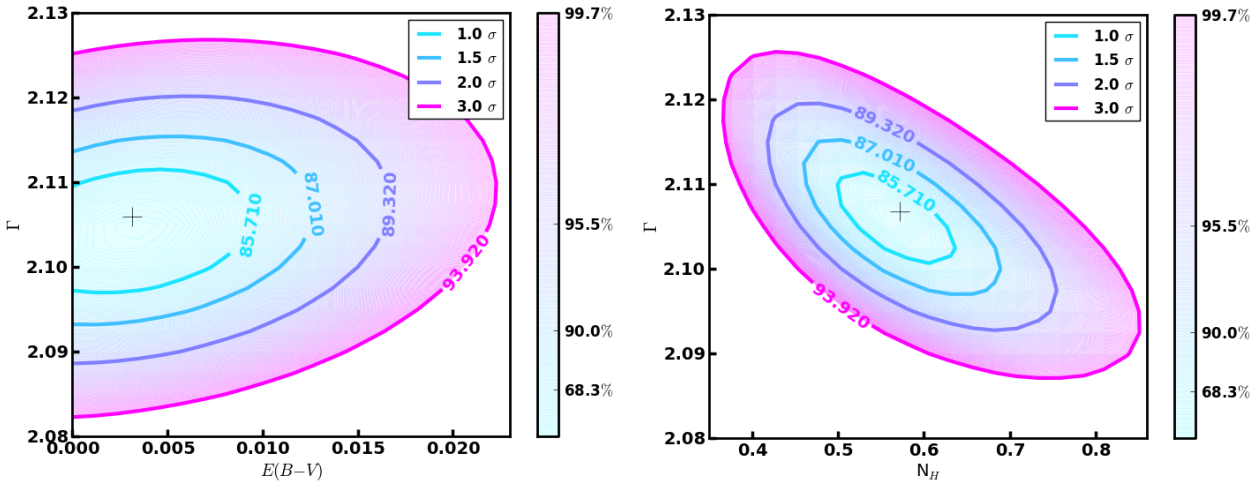

(a) Γ vs $A_{\rm v}^{\rm host}$ **(b)** Γ vs $N_{\rm H}^{\rm host}$

Figure 5.7: Contour plots showing the dependency of the photon index $\Gamma=\beta+1$ and $A_{\rm v}^{\rm host}$ and $N_{\rm H}^{\rm host}$ in the left and right, respectively.

5.3 Broadband SED analysis

After determine the slope of the SED in the X-ray and optical/NIR regions, the next step on the analysis is the incorporation of the submm and radio data. The first analysis on the broadband SED has the aim to measure all the break frequencies for each of the eight epochs (Table 5.4). The fit is a double broken power-law with smooth breaks Eq. 3.1 with the only constraints being $A_{\rm v}^{\rm host}$ and $N_{\rm H}^{\rm host}$ derived in the previous sections. The slope of the GROND and XRT bands is not fixed but allowed to vary only within a 3σ uncertainty interval as obtained in the previous section. The smoothness of each break depends on the temporal slopes in the optical/NIR and the X-ray (Granot & Sari 2002). All the epochs were fitted simultaneously. The simultaneous fit assures a unique spectral slope β, dust and gas effect $A_{\rm v}^{\rm host}$ and $N_{\rm H}^{\rm host}$ due to the host environment and a smooth transition between different spectral regimes. Fig. 5.8 shows the final fit for each one of the SEDs. The frequencies measured for the different epochs are used to derive the afterglow model parameters reported in Table 5.6. The details on the frequencies are given in Table 5.5.

Once the frequencies are determined for the different epochs, they are used to derive the afterglow model parameters reported in Table 5.6. Applying the closure relations, the observed plateaus in the optical and X-ray light curves were associated to an energy injection phase. This phase ends at about 80 ks and therefore this effect is not included in the derivation of the parameters. The analysis for the SED during the fast cooling regime and the slow cooling regime is done separately

as the dependencies of the break frequencies on the parameters changes between both cooling regimes. The observations are analysed under the main assumption of a emission dominated by synchrotron radiation and including the effect of inverse Compton scattering as an additional possible way of the Fermi accelerated electrons to cool down. All the results are reported in Table 5.6 and Table 5.7.

Table 5.4: Observed magnitudes of the GRB 100418A afterglow of the highlighted epochs in Fig. 5.3. The host contribution was subtracted and the magnitudes are corrected for $A_{\rm v}^{\rm Gal}$=0.22 mag.

SED	mid-time [ks]	$g'(\mathrm{m_{AB}})$	$r'(\mathrm{m_{AB}})$	$i'(\mathrm{m_{AB}})$	$z'(\mathrm{m_{AB}})$	$J(\mathrm{m_{Vega}})$	$H(\mathrm{m_{Vega}})$	$K_{\rm s}(\mathrm{m_{Vega}})$
I	173	20.59±0.05	20.26±0.04	19.95±0.06	19.72±0.08	19.31±0.13	18.99±0.15	18.67±0.24
II	259	21.21±0.04	20.88±0.04	20.57±0.06	20.34±0.08	19.92±0.14	19.61±0.15	19.28±0.23
III	450	21.84±0.05	21.51±0.04	21.31±0.06	21.18±0.07	20.55±0.13	19.89±0.15	>20.12
IV	1065	23.35±0.05	23.02±0.05	22.71±0.07	22.48±0.08	22.06±0.14	21.75±0.14	>21.42
V	1555	23.92±0.05	23.59±0.05	23.28±0.06	23.05±0.09	22.63±0.14	22.33±0.15	>21.99
VI	2246	24.48±0.06	24.15±0.04	23.84±0.07	23.61±0.08	23.18±0.16	22.88±0.18	>22.56
VII	3283	25.05±0.05	24.72±0.06	24.42±0.07	24.18±0.09	23.76±0.16	23.46±0.17	>23.13
VIII	5788	25.91±0.07	25.58±0.06	25.27±0.08	25.05±0.10	24.62±0.15	24.32±0.17	>23.99

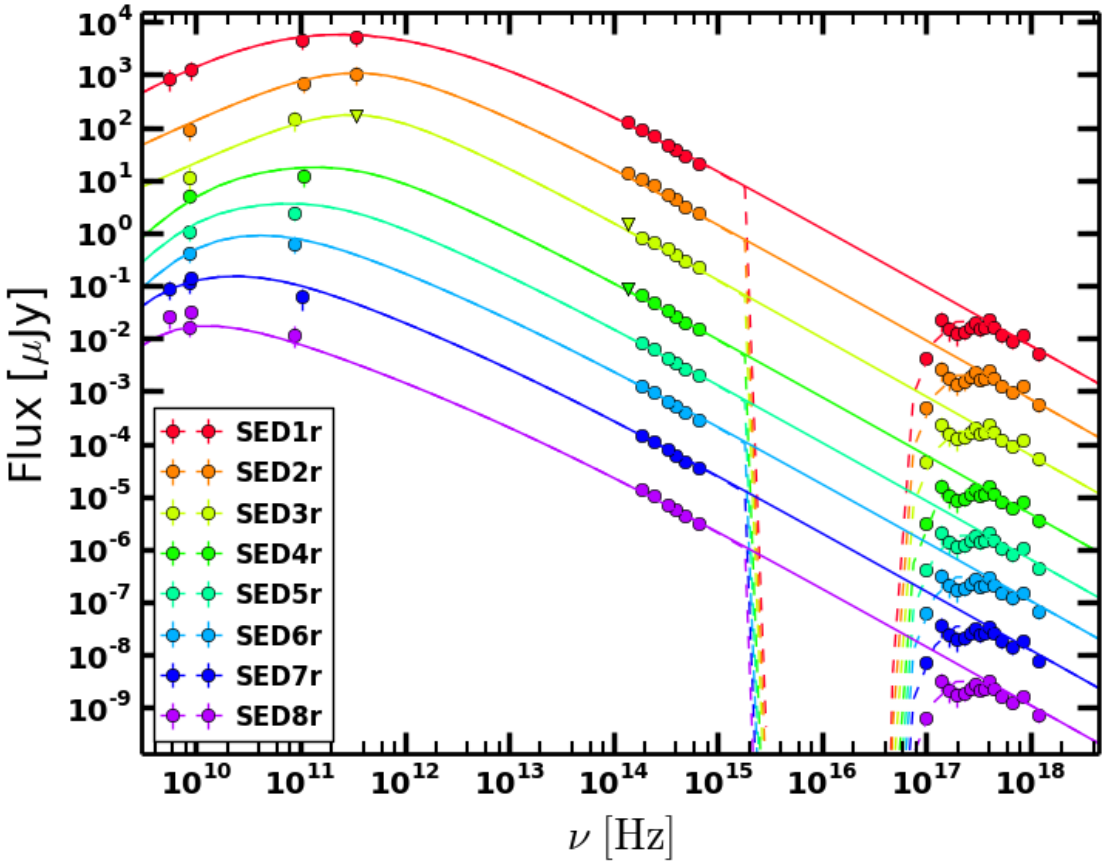

Figure 5.8: Broadband SED analysis for GRB 100418A. Eight epoch analysed using multi-epoch broad observations of GR 100418A. The first three epochs correspond to the fast cooling regime (SED1r - SED3r). The last five epochs (SED4r - SED8r) correspond to the slow cooling regime. The best fit model for all the SEDs is a double broken power-law with smooth breaks. Details on the magnitudes and the slopes and breaks are in the text and in tables.

Table 5.5: GRB 100418A afterglow SED analysis. Results for the best fit parameters using a double broken power-law The goodness of the fit is χ^2/d.o.f=183.9/159.

SED	mid-time [ks]	$\nu_{c,12}$ [Hz]	$\nu_{m,11}$ [Hz]	$\nu_{sa,10}$ [Hz]
I	173	$0.22^{+0.02}_{-0.04}$	$93.3^{+14.7}_{-26.8}$	$4.88^{+2.54}_{-2.34}$
II	259	$0.49^{+0.26}_{-0.23}$	$22.1^{+3.3}_{-3.6}$	$3.31^{+2.01}_{-0.89}$
III	450	$0.61^{+0.09}_{-0.35}$	$9.12^{+2.08}_{-2.35}$	$2.26^{+0.31}_{-0.12}$
IV	1065	$1.24^{+0.43}_{-0.10}$	$4.96^{+3.27}_{-0.95}$	$0.91^{+0.86}_{-0.51}$
V	1555	$1.34^{+0.36}_{-0.31}$	$2.25^{+1.21}_{-0.14}$	$0.85^{+0.91}_{-0.28}$
VI	2246	$2.06^{+0.31}_{-0.22}$	$0.79^{+0.41}_{-0.11}$	$0.76^{+1.03}_{-0.29}$
VII	3283	$2.20^{+0.19}_{-0.70}$	$0.44^{+0.42}_{-0.18}$	$0.62^{+0.35}_{-0.28}$
VIII	5788	$4.40^{+1.46}_{-0.98}$	$0.17^{+0.05}_{-0.03}$	$0.44^{+0.61}_{-0.03}$

5.4 Physical parameters of the standard afterglow model

5.4.1 Closure relations

The study of the energetics and the microphysics during the afterglow phase starts with the closure relations to determined the external density profile, the spectral regime and the electron index of the distribution of the accelerated electrons p. Using the pre-break slopes for the optical and X-ray observations, the plateau phase can be explained by an ongoing energy injection phase. The observing frequencies ν_{obs} can be either above the cooling break, ν_c, or the injection break, ν_m, in a stellar wind-like or an ISM external density profiles. This means that during this plateau phase, the afterglow is undergoing a cooling phase that can be either in the fast or in the slow cooling regimes. The end of the plateau phase can be associated with the end of an ongoing energy injection phase, a jet break, or both. Applying the closure relations and based on the measured post-break temporal slope, and because no spectral evolution is detected between the observations before and after the break in the X-ray or optical bands, three possible scenarios are in agreement with the observations:

1. An afterglow with the plateau phase associated to an ongoing energy injection into the outflow. This is followed by a normal decaying phase associated to a radial outflow with no energy injection. The outflow is evolving into an ISM external medium and the optical and X-ray data is on the spectral segment between ν_m and ν_c.

2. A break in the light curve associated with a uniform non-spreading jet at the end of the energy injection phase. In this case the observations imply that the outflow is propagating into a stellar wind-like external medium. The observing frequencies are above ν_c and ν_m. The cooling regime can be in either a fast or a slow cooling phase. An evolution of the cooling regime can not be discarded, as there is no difference in the closure relation in this scenario between the fast or slow cooling regime.

3. The final scenario can be a plateau phase associated to an ongoing energy injection phase. The end of the plateau phase is associated to the end of the prolonged energy injection but also to a uniform spreading jet. Within a 3σ uncertainty error bars, the external medium is consistent with both ISM or stellar wind-like medium.

After the analysis of the XRT and optical/NIR data, the temporal evolution of the radio data is included to determine which of the three proposed scenarios using only GROND and XRT data

describe the observations at low frequencies. First, the SMA data is constant or slowly decreasing. Therefore, the optical and SMA data have to be in different segments of the synchrotron spectrum. The SMA data would be consistent with an ISM or stellar wind-like external medium in the fast cooling regime for $\nu_c<\nu_{SMA}<\nu_m$. It could also be consistent with a stellar wind-like external density profile in the slow cooling regime with the SMA wavelength between ν_{sa} and ν_m. This is only consistent if the afterglow is evolving in a stellar wind-like density profile with ν_c below the optical data, and the end of the plateau phase is associated to both the end of the energy injection phase and a non-spreading jet break. The PdBI data at 106 GHz, 103 GHz and 86.7 GHz are consistent with this model where the fast cooling regime continues until $t \sim 600$ ks, and the PdBI wavelengths lie between ν_{sa} and ν_c . The radio data obtained with ATCA and VLA is difficult to reconcile with either a fast cooling or a slow cooling regime during this first observations. It might be strongly affected by interstellar scintillation. The effect of the scintillation is included as an additional 30% on the error bars in each measurement in the SED analysis. After the transition to the slow cooling regime, the radio data taken with ATCA is consistent with the expected slopes, but the VLA data increases faster than the theoretical expectations ($\alpha_{theory} = 1.0$). The reason for this fast increase is not clear, the ISS effects had already been included as additional error to the individual data points and therefore an additional effect that can not be be clearly state with the available data must being ongoing. The favoured scenario if therefore a plateau phase associated to an energy injection phase, and the end of the plateau phase is associated to the end of the ongoing energy injection together with a uniform non-spreading jet break expanding into a stellar wind-like density profile.

5.4.2 Afterglow parameters

Applying the closure relations to the GROND and XRT data, and the submm and radio light curves, give as a result that the external medium is a stellar wind-like density profile. GROND and XRT data are above ν_c and ν_m and therefore the value for the electron index is p=2.22$\pm$0.04. By analysing the broad-band SED it is possible to derive the parameters that characterise the standard model. The analysis for the SED during the fast cooling regime and the slow cooling regime was done separately as the dependencies of the break frequencies on the parameters changes between both cooling regimes (Chap. 5.3). The observations are analysed under the main assumption of a emission dominated by synchrotron radiation and including the effect of inverse Compton scattering as an additional possible way of the Fermi accelerated electrons to cool down. All the results are reported in Table 5.6 and Table 5.7.

Fast cooling: The first three epochs of the observations from SED1-SED3 are included in this case. During this fast cooling regime it is expected that inverse Compton scattering plays an important role in the cooling of the electrons (Chap. 2). It is especially important when the fast cooling phase lasts longer than a few minutes, because it could be a key feature causing the delay in the transition from the fast to slow cooling regime as IC scattering lowers the cooling frequency ν_c by a factor of Y^2. We test the strength of the inverse Compton scattering and observe that the values for ε_B are $\gg 1$, leaving the model with no physical meaning. To test whether the problem is that inverse Compton scattering is not important in the emission process or if there is an additional component besides synchrotron radiation to the observed flux, we derive the parameter C (Chap. 2). This parameter depends only on the observables (i.e., break frequencies). When $C > 1/4$, there is no available solution for the Eq. 2.26. This implies that synchrotron emission can not the only mechanism accounting for the whole emission. It is however important to note that the parameter

C is quite sensitive to the break frequencies magnitudes e.g., 2σ lower limits of the frequencies are used, $C < 1/4$. The additional component is not inverse Compton as seen in Fig. 5.11 and Fig. 5.13. Therefore it is assumed that if $C > 1/4$, it is just an indication that there must be an additional feature affecting the emission during the fast cooling regime. The microphysical and dynamical parameters for the model are derived assuming only synchrotron emission. The results are shown in Table 5.6 and Table 5.7. The parameters ε_e and ε_B are consistent with being < 1. ε_B is about two orders of magnitude lower than in the slow cooling regime, while A_* is three order of magnitude larger. ε_e is close to unity, not consistent with the assumed adiabatic nature of the outflow and with being a fraction of the total energy in the jet. θ_0 is larger than unity implying a spherical outflow and therefore not consistent with the collimated nature of the jets. Fig. 5.10 and Fig. 5.12 in the discussion section, show the result values for the parameters, together with a fit to their evolution in the shaded regions (1σ) and the average value for each parameter. The first epoch is not taken into account (hollow circle) as it is largely affected by interstellar scintillation.

Slow cooling: The last five epochs of the afterglow observations, i.e., SED4-SED8 are used in this case. The dynamical and microphysical parameters are in complete agreement with the theory. The inverse Compton scattering contribution was tested (Fig. 5.11), resulting in $C < 1/4$ and with the IC scattering contribution not being dominant during the slow cooling phase. Although IC scattering could be included it is discarded for the final analysis as it turns out to not be consistent with the observations during the fast cooling regime.

Table 5.6: Derived microphysical and dynamical parameters for the afterglow GRB 100418A. The first three epochs correspond to the fast cooling regime and the last five epochs correspond to the slow cooling regime. $\bar{\varepsilon}_e=\varepsilon_e\times(|p-2|)/(p-1)$ and $E_{K,iso,52}=E_{K,iso}/10^{52}$. $n = Ar^{-2}$ with $A = \dot{M}/4\pi v_w = 5\times10^{11}A_*$ g cm^{-1} (Chevalier & Li 2000). For $k = 2$ we report the density in terms of A_*. The subscript of each quantity are $C_x = C\times10^x$. If ε_e=1 then $\bar{\varepsilon}_e$=0.18±0.03 for p=2.22±0.04.

SED	mid-time [ks]	$\bar{\varepsilon}_{e-2}$	$\varepsilon_{B,-1}$	A_*	$E_{K,iso,52}$ [erg]
I	173	$28.8^{+5.1}_{-4.3}$	$1.32^{+0.62}_{-0.08}\times10^{-2}$	$98.6^{+31.5}_{-21.2}$	$1.05^{+0.06}_{-0.03}$
II	259	$46.3^{+9.4}_{-6.2}$	$1.19^{+0.25}_{-0.04}\times10^{-3}$	$334.1^{+84.2}_{-29.2}$	$0.33^{+0.03}_{-0.02}$
III	450	$38.9^{+7.1}_{-4.7}$	$6.60^{+0.46}_{-0.06}\times10^{-4}$	$716.1^{+108.1}_{-42.1}$	$1.06^{+0.15}_{-0.05}$
IV	1065	$6.82^{+2.35}_{-1.36}$	$1.51^{+0.27}_{-0.05}$	$2.28^{+1.74}_{-0.68}$	$2.29^{+0.12}_{-0.07}$
V	1555	$6.79^{+2.24}_{-1.24}$	$1.40^{+0.36}_{-0.06}$	$2.33^{+1.89}_{-0.66}$	$1.61^{+0.13}_{-0.06}$
VI	2246	$5.62^{+1.84}_{-1.01}$	$1.30^{+0.29}_{-0.21}$	$2.11^{+1.76}_{-0.62}$	$1.41^{+0.10}_{-0.03}$
VII	3283	$5.23^{+1.49}_{-0.92}$	$1.53^{+2.06}_{-0.03}$	$2.30^{+1.19}_{-0.52}$	$1.48^{+0.08}_{-0.04}$
VIII	5788	$5.64^{+1.73}_{-0.99}$	$0.97^{+0.15}_{-0.18}$	$1.57^{+1.89}_{-0.71}$	$1.49^{+0.11}_{-0.06}$

5.5 Discussion

I presented a detailed analysis of the multi-wavelength observations of the afterglow of GRB 100418A. The X-ray and optical light curves have a plateau phase with comparable break times and, within 3σ comparable temporal decay indexes. This plateau phase is associated to a prolonged energy injection phase with injection parameters q=0.00±0.04 and q=0.23±0.05, for the X-ray and optical bands, respectively. Theoretically, if the X-ray and optical emissions are both associated to the same source emission location, the injection parameter q have to be the same for all the bands. In this case, the derived q values for the optical and X-ray bands are different. This

Table 5.7: Secondary parameters derived using the values of the afterglow parameters reported in Table 5.6. The half-opening angle is derived using Eq.(4) from Granot et al. (2005). The subscript of each quantity are $C_x = C \times 10^{-x}$. $\dot{M}_{\rm W}$for a wind velocity of 1000 km. $E_{\rm jet}$=$E_{\rm K,iso}\times{\theta_0}^2/2$. $E_{\rm jet,\gamma}$=$E^{\gamma}_{\rm iso}\times{\theta_0}^2/2$. $E^{\gamma}_{\rm iso}$=$9.9^{+6.3}_{-3.4}\times10^{50}$ erg. $E_{\rm jet,tot}$=$E_{\rm jet}$+$E_{\rm jet,\gamma}$

SED	mid-time [ks]	θ_0[rad]	η	B [G]	$\dot{M}_{\rm W,-5}$	$E_{\rm jet,tot,50}$ [erg]
I	173	$0.62^{+0.05}_{-0.04}$	$0.09^{+0.01}_{-0.01}$	$2.65^{+0.09}_{-0.07}$	$0.98^{+0.49}_{-0.18}$	$20.3^{+1.1}_{-1.2}$
II	259	$1.13^{+0.11}_{-0.09}$	$0.23^{+0.02}_{-0.02}$	$1.96^{+0.05}_{-0.04}$	334^{+80}_{-38}	$20.9^{+0.9}_{-1.9}$
III	450	$1.02^{+0.08}_{-0.08}$	$0.08^{+0.01}_{-0.01}$	$1.27^{+0.04}_{-0.04}$	717^{+107}_{-112}	$55.0^{+1.4}_{-1.7}$
IV	1065	$0.20^{+0.02}_{-0.03}$	$0.02^{+0.01}_{-0.01}$	$0.35^{+0.02}_{-0.01}$	$2.28^{+1.74}_{-0.69}$	$4.78^{+0.12}_{-0.08}$
V	1555	$0.22^{+0.03}_{-0.02}$	$0.06^{+0.01}_{-0.02}$	$0.28^{+0.01}_{-0.01}$	$2.34^{+1.89}_{-0.66}$	$3.98^{+0.14}_{-0.07}$
VI	2246	$0.21^{+0.03}_{-0.03}$	$0.07^{+0.01}_{-0.01}$	$0.19^{+0.02}_{-0.01}$	$2.12^{+1.76}_{-0.58}$	$3.67^{+0.10}_{-0.04}$
VII	3283	$0.22^{+0.04}_{-0.02}$	$0.06^{+0.01}_{-0.01}$	$0.15^{+0.01}_{-0.01}$	$2.02^{+1.19}_{-0.52}$	$3.66^{+0.09}_{-0.05}$
VIII	5788	$0.23^{+0.02}_{-0.02}$	$0.06^{+0.02}_{-0.01}$	$0.09^{+0.01}_{-0.02}$	$2.31^{+1.89}_{-0.71}$	$3.92^{+0.13}_{-0.07}$

may be associated to an external source, such an X-ray flare, overlapping with the plateau phase that affects the X-ray measurements at this time interval. Due to the potential X-ray flare, the q value 0.23±0.05 derived using $\alpha^{\rm opt}_{\rm EI}$ is more reliable and is used in the rest of the discussion. There are three possible scenario for the energy injection phase:

- A magnetar model where the flux is constant implying a q value of 0. For this afterglow q value is more than 4σ away from 0, and therefore a magnetar model is unlikely.
- A long-lived central engine with q < 1, where a relativistic reverse shock produces an additional component observed as an energy injection phase. In this case a strong reverse shock at low frequencies is usually in this model. The observations do not show any indication of a reverse shock at radio wavelengths.
- A plateau phase that does not require a long-lasting central engine, i.e., the stratification of the mass shells. The inferred q value is less than 1 as expected for this model, with a power-law index s = 3.76. This value is consistent with the limit for s > 1 for an observable change in the dynamics of the afterglow, here observed as an energy injection phase. This last scenario is therefore the most likely and physically plausible scenario to explain the plateau phase.

Further more, after applying the closure relations it was shown that the observed break in the light curves that marks the plateau phase is not only related to the end of the energy injection, but to a uniform non-spreading jet. This means that only a geometrical effect is ongoing and the dynamics of the outflow have not change yet. The jet break detection is supported by the achromatic break and the lack of spectral evolution. The jet break supports the expectations from the theory of a collimated outflow, with a measured collimation angle from of about 0.22 rad.

Another model parameter that is usually identified by means of the closure relations is the CBM profile. I show here that optical and X-ray data are not always enough to define the density profile. Actually, it is necessary to include sub-mm and radio observations.. The expected evolution of the observed flux at low frequencies is only in agreement with a stellar wind-like density profile. Previous analysis on the GRB afterglow density profile usually point towards an homogeneous density profile. However, those analysis are based on data sets containing only optical and X-ray

observations. As shown in the Chap. 2 and in the analysis presented here, the closure relations above the cooling break do not distinguish between different density profiles. The X-ray observations usually lie on this segment (i.e., ν_c<ν_{XRT}) of the spectrum, and thus they cannot constrain the density profile by themselves. When optical observations are introduced the ambiguity also remains. On one hand, if the optical data lie above ν_c then as for the X-ray data, the density profile is unconstrained. On the other hand, if the optical data lie below ν_c , unless the temporal evolution of ν_c is clearly established, the type of external medium density is not always uniquely determined.

The analysis of the complete SED (from radio to X-ray band) at different epochs, give important results. First, there is an evolution from the fast cooling regime to slow cooling regime. This transition from fast to slow cooling regimes is required by the observed temporal evolution in the submm wavelengths. The fast cooling regime is expected to last just a few thousand seconds if the canonical values for the parameters are used (Chap. 2). If synchrotron-self Compton scattering is strong the initial values for ν_c are lowered by a factor of $(1+Y)^{-2}$. This implies a longer duration of the fast cooling regime ($\sim$ hours) than when only synchrotron cooling is included. The contribution of the SSC effect to both regimes was tested, but the resulting values are outside of the range allowed by physics. Therefore, SSC by itself does not explain the late transition from slow cooling to fast cooling. Even though it is an unusual late transition phase, it is not prohibited by physical reasoning and therefore it does not contradict the model.

From the broad band SED analysis the break frequencies were measured at all of the eight epochs that were described in detail in the previous sections. As a first test of the standard model, we check for the evolution of each of the break frequencies (Fig. 5.9). The occurrence time of all the eight epochs is larger than the end of the energy injection phase and jet break. As it is a uniform non-spreading jet, the formalism described in Chap. 2 for a spherical outflow is still valid where the proper correction for the observed flux density that accounts for the difference from the spherical case is included. As a result, it can be seen that all the break frequencies, during both, the fast and slow cooling regimes follow the expected evolution from the standard model when only synchrotron emission is included as the dominant emission component. The shaded regions in Fig. 5.9 for each frequency show the actual results of the fit of the temporal evolution. ν_c evolves with a slope of 0.57$\pm$0.04, ν_m has a slope -1.72$\pm$0.06 and ν_{sa} evolves with slope -0.56$\pm$0.06. ν_c and ν_{sa} are within 1σ uncertainty of the expected evolution of -0.5 and 0.6 respectively. ν_m is 3.6σ away from the expected 1.5 value.

I derived the microphysical and dynamical parameters using the measured break frequencies. The electron index p is 2.22$\pm$0.04 in complete agreement with an electron energy distribution from Fermi accelerated electrons. The final results for the model parameters are presented in Fig. 5.10. Assuming a power-law fitting profile (t^{α}), the best fitting slopes for the parameters are -0.14$\pm$0.06, 0.20$\pm$0.11, 0.02$\pm$0.05 and 0.22$\pm$0.12 for ε_e, ε_B, A_* and $E_{K,iso}$, respectively. These slopes are consistent within 2σ with a constant behaviour of the parameters as expected from theory. The values of the afterglow parameters for the slow and fast cooling regimes are not the same (with or without SSC component). One of the reason is that there must be an actual additional component during the fast cooling phase as suggested by the result of the parameter C being larger than 1/4. The contribution from SSC scattering was tested as a possible additional component, but the resulting value for ε_B much larger than 1 when it has to be < 1. All the other parameters have values that are within the physical expectations, i.e., ε_e about 0.8, A_* about 0.1 and $E_{K,iso}$ about 0.02, when SSC is included. There are two main reasons why the SSC component is not discarded: first the

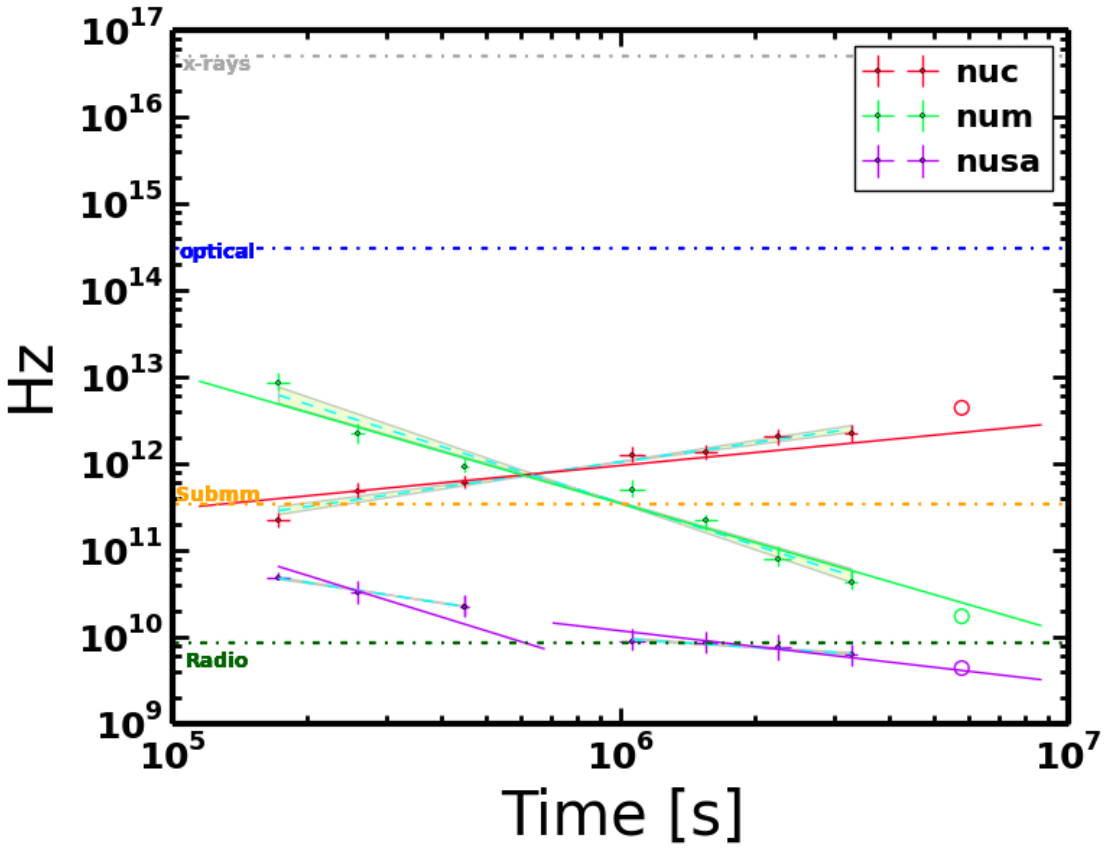

Figure 5.9: Evolution of the measured frequencies for the eight multi-wavelength SEDs that were analysed of the afterglow of GRB 100418A. The solid lines represent the expected theoretical evolution. The dashed lines and shaded regions represent the results from the fit of the observed temporal evolution. The horizontal dashed lines show the main frequency range for the observations (X-rays, optical, submm, radio).

low frequency of ν_c can be explained if SSC is strong during early stages. Second without SSC the average value for A_* is about 500, when A_* is larger than 10, SSC is expected to be dominant. Therefore, besides SSC there must be an additional component, however it can not be derived from the available data.

During the slow cooling regime all the values with and without SSC cooling are within the expected values from the theory. The main difference when SSC is included is observed in the reduction by a factor of 10 of the value for ε_B , and the increase by a factor of 7 for the value of A_*. The average value for ε_e is about 0.36 and for $E_{K,iso}$ is about 2×10^{52} erg. The relation $\varepsilon_e/\varepsilon_B$ is < 10 which is in agreement with the SSC contribution being negligible during the slow cooling phase, and therefore is no longer included for the rest of the discussion. The value of A_* (no SSC included) is of order unity as expected for Wolf-Rayet stars, assuming $\dot{M}_W$=10^{-5} $M_\odot$ yr^{-1} and v_W=1000 km/s. For a seed magnetic field in the external medium of about 10 μG in a stellar wind-like density profile at a radius r=10^{17} cm, ε_B is about 10^{-10}. For this afterglow, the value of ε_B is about 0.1, which would require a larger value of B in the shocked region. However, the evolution of B (α=-0.81$\pm$0.05), as seen in Fig. 5.12b, is as expected (α=-3/4) of a magnetic field generated by shock compression of the seed magnetic field in the CBM medium. Therefore, the difference in the expected values might just be related to the actual magnitude of B_0. If B_0 is of order of a few mG, the value derived for ε_B is repdouced by theory.

$E_{\rm K,iso}$ has an average value 2×10^{52} erg, and when compared with $E^{\gamma}_{\rm iso}$ for this GRB, the required efficiency[2] is about 6%. This result is lower than most of the efficiency values estimated from optical and X-ray data, where η can be 100% and, it is close to the predicted 10%. The half-opening angle is about 0.22 rad and the mass loss rate is of order $2\times10^{-5}\dot{M}_{\odot}$ yr^{-1} indicating a possible relation with Wolf-Rayet stars as a progenitor.

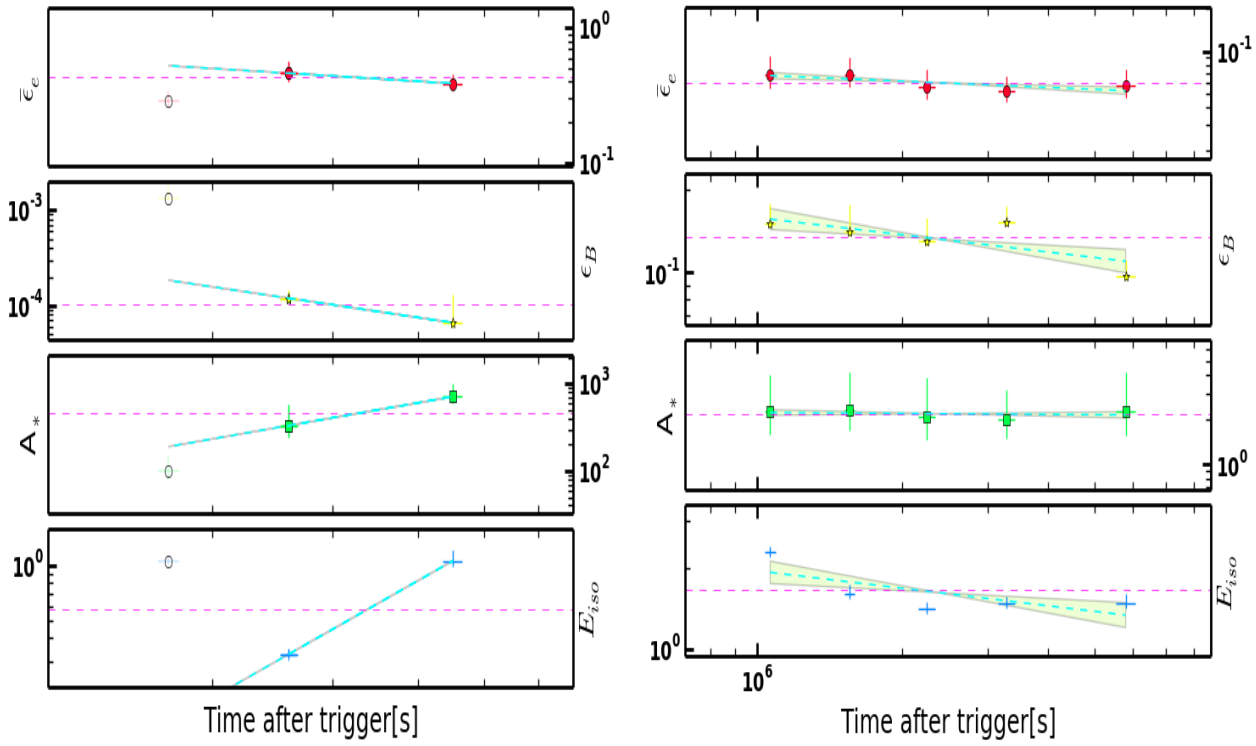

(a) GRB100418A - Fast cooling regime.

(b) GRB100418A - Slow cooling regime.

Figure 5.10: Evolution of the derived microphysical and dynamical parameters of the afterglow of GRB 100418A. The blue dashed lines and shaded regions represent the results from the fit of the observed temporal evolution. The horizontal dashed purple lines show the average value for each parameter. $E_{\rm K,iso}$ is in units of 10^{52} erg. If $\varepsilon_{\rm e}$=1 then $\bar{\varepsilon}_{\rm e}$=0.18$\pm$0.04 for p=2.22$\pm$0.02.

[2]Efficiency of the conversion of the kinetic energy in the outflow to gamma-rays during the prompt emission η=$E_{\rm K,iso}$/($E^{\gamma}_{\rm iso}$+$E_{\rm K,iso}$). $E^{\gamma}_{\rm iso}$ is the isotropic energy released in the prompt gamma-ray emission. In this case $E^{\gamma}_{\rm iso}$=$9.9^{+6.3}_{-3.4}\times10^{50}$ erg (Butler & Kocevski 2007) (http://butler.lab.asu.edu/Swift/index.html) and $z=0.6235$. It is calculated using $E^{\gamma}_{\rm iso}$=$4\pi d_{\rm L}^2{\rm F}/(1+{\rm z})$, where F is the fluence in the gamma-ray band. BAT: from $15-150$ keV in the observer-frame. $E_{\rm K,iso}$: energy range $1-10^4$ keV in the rest frame.

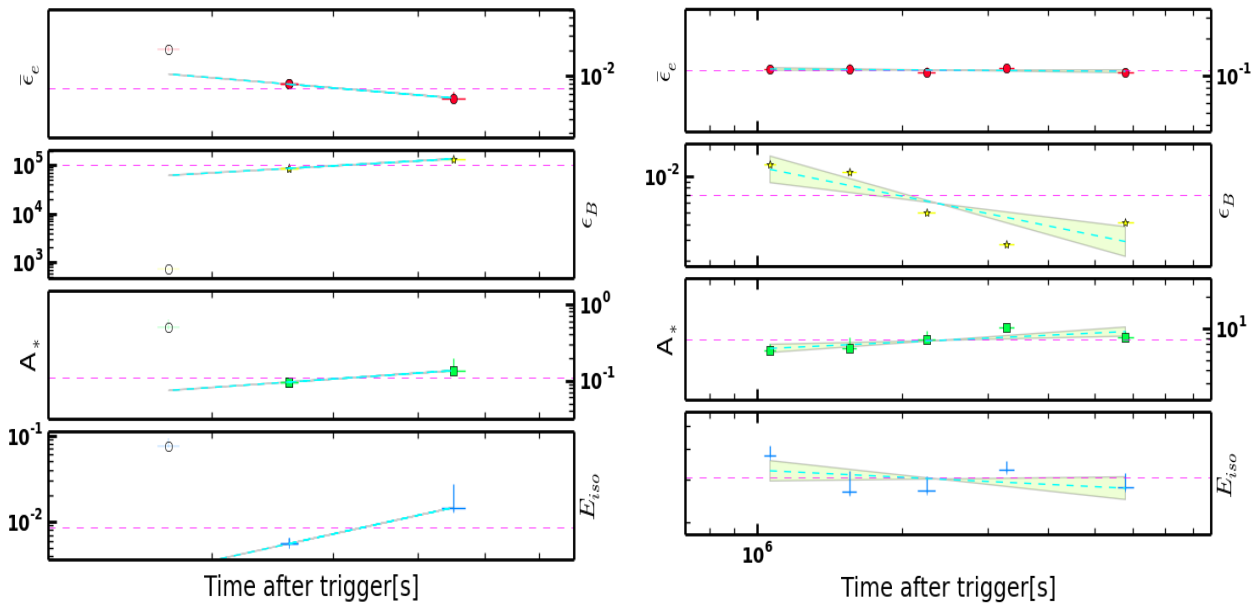

(a) GRB100418A - Fast cooling regime. SSC

(b) GRB100418A - Slow cooling regime. SSC

Figure 5.11: Evolution of the derived microphysical and dynamical parameters of the afterglow of GRB 100418A including SSC to the cooling of the electrons. The blue dashed lines and shaded regions represent the results from the fit of the observed temporal evolution. The horizontal dashed purple lines show the average value for each parameter. $E_{\mathrm{K,iso}}$ is in units of 10^{52} erg.

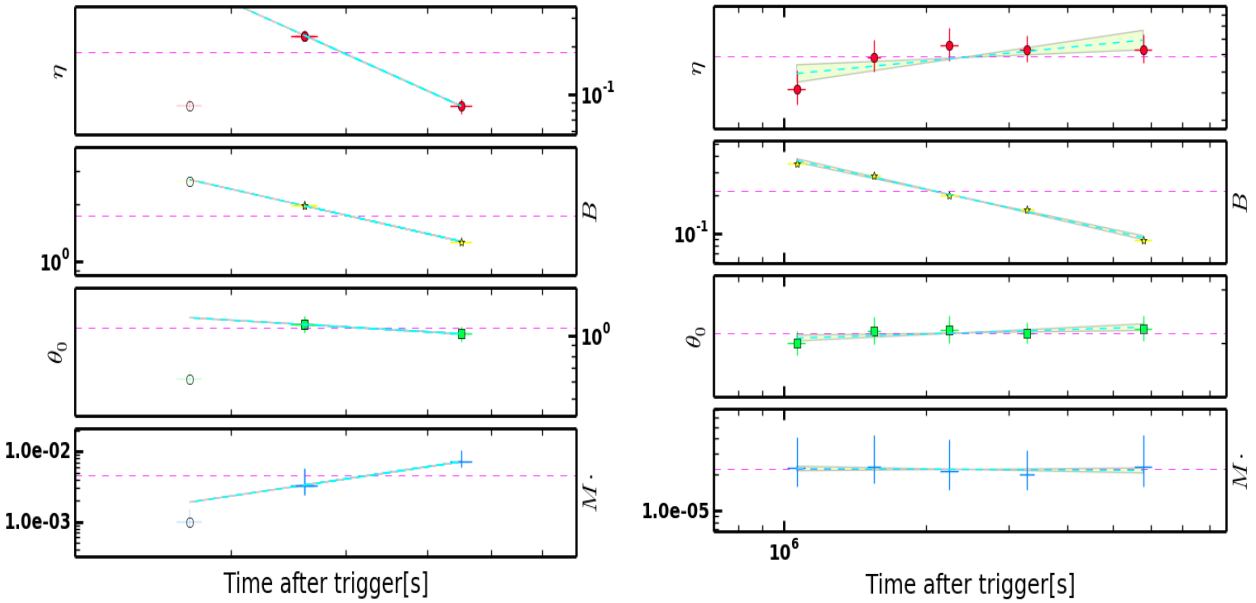

(a) GRB100418A - Fast cooling regime.

(b) GRB100418A - Slow cooling regime.

Figure 5.12: Evolution of the energy efficiency η, magnetic field magnitude B, $\dot{M}_{\mathrm{W}}$, opening angle θ_0 derived from the measured microphysical and dynamical parameters of the afterglow of GRB 100418A. The blue dashed lines and shaded regions represent the results from the fit of the observed temporal evolution. The horizontal dashed purple lines show the average value for each parameter.

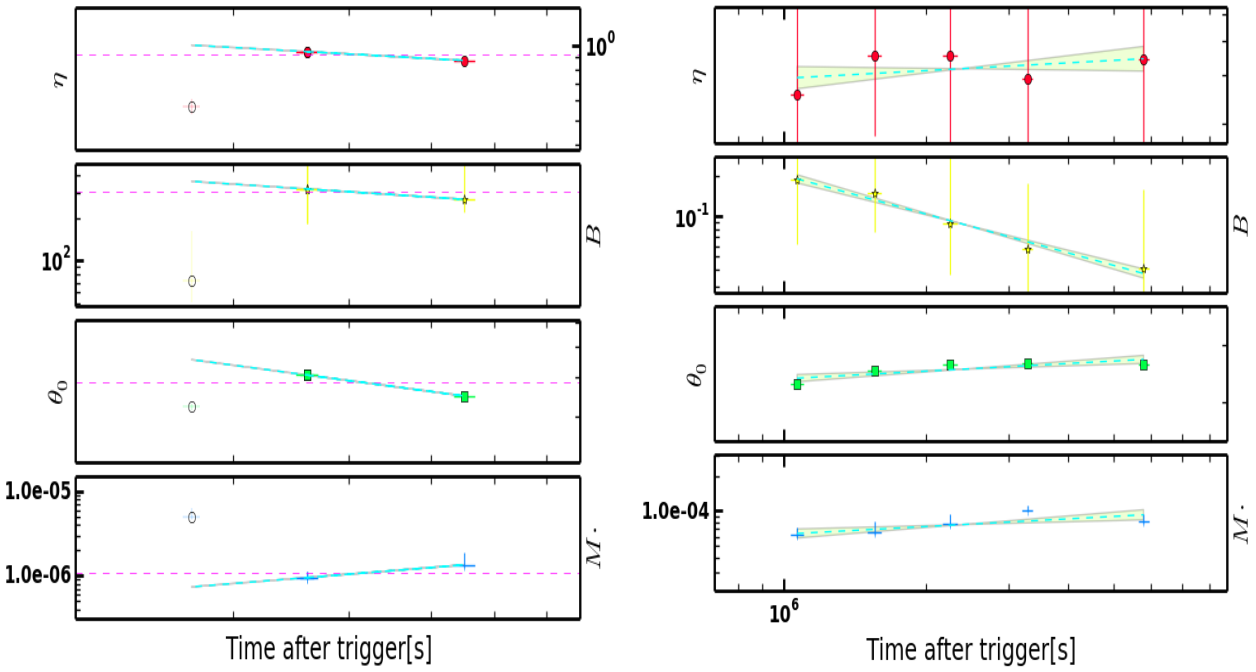

(a) GRB100418A - Fast cooling regime. SSC

(b) GRB100418A - Slow cooling regime. SSC

Figure 5.13: Evolution of the energy efficiency η, magnetic field magnitude B, $\dot{M}_{\rm W}$, opening angle $\theta_0$derived from the measured microphysical and dynamical parameters of the afterglow of GRB 100418A including SSC to the cooling of the electrons. The blue dashed lines and shaded regions represent the results from the fit of the observed temporal evolution. The horizontal dashed purple lines show the average value for each parameter.

Chapter 6

GRB 110715A

The afterglow of GRB 110715A has multi-epoch broad band observations covering the energy range from radio to X-ray wavelengths. It was followed up by the *Swift* satellite and several ground-based telescope during more than 2.5 months. The VLT/X-shooter instrument was used to determined its redshift with a measurement of z = 0.820. The data was analysed in the framework of the standard afterglow model with additional components such as energy injection phases and inverse Compton scattering. The X-ray data are best described by a double broken power-law . The optical and radio observations were taken after the second break in the X-ray light curve. All the data are best explained by a model where the outflow is expanding into a stellar wind-like density profile. Additionally an energy injection component is associated to the X-ray plateau phase. Finally, the end of the plateau phase coincides with a uniform non-spreading jet. The injection parameter is q = -0.36$\pm$0.15 with the minus sign associated to the X-ray flare. The preferred model for the energy injection component is a stratification of the mass shells. The stellar wind-like density profile is in agreement with the GRB-SNe connection. The broadband analysis at different epochs allowed the measurement of all the three break frequencies. The evolution of the break frequencies was analysed and it is in agreement with the expectations for a stellar wind-like density profile. The derived afterglow parameters are within the expected values from theory and show no evolution over time. The jet break in the light curve confirmed the collimated nature of the outflow. The total energy in the outflow after the breaming correction is $E_{\rm jet}$= 2.27×10^{51} erg. Finally, the evolution of the magnetic field in the shock regions supports a shock amplification as the mechanism responsible for the magnetic field production. A seed magnetic field of a few mG would be required to explained the derived value of $\varepsilon_{\rm B}$.

6.1 Observations and data reduction

6.1.1 *Swift*

On 2011 July 15 at T_0 13:13:50 UT (Sonbas et al. 2011) the *Swift* Burst Alert Telescope triggered on and located GRB 110715A. *Swift* slewed immediately to the position of the burst and the observations started 90.0 s after the trigger with the X-ray Telescope. The afterglow was located at RA, Dec (J2000) = 15:50:44.07, -46:14:09.0 with an uncertainty of $2\farcs2$ (Evans et al. 2011). The observations started in a Windowed Timing (WT) mode up to a few thousand seconds, during this time the flux is decaying with a temporal slope α of about 0.5. The observations continued in a Photon Counting (PC) mode until T_0 + 1 Ms, with two observed breaks in the light curve. The *Swift*/XRT light curve and spectral data in the energy range from 0.3 - 10 keV were obtained from

the XRT repository (Evans et al. 2007, 2009). The Ultraviolet/Optical Telescope observed the afterglow in the same time interval. The preliminary analysis located the source at RA, Dec (J2000) = 15:50:44.09, -46:14:06.5 with an uncertainty of $0\farcs56$ (Kuin & Sonbas 2011). The observations show an initial decay phase up to $T_0 + 22$ ks followed by a plateau phase up to $T_0 + 50$ ks and a final decay phase.

6.1.2 GROND

Optical/NIR observations in a wavelength range from 400 - 2400 nm ($g'r'i'z'JHK_s$) using GROND were performed on the afterglow source reported by (Updike et al. 2010). The observations started on July 18 2011 at 00:35 UT and continued for the next 2 hours during the first night. The afterglow was detected in all 7 bands at position RA, Dec (J2000) = 15:50:44.10, -46:14:06.2 with an uncertainty of $0\farcs4$ in each coordinate (Fig. 6.1). Observations of the GRB field continued on the 2nd, 4th, 6th and 8th night after the burst. The optical/NIR data were reduced using standard IRAF tasks (Tody 1993; Krühler et al. 2008). The data were corrected for the Galactic foreground reddening of $E(\mathrm{B}-\mathrm{V})$=0.59 mag (Schlafly & Finkbeiner 2011), corresponding to an extinction of $A_\mathrm{v}^\mathrm{Gal}$=1.82 mag for $R_\mathrm{v} = 3.08$. The optical magnitudes were calibrated against secondary stars in the GRB field (Table 6.1). On 2011 July 24 a Sloan Digital Sky Survey (SDSS) field (Aihara et al. 2011) at RA, Dec(J2000)=17:34:16.8, +08:49:12 and the field of GRB 110715A were consecutively observed during photometric conditions. The calibration of the secondary stars was done against the corrected zeropoints of the GRB field based on the SDSS field. The NIR magnitudes were calibrated against Two Micron All-Sky Survey (2MASS, Skrutskie et al. 2006) catalogue stars in the field of the GRB.

Table 6.1: Secondary stars for photometric calibration. See Fig. 6.1

Star	RA, Dec J(2000)	$g'(\mathrm{mag_{AB}})$	$r'(\mathrm{mag_{AB}})$	$i'(\mathrm{mag_{AB}})$	$z'(\mathrm{mag_{AB}})$	$J(\mathrm{mag_{Vega}})$	$H(\mathrm{mag_{Vega}})$	$K_\mathrm{s}(\mathrm{mag_{Vega}})$
I	15:50:45.34, -46:14:18.0	21.89±0.04	20.18±0.05	19.37±0.05	18.98±0.07	16.41±0.16	15.92±0.09	15.85±0.07
II	15:50:44.05, -46:13:57.5	21.75±0.04	20.53±0.04	20.13±0.04	19.73±0.07	17.18±0.12	16.42±0.12	—
III	15:50:43.79, -46:13:48.0	22.07±0.05	20.90±0.04	20.36±0.04	19.97±0.07	18.85±0.36	—	—
IV	15:50:46.02, -46:14:05.8	22.05±0.06	20.19±0.05	21.07±0.07	20.35±0.08	17.87±0.14	15.71±0.08	15.64±0.08
V	15:50:42.87, -46:14:35.8	22.28±0.07	20.88±0.06	20.32±0.07	19.86±0.08	17.28±0.16	—	—

6.1.3 Submillimeter

The afterglow of GRB 110715A was followed up in the submm wavelength range using the LABOCA bolometer camera (Siringo, G. et al. 2009) in the Atacama Path Experiment Telescope APEX and with the antennas of the ALMA array. It was observed at a mid frequency of 345 GHz with both instruments with one epoch taken with each. See Table 6.2 and Fig. 6.4.

LABOCA: started observations on July 16 at 23:21 UT, observed for about 1.47 hours, and detected the source with a flux of 11.0±2.3 mJy (de Ugarte Postigo et al. 2011).

ALMA: observed the source 2.5 days after the detection by *Swift* . The source was detected with a flux of 4.9±0.60 mJy (de Ugarte Postigo et al. 2012).

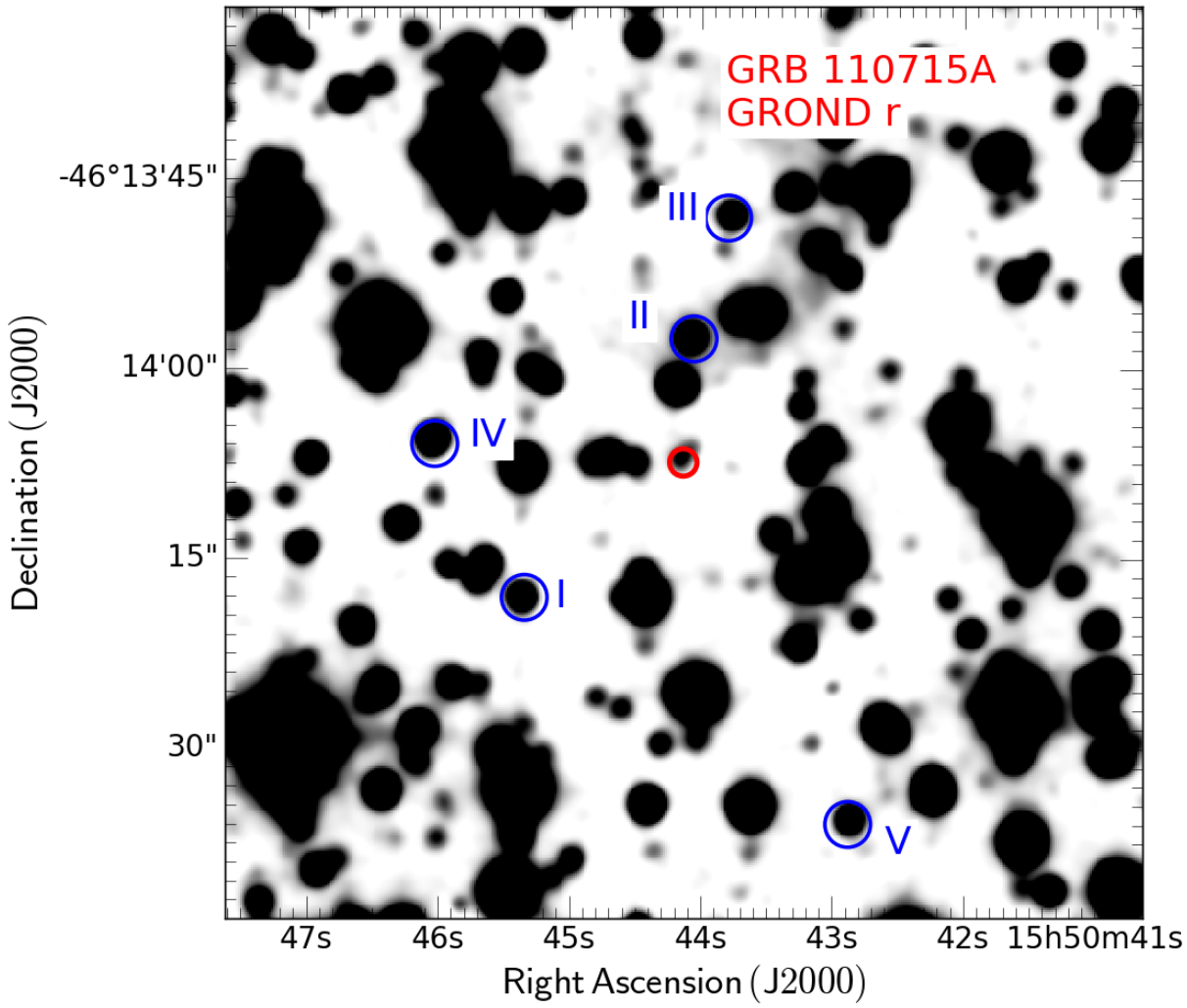

Figure 6.1: GROND r'-band finding chart. The secondary stars are reported in Table 6.1 and are labeled from I-V. North is up and East to the left.

6.1.4 Radio : ATCA

Radio observations were performed with the Australian Telescope Compact Array ATCA. The observations started on July 18 at 12.2 UT (Hancock et al. 2011) and continued for more than 2.5 months. The counterpart was observed at four different frequencies 5.5 GHz, 9.0 GHz, 18.0 GHz and 44.0 GHz. At 44 GHz the first two epochs show an increase in the flux followed by four further epochs with a decrease in flux. At 18 GHz there were four epochs of observations and the source is well detected in all of them. It starts with a slow increase in the flux follow by a decay phase. The observations at 9.0 GHz had four successful detections and one upper limit. The behaviour of the flux is almost constant. Finally the observations at 5.5 GHz have six successful detections with a constant flux with the exception of the last detection that show a steep flux decrease (Chandra & Frail 2012). Details on the fluxes are given in Table 6.2 and Fig. 6.4.

Table 6.2: Submm and radio fluxes. The epochs corresponds to the eight highlighted epochs in Fig. 6.4. Radio observations include an additional error to take into account the effects of interstellar scintillation.

SED	mid-time [ks]	APEX [mJy] 345 GHz	ALMA [mJy] 345 GHz	ATCA [mJy] 5.5 GHz	ATCA [mJy] 9 GHz	ATCA [mJy] 18. GHz	ATCA [mJy] 44.0 GHz
I	123	11.0±2.0	–	–	–	–	–
II	173	–	–	–	–	–	0.51±0.24
III	254	–	–	–	–	–	2.05±0.66
IV	345	–	4.90±0.60	0.53±0.17	0.44±0.13	0.73±0.22	–
V	1014	–	–	0.43±0.13	–	1.47±0.44	1.89±0.59
VI	1514	–	–	0.58±0.17	0.71±0.17	1.10±0.33	1.18±0.66

6.2 Phenomenological data analysis

6.2.1 Afterglow light curve fitting

The X-ray temporal evolution is well described by a double broken power-law with smooth breaks (Eq. 3.1). It starts with an initial decay up to t_{b_1}= 22.8±1.01 ks with α_{pre}= 1.55±0.08 and a break with smoothness sm_1= 2.54±0.51. This is followed by a changed in slope due to either an energy injection phase or a superimposed flare. There is no distinction between the flare and/or plateau phase here due to the lack of enough data describing the flare, to study each of the components separately. However in the following section it is shown that it is consistent with an energy injection phase. The slope of the flare and plateau phase is α_{EI}= -0.34±0.14 and lasts until t_{b_2}= 50.7±3.3 ks with smoothness in the break of sm_2= 2.84±1.09. The final decay is best described by a slope of α_{pos}= 1.34±0.07. The goodness of the fit is χ^2/d.o.f= 147.2/122. The results are shown in Fig. 6.2.

The optical/NIR light curves have four epochs, where the afterglow was detected, in all of the seven GROND bands ($g'r'i'z'JHK_s$). The observations are well described by a simple power-law with slope α= 1.51±0.03 and the goodness of fit χ^2/d.o.f= 28.5/20 with no host contribution. The fit is used to obtain the magnitudes in the optical/NIR bands at the same time as the six radio band epochs that are used in the spectral energy distribution analysis in the following sections (see Table 6.3). The plateau phase was covered by UVOT observations and Rc band observations (Nelson 2011). The observations show a plateau phase like that seen in the XRT light curve. This is an indication that even though the plateau phase in X-rays has a contribution from a flare, there is an actual plateau phase ongoing during the same period of time.

Table 6.3: Observed magnitudes of the GRB 110715A afterglow for the epochs used in the SED analysis. The Galactic foreground extinction is A_v^{Gal}=1.82 mag.

SED	mid-time [ks]	$g'(m_{AB})$	$r'(m_{AB})$	$i'(m_{AB})$	$z'(m_{AB})$	$J(m_{Vega})$	$H(m_{Vega})$	$K_s(m_{Vega})$
I	122.7	21.11±0.04	19.96±0.05	19.24±0.04	18.78±0.04	18.11±0.05	17.56±0.05	17.26±0.05
II	173.2	21.67±0.05	20.53±0.04	19.79±0.04	19.34±0.04	18.67±0.04	18.12±0.04	17.82±0.04
III	254.5	22.29±0.04	21.15±0.04	20.42±0.04	19.96±0.04	19.31±0.04	18.74±0.04	18.45±0.04
IV	344.9	22.79±0.06	21.65±0.06	20.92±0.06	20.46±0.06	19.79±0.06	19.24±0.06	18.94±0.06
V	1014.2	24.54±0.05	23.41±0.04	23.41±0.08	22.22±0.06	21.56±0.22	20.99±0.21	20.69±0.32
VI	1513.8	25.19±0.08	24.06±0.08	23.33±0.09	22.87±0.20	22.21±0.21	21.64±0.34	21.35±0.31

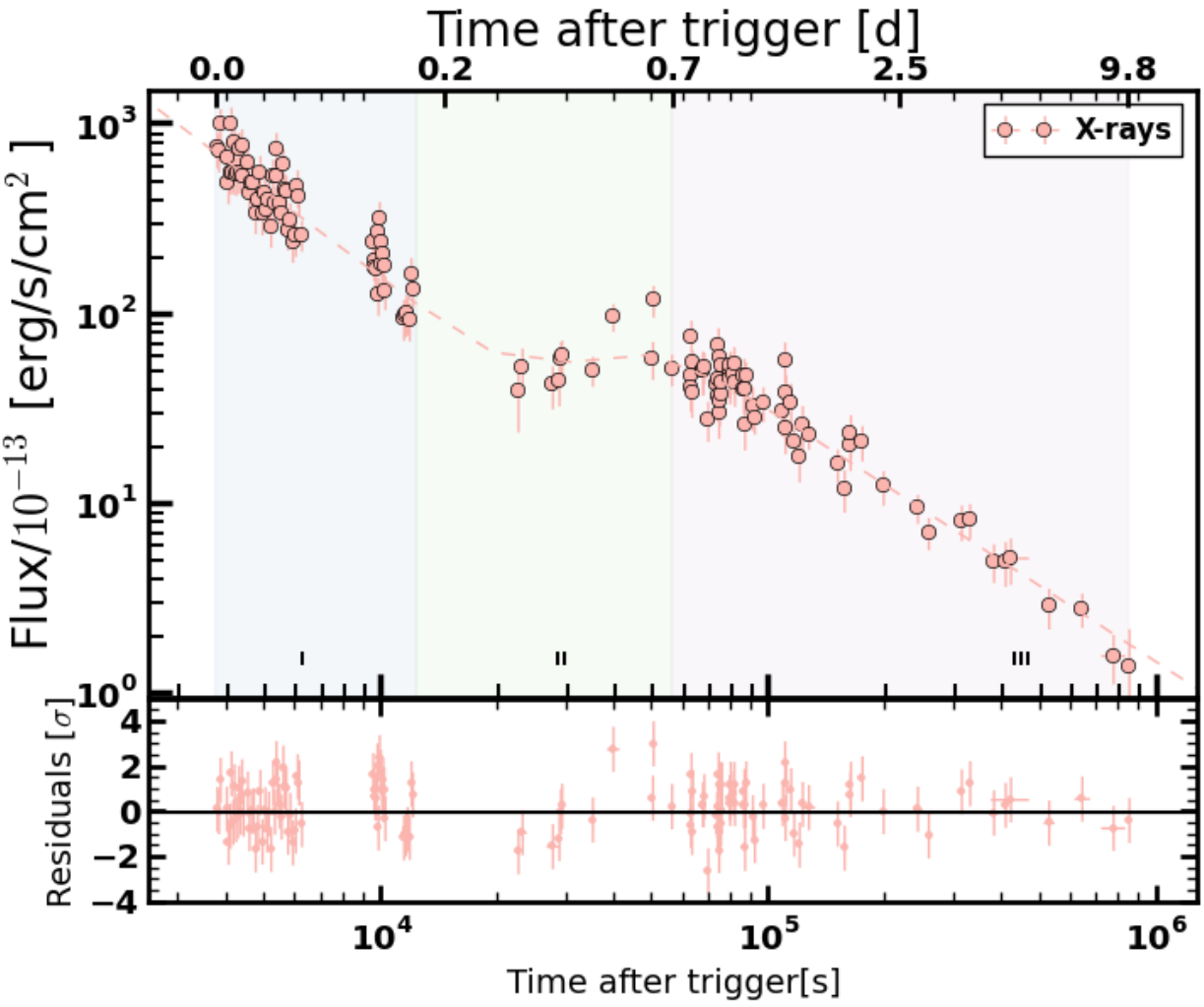

Figure 6.2: X-ray LC of GRB 110715A described by a smooth double broken power-law shown in dashed lines. The regions used in the spectral energy distribution analysis are shown in the plot as shaded vertical regions. Region I corresponds to the first decay following the prompt GRB emission. Region II corresponds to the plateau phase. Region III corresponds to the final decay phase.

Time coverage of the optical/NIR observations corresponds to the time interval of the XRT observations after the second break. The individual fits of the light curves show a similar slope between the optical/NIR observations and the last part of the XRT observations, therefore a combined fit is performed to obtain better constraints on the slopes and the break time for the XRT observations. As a result, a smooth broken power-law gives the best description for the complete data set with best fitting parameters of $\alpha_{\rm pre}^{\rm XRT}$= 1.55±0.06 for the first decay until $t_{\rm b_1}$= 21.4±1.4 ks with smoothness sm_1= 2.93±0.42, followed by a plateau phase with $\alpha_{\rm El}^{\rm XRT}$= -0.33±0.12 up to a break at $t_{\rm b_2}$= 52.7±2.3 ks with smoothness sm_2= 2.74±0.98 and a final decay with slope for both, optical/NIR and XRT observations of $\alpha_{\rm pos}^{\rm XRT}$= 1.48±0.05. The goodness of the fit is χ^2/d.o.f= 191.8/143.

Observations at a frequency of 345 GHz show a decaying flux between the two epochs, with a slope of $\alpha_{\rm sub}$ = 0.87±0.23. The six epochs of observations at 44.0 GHz are described by a smooth broken power-law. It starts with an increase in the flux with a slope of $\alpha_{\rm pre}$= -3.61±0.71 up to a

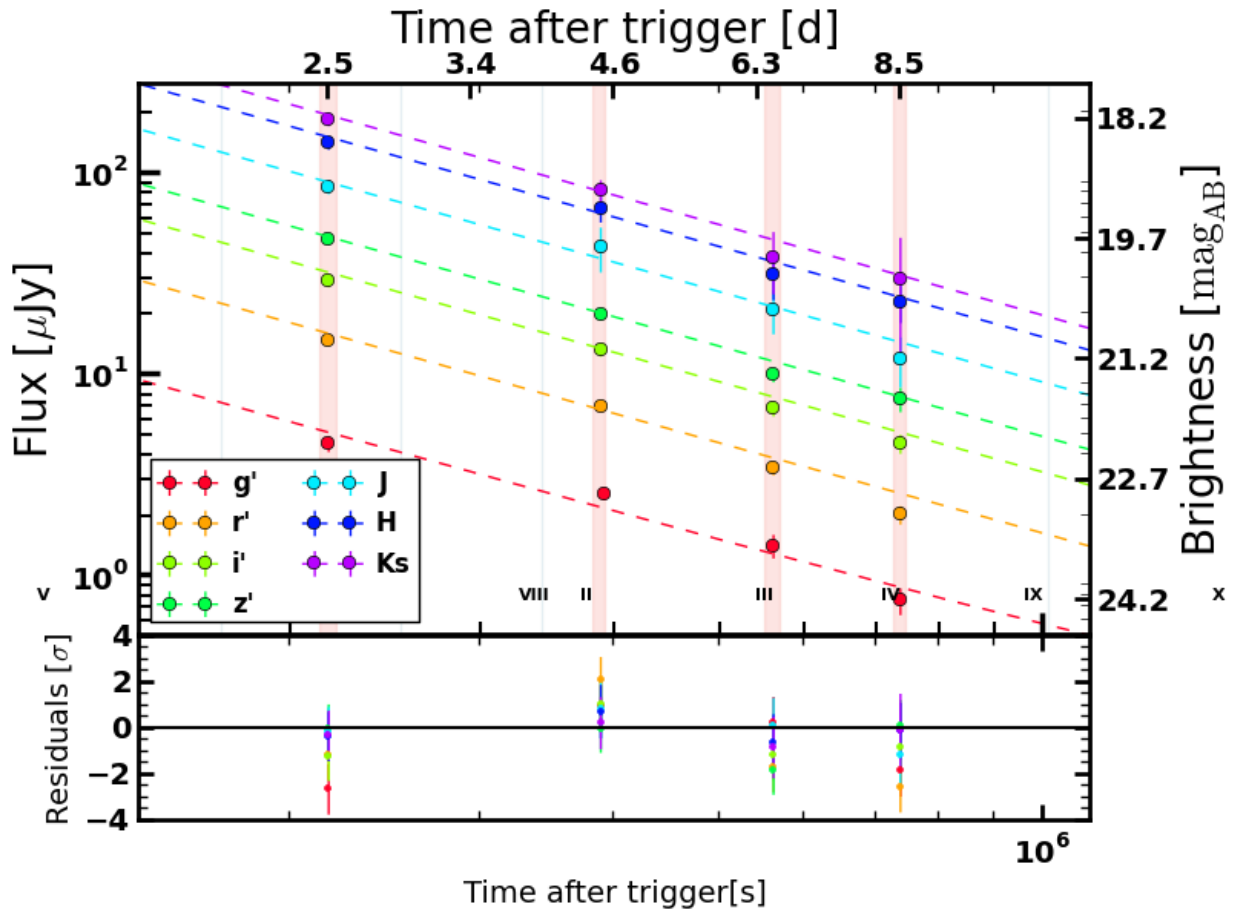

Figure 6.3: GROND $g'r'i'z'JHK_s$ LCs of the GRB 110715A afterglow. The best fit is a simple power-law with α= 1.51±0.03 as shown with the dashed lines. The epochs used for the spectral analysis are highlighted with the vertical bars. All the four epoch are after the energy injection phase and the jet-break.

break time of t_b= 325.2±28.2 ks, followed by a decaying slope α_{pos}= 0.91±0.12. This second decaying slope is consistent with the observations at the 345 GHz frequency. A similar behaviour is observed at 18 GHz but with a late break time. At this wavelength the flux initially increases with slope α_{pre}= 2.01±0.67 up to t_{b_2}= 612.7±102.5 ks, and then the flux decays with α_{pos}= 0.95±0.47. Finally at frequencies of 9.0 GHz and 5.5 GHz the flux remains almost constant through out the observations, with α= 0.09±0.07 and α= 0.08±0.11, respectively. At 5.5 GHz there is a change in the temporal evolution just before the last epoch were there is a steep decrease in flux with slope $\alpha\sim$2.0. The results for the submm and radio observations are shown in Fig. 6.4.

6.2.2 Afterglow SED fitting

After the analysis of the individual light curves, the analysis of the spectral energy distribution in the X-ray and optical/NIR bands is performed. The optical data is corrected for the Galactic reddening of $E(B-V)$= 0.59 mag, or its equivalent extinction of A_v^{Gal}=1.82 mag (Schlafly & Finkbeiner 2011) for a Milky Way (MW) reddening law. The values for the dust extinction and gas absorption from the host are linked between all the epochs.

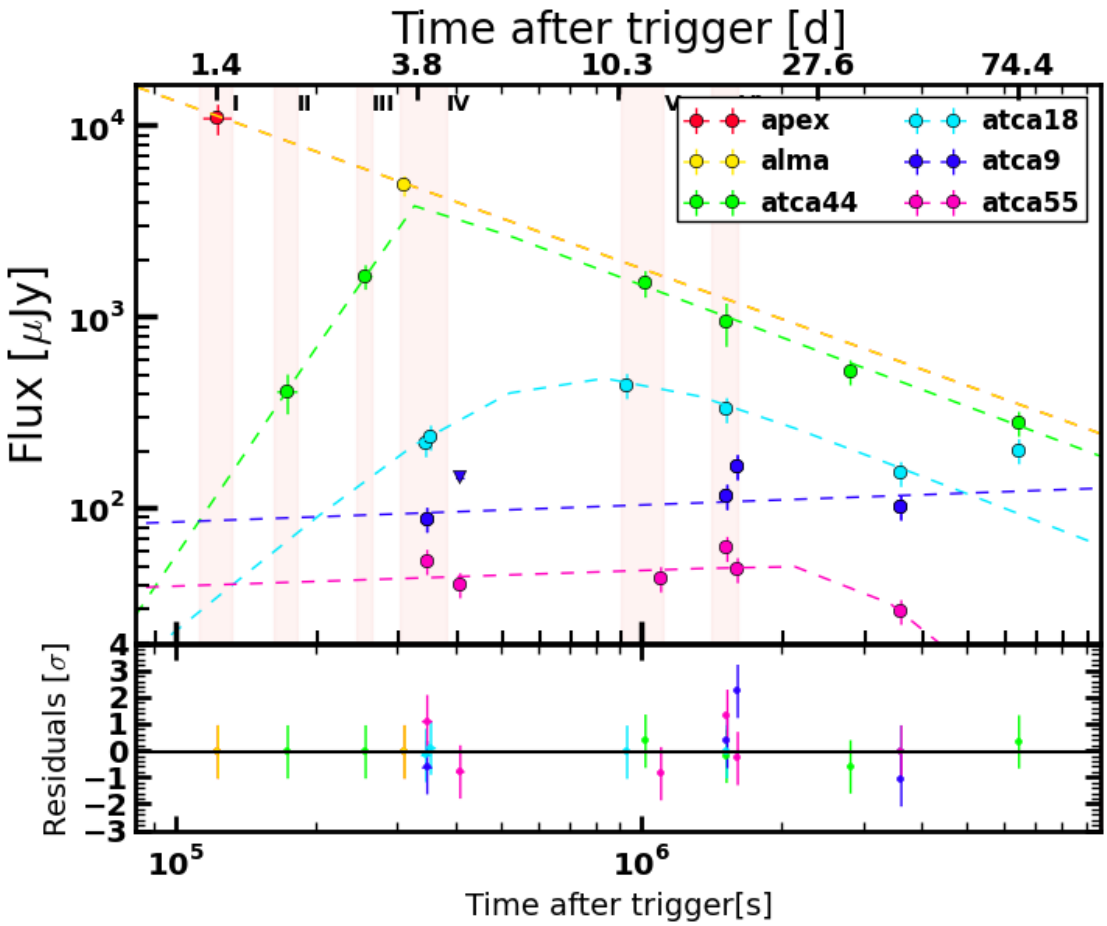

Figure 6.4: Submm and radio light curves of the GRB 110715A afterglow. The best fit for each of the bands is represented by dashed lines. The six highlighted vertical regions correspond to the epochs used in the broadband multi-epoch SED analysis. The light curves are scaled to an arbitrary factor for clarity of the plot.

The analysis begins with the X-ray observations. Three SEDs are analysed: the preXRT phase from 3.7 - 12.1 ks, the EIXRT corresponding to the plateau phase in the time interval from 22.3 - 56.4 ks and, the postXRT period that covers the last decay phase in the time interval from 62.3 - 849.1 ks (see Fig. 6.5). The three epochs are fitted at the same time with a fixed $N_{\rm H}^{\rm Gal}$= 0.43×10^{22} cm^{-2} and $N_{\rm H}^{\rm host}$ linked among the SEDs. The slopes are free to vary and are unlinked between the SEDs. As a result, the best fitting profile is a simple power-law with $N_{\rm H}^{\rm host}$= 0.55±0.11×10^{22} cm^{-2} and slopes $\beta_{\rm pre}$= 1.01±0.15, $\beta_{\rm EI}$= 0.85±0.09 and $\beta_{\rm pos}$= 1.06±0.13 for the preXRT, the EIXRT and the postXRT SEDs, respectively. The goodness of the fit is χ^2/d.o.f=87.8/80. No spectral evolution is observed among the SEDs and therefore the change in temporal slopes during the observations must have a dynamical origin. As explained below, the breaks are associated with the start and end of an energy injection phase and the jet break.

Then the analysis of the optical/NIR SEDs takes place. The host dust extinction $A_{\rm v}^{\rm host}$ is linked among the four epochs and the slopes are left unlinked and free to vary. The best fit is given by a single power-law with dust extinction given by a Small Magellanic Cloud (SMC) reddening law (Pei 1992). The results show that, within 1σ uncertainty all four slopes are consistent and, therefore a new fit with the slopes linked is performed to obtain a better constrained β and $A_{\rm v}^{\rm host}$ values.

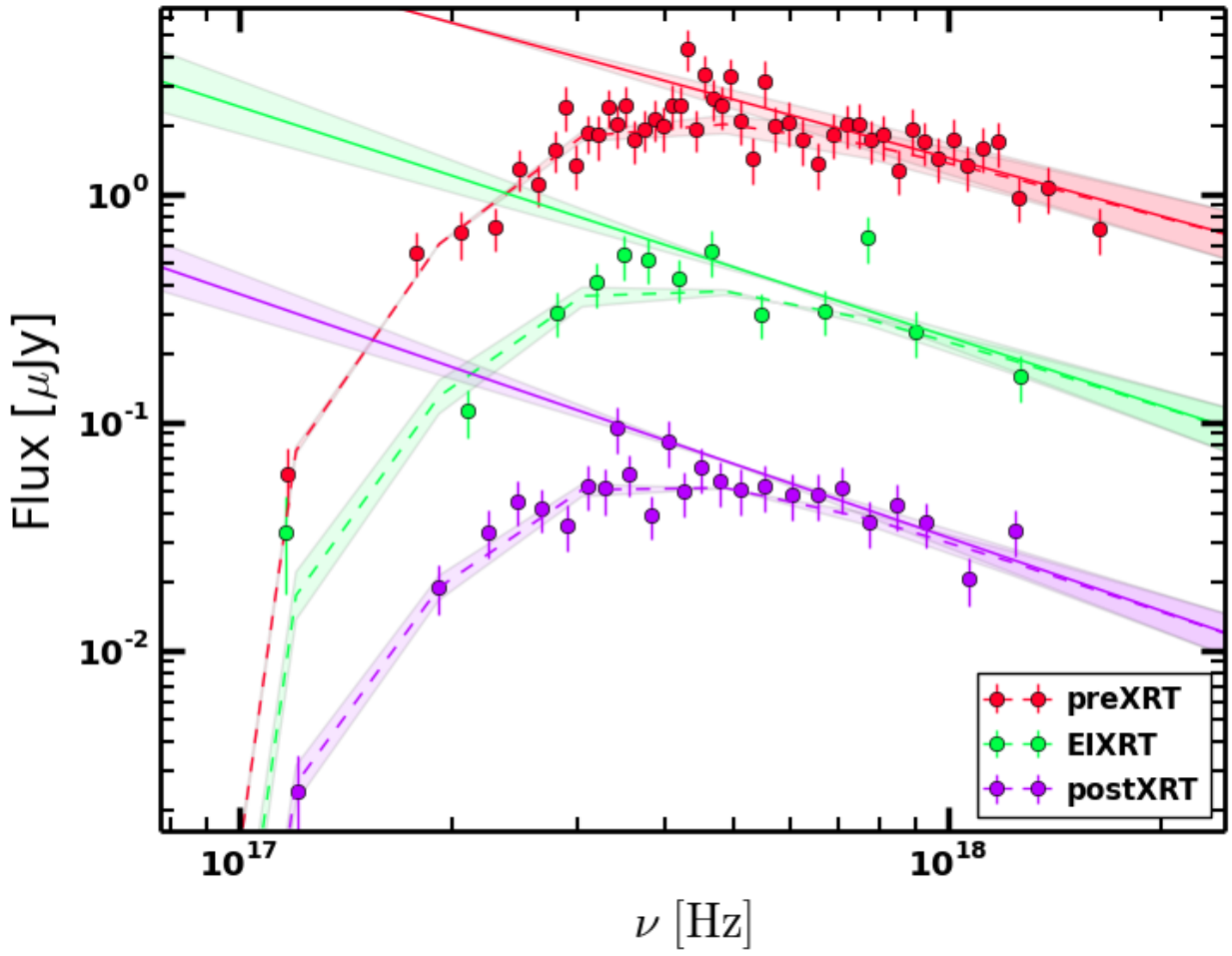

Figure 6.5: X-ray spectral energy distribution. Three different epochs are analysed. **preXRT** corresponds to the time interval from 3.7 - 12.1 ks. **EIXRT** covers between 22.3 - 56.4 ks and corresponds to the plateau phase. **postXRT** corresponds to the time interval from 62.3 ks to 849.1 ks. Each epoch is scaled to an arbitrary factor to make the plot clearer.

The best fitting results are A_v^{host}= 0.21±0.05 mag and β= 0.35±0.12 with a goodness of the fit of χ^2/d.o.f= 14.2/22. The best fitting results for β in the case of XRT and optical/NIR observations have a difference of about 0.65, close to the expected difference of 0.5 for a synchrotron spectrum with a cooling break between XRT and optical wavelengths. As seen in the previous sections α_{opt} and α_{XRT} are the same, therefore they are expected to be in the same spectral regime unless the outflow is already in the spreading phase where it is expected to have reached a sub-relativistic phase.

A combined analysis of the XRT and optical/NIR observations is performed in order to check if a simple power-law can successfully describe the observations or if the suggested 0.65 difference between β_{opt} and β_{XRT} suggested by the individual fits is real. Four epochs in the optical/NIR range and the X-ray SED after the plateau phase are included. The XRT SED is renormalize to match the mid-time X-ray flux at the time of each of the optical SEDs. Three different fitting profiles are tested: a single power-law with unlinked slopes between the four epochs (χ^2/d.o.f= 113.3/121), a single power-law with linked slopes (χ^2/d.o.f= 102.9/118) and, a smooth broken power-law with linked slopes with $\Delta\beta$=0.5 between the X-ray and optical spectral slopes (χ^2/d.o.f= 109.4/117).

All the fits give a good description of the data, an F-test is applied to define if the simplest model is the one that best describes the data or if additional parameters to the model are a better to fit the observations. The F statistical values between the single power-law with linked slopes and the broken power-law fit is 1.04, which suggests that the single power-law is better. A comparison between the broken power-law and the single power-law with unlinked slopes is not possible as the χ^2 does not improve with the broken power-law. The fit with a single power-law with free slopes shows that all of the four slopes are within 1σ from each other and therefore there is no actual SED evolution, therefore the best fitting profile is a single power-law with linked slopes. The best fitting parameters are β=1.05±0.01, $N_{\rm H}^{\rm host}$=$0.16^{+0.03}_{-0.04}$, $A_{\rm v}^{\rm host}$= 0.05 ± 0.01 (see Fig. 6.6).

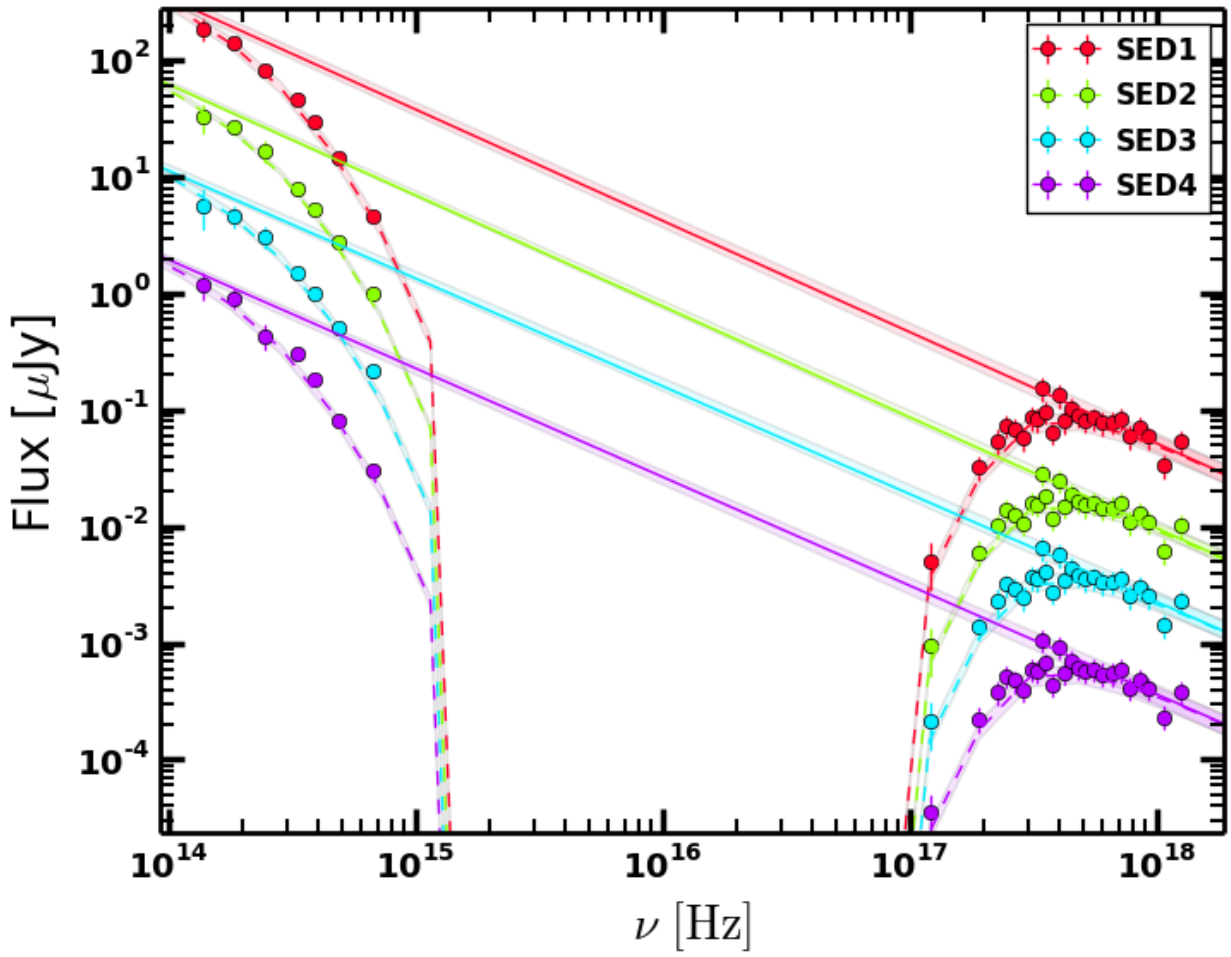

Figure 6.6: Composed SED between GROND and XRT observations. The times of each SED are t_{SED1} = 217.2 ks, t_{SED2} = 391.3 ks, t_{SED3} = 561.8 ks and t_{SED4} = 736.8 ks.

Figures 6.7a and 6.7b show the dependency between the spectral slopes and $A_{\rm v}^{\rm host}$ and $N_{\rm H}^{\rm host}$, respectively. It is observed that the parameters are well constrained and the dependencies are not strong. Based on this low dependency between the SED slope and $A_{\rm v}^{\rm host}$ and $N_{\rm H}^{\rm host}$, these values are used in further analysis. An analysis of the relation between β and α assuming a synchrotron spectrum composed by three main breaks (Chap. 2) and the inclusion of the submm and radio observations to finally derive the microphysical and dynamical parameters of the afterglow follows.

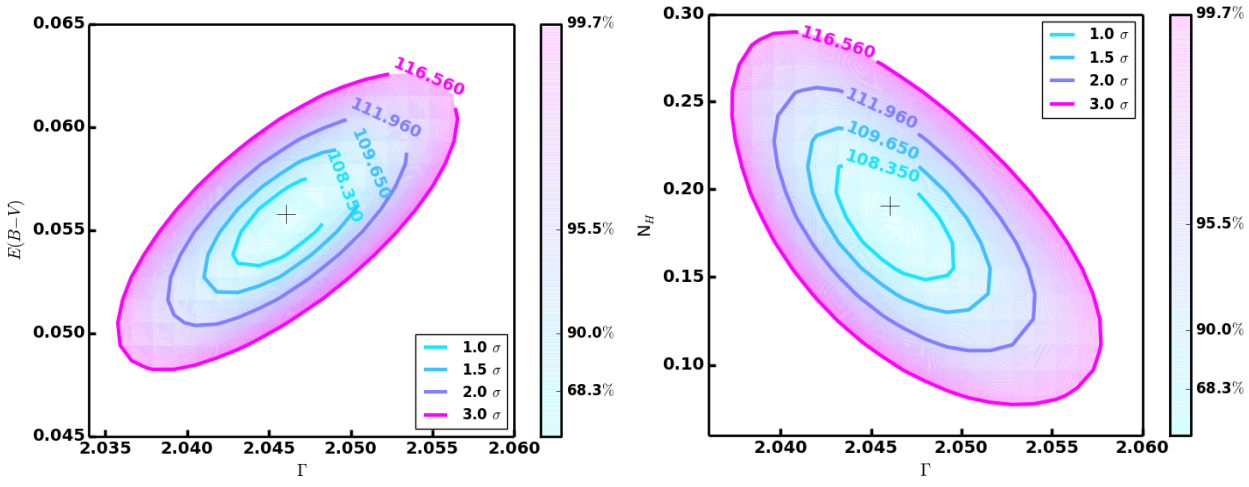

(a) Γ vs $A_{\rm v}^{\rm host}$ **(b)** Γ vs $N_{\rm H}^{\rm host}$

Figure 6.7: GRB 110715A. Countour plots showing the dependency of the photon index $\Gamma = \beta + 1$ and $A_{\rm v}^{\rm host}$and $N_{\rm H}^{\rm host}$in the left and right, respectively.

6.3 Broadband SED fitting

After determining the slope of the SED in the X-ray and optical/NIR bands, the next step of the analysis is the incorporation of the submm and radio data. The first analysis on the broadband SED has the aim to measure all the break frequencies. Six epochs are fitted using a double broken power-law with smooth breaks (Eq. 3.1). The dust $A_{\rm v}^{\rm host}$ and metal $N_{\rm H}^{\rm host}$ attenuation effects were derived in the previous sections and are directly included here. The slopes are linked between the six epochs to ensure a unique spectral slope but the breaks are free to vary. The slope in the GROND and XRT bands is not fixed but allowed to vary only within a 3σ uncertainty interval based on the results from the previous sections. The smoothness of each break depends on the temporal slopes in the optical/NIR and the X-ray (Granot & Sari 2002). Table 6.4 has all the results for the six epochs. The observation at ATCA 44 GHz in the second epoch does not follow the synchrotron spectrum, but this was already expected form the temporal analysis as discussed above.

Table 6.4: Break frequencies for the six epochs of GRB 110715A using broad-band observations. The epochs are highlighted in Fig. 6.4 and the final SED fitting is presented in Fig. 6.8.

SED	mid-time [ks]	$\nu_{c,13}$ [Hz]	$\nu_{m,12}$ [Hz]	$\nu_{sa,10}$ [Hz]
I	122.7	$2.49^{+0.83}_{-0.38}$	$2.78^{+0.82}_{-0.25}$	$5.17^{+1.05}_{-1.10}$
II	173.2	$3.94^{+0.92}_{-0.39}$	$2.15^{+0.49}_{-0.23}$	$2.85^{+0.77}_{-0.84}$
III	254.5	$4.96^{+0.75}_{-0.44}$	$1.26^{+0.23}_{-0.17}$	$2.36^{+0.62}_{-0.36}$
IV	344.9	$6.12^{+0.81}_{-0.36}$	$0.82^{+0.02}_{-0.02}$	$1.87^{+0.55}_{-0.38}$
V	1014.2	$8.78^{+0.94}_{-0.93}$	$0.18^{+0.02}_{-0.02}$	$0.99^{+0.23}_{-0.16}$
VI	1513.8	$9.70^{+0.86}_{-0.82}$	$0.11^{+0.02}_{-0.03}$	$0.76^{+0.25}_{-0.18}$

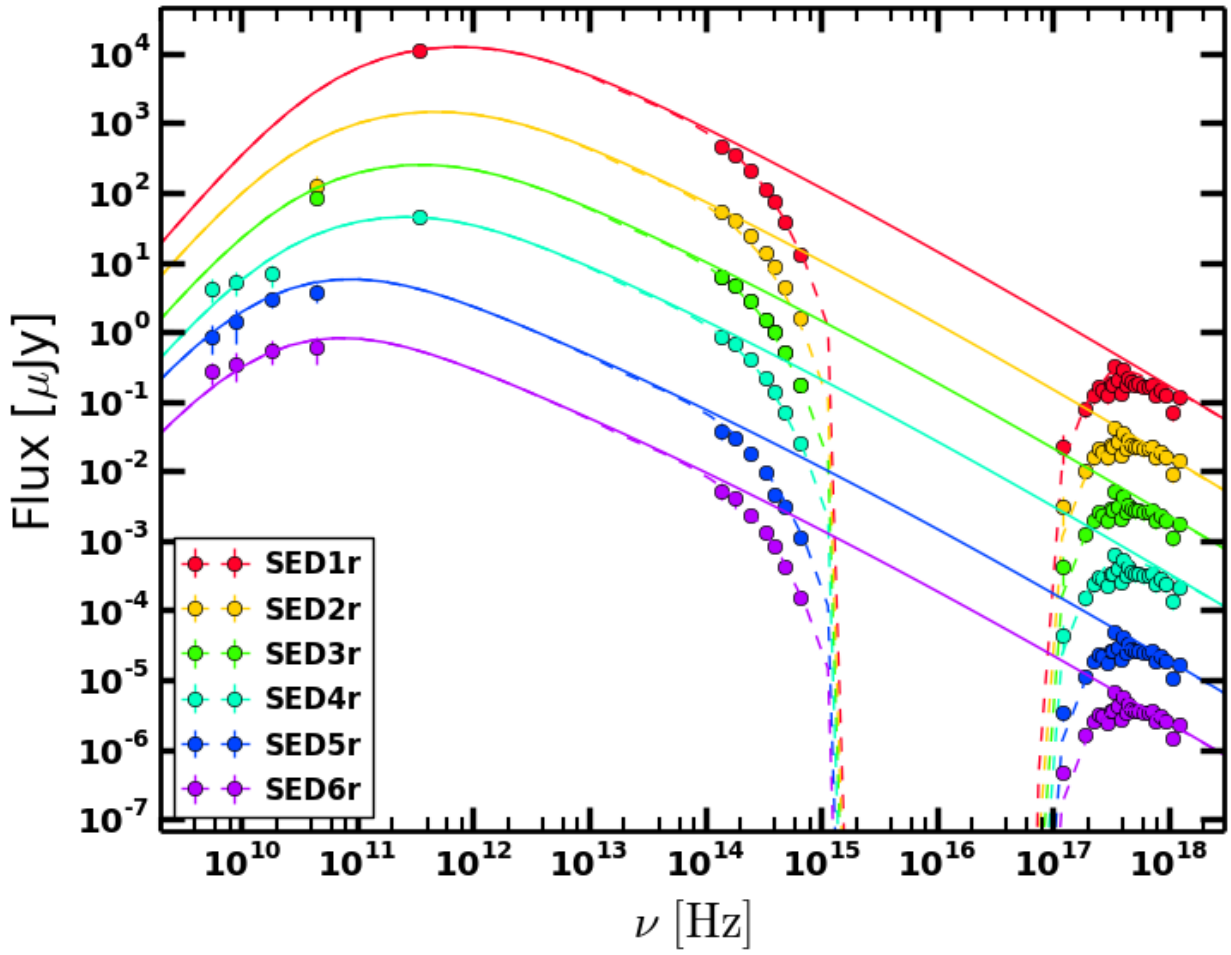

Figure 6.8: Broad band analysis of the GRB 110715A afterglow. Six epochs are presented with all the breaks measured.

6.4 Physical parameters of the standard afterglow model

6.4.1 Closure relations

The observations of the afterglow in the X-ray wavelength range are described by a double broken power-law. The optical/NIR observations are described by a single power-law that overlaps with the last epoch of the X-ray observations. The analysis of the first segment of the XRT observations (t < 21.4 ks) is in agreement with $\nu_m < \nu_{XRT} < \nu_c$ with an energy injection component in an ISM or stellar wind-like density profile, or with $\nu_m < \nu_{XRT} < \nu_c$ in an ISM density profile without the energy injection component. However the observations during this time interval might be altered by the contribution from SSC and therefore the closure relations could be modified (Chap. 2), i.e., α is steeper when SSC is dominant. If SSC is included only $\nu_c < \nu_{XRT}$ is in agreement with the observations for either an ISM or a stellar wind-like density profile. A strong reason to have a SSC contribution is that it could explain the first break in the light curve, otherwise, the plateau phase would require a central engine that can "restart" itself after 10^4 s which is unlikely. Therefore the break would just be associated with the end of a dominant inverse Compton phase and the energy injection phase would just continue until the second break. A jet break as an explanation for the first break in the light curve is not in agreement with observations as the temporal slope is actually

flatter instead of a steep decay as expected in a jet break. The plateau phase is in agreement with two scenarios: an energy injection phase where $\nu_{XRT} < \nu_c$and q = -0.25±0.10 for an ISM external medium and p = 3.10±0.02. And, $\nu_{XRT} > \nu_c$ with q = -0.36±0.15 for p = 2.10±0.02 in either a stellar wind-like or an ISM density profile. The second break in the X-ray light curve is associated with the end of the energy injection phase and/or with a jet break. Observations at the optical and X-ray frequencies have the same temporal slope during this last time interval, which is in agreement with both, the end of an energy injection phase or with a non-spreading jet break. Three cases fit the data during this last time interval: first, for $\nu_{XRT} < \nu_c$ with the break associated only to the end of the energy injection phase in an ISM density profile. Second, where $\nu_c < \nu_{XRT}$ and the break is associated with both the end of an energy injection phase and a uniform non-spreading jet break in a stellar wind-like density profile. Third, $\nu_c < \nu_{XRT}$ with the break in the light curve associated uniquely to a non-spreading jet break but with an ongoing energy injection phase.

To define the spectral regime an analysis of the radio observations is included. First, it is known that below ν_m the flux at submm and radio wavelengths evolves with the same slope in an ISM density profile, however this is not observed. This discards any scenario where the CBM has an homogenous type. The evolution of the frequencies as shown in the next sections supports a stellar wind-like density profile. Therefore, based on this, the plateau phase can only be explained by a stellar wind-like density profile when q = -0.36±0.15 and $\nu_c < \nu_{XRT}$. As no SED evolution is detected in the XRT or optical/NIR bands, this implies that the observations during the pre- and post-plateau phase must be in the same spectral regime. Therefore the pre-plateau phase is explained by an inverse Compton contribution in a spectral regime where $\nu_c < \nu_{XRT}$ and the density profile is stellar wind-like . Finally, the post-plateau phase observations can be described by a spectral regime in $\nu_c < \nu_{XRT}$ with a stellar wind-like CBM and the break associated with a uniform non-spreading jet with or without the end of the energy injection phase. In this last scenario, however, not only there are simulations predicting the end of the energy injection phase at about 10 ks but it is not common to have an astrophysical source that could provide such long energy injection and evenmore not a sign of this prolonged energy injection at least in the submm observations. Therefore, the only possible scenario is the association of the break in the light curve after the plateau phase with the end of the energy injection phase together with a uniform non-spreading jet in a stellar wind-like density profile for $\nu_c < \nu_{XRT}$. In this last scenario a change in the flux evolution due to the non-spreading jet break will take place compared to the normal evolution. The change is of (k-3)/(4-k), i.e., -3/2, for an ISM density profile and -1/2, for a stellar wind-like density profile.

The radio and submm observations have some discrepancies from the theoretical results. The flux from observations at 9.0 GHz and 5.5 GHz have an evolution with temporal slopes α= -0.08±0.11 and α= -0.09±0.07, respectively. In the case of a stellar wind-like density profile with a non-spreading jet break the expected slope is α= -1/2, which is 3.5σ and 5.3σ away from the observed α at 9.0 GHz and 5.5 GHz, respectively. This could be associated to a strong interstellar scintillation effect which is stronger at lower radio frequencies. Observations at 18 GHz are expected to have an initial slope of α= -1/2 and then a decreasing flux with α= 1/2. The observations are consistent with this within 2σ uncertainty. Finally for observations at 44 GHz and 345 GHz, the flux is expected to decrease with α=1/2. Observations at 345 GHz, and after the second epoch at 44 GHz show a decrease in flux with an α of about 0.91±0.12, although it is 3.4σ away from the expected value, the difference might just be due to the low statistics in the sample. It is however not clear why the first two epochs, at a frequency of 44 GHz does not follow the expected values and are rapidly increasing with a slope of about -2. There is clearly an external effect that must

be affecting the observations during these epochs, specially the first observation. If the flux at the first epoch is larger, then the rate of the increase in the flux would be slower and it could be in agreement with the -0.5 if $\nu<\nu_{sa}$. This is a possible scenario where ν_{sa} just crosses ν at 44 GHz as seen in the following section.

6.4.2 Afterglow parameters

From the analysis so far we conclude that the best scenario describing the (late) observations is a uniform non-spreading jet expanding into a stellar wind-like density profile. The afterglow evolution went through an energy injection phase before the jet break. The power-law index p of the non-thermal electron population is p = 2.10±0.02. The cooling break is located below the NIR wavelengths thus no spectral evolution in the optical/NIR or X-ray bands is observed. The measured break frequencies are used to derive the dynamical and microphysical parameters (Chap. 3). The effect of energy injection is not taken into account as it finishes before the start of the six analysed epochs. The effect of the jet break is included as a correction in the flux. As long as the jet does not start to spread sideways it is possible to treat it as an spherical outflow. The results for all the parameters are reported in Tables 6.5 and 6.6. The effect of SSC was also included in order to test its importance. The results are presented in Fig. 6.10b and Fig. 6.11b where it can be observed that the introduction of inverse Compton scattering gives nonphysical microphysical parameters and their evolution is changed. As a second test on the importance of the inverse Compton scattering is performed using the parameter C (Sari & Esin 2001). This parameter is based only on observables, i.e., the break frequencies. If $C > 1/4$ then the Eq. 2.26 does not have a real solution and, either IC is not an important process or there is an additional emission process contributing to the basic synchrotron emission. In this case we obtain values for C that are of order unity, which would be an indication that an additional emission beyond synchrotron should be included. It is however important to note that C has a high dependency on ν_{sa} and ν_c, and within 1σ error bars form the measured break frequencies, C is completely consistent with being less than 1/4.

Table 6.5: $\bar{\varepsilon}_e$, ε_B, $E_{K,iso}$, A_* and θ_0 for the models described in sections 4.3.1, 4.3.1, 4.3.2 and 4.3.3. $\bar{\varepsilon}_e$= $\varepsilon_e\times(|p-2|)/(p-1)$. The half-opening angle is derived using Eq.4 from Granot et al. (2005). $n = Ar^{-2}$ with $A = \dot{M}/4\pi v_w = 5\times10^{11}A_*$ g cm^{-1} (Chevalier & Li 2000). For $k = 2$ we report the density in terms of A_*. If ε_e=1 then $\bar{\varepsilon}_e$=0.09±0.02 for p=2.10±0.02.

SED	mid-time [ks]	$\bar{\varepsilon}_{e,-2}$	$\varepsilon_{B,-3}$	$A_{*,+1}$	$E_{K,iso,53}$ [erg]
I	122.7	$6.68^{+0.39}_{-0.27}$	$1.53^{+0.11}_{-0.02}$	$1.30^{+0.72}_{-0.31}$	$1.22^{+0.16}_{-0.14}$
II	173.2	$7.26^{+0.36}_{-0.35}$	$1.89^{+0.02}_{-0.01}$	$0.98^{+0.51}_{-0.26}$	$1.22^{+0.21}_{-0.12}$
III	254.5	$7.97^{+0.43}_{-0.26}$	$1.53^{+0.02}_{-0.02}$	$1.10^{+0.57}_{-0.26}$	$1.12^{+0.32}_{-0.23}$
IV	344.9	$7.62^{+0.12}_{-0.10}$	$1.62^{+0.02}_{-0.01}$	$1.07^{+0.10}_{-0.07}$	$1.36^{+0.21}_{-0.24}$
V	1014.2	$7.73^{+0.25}_{-0.19}$	$1.81^{+0.01}_{-0.02}$	$1.08^{+0.41}_{-0.18}$	$1.34^{+0.38}_{-0.23}$
VI	1513.8	$8.60^{+0.24}_{-0.26}$	$1.74^{+0.01}_{-0.01}$	$1.12^{+0.57}_{-0.29}$	$1.17^{+0.27}_{-0.30}$

Table 6.6: Energy efficiency, magnetic field magnitude, mass loss rate, opening angle and Compton parameters are presented here. The half-opening angle, is derived using Eq.4 from Granot et al. (2005). The subscript of each quantity is $C_x = C \times 10^{-x}$. $\dot{M}_{\rm W}$ for a wind velocity of 1000 km. $E_{\rm jet}$=$E_{\rm K,iso}\times{\theta_0}^2/2$. $E_{\rm jet,\gamma}$=$E^{\gamma}_{\rm iso}\times{\theta_0}^2/2$. $E^{\gamma}_{\rm iso}$=$2.93^{+5.79}_{-2.81}\times10^{52}$ erg. $E_{\rm jet,tot}$=$E_{\rm jet}$+$E_{\rm jet,\gamma}$.

SED	mid-time [ks]	θ_0[rad]	η	B [G]	$\dot{M}_{\rm W,-4}$	$E_{\rm jet,51}$ [erg]
I	122.7	$0.18^{+0.02}_{-0.02}$	$0.19^{+0.02}_{-0.02}$	$0.48^{+0.03}_{-0.02}$	$1.30^{+1.08}_{-0.47}$	$2.45^{+0.17}_{-0.13}$
II	173.2	$0.17^{+0.01}_{-0.01}$	$0.19^{+0.02}_{-0.01}$	$0.33^{+0.01}_{-0.01}$	$0.98^{+0.76}_{-0.39}$	$2.12^{+0.20}_{-0.15}$
III	254.5	$0.18^{+0.02}_{-0.01}$	$0.21^{+0.02}_{-0.02}$	$0.25^{+0.01}_{-0.01}$	$1.10^{+0.86}_{-0.39}$	$2.19^{+0.31}_{-0.22}$
IV	344.9	$0.17^{+0.01}_{-0.01}$	$0.18^{+0.01}_{-0.01}$	$0.19^{+0.01}_{-0.01}$	$1.07^{+0.15}_{-0.01}$	$2.30^{+0.21}_{-0.26}$
V	1014.2	$0.17^{+0.02}_{-0.01}$	$0.18^{+0.02}_{-0.02}$	$0.09^{+0.01}_{-0.01}$	$1.08^{+0.60}_{-0.27}$	$2.29^{+0.30}_{-0.28}$
VI	1513.8	$0.18^{+0.01}_{-0.01}$	$0.20^{+0.01}_{-0.01}$	$0.07^{+0.01}_{-0.01}$	$1.13^{+0.87}_{-0.44}$	$2.25^{+0.22}_{-0.33}$

6.5 Discussion

I presented a detailed analysis using multi-epoch broad band observations of the GRB 110715A afterglow. The X-ray LC shows a plateau phase that might also contain a contribution from a superimposed X-ray flare. However, when the X-ray data is fit simultaneously with the optical/NIR data, the plateau phase is associated with an energy injection phase with injection parameter of q = -0.36$\pm$0.15. The negative sign of the q parameter would indicate that the energy is constantly increasing. A magnetar model requires q = 0 and the observed flux would at most be constant, so it is not in agreement with the observations. A better scenario describing the energy injection phase is a stratification of the mass shells or or an outflow with a significant contribution from the Poynting flux that is not transferred to the CBM but instead observed as a continuous energy injection. For the latter option a strong reverse shock signature is expected at low frequencies, however no sign of a reverse shock is observed. In the former case, with a stratification of the shells, it is possible to have an increase in the flux. Especially the larger the value of s is the more strong the change in the dynamics of the outflow (Zhang et al. 2006), in this case s = 7.54 for the measured q value. Due to the lack of simultaneous optical and X-ray data during the plateau phase it is not possible to discriminate between a flare or a plateau phase. It is however intriguing that the plateau phase is not observed from the beginning (after the expected α=3) but just after an apparently normal decaying phase with $\alpha_{\rm pre}$=1.55$\pm$0.06. A possible contribution to the cooling of the electron by SSC might be an explanation to this initial faster decay. It is possible and expected from theory SSC is important only during the early epochs of the afterglow evolution in the X-ray band (Chap. 2). The expected temporal slope when $\nu_{\rm XRT} > \nu_{\rm c}$ for p = 2.10$\pm$0.02 and $k = 2$ in a dominant IC phase is an α of about 1.3 which 4σ away from the observed value. I proposed the stratification of the shells as the favourable scenario for the energy injection phase with a strong contribution from IC during the early epochs, however a magnetar model with q=0 is within a 3σ range from the measured q and therefore cannot be discarded.

The observed break in the light curve and the closure relations shows that there is a geometrical jet break (non-spreading jet) that is in complete agreement with the collimated nature of the outflow. The θ_0 is of the order of 0.17 radians, this collimation ensures that the required energy from the source is lower than the actual observed isotropic energy ($E_{\rm jet}\sim E_{\rm K,iso}\times{\theta_0}^2$), for this afterglow is $E_{\rm jet}\approx 2.2\times10^{51}$ erg. The closure relations also show that the external density profile is a stellar wind-like profile. Commonly the observed profile is an ISM density profile, but that is generally based only on optical and X-ray observations. The inclusion of radio data provides a more accurate

measurement ν_c evolution which gives an additional indication of the density profile type. Actually, it is the temporal evolution of the observations at submm and radio wavelengths that makes it possible to define a single model for the observations, i.e., a plateau phase associated with a prolonged energy injection followed by the end of the energy injection together with a uniform non-spreading jet in a stellar wind-like density profile. The evolution of the radio and submm light curves shows a decreasing or constant flux that is only explained by a non-spreading jet break in a stellar wind-like density profile. Analysis of the six epochs using the broadband observations allow the measurement of the evolution of the break frequencies. In Fig. 6.9 the evolution expected from synchrotron theory is plotted in solid-lines while the best-fit results are plotted in dashed-lines. ν_{sa} is evolving within 1σ of the theoretical expectation, α= -0.72±0.10. ν_m evolves with a slope α= -1.34±0.06 that is 2.6σ away from the predicted theoretical value of α= 1.5. Finally ν_c evolves as expected, with α= 0.56±0.10.

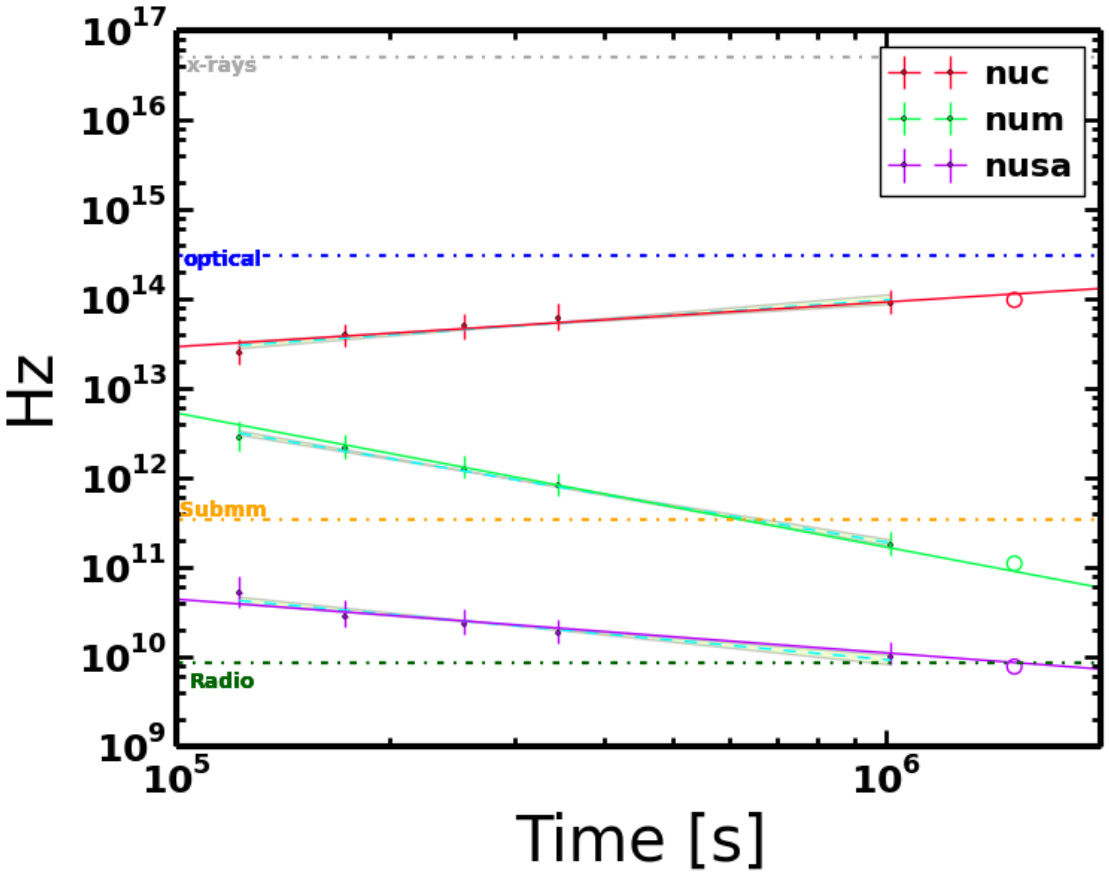

Figure 6.9: Evolution of the break frequencies of the afterglow of GRB 110715A. The last SED is not included in the fit. This last data point required extrapolation of the optical flux and therefore a possible contribution from the host galaxy might affect the results.

After the analysis of the evolution of the break frequencies, we proceed with the derivation and analysis of the microphysical and dynamical parameters. The electron index p=2.10±0.02 is well constrained and within the range predicted by previous statistical studies of p. The results for the parameters are presented in Fig. 6.10a and Fig. 6.11a. The last SED is not included in the fit for the evolution of the parameters because the values for the optical/NIR bands were extrapolated. All the microphysical and dynamical parameters are assumed (see Chap. 2) to be constant in

the standard afterglow model. Here in Fig. 6.10a it can be seen how all four parameters ε_e, ε_B, $E_{K,iso}$ and A_* are constant in time, with measured slopes of 0.06±0.04, 0.04±0.06, -0.05±0.07 and 0.06±0.05, respectively. The pink dashed line shows the average value for each parameter. ε_e has an average value of 0.84 while ε_B has an average value of 1.42×10^{-3}. This implies that most of the energy went into the accelerated electrons in the shock front and not into the magnetic field. In fact the ratio $\varepsilon_e/\varepsilon_B > 590$ implies that SSC could have played an important role in the cooling of the electrons. The results including SSC are shown in Fig. 6.10b. The resulting values for ε_B are about 10 and therefore not valid within a physical framework where $\varepsilon_B < 1$. This could just indicates that SSC does not play a dominant role during these last stages of afterglow evolution. I therefore assume that SSC was not relevant during the six analysed epochs presented here. Even though SSC is not important during this late stages, it is important to mention its contribution as explained at the beginning of this section, SSC could be playing a key role in the X-ray flux evolution at early times. I show how the observed slope is in agreement with expectations when SSC is dominant. The parameters for this initial phase can not be derived as there are only X-ray observations. For the dynamical parameters, $E_{K,iso}$ is observed to have an average value of about 10^{53} erg, in agreement with the theory and the possible isotropic energy values that can be emitted by a source in the collapsar or in a magnetar model after correction by the beaming factor. In the case of A_* it is of order 10, which, if the progenitor is a Wolf-Rayet star, implies a mass loss rate $\dot{M}_W$ of about 10^{-4} $M_\odot$ yr^{-1} for a wind velocity of 1000 km/s. This $\dot{M}_W$ value is at the upper limit of the mass loss rate expected from a Wolf-Rayet star.

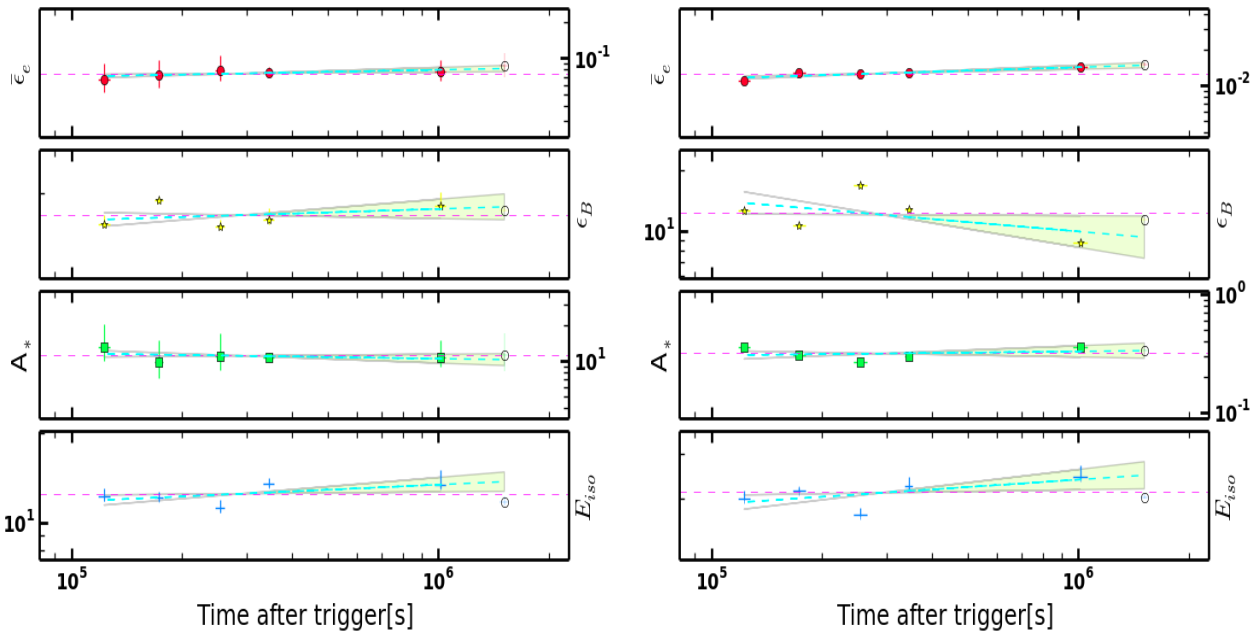

(a) Model parameters GRB110715A.

(b) Model parameters GRB110715A with IC

Figure 6.10: Evolution of the energy efficiency η, magnetic field magnitude B, mass loss rate $\dot{M}_\odot$, and opening angle θ_0 derived from the measured microphysical and dynamical parameters of the afterglow of GRB 110715A. The dashed-lines in cyan and shaded regions represent results from the fit of the observed temporal evolution. The horizontal pink dashed-line shows the average value for each parameter. $E_{K,iso}$ is in units of 10^{52} erg. **Left:** Parameters without IC being included. The average value for ε_B is 1.42×10^{-3}. **Right:** Parameters with IC included. The average value for $E_{K,iso}$ is 2×10^{52} erg.

The measured microphysical and dynamical parameters were used to derive the half-opening angle θ_0 of the collimated outflow, the magnitude of the magnetic field B in the shock region, the efficiency of conversation of the kinetic energy η[1], and the mass loss rate for a stellar wind velocity 1000 km/s. θ_0, $\dot{M}_{\rm W}$ and η do not evolve in time while B is evolving with α=-0.77$\pm$0.04, this evolution is just 1σ away from the theoretical value for the evolution of B of -0.75. The values for the efficiency are of the order of 19% which is just within the expected range of values $10\% - 20\%$. The values for the mass loss rate are on the high end of a typical Wolf-Rayet star, which has $\dot{M}_{\rm W} \sim 10^{-5} - 10^{-4}\ M_\odot\ {\rm yr}^{-1}$. The collimation angle θ_0 is about 0.17 rad, which implies a total energy in the jet after the beaming correction, of $E_{\rm jet}$= 2.27×10^{51} erg. This is in complete agreement with the values expected from theory of order $10^{50} - 10^{51}$ erg in both the collapsar and magnetar model.

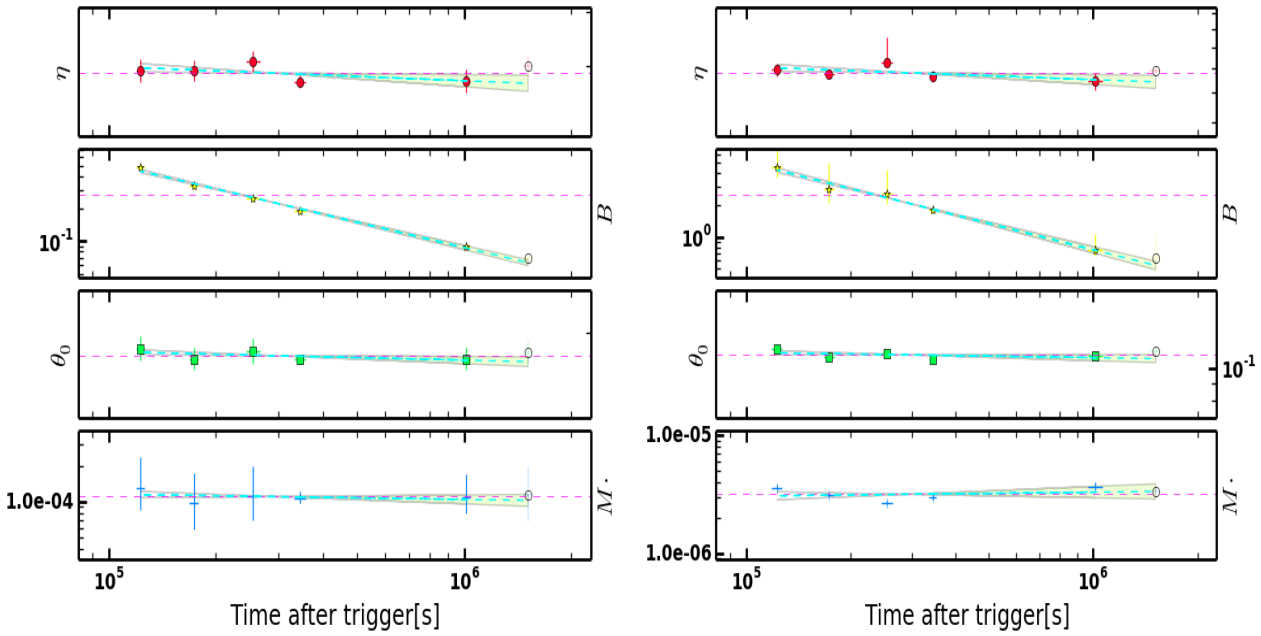

(a) Model parameters GRB110715A **(b)** Model parameters GRB110715A with IC

Figure 6.11: Evolution of the energy efficiency η, magnetic field magnitude B, mass loss rate $\dot{M}_\odot$, and opening angle θ_0 derived from the measured microphysical and dynamical parameters of the afterglow of GRB 110715A. The cyan dashed-lines and shaded regions represent the results from the fit of the observed temporal evolution. The horizontal pink dashed-line represents the average values for the parameters. $t_{\rm b}$Left: Parameters without IC. The average value for η is 0.19 and for θ_0 is 0.17 rad. $t_{\rm b}$Right: Parameters with IC included. The average value for η is 0.59.

[1]Efficiency of the conversion of the kinetic energy in the outflow to gamma-rays during the prompt emission η=$E_{\rm K,iso}$/($E^\gamma_{\rm iso}$+$E_{\rm K,iso}$). $E^\gamma_{\rm iso}$ is the isotropic energy released in the prompt gamma-ray emission. In this case $E^\gamma_{\rm iso}$= $2.93^{+5.79}_{-2.81} \times 10^{52}$ erg (Butler & Kocevski 2007) (http://butler.lab.asu.edu/Swift/index.html) and $z = 0.820$. It is calculated using $E^\gamma_{\rm iso}$= $4\pi d_{\rm L}^2 {\rm F}/(1+{\rm z})$, where F is the fluence in the gamma-ray band. BAT: from $15 - 150$ keV in the observer-frame. $E_{\rm K,iso}$: energy range $1 - 10^4$ keV in the rest frame.

Chapter 7

GRB 130418A

Abstract :

The GRB 130418A afterglow was detected on April 18 2013 by the BAT instrument onboard of the *Swift* satellite. It was followed up by ground-based telescopes on the optical and NIR wavelengths for over two weeks with simultaneous observations at submm and radio wavelengths by APEX, SMA, CARMA and WSRT. The measured redshift is z = 1.218 and the afterglow isotropic energy in the γ-ray band is $E^{\gamma}_{\rm iso}$= 3.9×10^{51} erg. The optical light curves show an initial plateau phase followed by a normal decay and a final second break with steeper slope. It was concluded that the plateau phase is associated to an energy injection phase with an injection parameter of q = 0.14$\pm$0.10. The second break in the light curve is associated to a uniform non-spreading jet expanding into a stellar wind-like density profile. The steeper temporal slope in the X-ray band during the plateau phase and its flatter spectral slope compared to the optical observations, are explained by a dominant contribution from SSC to the cooling of the accelerated electrons and therefore to the emission itself. This SSC contribution is negligible and not consistent with the late epoch observations. Three epochs using multi-wavelength observations from radio to X-rays are analysed. The epochs are taken in a time interval after the second break in the optical light curve. The break frequencies are measured and their evolution is consistent with predictions from the standard afterglow model. The frequencies were used to derived the microphysical parameters and the of evolution of these is also analysed. The parameters are consistent with the theoretical predictions, with $\varepsilon_{\rm e}$ and $\varepsilon_{\rm B}$ being less than unity. The value for $\varepsilon_{\rm B}$ implies a large seed magnetic field in the CBM of order of mG. The break in the light curve confirmed the collimated nature of the outflow and allowed the measurement of θ_0. It also allow the derivation of the real energy of the outflow after the beaming correction, with θ_0= 0.4 rad and $E_{\rm jet}$= 1.17×10^{51}.

7.1 Observations and data reduction

7.1.1 *Swift*

On April 18th 2013 the *Swift* Burst Alert Telescope detected GRB 130418A (de Pasquale et al. 2013) at 19:00:53 UT. Immediately after the BAT trigger, *Swift* slewed to the position of the GRB and started the observations 129.7 seconds after the trigger. A GRB afterglow X-ray counterpart was detected by the *Swift* /XRT at a position RA,DEC(J2000) = 09:56:9.05, 13:39:55.4 with an uncertainty of $5\farcs3$. The observations were performed in Windowed Timing (WT) mode within the time interval from $T_0 + 136$ s to $T_0 + 353$ s. The observations continued in Photon Counting (PC)

mode in the time interval from $T_0 + 3.6$ ks to $T_0 + 407$ ks. The *Swift* /XRT light curve and spectral data in the energy range from 0.3 - 10 keV were obtained from the XRT repository (Evans et al. 2007, 2009). The X-ray counterpart was also detected by the Ultraviolet/Optical Telescope. It was located by UVOT at a position of RA,DEC(J2000) = 09:56:08.88, 13:40:02.7 with an uncertainty of $0\farcs5$ and a magnitude in the *white* band of 14.85±0.05 in the first 150 s of exposure (Kuin & de Paquale 2013).

7.1.2 GROND

Optical/NIR observations of the field of GRB 130418A with GROND started on April 19 2013 at 01:20:33 UT, 6.3 hours after the trigger (Nardini et al. 2013) and continued for the next three hours. The observations were performed simultaneous in 7 bands in a wavelength range from 400-2400 nm ($g'r'i'z'JHK_s$). The optical counterpart was detected in all 7 bands at a position RA, DEC(J2000) = 09:56:8.85, 13:40:02.0 with an uncertainty of $0\farcs4$ in each coordinate (Fig. 7.1). The observations continued on the third night, and on February 2014 with deep observations of the field to determine the possible host contribution. The optical/NIR data were reduced using standard IRAF tasks (Tody 1993; Krühler et al. 2008). The data were corrected for Galactic foreground reddening of $E(\mathrm{B}-\mathrm{V})$= 0.03 mag (Schlafly & Finkbeiner 2011), corresponding to an extinction of $A_\mathrm{v}^\mathrm{Gal}$= 0.09 mag for $R_\mathrm{v} = 3.08$. The optical magnitudes were calibrated against Sloan Digital Sky Survey (SDSS) stars in the GRB field. The NIR magnitudes were calibrated against the Two Micron All-Sky Survey (2MASS, Skrutskie et al. 2006) catalogue stars in the field of the GRB.

Table 7.1: Secondary stars for photometric calibration. Fig. 7.1

Star	RA, Dec J(2000)	$g'(\mathrm{mag_{AB}})$	$r'(\mathrm{mag_{AB}})$	$i'(\mathrm{mag_{AB}})$	$z'(\mathrm{mag_{AB}})$	$J(\mathrm{mag_{Vega}})$	$H(\mathrm{mag_{Vega}})$	$K_\mathrm{s}(\mathrm{mag_{Vega}})$
I	9:56:16.99, +13:39:44.9	17.15±0.04	16.02±0.05	15.59±0.04	15.49±0.05	13.90±0.12	13.47±0.11	13.42±0.09
II	9:56:15.39, +13:38:34.6	18.26±0.04	17.55±0.05	17.32±0.05	17.30±0.05	15.88±0.17	15.62±0.14	15.62±0.10
III	9:56:11.40, +13:39:20.3	15.64±0.04	14.96±0.06	14.73±0.05	14.72±0.05	13.34±0.17	12.98±0.12	13.10±0.10
IV	9:56:06.01, +13:38:47.9	20.24±0.06	18.87±0.05	18.28±0.07	18.12±0.06	16.57±0.16	16.16±0.11	—
V	9:56:13.74, +13:40:16.9	—	20.24±0.06	19.09±0.07	18.71±0.07	16.95±0.13	16.50±0.18	—

7.1.3 APEX

The afterglow of GRB 130418A was observed using the LABOCA bolometer camera (Siringo, G. et al. 2009)[1] located on the APEX telescope starting on April 19th 2013 at 23:50 UT, about 22 hours after the trigger. The observations were taken in mapping mode and the reduction of the data was done using the Bolometer Array analysis software (BoA, Schuller 2012). There is an initial detection of the source with a flux of about 40 mJy with a fast decay after just a couple of hours, with a subsequent faint detection of a flux of 17 mJy. It was followed up for one the night of April 20th with no detection and a 2σ limit of 10 mJy and r.m.s 4.9 mJy.

[1]Based on observations collected during ESO time at the Atacama Pathfinder Experiment (APEX) under proposal 091.D-0131.

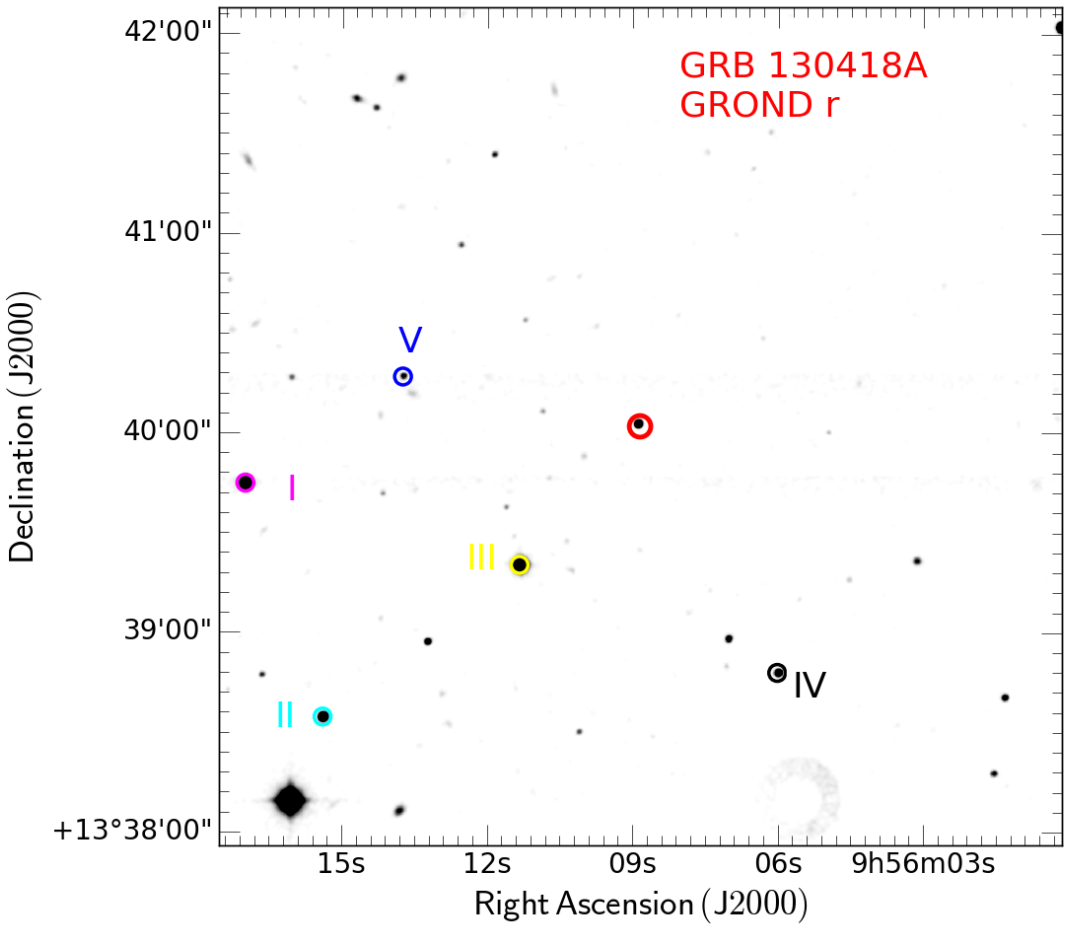

Figure 7.1: GROND r'-band finding chart. The secondary stars are reported in Table 7.1 and are labeled from I-V. North is up and East to the left.

7.1.4 Additional observations

Additional observations in submm, millimetre and radio wavelengths were performed. The results of this observations were included in our analysis using the reported magnitudes in the GCN reports.

Submm observations were also performed using the Submillimetre Array (SMA) at Mauna Kea at a central observing wavelength of 340 GHz. The observations were performed on April 19 2013 at 06:30 UT for 1.25 hours. No source was detected at the GRB afterglow position down to a 3σ limit of 14.5 mJy and r.m.s 4.8 mJy (Martin et al. 2013).

Millimetre observations using the Combined Array for Research in Millimetre-Wave Astronomy (CARMA) started observations of the field of GRB 130418A at a frequency of 93 GHz at 02:50 UT on April 19 2013 and continued during 0.5 hours. The millimetre counterpart was detected with a flux of 3 mJy (Perley 2013).

Radio observations of the GRB 130418A field with the Westerbork Synthesis Radio Telescope were also performed. They were taken between April 21 2013 13.53 UT and April 22 01.49 UT. No radio counterpart was detected with a 3σ limiting magnitude of 69 μJy (van der Horst 2013).

7.2 Phenomenological data analysis

7.2.1 Afterglow light curve fitting

The evolution of the X-ray data starts with a shallow decay with α about 0.77 during the WT mode observations, thereafter, the observations in the PC mode are described by a single power-law or by a smooth broken power-law (Eq. 3.1). Both fitting profiles have a similar goodness of the fit. The long gap in the XRT observations between 20 - 300 ks, makes it difficult to constrain the break in the light curve. The best fitting parameter for a single power-law is α= 1.47±0.06 with a goodness of the fit χ^2/d.o.f= 28.4/18. The best fitting parameters for a smooth broken power-law are a pre-break slope $\alpha_{\rm pre}$= 1.18±0.18, a post break slope $\alpha_{\rm pos}$= 1.93±0.75, a break time $t_{\rm b}$= 45.4±87.8 ks and smoothness of *sm*= 1.4±9.0. The goodness of the fit is χ^2/d.o.f= 24.1/15. The F-test between the power-law and the broken power-law gives and F value of 0.89 and probability of 0.45 indicating that the broken power law does not imply a big improvement to the fit compared with the single power-law.

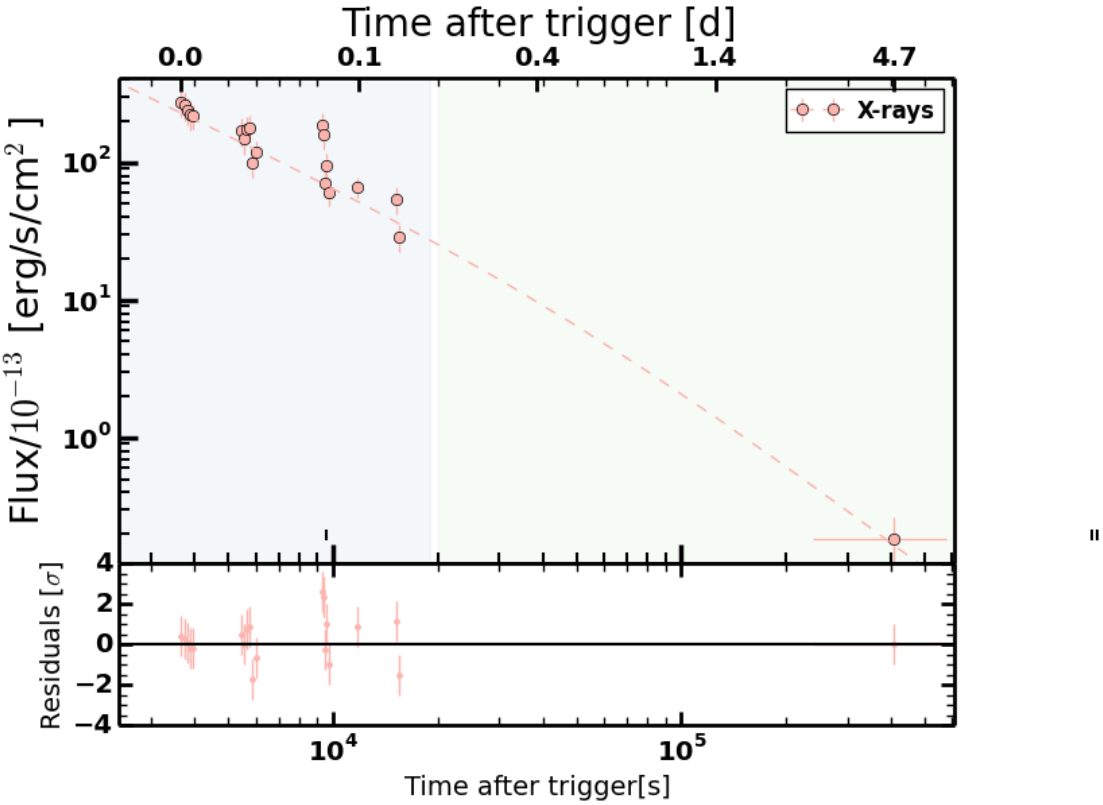

Figure 7.2: X-ray light curve of the afterglow of GRB 130418A. The final fit is a smooth broken power-law with $t_{\rm b}$=45.4±87.8 ks. The highlighted vertical regions corresponds to the two main phases that are analysed in the spectral energy distribution. The light blue region corresponds to a plateau phase and the light orange region to a normal decaying phase after the end of energy injection and with a jet break.

The optical/NIR light curves (Table 7.2) in all 7 bands ($g'r'i'z'JHK_s$) have an initial decay with $\alpha_{\rm pre}$= 0.91±0.07 followed by a decay with slope of α= 2.50±0.13. GROND data is well described by a smooth broken power-law, however, when additional observations in the optical bands are included, it is clear that there are two breaks in the evolution of the optical observations. Both

fitting profiles are tested, a smooth broken power-law (χ^2/d.o.f=221.6/176) and a smooth double broken power-law (χ^2/d.o.f=214.3/173). The goodness of the fit is similar for both fitting profiles. An F-test is used to check if the double broken power-law fitting profile is a better description of the data. A resulting F value of 1.96 with a probability of 0.09 suggest that the improvements to the fit might be important and can be included. The best fitting parameters of the combined observation between GROND and the additional optical/NIR observations (Fig. 7.3) reported in the literature[2] are given by: $\alpha_{\rm pre}^{\rm opt}$= 0.39±0.03, $\alpha_{\rm EI}$= 0.93±0.04, $\alpha_{\rm pos}^{\rm opt}$= 2.39±0.19, $t_{\rm b_1}$= 11.7±3.4 ks, $t_{\rm b_2}$= 45.2±8.1 ks, sm_1= 9.6±0.2 and sm_2= 2.6±0.5. The initial plateau phase in the optical bands can be associated with energy injection phase. The difference in the slope in the X-ray band could be associated to a dominant SSC contribution to the cooling of the electrons during the first stage of the afterglow evolution. The SSC can be observed as a steep decay with $\alpha\sim$1.4 and with the contribution from the energy injection phase, the slopes will be flattened. This will be analysed in detailed later in the chapter.

A combined fit using GROND, XRT and additional observations in the optical/NIR wavelength range was performed. The initial slope is left untied between X-rays and optical/NIR. The break times are linked to find a better constrained on those. The best fitting results are initial slopes $\alpha_{\rm pre}^{\rm XRT}$= 1.11±0.14 and $\alpha_{\rm pre}^{\rm opt}$= 0.31±0.08, a break time $t_{\rm b_1}$= 18.8±3.5 ks with smoothness sm= 5.4±1.3 followed by a decay with slopes $\alpha_{\rm EI}$= 1.11±0. 14 up to $t_{\rm b_2}$= 61.7±8.1 ks with smoothness sm_1= 3.3±0.8 and a final decay slope of $\alpha_{\rm pos}$= 2.40±0.19. The goodness of the fit is χ^2/d.o.f= 241.6/195.

Table 7.2: Observed magnitudes of the GRB 130418A afterglow for the seven analysed epochs. Three epochs during the energy injection phase and four epochs after the break in the light curve. The host contribution was subtracted for each band. The magnitudes are corrected for Galactic foreground extinction $A_{\rm v}^{\rm Gal}$= 0.09 mag.

SED	mid-time [ks]	$g'(\rm m_{AB})$	$r'(\rm m_{AB})$	$i'(\rm m_{AB})$	$z'(\rm m_{AB})$	$J(\rm m_{Vega})$	$H(\rm m_{Vega})$	$K_{\rm s}(\rm m_{Vega})$
I	24.8	18.87±0.06	18.54±0.04	18.31±0.04	18.02±0.04	17.69±0.14	17.34±0.15	17.11±0.16
II	26.7	18.97±0.05	18.66±0.04	18.43±0.05	18.09±0.05	17.83±0.10	17.43±0.10	17.23±0.12
III	33.4	19.29±0.04	18.94±0.04	18.72±0.05	18.41±0.05	18.10±0.07	17.70±0.07	17.51±0.12
IV	194.7	24.24±0.50	23.54±0.50	23.31±0.50	23.29±0.50	22.42±0.50	21.67±0.00	20.55±0.00
Ir	28.8	19.03±0.02	18.74±0.07	18.49±0.02	18.19±0.04	17.85±0.04	17.43±0.05	17.29±0.07
IIr	41.5	19.41±0.06	19.12±0.06	18.97±0.07	18.64±0.06	18.29±0.12	18.13±0.13	17.93±0.28
IIIr	96.8	20.93±0.25	20.65±0.21	20.42±0.22	20.18±0.32	19.91±0.33	19.41±0.40	19.21±0.40

The observations in the submm and radio wavelength range are shown in Fig. 7.4. The flux of the observations at 345 GHz is increasing during the first epoch and then it starts to decrease. This indicates that $\nu_{\rm sa}$ is initially above 345 GHz and then it will cross this frequency towards a lower value. In the case of the radio observations it is difficult to conclude because there are only 2 observations and each one was taken at a different wavelength. It is however clear that the observations at 93 GHz are at least below $\nu_{\rm m}$ at the beginning and at some point $\nu_{\rm sa}$, otherwise there would be in contradiction with the submm observations (Fig. 7.4).

[2](Gorosabel et al. 2013; Quadri et al. 2013; Klotz et al. 2013; Butler et al. 2013)

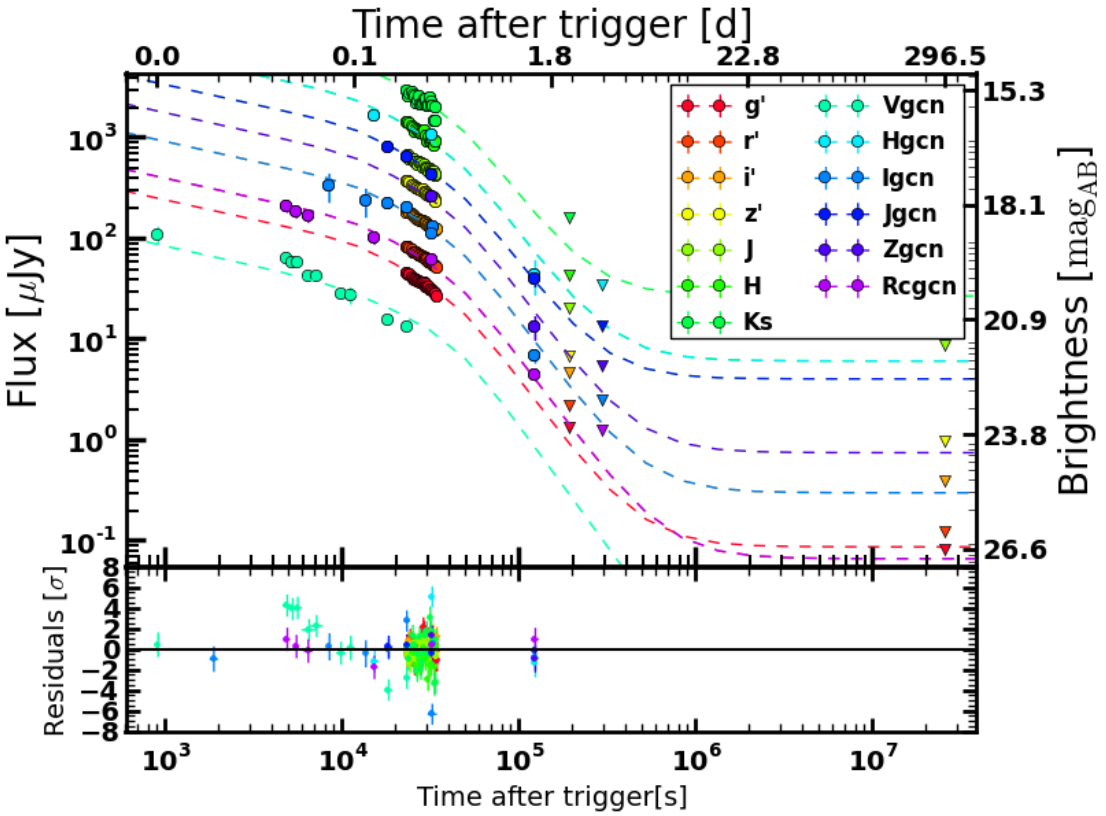

Figure 7.3: Optical/NIR light curve of the afterglow of GRB 130418A observed with GROND and optical/NIR data. The best fit model describing the data is a double broken power-law with smooth breaks.

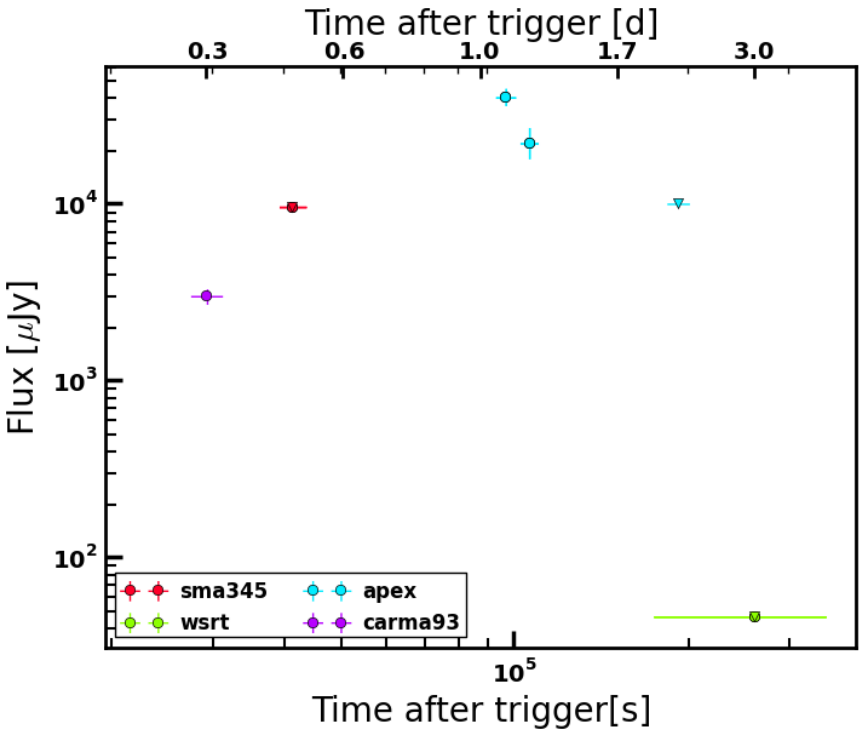

Figure 7.4: Submm and radio observations of the afterglow of GRB 130418A.

7.2.2 Afterglow SED fitting

The second step in the study of the afterglow physics is the analysis of the spectral energy distribution SED. The analysis begins with the spectral energy distribution at the X-ray band. The effects of metal attenuation along the line of sight due to the local environment $N_{\rm H}^{\rm Gal}$ and, due to the host environment $N_{\rm H}^{\rm host}$ are included. $N_{\rm H}^{\rm Gal}$= 2.93×10^{20} cm^{-2} (Kalberla et al. 2005). The data is best described by a single power-law with slope β= 0.58±0.11 with $N_{\rm H}^{\rm host}$= 8.63±8.42×10^{20} cm^{-2} and a goodness of the fit χ^2/d.o.f= 12.9/17. Fig. 7.5a shows the result for the SED of the XRT observations. To check the dependency between the spectral slope and $N_{\rm H}^{\rm host}$ I show the contour plot in Fig. 7.5b. The slope is well constrained and $N_{\rm H}^{\rm host}$ does not have a high dependency on β.

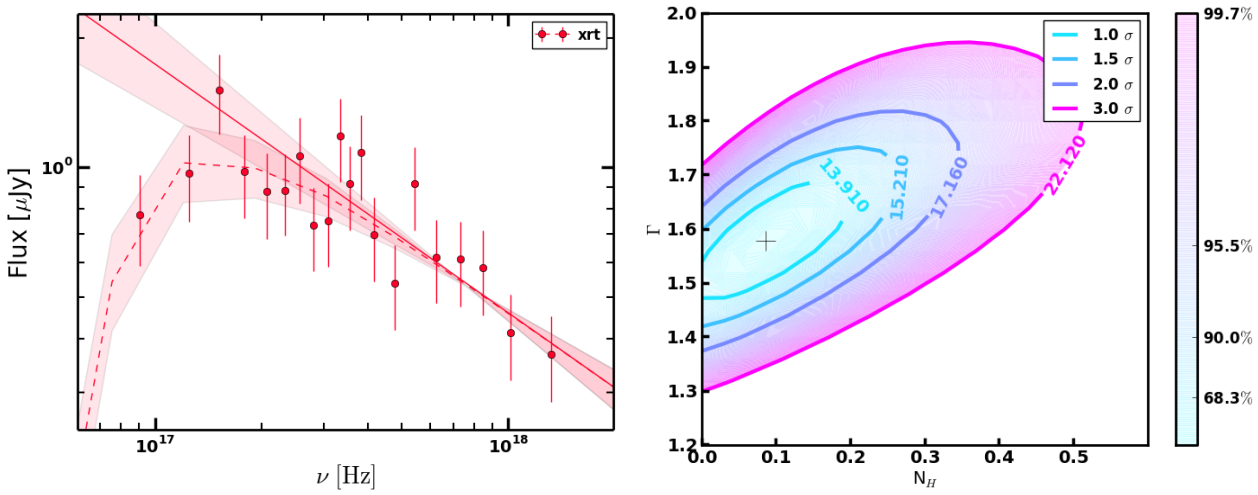

(a) XRT SED

(b) Γ vs $N_{\rm H}^{\rm host}$

Figure 7.5: Left: XRT SED before the break in the XRT light curve ($t_{\rm b}$=45.4 ks) that corresponds to the blue highlighted region in Fig. 7.2. The SED slope is β=0.58±0.11. **Right**: Contour plots showing the dependency of the photon index Γ=β+1 and $N_{\rm H}^{\rm host}$.

The analysis of the SED using only GROND data is included. Four SEDs are used, three before the break in the light curve at $t_{\rm b}$= 45.4 ks and one SED after the break in the light curve. XRT data was not included as the coverage is just before the start of GROND observations with one single data point at a late time. Dust attenuation effects along the line of sight due to the host $A_{\rm v}^{\rm host}$ and local $A_{\rm v}^{\rm Gal}$ environment are included. The SED analysis for the four SEDs (Table 7.2) use a Galactic reddening E(B − V)=0.03 mag, corresponding to an extinction of $A_{\rm v}^{\rm Gal}$= 0.09 mag (Schlafly & Finkbeiner 2011) for a Milky Way (MW) reddening law and the host magnitude was subtracted from the optical/NIR data. The values for the host extinction and absorption are tied between all the epochs and the spectral slopes are left free to vary. The best fit to the data is a single power-law. The first three SEDs show no spectral evolution. The fourth SED has an apparent change in the slope of about 0.5 but with an uncertainty of about 0.6 and therefore is not conclusive. Therefore the fit is done simultaneously for all the SEDs linking the individual slopes free and the host dust extinction $A_{\rm v}^{\rm host}$. The best fit is given then by a power-law with goodness of the fit χ^2/d.o.f=12.94/16, with best fitting parameters $A_{\rm v}^{\rm host}$ of 0 and spectral slope β=1.16±0.07 (Fig. 7.6a). The dependency of the dust extinction on the spectral slope is presented in Fig. 7.6b. It can be seen that the dependency is almost null and the spectral slope is well constrained.

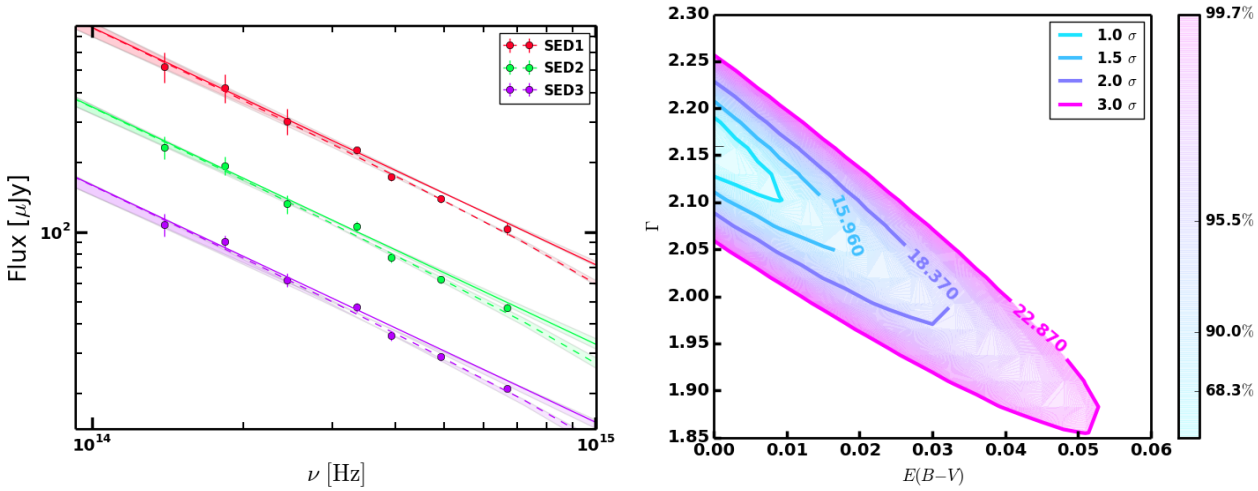

(a) GROND SED

(b) Γ vs $A_{\rm v}^{\rm host}$

Figure 7.6: Left: GROND SEDs for the three epochs at: SED1 t=24.8 ks, SED2 t=26.7 ks and SED3 t=33.4 ks. The SED slope is β=1.05$\pm$0.07. **Right**: Contour plots showing the dependency of the photon index Γ=β+1 and $A_{\rm v}^{\rm host}$

7.3 Broadband SED analysis

Now, the radio and submm data are included in the analysis and the broad band SED at three different epochs is studied. The microphysical parameters are derived from the measured break frequencies. From the previous section it was concluded that the external density profile is a stellar wind-like and the spectral index p=2.32$\pm$0.14. To perform the broadband SED analysis the values for the dust and gas attenuation effects $A_{\rm v}^{\rm host}$, $A_{\rm v}^{\rm Gal}$, $N_{\rm H}^{\rm host}$, $N_{\rm H}^{\rm Gal}$ along the line of sight to to the host and local environments are set to the values obtained in the previous sections for the SED analysis of the X-ray and optical observations. From the broadband SED it can be observed that the cooling frequency $\nu_{\rm c}$ lies below the NIR band during the three epochs. The injection frequency $\nu_{\rm m}$ and the self absorption frequency $\nu_{\rm sa}$ lies above the radio data during the first two epochs and the last epoch only an upper limit on $\nu_{\rm sa}$ is obtained. The results are shown in Table 7.3 and in Fig. 7.7.

Table 7.3: Results for the best fit parameters using a double broken power-law. Fig. 7.7.

SED	mid-time [ks]	$\nu_{c,13}$ [Hz]	$\nu_{m,12}$ [Hz]	$\nu_{sa,11}$ [Hz]
I	28.8	$1.66^{+0.18}_{-0.23}$	$3.26^{+0.33}_{-0.21}$	$6.04^{+0.63}_{-0.48}$
II	41.5	$1.98^{+0.12}_{-0.19}$	$1.73^{+0.23}_{-0.18}$	$4.64^{+0.61}_{-0.46}$
III	106.8	$3.65^{+2.48}_{-2.16}$	$0.47^{+0.03}_{-0.02}$	2.93 UL

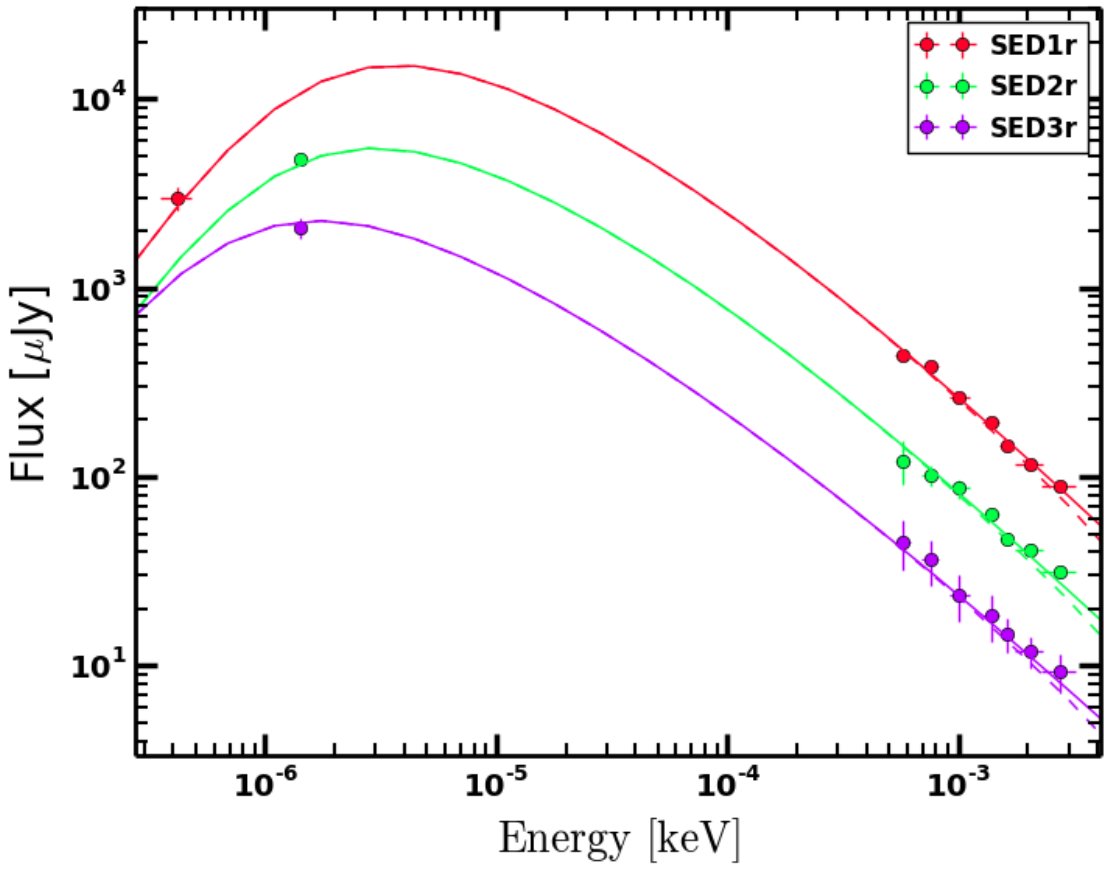

Figure 7.7: Broad band SED analysis of GRB 130418A. The three epochs are at SED1 t=28.8 ks, SED2 t=41.5 ks and SED3 t=106.8 ks. The magnitude are given in Table 7.2.

7.4 Physical parameters of the standard afterglow model

7.4.1 Closure relations

The combination of the temporal and SED information by means of the closure relations lead to the following results. The observations have an initial energy injection phase. The optical data (ν_{opt}) are in agreement with two scenario: 1) ν_c<ν_{opt} with an injection parameter q = 0.14±0.10 and an ISM or stellar wind-like density profiles. 2) ν_{opt}<ν_c with q = 0.09±0.08 and an ISM density profile. In the case of the X-ray data (ν_{XRT}) it is seen that ν_{XRT}<ν_c with an injection parameter q = 0.88±0.16, p=2.32±0.14 and a stellar wind-like density profile. Within a 3σ uncertainty level, the data is also in agreement with ν_{XRT}<ν_c for either a stellar wind-like or an ISM density profile. This last scenario is not consistent with the optical data. Additionally, the spectral slope in the X-ray band β_{XRT} is flatter than the spectral slope in the optical/NIR bands β_{opt} . It could be explained by a spectral evolution in the XRT band at $t < 18.8$ ks or by a strong contribution fromSSC during the first stages of the afterglow evolution in the X-ray band. However, an evolution in β_{XRT} implies an evolution in β_{opt}. If there is a SED evolution in the X-ray wavelengths it implies ν_{XRT} going from the segment where ν_m<ν_c<ν_c to the segment where ν_c<ν_{XRT} . This is not possible because for ν_{XRT}<$\nu_c$the circumburst medium has a stellar wind-like density profile where ν_c increases with time and could not cross through the X-ray bands. Also ν_{opt} should lie in the same segment as ν_{XRT} in order to have the same electron index p. This means that there has to be an evolution

on the optical bands, this evolution is not observed. Moreover this would be in contradiction with the results form the X-ray observations if $\nu_{\rm XRT}<\nu_{\rm c}$, i.e., the X-ray requires an stellar wind-like environment in the energy injection scenario while the optical observations require an ISM density profile. It is therefore clear that there is an energy injection phase and the X-ray data is affected by a strong inverse Compton scattering component, at least during the early stages of the afterglow evolution, i.e., before the break in the light curve at $t_{\rm b_2}$=18.8$\pm$3.5 ks. IC affects mainly the observations at soft X-rays. It lowers the initial value of $\nu_{\rm c}$ by a factor of $(1+{\rm Y})^{-2}$ and change the observed flux evolution to α=1.39 when it is the dominant cooling effect. It also flattens the spectral slope above $\nu_{\rm c}$ with an expected β=1/3, which is in complete agreement with the observations. The first break in the optical light curve is therefore associated to the end of an energy injection phase. The second break is an achromatic break consistent with a uniform non-spreading jet. The submm and radio data confirm that $\nu_{\rm c}<\nu_{\rm opt}$ and the evolution of the jet is in a stellar wind-like density profile.

7.4.2 Afterglow parameters

Using the measured break frequencies in Sec. 7.3 I derived the microphysical and dynamical parameters, i.e., $\varepsilon_{\rm B}$, $\varepsilon_{\rm e}$, $E_{\rm K,iso}$, A_*. The results are reported in Table 7.4. The energy injection phase ended by the time of the first break in the light curve at $t_{\rm b_1}$=18.8$\pm$3.5 ks and the non-spreading jet starts at $t_{\rm b_2}$=61.7$\pm$8.1 ks. Therefore the effect of the energy injection is not included in the derivation of the parameters but the effect of the geometrical jet is included as a renormalisation of the peak flux to account for the difference with the expected spherical flux. To test the importance of the SSC and the effect it has on afterglow parameters, the derivation of the microphysical and dynamical parameters is performed with and without the SSC effect included. As a result, it is observed that when SSC is included the value for $\varepsilon_{\rm B}$ is of order 10^3, which is not physically possible and therefore SSC is not included in the final results. However, as expected by theory and needed by the early time observations, SSC was a dominant effect during the first stages of the afterglow evolution. In Table 7.4 and Table 7.5. In Fig. 7.9 and Fig. 7.10 a dashed pink line it is plotter the average value for each parameters and, it becomes clear that all the values are 1σ away from this average value.

Table 7.4: Derived microphysical and dynamical parameters for the afterglow GRB 100418A. The first three epochs correspond to the fast cooling regime and the last five epochs correspond to the slow cooling regime. $\bar{\varepsilon}_{\rm e}$=$\varepsilon_{\rm e}\times(|p-2|)/(p-1)$ and $E_{\rm K,iso,52}$ =$E_{\rm K,iso}/10^{52}$. $n={\rm Ar}^{-2}$ with ${\rm A}=\dot{\rm M}/4\pi{\rm v_w}=5\times10^{11}{\rm A}_*$ g cm^{-1} (Chevalier & Li 2000). For $k=2$ we report the density in terms of A_*. The subscript of each quantity are $C_x=C\times10^x$. For $\varepsilon_{\rm e}$=1 then $\bar{\varepsilon}_{\rm e}$=0.24$\pm$0.08 for p=2.32$\pm$0.14.

SED	mid-time [ks]	$\bar{\varepsilon}_{\rm e-1}$	$\varepsilon_{\rm B,-5}$	$A_{*,+1}$	$E_{\rm K,iso,51}$ [erg]
I	288.1	$0.96^{+0.07}_{-0.08}$	$7.67^{+1.25}_{-0.22}$	$4.47^{+2.14}_{-1.38}$	$7.40^{+0.32}_{-0.39}$
II	415.7	$1.07^{+0.21}_{-0.16}$	$6.55^{+1.89}_{-0.14}$	$5.33^{+1.68}_{-0.87}$	$7.76^{+0.28}_{-0.15}$
III	106.8	0.86 LL	8.40 UL	3.90 LL	7.76 UL

Table 7.5: Energy efficiency, magnetic field magnitude, mass loss rate, opening angle and Compton parameters are presented here. The half-opening angle is derived using Eq.(4) from Granot et al. (2005). The subscript ofeach quantity are $C_x = C \times 10^{-x}$. Mass loss rate for a wind velocity of 1000 km. $E_{\rm jet}$=$E_{\rm K,iso} \times {\theta_0}^2/2$

SED	mid-time [ks]	θ_{0-1} [rad]	η	B	$\dot{M}_{\rm W,-4}$	$E_{\rm jet,51}$ [erg]
I	288.1	$4.52^{+0.49}_{-0.43}$	$0.35^{+0.05}_{-0.04}$	$1.68^{+0.11}_{-0.09}$	$4.48^{+2.81}_{-1.57}$	$1.15^{+0.38}_{-0.41}$
II	415.7	$4.67^{+0.44}_{-0.38}$	$0.33^{+0.03}_{-0.05}$	$1.31^{+0.09}_{-0.07}$	$5.34^{+2.47}_{-1.15}$	$1.27^{+0.39}_{-0.23}$
III	106.8	4.27 LL	0.33 LL	0.69 LL	3.90 LL	1.09 UL

7.5 Discussion

In the previous sections I presented a detail analysis of the multi-epoch multi-wavelength observations of the afterglow of GRB 130418A. The light curves of the optical and NIR observations have a plateau phase before $t_{\rm b}$= 18.8±3.5 ks. This plateau phase is not directly observed in the X-ray data, but it could be related to a dominant SSC constribution to the cooling of the electrons in the early stages of the afterglow. The steep slope α= 1.11±0.14 can be explained as the result from the combined contribution of the SSC flux and the prolonged energy injection phase. Actually, if SSC is the dominant emission component, the evolution of the SSC light curve for a stellar wind-like density profile when $\nu_{\rm c}$<$\nu_{\rm XRT}$ has a slope of α about 1.39 for p=2.32, which is in agreement with the X-ray data before 18 ks. The SSC contribution also explains the flatter SED slope $\beta_{\rm XRT}$ compared to the one in the optical range $\beta_{\rm opt}$. Therefore, at early times the SSC plays an important role, and the reported values for the injection parameter are therefore based on the optical data, which are not affected by SSC. The plateau phase is explained as an ongoing energy injection phase with injection parameter q = 0.14±0.10. This parameter is in agreement with both of the two most accepted scenarios for a prolonged energy injection: a stratified mass shells, with parameter *s* of about 4.2 in a stellar wind-like density profile, which is in agreement with the change in dynamics that requires s > 1. Or a magnetar model with an emission dominated by a Poynting flux that requires $q \sim 0$. The value of q make it also possible a long lived central engine based on a continuous infall into the black hole, however the signature of the reverse shock is not observed. The second break in the light curve is identified by means of the closure relations with a uniform non-spreading jet expanding in a stellar wind-like density profile. This is in agreement with the expected collimated nature of the outflow, with $\theta_0 \sim$0.45 rad.

The broad-band SED analysis is performed at three different epochs. The cooling break $\nu_{\rm c}$ is well detected in the three epochs presented for the afterglow as seen in Fig. 7.8. The evolution has a temporal slope α=0.61±0.03 which is within a 4σ level consistent with the expected 0.5. The injection frequency $\nu_{\rm m}$ was also detected in all three epochs moving with a temporal evolution of α=-1.45±0.06, which is in complete agreement with the theoretical value for a synchrotron emission where α=-1.5. Contrary to the cooling, $\nu_{\rm c}$, and injection, $\nu_{\rm m}$, breaks, the self-absorption frequency, $\nu_{\rm sa}$, was only measured in the first two epochs, and an upper limit was obtained for the last epoch. The decay between the first two epochs has a rate of -0.68±0.08 within a 1σ interval from the theoretical -0.6 value. Besides the evolution of the frequencies, it is also interesting to study the initial position of the break frequencies. The effect of SSC was fount to not be a dominant component during the late observations of the afterglow evolution. It is however an important component during the early epochs of the afterglow evolution, with different observational evidences pointing towards this conclusion. First, the position of the break frequencies, one of the effects of the SSC on the break frequencies during the slow cooing regime is to lower the initial position

ν_c by a factor of $(1+Y)^{-2}$ and increase the position of ν_{sa} by a factor of (1+Y) (see chapter 2). For this GRB afterglow, this effect is observed: ν_{sa} has larger values than usually expected, i.e., above submm frequencies rather than being closer to radio frequencies and the cooling break $\nu_c$has lower values than commonly observed, i.e., closer to X-rays.

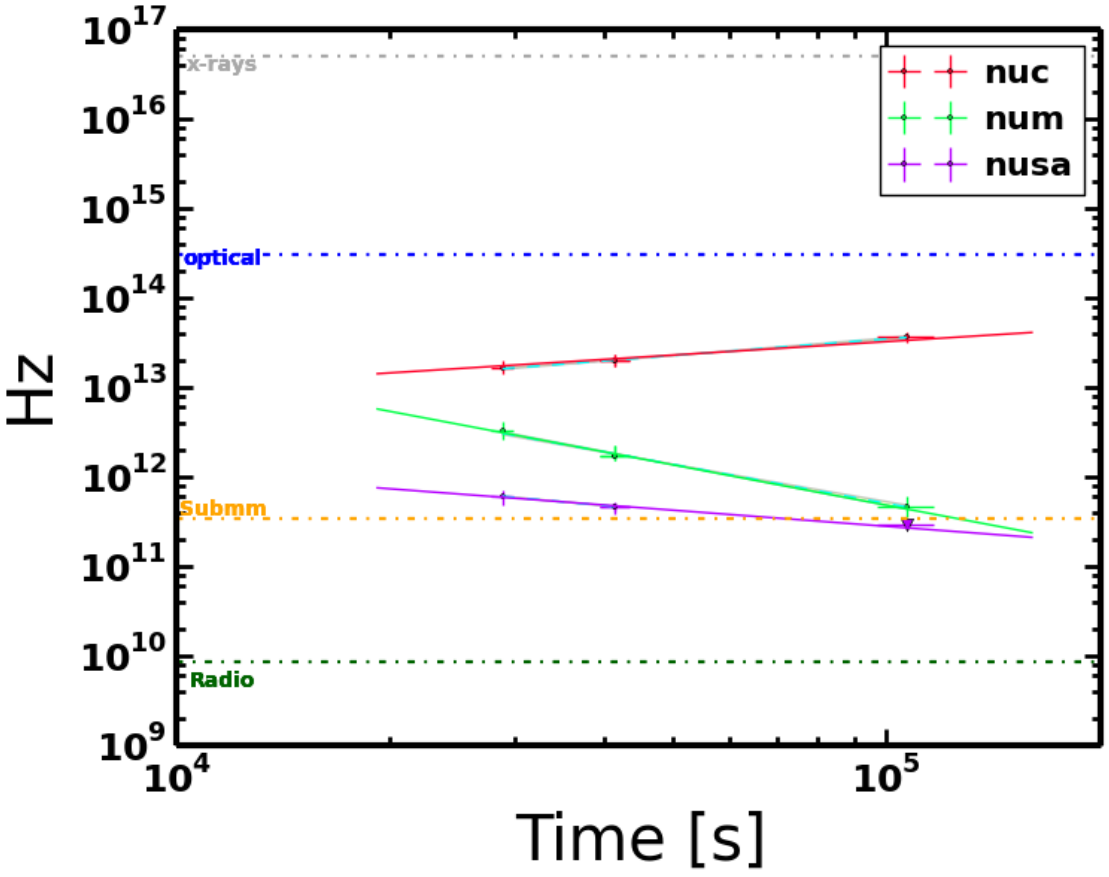

Figure 7.8: Evolution of the break frequencies of the GRB 130418A afterglow.

Once the break frequencies are measured and analysed, it is possible to derive the microphysical parameters. From the spectral energy distribution slope above ν_c the electron index p is derived with a value of 2.32±0.14, consistent with Fermi acceleration processes. The other two microphysical parameters ε_B and ε_e have values on the range of 10^{-5} and 10^{-1}, respectively. First, and even though the radio between $\varepsilon_e/\varepsilon_B > 10^4$ suggesting and important contribution from SSC, it was already tested and it is not important during the late stages of the evolution. Second, the final values for both parameters are below < 1 which is expected as they are just a fraction of the total energy. Even more important ε_B is about 4 orders of magnitude larger than the expectations for a magnetic field from shock compression assuming a seed magnetic field of a few μJy in a stellar wind-like density profile. This could mean that the seed magnetic field is larger of order mG, or that an additional amplification of about 10^2 times of the magnetic field in the shock region. Alternative mechanism to create such strong magnetic fields has been proposed such as magnetohydrodynamics processes (Medvedev & Loeb 1999) or Weibel instabilities (Weibel 1959), with the last one being most likely due to efficiency requirementsThe density normalisation A_* has an average value of 47, this is larger by a factor of 10 of the expected values for a Wolf-Rayet star as a progenitor of the GRB. It is however in the upper limit of the expected density if we assume a larger mass

loss rate. Also, it is in agreement with the IC scattering importance during the early stages of the afterglow phase, as A_* has to be larger than 10 if IC scattering is the dominant cooling process (Sari & Esin 2001).

In terms of the energetics of the outflow, the measured isotropic energy $E_{\rm K,iso}$ in the outflow is 7.70×10^{51} erg which, when compared with $E^{\gamma}_{\rm iso}$gives and efficiency η[3] of 0.33. The outflow is collimated with θ_0 average about 0.45 rad which translates into a real energy in the outflow of $E_{\rm jet}0.27\times10^{51}$ erg. Finally $\dot{M}_{\rm W}$is of the order $5\times10^{-4}\ M_\odot\ {\rm yr}^{-1}$ for a wind velocity of 1000 km/s which is within the expected range from a Wolf-Rayet star.

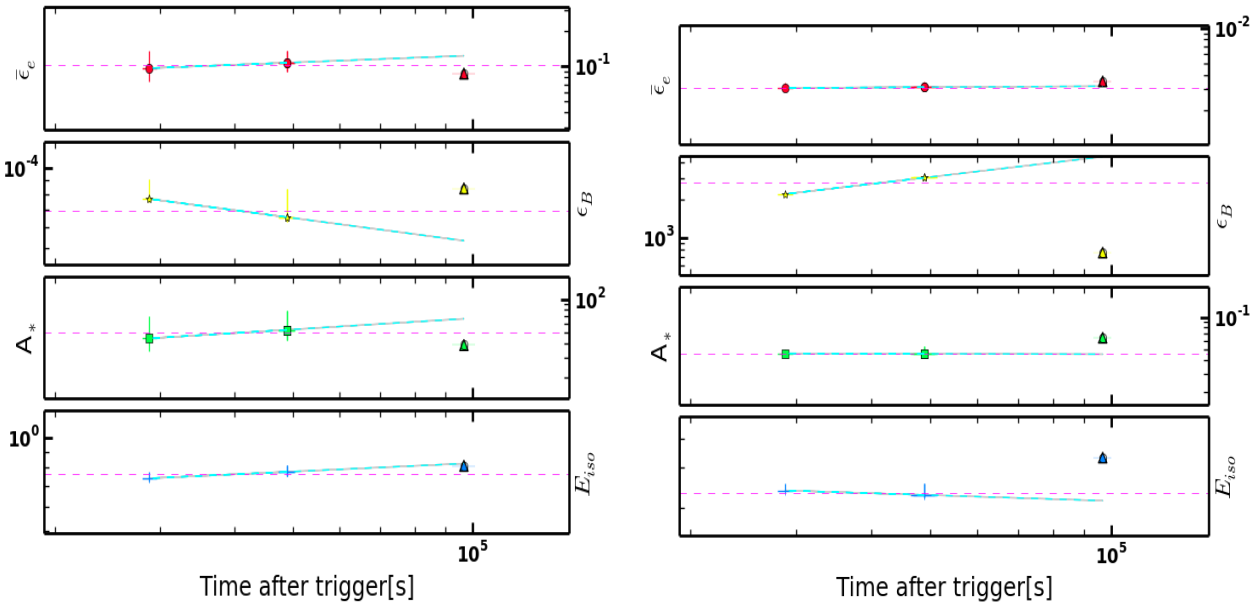

(a) GRB130418A evolution params.

(b) GRB130418A evolution params IC

Figure 7.9: Evolution of the derived microphysical and dynamical parameters of the afterglow of GRB 130418A. The dashed lines and shaded regions represent the results from the fit of the observed temporal evolution. The horizontal dashed purple lines shows the average value for each parameter. $E_{\rm K,iso}$ is in units of 10^{52} erg with an average value of 2.30×10^{50} erg in the case of IC. This temporal slope is given as a reference value but it is not the actual evolution of the parameters. The fit was performed only with two epoch and therefore the number of variables is equal to the number of free parameters and no goodness of the fit can be measured.

[3]Efficiency of the conversion of the kinetic energy in the outflow to gamma-rays during the prompt emission η=$E_{\rm K,iso}$/($E^{\gamma}_{\rm iso}$+$E_{\rm K,iso}$). $E^{\gamma}_{\rm iso}$ is the isotropic energy released in the prompt gamma-ray emission. In this case $E^{\gamma}_{\rm iso}$=$0.39^{+0.51}_{-0.36}\times10^{52}$ erg (Butler & Kocevski 2007) (http://butler.lab.asu.edu/Swift/index.html) and z=1.218. It is calculated using $E^{\gamma}_{\rm iso}$=$4\pi d_{\rm L}^2{\rm F}/(1+{\rm z})$, where F is the fluence in the gamma-ray band. BAT: from $15-150$ keV in the observer-frame. $E_{\rm K,iso}$: energy range $1-10^4$ keV in the rest frame.

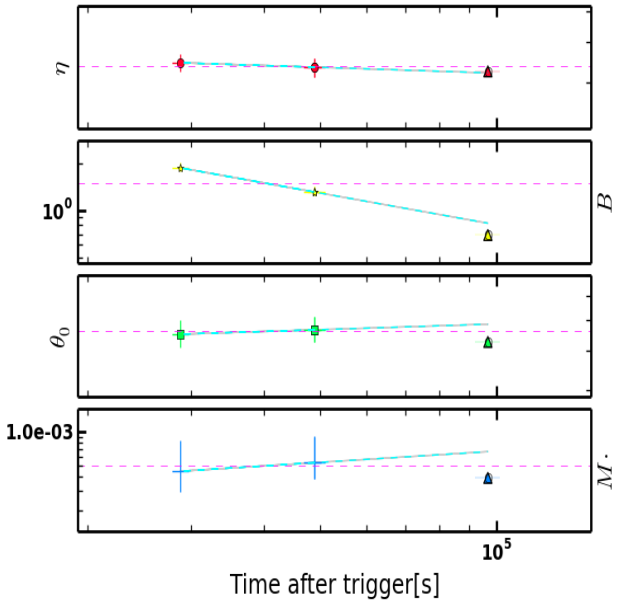

(a) GRB130418A evolution secondary quantities.

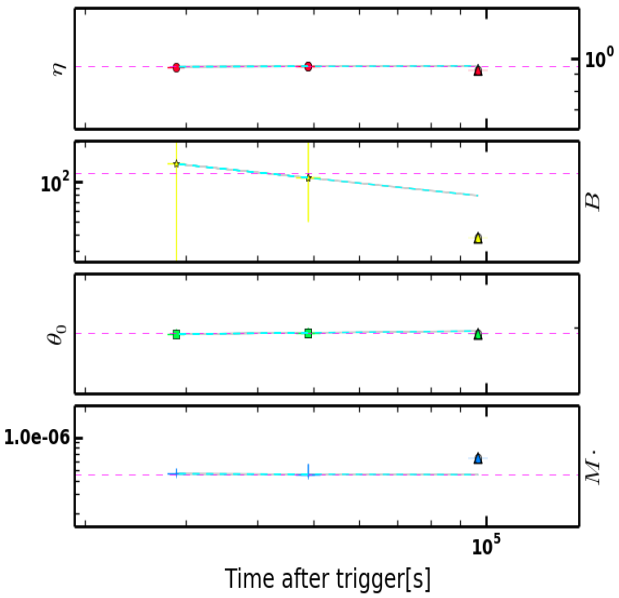

(b) GRB130418A evolution secondary quantities.

Figure 7.10: Evolution of the energy efficiency η, magnetic field magnitude B, mass loss rate $\dot{M}_{\odot}$, opening angle θ_0 derived from the measured microphysical and dynamical parameters of the afterglow of GRB130418A. The dashed lines and shaded regions represent the results from the fit of the observed temporal evolution. η has an average value of 0.35 in the case where there is no IC included $\theta_0$has na average value of 0.19 rad in the case of IC included.

Chapter 8

GRBs broadband SEDs in context

8.1 Overview

It has been more than 4 decades since the start of dedicated theoretical and observational studies on GRBs. Great advances towards a complete physical model, explaining the observed radiation from both the GRB itself and the subsequent afterglow emission have been achieved. However, there are still different features of the observations that can not be explained by the actual models. The most widely accepted model for the afterglow emission is known as the standard afterglow model. In this model, long GRBs are associated to the death of massive stars (Stanek et al. 2003; Woosley & Heger 2003). Under a set of specific circumstances, the collapse of a massive star leads to the formation of a black hole with a torus system surrounded by a fireball. The system evolves ultra-relativistically, with the blast-wave propagating into the surrounding cold external medium. Electrons are accelerated within the collisionless shocks due to the interaction between the blast-wave and the external medium. When enough material from the cold medium is swept-up, the blast wave starts the deceleration phase. A fraction of the total accelerated electrons will cool down (decelerate) via a dominant synchrotron radiation process and, in some cases, via secondary processes such as inverse Compton (IC) scattering. If the emission region is optically thin, the emitted radiation will be observed as a typical synchrotron spectrum (Mészáros & Rees 1997). The observed synchrotron spectrum is generally described by power-law segments joined at specific break frequencies. The observed flux is given by $F \sim t^{-\alpha}\nu^{-\beta}$, where β and α are the spectral and temporal slopes, respectively.

Here, I present a detailed analysis using multi-epoch broad-band observations. The analysis is based on a combination of the temporal and spectral information through the *snapshot method*. Fig. 8.1 and Fig. 8.2 show in an illustrative way the main steps and characteristics of the *snapshot method* (see details in Chap. 3). The basic features of the GRBs analysed here are presented in Table 8.3 and Table 8.4. In this chapter, the results for the individual GRBs are analysed in the context of the broad picture of the current state in GRB studies. The analysis is performed in the framework of the standard afterglow model, with additional components, such as SSC and energy injection, included. Details about the derivation of the afterglow parameters for a hard electron spectrum (1<p<2), as well as the inclusion of any additional component to the standard afterglow model are given in Chap. 2. The notation $Q_x = Q/10^x$ in CGS is used through out the analysis.

Table 8.1: Schematic of the model independent analysis. **Left top Table**: key features of step 1. **Left Figure**: Optical/NIR light curve. **Right top Table**: key features of step 2. **Right Figure**: Optical and X-ray SED. **Bottom Table**: Step 3 is the combination of step 1 and 2 via the closure relations.

Model-independent

Step 1: Analysis of the light curve:
✶Temporal slope α.
✶Flares.
✶Bumps.
✶Plateau phases.
✶Breaks - Jet breaks.
✶Host Galaxy contribution.

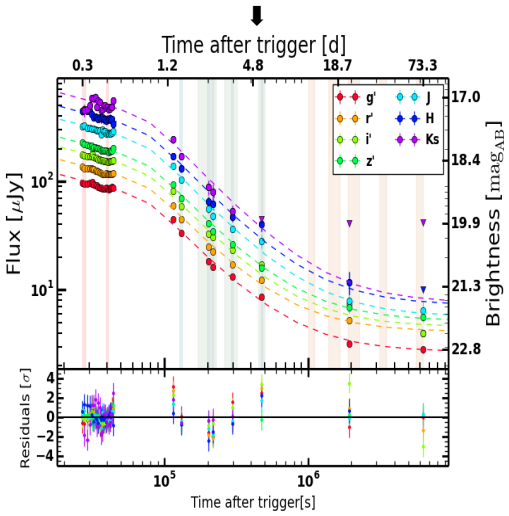

Step 2: Analysis of the SED:
✶Optical and X-ray data only.
✶Spectral index β.
✶Electron index p.
✶Spectral evolution.
✶Host X-ray absorbtion ($N_{\rm H}^{\rm host}$)
✶Host dust extinction ($A_{\rm v}^{\rm host}$)

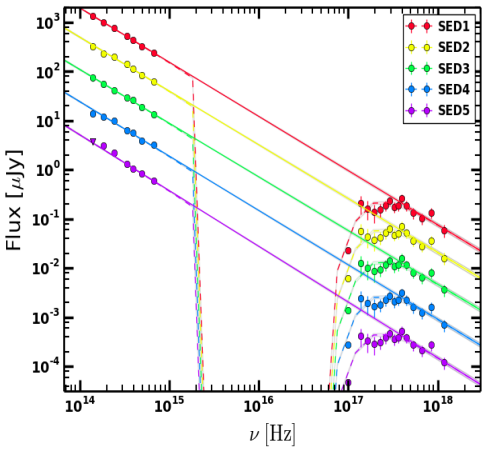

Step 1 + step 2

Step 3: Closure relations
✶Density profile: ISM or stellar wind-like
✶Spectral regime

Table 8.2: Schematic of model-dependent analysis. **Left:** Main features analysed and derived in this phase. **Right:** Observed SED evolution.

Model-dependent

Broadband analysis from radio to X-ray wavelengths:
✶Measurement of the three break frequencies.
✶Relation between the break frequencies.
✶Spectral regime.
✶Cooling regime.
✶Evolution of the break frequencies.
✶Model parameters.

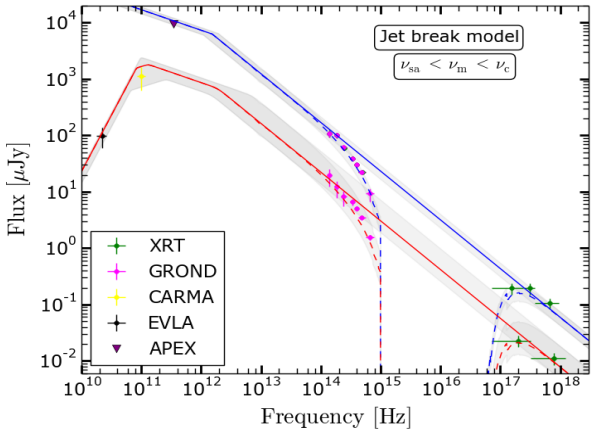

8.2 Highlights and advantages of the broadband SED analysis

I present a detailed analysis on the evolution of all the three break frequencies (i.e., $\nu_{\rm sa}$, $\nu_{\rm m}$, $\nu_{\rm c}$) of the afterglow's SED using the *snapshot method* (Sari et al. 1998). Furthermore, I use the measured

Table 8.3: Main features for the individual studied GRB afterglows. The number of epochs corresponds to the number of time slices used for the SED analysis. The details for each GRB are given in the individual GRB chapters. *EI: Energy injection. ISS: Interstellar scintillation. JB: Jet break. UL: Upper limit. Det: detection.

GRB	X-ray	GROND	Sub-mm	Radio	Notes*
100418A	✗Steep decay. ✗Plateau phase. ✗EI, JB ✗No SED evol.	✗8 epochs ✗Plateau phase. ✗No SED evol. ✗EI, JB	✗SMA: 3 det. ✗PdBI: 7 det. ✗Evol. of α	✗VLA: 7 det. ✗ATCA: 6 det. ✗ISS	✗Non-spreading JB. ✗Fast/slow sooling. ✗Wind
110715A	✗2 breaks. ✗Plateau phase. ✗EI.	✗6 epochs.	✗APEX: 1 det. ✗ALMA: 1 det.	✗ATCA: 22 det, 1 UL. ✗ISS	✗EI. ✗Non-spreading JB. ✗Wind. ✗Early IC.
121024A	✗Plateau phase. ✗EI ✗Achromatic break. ✗No SED evol. ✗JB	✗6 epochs. ✗Plateau phase. ✗EI. ✗Achromatic break. ✗No SED evol. ✗Jet break	✗APEX: 2 UL	✗EVLA: 1 det ✗CARMA: 1 det	✗$1 < p < 2$ ✗EI before t_b, p>2 ✗Jet break, $1 < p < 2$ ✗EI after t_b, $p > 2$ ✗Polarimetry det. ✗Wind
130418A	✗$< 10^4$ ks ✗Jet break ✗α too steep for EI. ✗β too flat vs β opt.	✗7 epoch 2 breaks. EI, jet. ✗EI. ✗Achromatic break. ✗JB	✗SMA: 1 UL. ✗APEX: 2 det, 1 UL.	✗CARMA: 1 det. ✗WSRT: 1 UL	✗No SED evol. ✗Early IC. ✗EI ✗Jet break. ✗Wind

Table 8.4: Parameters used and derived in the analysis. The magnitudes for the Galactic gas absorption and dust extinction are taken from Schlafly & Finkbeiner (2011). The host magnitudes are derived from the analysis of the combined SED using optical/NIR and X-ray data. The last column show the final result for the circumburst medium derived from the closure relations. *This value was derived using the DC formalism Chap. 4. The value for the GS formalism corresponds to 5e49 erg.

GRB	$A_{\rm v}^{\rm Gal}$ mag	$A_{\rm v}^{\rm host}$ mag	$N_{\rm H}^{\rm Gal}{}_{,22}$ cm^{-2}	$N_{\rm H}^{\rm host}{}_{,22}$ cm^{-2}	z	ρ	$E^{\gamma}_{\rm iso,52}$ [erg]	$E_{\rm jet,51}$ [erg]
GRB 100418A	0.22	$0.01^{+0.03}_{-0.01}$	0.06	$0.57^{+0.09}_{-0.08}$	0.625	wind	$0.10^{+0.06}_{-0.03}$	$0.40^{+0.11}_{-0.08}$
GRB 110715A	1.82	$0.05^{+0.01}_{-0.01}$	0.43	$0.16^{+0.03}_{-0.04}$	0.820	wind	$2.93^{+5.79}_{-2.81}$	$2.27^{+0.26}_{-0.24}$
GRB 121024A	0.27	$0.18^{+0.04}_{-0.04}$	0.08	$0.30^{+0.46}_{-0.29}$	2.298	wind	$8.40^{+2.60}_{-2.20}$	$^{*}0.40^{+0.15}_{-0.21}$
GRB 130418A	0.09	$0.00^{+0.01}_{-0.01}$	0.03	$0.08^{+0.08}_{-0.08}$	1.218	wind	$0.39^{+0.51}_{-0.36}$	$1.17^{+0.39}_{-0.32}$

break frequencies for each afterglow, to derive the model parameters and to test their temporal behaviour. Previous studies usually depend on imposed additional assumptions to the standard afterglow model when there is no simultaneous coverage of all the break frequencies during the observations (e.g., Galama et al. 1998c; Harrison et al. 1999; Panaitescu & Kumar 2001; Corsi et al. 2005). A common example of these additional assumptions, is fixing the parameters to canonical[1] values to reduce the number of free variables. These additional assumptions, however, give in ambiguous results and do not allow an independent test of the model. Besides the *snapshot*

[1]The canonical values are not obtained from first principles. Those are just the commonly values used to test the model when not enough information is given. For example $\epsilon_{\rm e}$=0.1, $\epsilon_{\rm B}$=0.01, n=1 cm^{-3} and $E_{\rm K,iso}$=$E^{\gamma}_{\rm iso}$(Zhang et al. 2007; Leventis et al. 2013).

method, previous studies have made use of numerical simulations (De Colle et al. 2012; van Eerten & MacFadyen 2012; van Eerten 2014). The test of the results from the simulations with data do not require simultaneous observations. However, in order to make a self-consistent test, they do require well sampled light curves in wavelengths from radio to X-rays. A well sampled light curve implies high-quality observations covering a long-time interval with a smooth behaviour. This smooth behaviour implies that any feature that deviates from the standard model predictions during the deceleration phase has to be ignored. The results from numerical simulations had been used together with samples of X-ray and/or optical data, but even in those cases additional assumptions on the parameters had to be included (Panaitescu et al. 2006; Guidorzi et al. 2014). It has been seen that a derived set of model parameters obtained only from X-ray and optical data, do not necessarily describe the submm and radio data. These inconsistencies can be the result from either intrinsic effects from the GRB afterglow itself (e.g., relativistic reverse shock Sari & Piran 1995; Mészáros & Rees 1999; Kobayashi 2000) or external effects from the local and host mediums (e.g., ISS from the local medium Frail et al. 1997). These effects can only be detected at low frequencies and, therefore analysis using only optical and X-ray data do not account for them.

8.2.1 Circumburst environment CBM

The environment of the GRB plays an important role in both, the dynamics and radiation processes of the afterglow (Blandford & McKee 1976; Chevalier & Li 2000). A detailed structure of the CBM close to the explosion provides basic information about the progenitor and the central engine of the GRB. The expected structure of the CBM in the region close to the progenitor (few pc) depends on the wind from the star over more than 1000 yr before the explosion (Panaitescu et al. 2006). The stellar wind depends on different parameters of the star, such as the rotation velocity, mass, mass loss rate and temperature (Harries et al. 1998; Ramirez-Ruiz et al. 2001; Crowther 2007). Numerical and observational studies of massive stars result in a CBM with an inhomogeneous structure. Due to the available data and observational tools, the CBM structure is assumed to have a smooth power-law profile with slope k. This smooth profile implies that the density oscillations are not taken into account. If a region has a density much higher than the average density profile (bumps), changes in the observed emission from the afterglow are expected (e.g., optical re-brightness Mészáros & Rees 1999; Dai & Lu 1999; Kumar & Piran 2000). Two main density profiles are commonly used: a homogenous profile ISM-like, with k=0 or, a stellar wind-like profile, with k=2. A constant wind velocity and mass-loss rate are assumed for the progenitor star in the stellar wind-like density profile.

More than 50% of the GRBs from samples based on X-ray and/or optical data sets, are associated with an ISM density profile (e.g., Panaitescu & Kumar 2002; Schulze et al. 2011). These results are opposite to both the theoretical expectations (e.g., MacFadyen et al. 2001) and the relation between GRBs and Type Ic supernovae SNe (e.g., GRB 030329, GRB 130427, Stanek et al. 2003; Fruchter et al. 2006; Xu et al. 2013; Cano et al. 2014). Even more, not only an ISM density profile (66% of the sample) is at odds with the collapsar model. The actual magnitudes of the density required in an ISM profile are at least 10^4 cm^{-3} (Schulze et al. 2011). Values that large are not expected from the basic models for massive stars evolution (Langer 1989; Crowther 2007). Indeed, simulations show that the density[2] at 0.1 pc is only about 1 - 10 cm^{-3} (Fryer et al. 2006; van Marle

[2]The wind termination shock radius is define as the point where the transition from an inhomogeneous profile to a homogenous ISM profile occurs (van Marle et al. 2006) and references therein. The shock termination radius has an

et al. 2007). Therefore, if the CBM was to be ISM-like, there must be additional mechanisms to explain the homogenisation of the CBM before 0.1 pc from the source.

The four GRB afterglows analysed in this study are uniquely explained by a relativistic outflow expanding into a stellar wind-like density profile. As mentioned before, this result is not what has been observed in the results presented in the literature. The differences in the results might be due to different reasons, from selection effects from quality of the data sets. Here I outline some of the main differences between a multi-epoch broad-band analysis and other analysis, that could lead to a misleading final result for the CBM profile. And, the importance and special results obtained from our unique data set. First, the selection criteria that is commonly used, can reduced the initial number of afterglow in the samples more than 70% (e.g., 26/90 GRBs Schulze et al. 2011 and 195/658 GRB Margutti et al. 2013). These selection criteria are not only related to quality and time coverage of the afterglow observations. For a good quality data set, all the afterglow with features in the light curves (e.g., flares, bumps, plateaus, faster or slower decays), that are not predicted by the standard afterglow model, are excluded. These selection effects represent a large bias in the study that could lead to a false identification of the CBM profile. Moreover the additional feature in the light curves contains important information on the model, that is excluded in this sample. For example, GRB 990123 requires and extremely dense medium to reproduce the optical flare (Dai & Lu 1999).

Second, the power-law segment of the SED where the observing frequency, $\nu_{\rm obs}$, lies. In the segment where $\nu_{\rm obs} > \nu_{\rm c}$ there is no distinction between ISM or stellar wind-like density profiles. If $\nu_{\rm obs} < \nu_{\rm c}$, then it is possible to use the closure relations to identify the CBM profile. In the literature, X-ray samples show that for a large fraction (70-90%) of the afterglows, $\nu_{\rm XRT}$ usually lies above $\nu_{\rm c}$ (e.g., 22/31 GRBs Zhang et al. 2007 and 280/300 GRBs Curran et al. 2010). Therefore, the CBM structure can not be determined. Optical samples, such as the one presented in Kann et al. (2010), suggest that less than 25% of the afterglows (10/42) have $\nu_{\rm opt}>\nu_{\rm c}$, if p is assumed to be larger than 2. Curran et al. (2009) and Panaitescu et al. (2006) show that > 70% of their samples (10 and 9 GRBs, respectively) have $\nu_{\rm obs} < \nu_{\rm c}$. However, they do not associated the CBM with a stellar wind-like density profile, instead they show that $1 < k < 2$, as expected for an inhomogeneous density profile. Additionally to these samples, about 60% of the afterglows in Greiner et al. (2011); Schulze et al. (2011) have a break between the optical and X-ray bands, i.e., $\Delta\beta = 0.5$ and/or $\Delta\alpha = \pm 0.25$ (+ISM, -stellar wind-like). On the one hand, Schulze et al. (2011) found that 38% of their afterglows are related to a stellar wind-like density profile, based on the measured values for α and β . On the other hand, Greiner et al. (2011) found that 50% of their afterglows have $A_{\rm v}^{\rm host}$ about 0. This is not expected in a stellar wind-like density profile and therefore those GRB might be associated to an ISM profile. These percentages, however, may not be fully decisive on the CBM density profile. The results based on α and β do not always agree with the closure relations, e.g., $\Delta\beta = 0.5$ but $\Delta\alpha = 0$. Furthermore, assumptions on the jet break to define the CBM profile are used, even when no jet break is actually observed. Additionally, $A_{\rm v}^{\rm host} = 0$ is not expected in the canonical picture (Greiner et al. 2011), not even for ISM, so this measurement might be misleading. Finally, the break between $\nu_{\rm opt}$ and $\nu_{\rm XRT}$ could be inaccurate, it has been seen that $A_{\rm v}^{\rm host}$ and $N_{\rm H}^{\rm host}$ have a high influence on the slopes in optical and X-rays, respectively. Therefore, the final percentages of the afterglows associated with a stellar wind-like density profile could be strongly altered.

upper limit of 0.1 in the sample of Schulze et al. 2011.

Third, the lack of high quality data and/or not a proper coverage, in both time and wavelength, lead to poor constraints of α and β. This caused ambiguous results in the interpretation of the analysis of the data. A clear example of this is seen for GRB 970228, GRB 970508, GRB 980326 and GRB 980519. Chevalier & Li (2000) associated the four afterglows with a stellar wind-like density profile, but other authors identified an ISM profile as the preferred CBM for those GRBs (e.g., Vietri 1997; Fruchter et al. 1999; Djorgovski et al. 1997; Garcia et al. 1998; Groot et al. 1998; Wang et al. 2000). A broad-band analysis can help to solve the ambiguity on the density profiles. This broad-band analysis does not only rely on the closure relations above ν_m, but in the evolution of the radio and submm data too. The analysis for GRB 121024A presented here is a specific example on the importance of the broad-band wavelength analysis to constrain the CBM profile. In this case the detection of the three break frequencies constrains the jet break scenario in a stellar wind-like external medium as the best and only scenario that could describe the observations. Without this broad band analysis an ISM density profile (with a prolonged energy injection) was a possibility too. GRB 110715A is another example of this broad-band analysis importance. The evolution of its light curves in the radio and submm range were the key factors to determine that the only possible scenario was a jet break in a stellar wind-like density profile.

There are reported studies in the literature where based on broad-band analysis (e.g., Panaitescu & Kumar 2002; Panaitescu 2005; Cenko et al. 2010, 2011). However, only in a few cases the parameters of the afterglow model have been determined without additional assumptions. The main problem is the lack of a good broad-band data set, and especially a set of simultaneous observations. Panaitescu & Kumar (2002) presents data for 10 GRBs, however only 5 out of 10 GRBs can be used in the comparison. There was no satisfactory model for GRB 970508 and GRB 010222, there is no redshift measurement for GRB 980519 and, GRB 000418A has no unique CBM profile and no jet break is observed, which is one of their requirements and, the values of the parameters for GRB 000301C should be use only as limits (Panaitescu 2001). I will refer to this set of 5 GRBs left (GRB 990123, GRB 990510, GRB 991208, GRB 991216 and GRB 000926), as *PK sample* along the following sections. Panaitescu & Kumar (2002) uses χ^2 minimisation to find the best fit parameters. The results show that 2 out of 3 GRBs are in agreement with a stellar wind-like density profile while the other half is described using an ISM density profile. This results however are not completely reliable as a strong constrains on the parameters. The parameters for GRB 990123, GRB 990510, GRB 991216 are taken from Panaitescu & Kumar (2001). There they state that the number of observables is less than the number of variables (ν_{sa} is usually not covered by the data), which introduces uncertainty in the derived parameters and does not allow to set proper constrains. GRB 991208 does not have a jet break (a requirement imposed by their fitting procedure), ν_c or ν_{sa} are not detected, and additionally it has a $p < 2$ which introduces more unknown parameters. Therefore the results for this afterglow are highly uncertain and, as they mention, only describe the data in a limited time interval. The last GRB 000926 has broad-band data set, however their model proved to be worst than the one proposed by Harrison et al. (2001). They themselves say that the results for these last three GRBs should only be taken as limits. As a conclusion, although it could be a useful numerical approach to set limits on the afterglow parameters, strong constrains are difficult to take out from their results.

Cenko et al. (2010, 2011) uses a similar method as Panaitescu & Kumar (2002) and applied it to seven GRBs. However, the data for GRB 090920B, GRB 09026A and GRB 080319B can only be modelled if ε_B is set to 0.33. Therefore I do not include this in the comparison with the analysis presented in this thesis. The four GRB left, GRB 050820A, GRB 060418, GRB 090323

and, GRB 090328, will be called the *Cenko sample* here after. The stellar wind-like density profile is the best fit for 3 out of the 4 GRBs, assuming all the GRBs are collimated. GRB 050820A data are best fitted with an ISM density profile. Although, the radio data is not well described by this model, unless the outflow is an spherical outflow, which would not be consistent with the optical and X-ray observations. Furthermore, the radio light curve shows a break after about 30 days, which suppoert the collimated outflow as the break is observed around the same time in the other bands. However, the radio flux is constant through out the observations, if ν_{sa} is below radio, this temporal evolution implies a stellar wind-like density profile, which is in contradiction with their results. Therefore, the derived values are not in agreement with the closure relations. GRB 060418 has ν_c below optical data and the radio data is not good enough to constrain the CBM profile. They prefer a stellar wind-like density profile over an ISM because there is no need to fix ε_B to 0.33, but they make it clear that it is not a strong constrain. Even more, there is only a lower limit for A_v^{host} which implies that β is not well constrained. GRB090323 the main restriction for this burst is the break time (required by their fitting procedure). There is no detection of a break in optical or X-rays, so they assumed it can be constrained by the radio data. However there is no strong break in the radio data at around 20 days where they expect the jet-break. GRB 090328 is, apparently well described by a model with a stellar wind-like density profile. Although, they say that the data quality is poor and the values does not set strong constraints on the parameter space. From the facts stated above, I considered that only GRB 090323 might be a well describe afterglow by the model, even though the unconstrained A_v^{host} could change the results.

Besides the sample papers mentioned above, in the literature there are analysis for three special GRBs: GRB 980703 (Frail et al. 2003), GRB 000926 (Harrison et al. 2001) and GRB 030329 (Resmi et al. 2005). These GRBs have broadband data with a coverage of all the break frequencies without the need of extrapolations of the fluxes or any additional assumptions and, they have measurements of the individual redshifts. GRB 000926 is associated with an ISM density profile with a dominant IC contribution. GRB 980703 can be explained by either an ISM or a stellar wind-like density profile. GRB 030329 is associated to the SN 2003dh (Stanek et al. 2003) and so it would have been expected to be uniquely associated with a stellar wind-like density profile. However, the best model describing the data is a double-jet outflow (narrow and wide jet) expanding into an ISM density profile (Resmi et al. 2005). This ISM density profile is at odds with the expected stellar wind-like density profile. Even though there is no unique model in the literature for this burst (e.g., Willingale et al. 2004; Frail et al. 2005), I include this burst in the discussion for one special reason: it shows the importance of the broad-band analysis. This is clearly seen in the analysis presented by Resmi et al. (2005), where, even for such a complex data set (e.g., re-brightening in the LC, SN contribution, high ISS contribution, jet break, transition to a non-relativistic phase), a broad-band analysis, where all the break frequencies are clearly detected, led to a "unique best model" (χ^2/d.o.f=23.3) describing almost-all the data set. Even more, it shows the complexity of the afterglow emission and the need of additional components to the standard model to describe all the observations.

The total sample of afterglow with broad band observations in the literature is therefore 12, however, only 3 have have an analysis that did not require additional assumptions or excluding observations. From those 3, 1 is uniquely associated to a stellar wind-like density profile (GRB 090323), 1 to and ISM density profile (GRB 000926) and 1 is equally described by either ISM or stellar wind-like density profiles. Here I include 4 GRB that are uniquely associated to a stellar wind-like environment. I divide two groups, *group A* composed by a total of 7 GRBs, the 4

GRBs presented in this thesis and 3 additional GRBs from the literature with broad-band analysis without further assumptions. The rest of the GRBs (9/16) with broad-band analysis with additional assumptions are in *group B* (see Table 8.5). From the GRBs in *group A*, 6 out of 7 afterglows are clearly identified to be expanding into a CBM with a stellar wind-like density profile, while only 1/16 GRB is associated with an ISM density profile. For *group B*, 4 out of 9 GRBs are associated to a stellar wind-like density profile, while 5 out of 9 GRBs are associated to an ISM density profile. It would be incorrect to make a strong statement such as that all GRBs are associated to a stellar wind-like profile based on these the results. However, the fact that 6 our of 7 GRBs are uniquely identified with a stellar wind-like density profile, shows that the large percentages ($> 50\%$) of GRBs associated with an ISM profile based only on data for individual bands, might be deviated. Even though these analysis provide useful limits on the CBM profile, broad-band analysis are required to set a final statement on the GRB environment (as for GRB 121024A presented here). Furthermore, early light curves, especially in the radio wavelengths are expected to be highly dependant on the density profile and thus can provide valuable information on the CBM profile.

Table 8.5: GRBs presented in the literature with a broad-band analysis. GA stands for *group A* and GB stands for *group B*. GA are those GRBs that were analysed without any additional assumptions and the model describes the data. *group B* are those GRB presented in the literature that have additional problems with the modelling. Details are given in the text. [a] The GRB 980703 is well described by both and ISM and stellar wind-like density profiles. I use the stellar wind-like profile as it is supported by theoretical expectations. [b] Two values are given for each parameter: narrow jet and wide jet (GRB 030329). [1] Panaitescu & Kumar (2002). [2] Cenko et al. (2010, 2011). [3] Frail et al. (2003); Harrison et al. (2001); Resmi et al. (2005).

Sample	# GRBs		CBM		p		ε_e	ε_B	$E_{K,iso}$	A_*	n_0	θ_0
	GA	GB	ISM	Wind	(1,2)	>2	$\times 10^{-1}$	$\times 10^{-3}$	$\times 10^{52}$ [erg]	[g cm^{-1}]	cm^{-3}	[deg]
PK[1]	—	5/5	3	2	3	2	0.1-1	0.7 - 60	0.01 - 0.03	4 - 18	0.001 - 22	2 - 8
Cenko[2]	1/4	—	—	1	0	1	0.7	8.9	116	0.1	—	2.8
	—	3/4	1	2	1	2	0.6 - 1.3	0.02 - 150	0.12 - 537	0.26 - 0.35	0.18	4 - 22
BB[3]	2/3	—	1[a]	1	0	2	1 - 7	1.8 - 8.0	12 - 18	1.42	27	8 - 17
	—	1/3	1	—	0	1	5.6, 0.9[b]	0.4 , 1.2[b]	0.14 , 0.11[b]	8.6	—	6.2 , 23.3[b]
Here	4	—	—	4	1	3	> 3	0.08 - 100	0.8 - 10	1 - 40	—	8 - 25

8.2.2 Dynamical and microphysical parameters

If the afterglow standard model accounts properly for all the physical processes regarding the afterglow evolution and emission, there should be a universal set of parameters that describe all the GRB afterglow observations (Yost et al. 2003). This set of parameters should depend only on the shock Lorentz factor. However, the measurements of the afterglow parameters so far do not show any sign of universality. The measurement of the parameters is possible based on the correlation between the afterglow parameters and the observed spectral (SED) features of the afterglow emission (i.e., break frequencies and break flux). Therefore in order to measure all the parameters, it is indispensable to have a high-quality multi-epoch broad-band wavelength observations of each GRB afterglow.

The excellent coverage in time and wavelength of the data sets presented in this thesis allow me to determine a set of parameters that can described the observations of the afterglow of every specific event. The break frequencies used for the derivation of the afterglow parameters are

measured after the end of the energy injection phase. At the given time interval, a uniform non-spreading jet break has already started for the four GRBs. Because the jet is not spreading yet, the formalism based on the self-similar evolution for an ultra-relativistic blast wave expanding into a cold external medium (Blandford & McKee 1976) is still valid. The results of the behaviour of the parameters throughout the time of the microphysical and dynamical parameters are presented in Fig. 8.1. I used the derived afterglow parameters to determine some of the main quantities related to the afterglow physics, i.e., magnetic field B, mass loss rate $\dot{M}_{\rm W}$, energy conversion efficiency η and half-opening angle θ_0. The temporal behaviour of this quantities is shown in Fig. 8.2. The best fit temporal slopes for each of the derived quantities, assuming a single power-law model, are given in Table 8.6 and Table 8.7. A discussion on the different parameters is given in the next paragraphs.

Table 8.6: Temporal slopes (α) using a simple power-law fitting profile $Q(t) \sim t^{-\alpha}$, where Q stands for the different microphysical and dynamical parameters.

SED	$\bar{\varepsilon}_{\rm e}$	$\varepsilon_{\rm B}$	A_*	$E_{\rm K,iso}$
GRB 100418A	-0.14±0.06	0.20±0.11	0.02±0.05	0.22±0.12
GRB 110715A	0.06±0.04	0.04±0.06	-0.05±0.07	0.06±0.05
GRB 130418A	0.20±0.04	-0.29±0.03	0.33±0.04	0.09±0.03

Table 8.7: Temporal slopes (α) using a simple power-law fitting profile $Q(t) \sim t^{-\alpha}$, where Q stands for the different secondary parameters.

SED	θ_0	η	B	$\dot{M}_{\rm W}$
GRB 100418A	0.05±0.03	0.21±0.12	0.81±0.05	0.02±0.05
GRB 110715A	-0.03±0.02	0.05±0.03	0.78±0.04	0.04±0.07
GRB 130418A	0.06±0.03	0.06±0.03	0.67±0.04	0.33±0.03

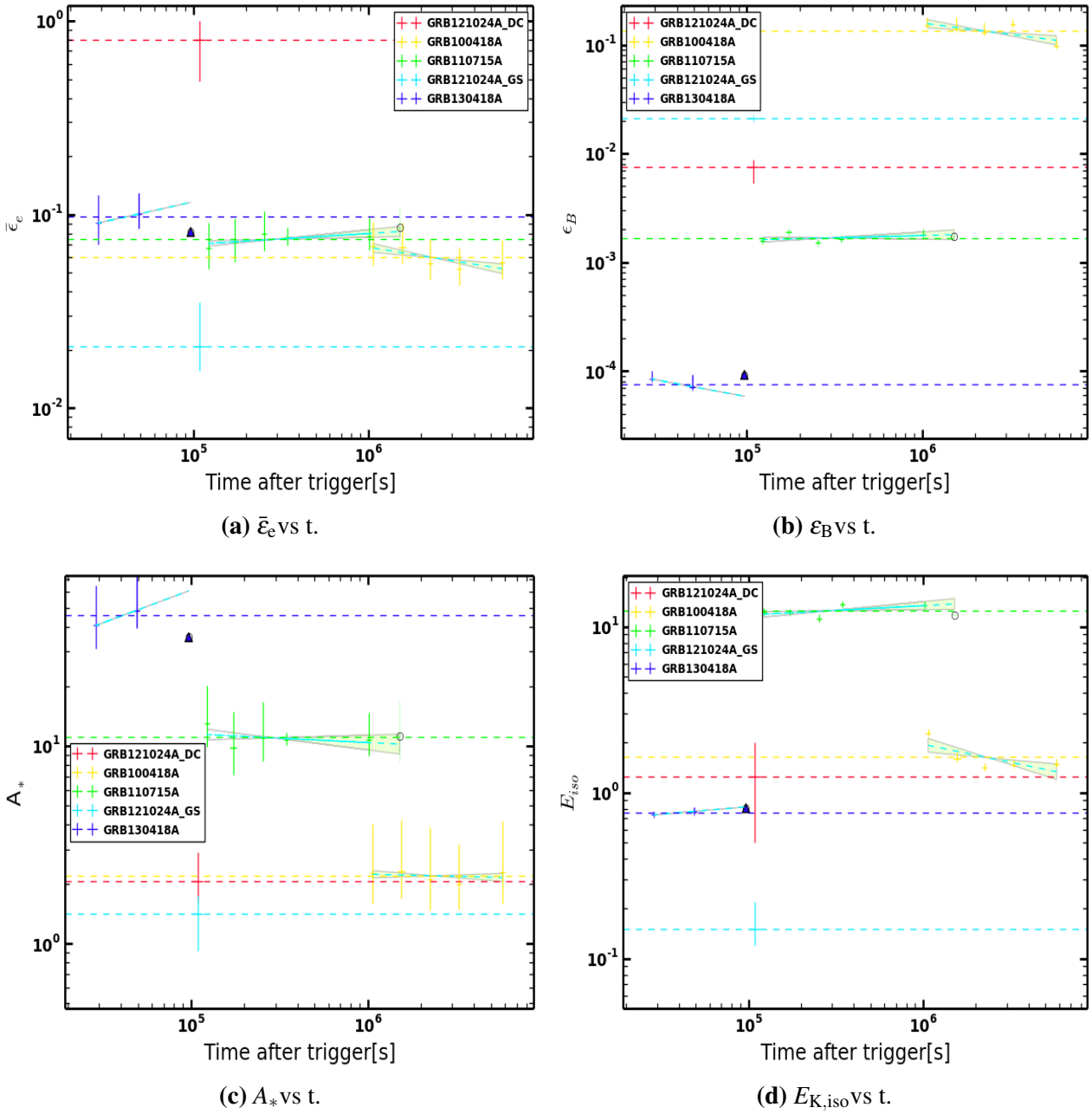

(a) $\bar{\varepsilon}_e$ vs t.

(b) ε_B vs t.

(c) A_* vs t.

(d) $E_{\mathrm{K,iso}}$ vs t.

Figure 8.1: Evolution of the microphysical and dynamical parameters of the afterglows of GRB 100418A, GRB 110715A, GRB 121024A and GRB 130418A. The dashed-lines show the average value of each parameter. The dotted lines represent the power-law fit to the data. The fit of two data points (GRB 130418A) does not have an statistical significance and therefore is not used in the study. The two epochs of GRB 130418A are in complete agreement with the average value and, are therefore consistent with being constant. $E_{\mathrm{K,iso}}$ is in units of 10^{52} erg and A_* is in units of 5×10^{11} g cm^{-1}

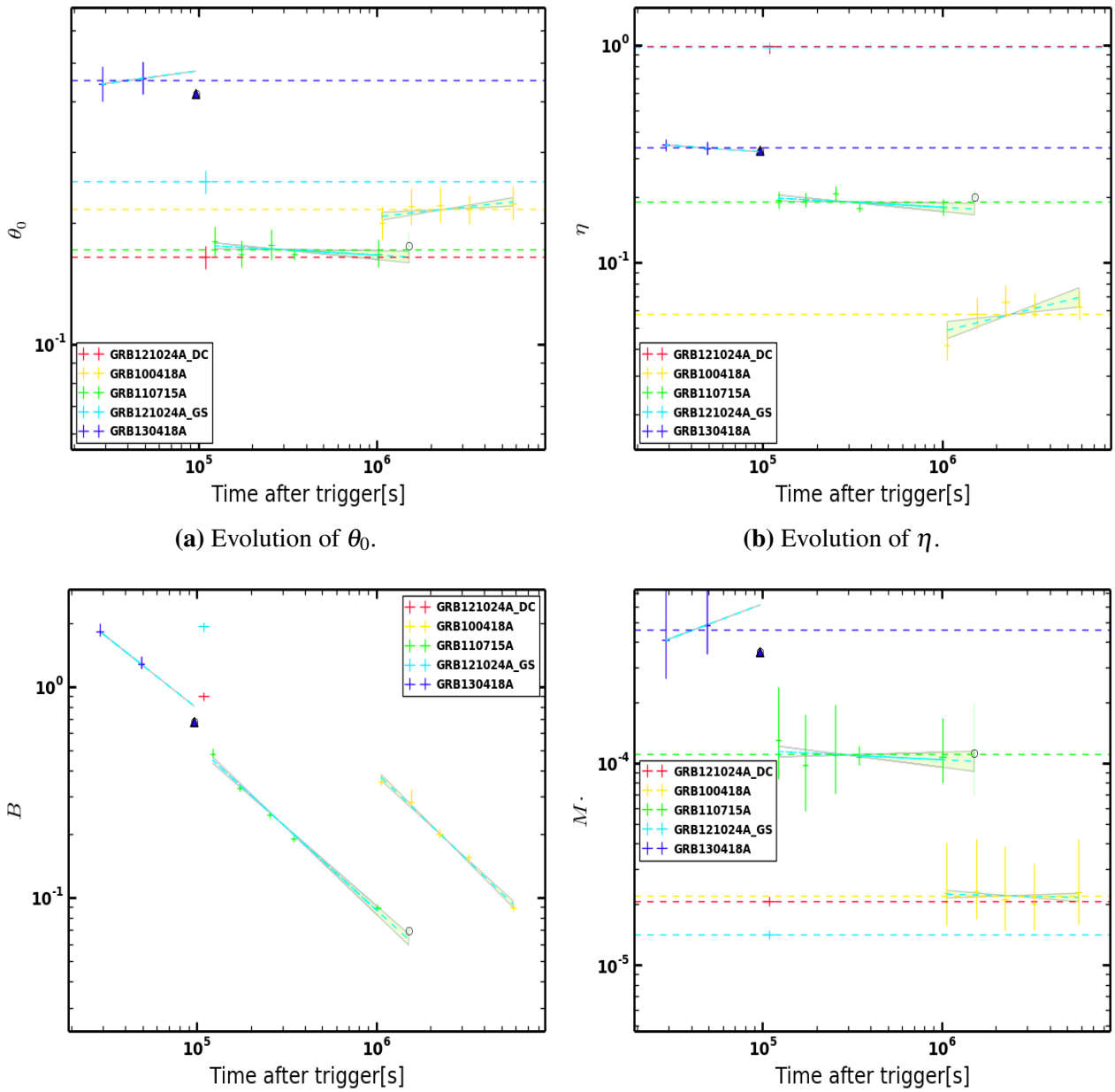

(a) Evolution of θ_0.

(b) Evolution of η.

(c) Evolution of B.

(d) Evolution of $\dot{M}_{\rm W}$.

Figure 8.2: Evolution of the secondary quantities for the GRB afterglow standard model. Afterglows of GRB 100418A, GRB 110715A, GRB 121024A and GRB 130418A. The dashed-lines show the average value of each parameter. The dotted lines represent the power-law fit to the data. The fit of two data points (GRB 130418A) does not have an statistical significance and therefore is not used in the study. The two epochs of GRB 130418A are in complete agreement with the average value and, are therefore consistent with being constant. B has a slope -3/4 as expected from a magnetic field amplified by shock compression. θ_0 is in rad, B is in G and $\dot{M}_{\rm W}$ is in units of $M_\odot$ yr^{-1}.

Acceleration mechanism

Collisionless shocks are expected to be one of the main places to produce particle acceleration in the Universe. GRBs are a perfect laboratory to test this process under extreme conditions. The acceleration mechanism of the electrons during the external shock in a GRB is expected to be diffusive shock acceleration, i.e., Fermi acceleration (Fermi 1949; Blandford & Ostriker 1978; Achterberg et al. 2001). The details of Fermi acceleration are poorly understood and constraints on the parameters are non-existent (Kirk et al. 2000; Sagi & Nakar 2012). The energy spectrum of the accelerated particles is predicted to have a power-law behaviour, with slope p. The slope's value is not known. In an ultra-relativistic regime, p depends on the ratio between the initial and final particles's energies and, on their escape probability (details in Chap. 2). The power-law slope will have a value in a range between 2.2 to 2.3, assuming a mean energy gain proportional to the Lorentz factor of the shocked fluid ($0.9\ \gamma^2$) and a escape probability of 0.5 (Achterberg et al. 2001). Values for p between 1 and 2 have been inferred in some previous GRB analysis When $1 < p < 2$, the energy of the shocked region is dominated by high energy particles even though most of the accelerated particles lie at the low-energy end. More over, the total energy of the shocked region diverge, unless an upper-cut in the Lorentz factor of the accelerated particles is introduced (Dai & Cheng 2001). These results are not expected in Fermi acceleration, in which both the number of particles and energy in the shocked region are dominated by low-energy particles (Sironi & Spitkovsky 2011).

Alternative particle acceleration processes that can lead to a non-thermal population of electron have been proposed. Sironi & Spitkovsky (2011) presented an acceleration mechanism previously discussed by Lyubarsky (2003), that is based on particle acceleration in a stripped wind. In this scenario, the hot plasma has stripes with magnetic fields of opposite polarities are compressed in the shock process. During the compression, the opposite magnetic fields in the stripped winds are annihilated and the resulting energy is transferred to the charged particles in the shocked region, this is known as *driven magnetic reconnection*. This process could lead to power-law distribution of the energy of the accelerated particles with slope p in the range $1 < p < 2$ and, when the magnetisation of the source is not strong enough the magnetic reconnection will not take place and the acceleration process will be a Fermi acceleration, with electron index $p > 2$.

Observationally, the value of p is related to SED slope above the cooling break. Curran et al. (2010) presented a sample of 300 GRB X-ray afterglows and showed that p has values between 2.1 to 2.4 for the different bursts. Zhang et al. (2007) and Kann et al. (2010) used samples based on X-ray data and as a result, more than 50% of the afterglows has $p < 2$ when $\nu_c < \nu_{XRT}$. The sample presented in Greiner et al. (2011) contains 39 GRB afterglows with optical and X-rays data. 11 out of the 39 afterglows, with the cooling break between the optical and X-ray bands, have a derived value of $p < 2$. Curran et al. (2009) shows that 5 out of 10 of the X-ray and optical afterglows of their analysis have a p value smaller than 2. The broad-band analysis (see Table 8.5), presented in the *PK sample* shoes that 3 out of 5 GRBs required $p < 2$ (Panaitescu & Kumar 2002). The results for the *Cenko sample* shows that only GRB 050820A requires $p < 2$, i.e., 3 out of 4 GRBs are described by $p > 2$ (Cenko et al. 2011). The three GRBs with broad-band analysis and coverage of all the three break wavelengths, i.e., GRB 980703, GRB 000926 and GRB 030329 (Frail et al. 2003; Harrison et al. 2001; Resmi et al. 2005), are described by a p value larger than 2. Finally, 3 out of the 4 GRBs presented here have a derived p values larger than 2. Therefore for *group A*, 6 out of 7 afterglows are described using $p > 2$ while only 1 requires $p < 2$. In the case of *group B* 5

out of 9 afterglows requires p > 2 while the other 4 are explained by p <2.

As of now, the mechanism of acceleration of the particles remains unclear. Even though the well describe data set for the GRB afterglows of *group A* suggest a p > 2, larger samples based on X-ray and/or optical data suggest that large fraction (> 50%) of afterglows requires p values much smaller than 2. Possible reason for this discrepancies between the broad-band and X-ray/optical analysis might be:

- A mis-interpretation of the power-law segment in which the observing frequency is located.
- Additional component to the synchrotron spectrum, such as a strong IC component, a prolonged energy injection or a geometrical or a spreading afterglow, that change the closure relations above ν_m and ν_c.
- Additional emission in the X-ray band from inverse Compton scattering from the electrons with the photon in the CBM medium (Dermer & Atoyan 2004).

In any case, to test if it is an additional mechanism for acceleration of particles, or an additional mechanism to the dynamics of the model, or simply a proper interpretation of the observed spectrum, what is required, a multi-epoch broad band data analysis to test the different possible scenarios. Here, for example, GRB 121024A could have been described by either a p > 2 or p < 2, if only X-ray and optical data would have been analysed. However, the broad-band analysis allowed the derivation of p = 1.73 as a unique possible value to describe the observations (details on Chap. 4).

Microphysics: ε_e

The microphysical processes in the shocked region are poorly understood and difficult to study. To overcome the uncertainties related to these processes a constant parameter ε_e is introduced. This parameter represents the faction of the energy in the shocked region that goes into the accelerated electrons. The energy that goes into the accelerated electrons, depends on the acceleration process. However, due to the poor knowledge on this acceleration mechanism, an specific model prediction for ε_e is difficult to make. The energy gain in a Fermi-like acceleration process is expected to be twice the initial energy of the particles. However, this gain factor has a high dependence on the escape probability[3] of the electrons (Achterberg et al. 2001). This probability depends on the time of each acceleration cycle and, especially on the strength of the magnetic field in the downstream region and, its efficiency to keep the electrons close to the shock front to help them go back into the upstream region to complete the cycle. This would imply a large uncertainty in ε_e introduced by all the unknown process behind the magnetic field in the shock and the acceleration of particles.

In practice, the determination of ε_e requires broad-band observations as ν_c does not depend on this parameters, and therefore ν_m and ν_{sa} are required to set at least limits on ε_e. Unexpectedly, the values derived for ε_e in the literature, seems to be less scattered than the values for ε_B , A_* and $E_{K,iso}$. The mean value is found to be around 0.2 (Santana et al. 2014 and references therein) with a spread of less than 1 order of magnitude. Studies in the literature use different approaches. If there are not enough data available to derive all the parameters (e.g., Kumar & Piran 2000; Cenko et al. 2010; Laskar et al. 2015), $\varepsilon_e = \varepsilon_B = 0.33$ assuming an equipartition[4] value 0.33 for ε_e (Daigne

[3]This is the probability of the electrons to complete one acceleration cycle.

[4]Equal distribution of the internal energy among the magnetic field, the accelerated electrons and the baryons. There is no physical reason to expect this equipartition.

& Mochkovitch 1998; Kumar & Piran 2000) value. It is also common to set $\varepsilon_e = 0.1$ (Zhang et al. 2007) and even linked the parameters with relations such as $\varepsilon_e = \varepsilon_B$ or ${\varepsilon_e}^2 = \varepsilon_B$ (Medvedev 2006; Leventis et al. 2013). Howver, if an assumption is made on the parameter, there is a strong bias against any kind of test of the model.

The broad-band analysis of the *PK sample* result in values for ε_e between 0.01 and 0.13 for the 5 GRB afterglows. The 3 GRBs of the sample with p < 2 have ε_e smaller than 0.06, while the 2 GRBs with p > 2 have ε_e larger than 0.1. The *Cenko sample* gives values for ε_e between 0.06 and 0.11 for the 3 GRB afterglows in a stellar wind-like density profile and p > 2. For GRB 050820A, ε_e is 013 in an ISM CBM with p < 2. The three GRB with all the breaks detected have derived values of order 10^{-1}. In detail GRB 000926 and GRB 980703 (ISM) have ε_e about 0.3. GRB 980703 has ε_e about 0.7 in a stellar wind-like density profile. GRB 030329 has ε_e about 0.1 for the wide jet and 0.56 for the narrow jet, however, the error bars of the narrow jet are about 0.5, so both jets have a consistent value within 1 σ uncertainty level (see Table 8.5).

In the case of the four GRBs presented here, two of the afterglows have a value for ε_e of about 0.3, p > 2 and energy injection phases (q about 0.2). Another GRB afterglow has ε_e about 0.86, p > 2 and a strong energy injection phase with q = -0.36. The fourth afterglow has ε_e almost of order unity, p < 2 and no energy injection phase. Two important points should be outline here, first, in the case of p < 2 with ε_e about 1, a large uncertainty for this value could have been introduced by the upper-cut γ_M imposed to the energy distribution of the non-thermal population of the electrons (Dai & Cheng 2001; Bhattacharya 2001). If the acceleration process is not Fermi acceleration, but a stripped wind acceleration (or any other process if possible), then the derivation of ε_e is just not accurate. Second, a strong relation between ε_e and the energy injection phase is difficult to state. However, it is observed that for the strongest injection phase, q = -0.36, the value of ε_e is larger than the other cases of energy injection (0.3). A strong energy injection affects the dynamics of the outflow and therefore the radiative processes. When the cooling process undergoes a radiative phase, ε_e is expected to be close to one (Panaitescu et al. 2006). Otherwise if the cooling process is in an adiabatic regime, ε_e is expected to be of order 0.1 or smaller (Sari et al. 1998). Furthermore, the energy in the outflow by the end of the energy injection phase is expected to be much larger (see following discussion on energy injection) than when the decaying phase started, and this can be reflected in the distribution of the energy.

In general, ε_e expands over a range between 0.06 - 1. For *group A* 6 out of 7 GRBs have ε_e larger than 0.3 and only one have a value for ε_e about 0.07 (0.1 within 3 σ) . *group B* has 4 out of 9 GRB with ε_e about 0.06 while 5 out of 9 GRBs have ε_e between 0.1 and 0.3. Finally, n the case of the GRBs analysed here, ε_e is constant through out the time for all the afterglows. This time dependency has not been measured before in an independent way, i.e., by analysing single snapshots at several times, without any linked values among the epochs.

Microphysics: ε_B

A third microphysical parameter is the fraction of the energy that goes into the magnetic field, ε_B. The general relation between ε_B and the magnetic field B is given by $B^2/8\pi = \varepsilon_B e$ (Blandford & McKee 1976; Rybicki & Lightman 1979), where e is the energy density in the shocked region. The origin of the magnetic field is not understood yet, and as a result different mechanisms have been proposed to explain the it. The natural mechanism is the amplification of the magnetic field B_0 in

the CBM interacting with the relativistic outflow due to shock compression. During this process, the density of the shocked region increases by a factor of 4Γ. This change in density results in an increase of the energy density by the same factor. The final magnetic field strength in the shock region is, therefore, given by $B = (32\pi m_p c^2 n)^{1/2}\gamma\ \varepsilon_B$ (Sari et al. 1996). The magnitude of the magnetic field in the CBM is not known. Studies assuming a seed magnetic field, B_0, of order of few μG let to an expected value for ε_B of about 10^{-10} (e.g., (Santana et al. 2014). However, this prediction relies not only on the assumed B_0, but on the density of the CBM. For the afterglows presented here, the magnitude of the magnetic field in the shock region varies between 0.1 to 1 G (see Fig. 8.1b and Fig. 8.2c). This can translates into a strength for the seed magnetic field B_0 of the order of 10 mG. This value of B_0 is much larger than the interstellar field strength commonly used as a reference value. However, there is no reason to expect a magnetic field strength in the CBM of the GRB, specially assuming GRBs are related to massive stars and highly in-homogeneous mediums.

There are other mechanism that have been proposed as an explanation to the origin of the magnetic field in the shocked region. Here I name three of the most studied and naturally expected in shock processes and highly turbulent plasmas. However, the magnetic field generation in hot plasmas remains an open question, not only in GRBs but in different astrophysical events, and therefore several studies can be found in the literature. The only parameter at the moment that can be used to test the different mechanisms is ε_B . However, some mechanisms give similar values for this parameter, so it is not possible to differentiate between all the models.

- A magnetic field originated in the progenitor and carried by the turbulent outflow or the wind from the progenitor up to the shocked region (e.g., Meszaros et al. 1993). B depends on the volume V as $B \sim V^{-2/3}$. If the magnetic field at the surface of the progenitor ($r \sim 10^6$ cm NS) is about 10^{16} G, the expected ε_B at $r \sim 10^{16}$ cm is about 10^{-7} (Medvedev & Loeb 1999).

- The amplification of the seed magnetic field by a magnetohydrodynamic MHD turbulent-dynamo (Meszaros et al. 1993). Zhang et al. (2009) presented three-dimensional simulations and conclude that these mechanism can amplify the seed magnetic field, resulting in ε_B about 5×10^{-3}.

- A two-stream Weibel instability (e.g., Weibel 1959; Medvedev et al. 2005), which is an extension of the Weibel instabilities in a non-relativistic outflow to relativistic plasmas, such as in the case of the outflows in GRBs. This instabilities are caused by currents of charged particles inside the plasma. Two-dimensional simulations shows that values for ε_B in the range between $5 \times 10^{-5}\eta_w \leq \varepsilon_B \leq 0.1\eta_w$ can be achieved, with η_w an efficiency factor that is less than 0.1 (Medvedev & Loeb 1999; Milosavljević & Nakar 2006).

In the case of the four GRB afterglows presented here, it is observed in Fig. 8.1b, that there is no evolution of ε_B, as expected in the standard afterglow model. The results in the literature shows large values for ε_B too. As seen in Table 8.5, the 3 GRB afterglows in the *group A* that are from the literature, have ε_B between $1.8 - 8.9 \times 10^{-3}$. The results for the GRB in this thesis have a wider spread, ε_B takes values between 8×10^{-5} to 0.1. The smallest value (GRB 130418A), might be related to the strong IC contribution to the electron cooling, this implies a low ε_B and large ε_e. Two other afterglows, GRB 110715A and GRB 121024A, have values within the same range as the other GRBs in *group A*. Finally, GRB 100418A has an ε_B about 0.1, which, is within the expected values (< 1). In the case of the *group B* the values for ε_B are on an interval between 10^{-5} to 0.15.

An important and unique result in the analysis of the magnetic field in the shocked region, is the test of the evolution of it. The evolution of the magnetic field for each afterglow is presented in Fig. 8.2c, and details are given in Table 8.7. The evolution, in all cases, follows the predicted evolution for an outflow expanding into a stellar wind-like density profile. More important, it follows the evolution predicted for a magnetic field, which origin is due to shock compression. The evolution of it is given by $t^{-3/(2(4-k))}$ (Blandford & McKee 1976; Rybicki & Lightman 1979). This is an interesting result for two reasons: (1) It has no additional assumptions or linked parameters among the analysed epochs of each afterglow. This implies that the observed evolution relies completely on the derived parameters for each SED and, actually test the evolution of the magnetic field in the shocked region independently. (2) The test of the magnetic field and its amplification usually relies on a value for $\varepsilon_{\rm B}$ at a single epoch, and therefore do not give complete information. With this test of the magnetic field evolution, a hint towards the origin of it is given. Previous analysis have implied that one of the main problems with the results for $\varepsilon_{\rm B}$ is that it implies large magnetic fields (see discussion above). This is based on assumptions of a seed magnetic field similar to the one of the Milky Way. But there is no physical reason to believe this is true. Here I show that the evolution is, in fact, according to just a magnetic field from shock compression, and therefore, the problem might not be the amplification mechanism, but the magnitude of B_0 that is commonly assumed.

Dynamics: A_*

Besides the microphysical parameters, there are two dynamical parameters $E_{\rm K,iso}$ and A_*, used in the parametrisation of the GRB afterglow model. In terms of the density, in Sec. 8.2.1 a detailed discussion on the CBM profile is given. Here, I focus the discussion on the normalisation (A) of the density profile which is a constant parameter in time ($\rho = Ar^{-k}$, k = 2 and A = A_* in a stellar wind-like density profile. k = 0 and A = n_0 for an ISM profile). This normalisation of the density is expected to be of order unity, for both, an ISM and a stellar wind-like density profile (Fryer et al. 2006; Crowther 2007).

The four GRB afterglows analysed here are in agreement with an outflow expanding into a stellar wind-like density profile. GRB 100418A and GRB 121024A have A_* about 1 g cm^{-1}, GRB 110715A has A_* about 10 g cm^{-1} and GRB 130418A has A_* about 45 g cm^{-1}. The measured values are consistent with the expected theoretical values, if the progenitor is Wolf-Rayet-like star. Simulation based on motion and state equation for massive stars (van Marle et al. 2006) shows that A_* can not be lower than 0.01 g cm^{-1}. Now, for typical values of a Wolf-Rayet star, such as a $\dot{M}_{\rm W}$ of about 10^{-5} $M_\odot$ yr^{-1} and a wind velocity $v_{\rm W}$ of 1000 km/s A_*, is expected to be of order unity (Chevalier & Li 2000; Crowther 2007). However, $\dot{M}_{\rm W}$ can be larger by an order of magnitude implying A_* of order 10 g cm^{-1}. The largest value that is derived for A_* is about 45 g cm^{-1} for GRB 130418A which has a dominant SSC stage during the early epochs. This is expected from theory, where A_* has to be larger than 10 for IC to be detected directly in a stellar wind-like density profile (Sari & Esin 2001). As a self-consistency test, I derived all the mass loss rates using a wind velocity of 1000 km/s. The results are presented in Fig. 8.2d and are consistent with the expected values for a Wolf-Rayet star as a progenitor (Chevalier & Li 1999).

From the values in the literature (see Table 8.5), specifically the 12 GRBs from *Cenko sample*, *PK sample* and there 3 afterglow with broad-band analysis (Harrison et al. 2001; Frail et al. 2003; Resmi et al. 2005). The 6 GRB afterglows associated with a stellar wind-like density profile, the

values for A_* range between 0.1 to 18 g cm^{-1}. This values are consistent with the values for the sample I presented here. For the other 6 GRB afterglows associated with an ISM profile, the values for n_0 lie in the range between 0.001 to 27 cm^{-3}. However, an ISM profile is at odds with the expected stellar wind-like density profile from a massive star progenitor. Then 6 out of 7 GRBs in *group A* are associated to a stellar wind-like density profile, with values between 1 to 45 g cm^{-1} f, in complete agreement with the expectations for a Wolf-Rayet star as a progenitor for the GRB. The 1 GRB of this *group A* that is associated to an ISM density profile has a density of 27 cm^{-3} which could have been achieve under some specific stellar evolution models for massive stars, under the assumption that the wind termination shock radius is close enough to the progenitor, that by the time of the afterglow the CBM is already homogeneous (Fryer et al. 2006; van Marle et al. 2006).

Dynamics: $E_{\rm K,iso}$

The isotropic kinetic energy in the outflow $E_{\rm K,iso}$, together with the isotropic energy released in γ-ray $E^{\gamma}_{\rm iso}$, are used to set constraints on the type of progenitor and central engine of the GRB. There are different aspects to be analysed in terms of the energy of the afterglow emission. (1) How fast is the energy injection? The standard model assumes an instantaneous energy injection. However, there has been an increased on the observational evidence pointing towards a prolonged energy injection, i.e., $L(t) = L_0 t^{-q}$ (see Chap. 2). (2) what is the true total energy of the outflow? The ultra-relativistic outflow is expected to be collimated, with an opening angle θ_0. This collimation of the outflow reduces $E_{\rm K,iso}$ by a beaming factor $f_{\rm b}{\sim}{\theta_0}^2/2$, as $E_{\rm K,jet}$= $f_{\rm b}E_{\rm K,iso}$. This is an important feature for the energetics of the outflow. The values for $E_{\rm jet}$are usually in a range that can be obtained by physical processes from progenitors that are already known (i.e., massive stars under specific circumstances). (3) What is the efficiency[5] η of the conversion of thermal energy into γ-ray radiation? This has been a highly debated topic on GRB physics and is still not well understood. In this subsection I focus the discussion on this last question related to η. The discussions for questions (1) and (2) are given later in the chapter.

Theoretical analysis on the efficiency in GRBs show that η should be lower than 15% (Kobayashi et al. 1997; Daigne & Mochkovitch 1998; Fan & Piran 2006). However, the measured efficiency values are extremely large, going as far as 100%. The reason for these large efficiencies is currently unknown, but some hypothesis on this problem has been made.

- It can be related to the method used in the derivation of $E_{\rm K,iso}$, e.g., not a good quality data or too many additional assumptions.
- It could also be related to the energy that is carried away by neutrinos (Kumar 1999) that do not allow to measure the actual $E_{\rm K,iso}$ of the outflow.
- It might be affected by the prolonged energy injection phase. $E_{\rm K,iso}$ should be measured just when the deceleration phase starts. This deceleration phase is assumed to be before the injection phase, however $E_{\rm K,iso}$ is commonly measure at late stages of the afterglow evolution (Fan & Piran 2006; Zhang et al. 2007).

[5]Efficiency of the conversion of the kinetic energy in the outflow to gamma-rays during the prompt emission η=$E_{\rm K,iso}/(E^{\gamma}_{\rm iso}$+$E_{\rm K,iso})$. $E^{\gamma}_{\rm iso}$ is the isotropic energy released in the prompt gamma-ray emission. It is calculated using $E^{\gamma}_{\rm iso}$=$4\pi d_{\rm L}^2 {\rm F}/(1+{\rm z})$, where F is the fluence in the gamma-ray band. BAT: from $15-150$ keV in the observer-frame. $E_{\rm K,iso}$: energy range $1-10^4$ keV in the rest frame.

There are two issues with this last argument: first, the efficiency will increase if $E_{\rm K,iso}$ is decreased, as suggested by the statement, therefore instead of solving the problem it will make it worst. Second, it is difficult to measure $E_{\rm K,iso}$ before the energy injection phase. In order to do this, radio observation are required during early stages of the afterglow, i.e., before $10^3 - 10^4$ s. However, the observations in radio either start during the late stages of the afterglow, or only provide upper limits during these early phases (t < 1000 s). The reason for the upper limits is that the radio flux is usually too low during the start of the afterglow phase and is expected to increase with time (opposite to X-ray and optical emission) (Ghirlanda et al. 2013).

Three out of the four GRB afterglow analysed here, have $E_{\rm K,iso}$ of order 10^{52} erg, The fourth afterglow, GRB 110715A, has $E_{\rm K,iso}$ one order of magnitude larger than the others. This last GRB, has the largest value of q and therefore the injection of the energy was stronger and, as expected, larger than the other GRBs. The exact time when the deceleration ($t_{\rm dec}$) phase starts is not known. I assumed it to be the time where the plateau phase starts. Using this time, the time of the end of the plateau phase ($t_{\rm inj}$) and the values reported in Table 8.8, I derive the ratio $E_{\rm K,iso}(t_{\rm dec})/\ E_{\rm K,iso}(t_{\rm inj})$ = $(t_{\rm dec}/t_{\rm inj})^{1-q}$. I found that the ratio is about 0.03, 0.3, 0.5 and 0.4 for GRB 100418A, GRB 110715A, GRB 121024A and GRB 130418A, respectively. This ratio implies that the energy actual $E_{\rm K,iso}$is less than half the value measured after the energy injection phase. However, only for RGB 100418A the initial energy can be assumed to be negligible (as usually assumed in the energy injection theory), while it should not be neglected for the other GRBs. Furthermore, these ratios imply that all the efficiencies are larger than the ones presented in Fig. 8.2b that were derived using $E_{\rm K,iso}$ after the energy injection phase. Actually, the values for η will be 80% for GRB 100418A and GRB 130418A, 50% for GRB 110715A and about 95% for GRB 121024A. Similar values for the ratio $E_{\rm K,iso}(t_{\rm dec})/\ E_{\rm K,iso}(t_{\rm inj})$ has been found by Panaitescu (2005). And, the increment in η was also observed in the analysis of the 31 afterglows using X-ray data presented by Zhang et al. (2007), where the η change from being 1% to be about 90%. However, this is just a qualitative statement as the ratios and change in η are highly dependant on the deceleration time and lasting of the plateau phase.

The true efficiency is therefore not known. A a general remark I point out two facts: first η is almost 100% only for GRB 121024A (both, before and after the energy injection phase). The reason is unknown, however, a large uncertainty factor is related to the imposed upper limit $\gamma_{\rm M}$due to the hard-electron spectrum for this burst, i.e., p = 1.73. The introduction of $\gamma_{\rm M}$implies larger dependencies on the p value for the afterglow parameters. Additionally new correlations between the afterglow and the beak frequencies are introduced. This high value for η has been seen before, e.g., more than 50% of the sample in Zhang et al. (2007) have η about 90%, and the sample in Granot et al. (2006) have also η about 90%. The *Cenko sample* has two GRBs with η larger than 70%, while the other two have η smaller than 15%. In terms of the individual GRBs with broadband SED, GRB 030329 has an efficiency of about 6%, while GRB 000926 and GRB 980703 have η about 30%. As a general feature, η for the afterglows presented here are within the energy range expected from the collapsar model (Kumar 1999).

8.2.3 Plateaus and energy injection

The standard model assumes an instantaneous energy injection, although the exact energy injection mechanism is not understood yet. The temporal behaviour in sample of X-ray and optical data have shown that the data deviates from the model predictions. Fast decays and/or plateau phases that do

not follow the closure relations are commonly detected. The canonical (observational) light curve in the X-ray band is presented in Fig. 8.3a (Nousek et al. 2006; Zhang et al. 2006). The plateau phase (segment II) during a time interval between 10^2 s - 10^4 s has been detected in more than 50% of the X-ray afterglow observations. This phase is normally associated to a prolonged energy injection. In the optical bands, there is no canonical light curve (Kann et al. 2010). The general behaviour is just a decaying phase as seen in Fig. 8.4a. When the observations are deep enough, a contribution from the host might be detected and a flattening in the LC is observed, as in Fig. 8.4b. However, with the introduction of earlier observations in the optical bands, there is an increase in the detection of the optical plateau phases (e.g., Panaitescu 2005).

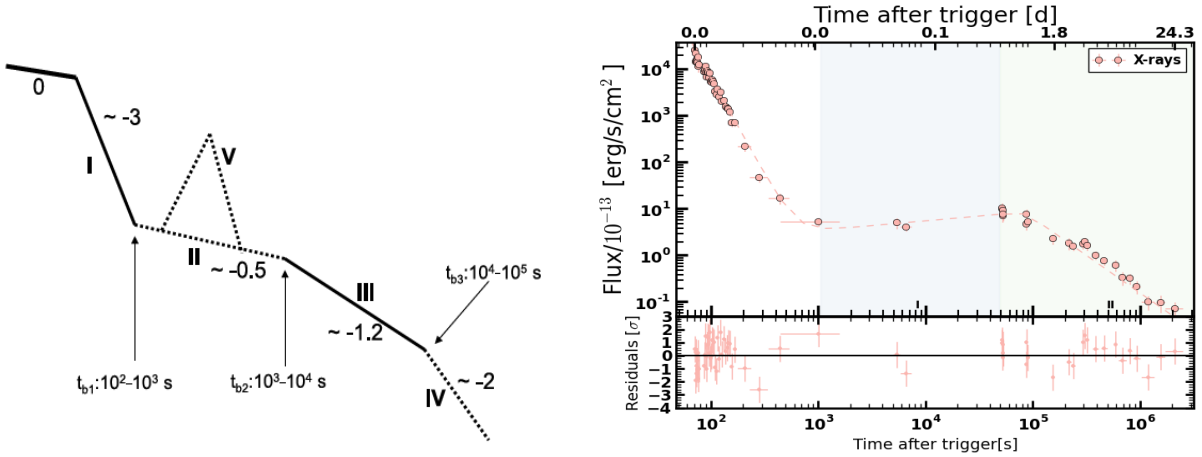

(a) Canonical X-ray light curve. **(b)** X-ray light curve GRB 100418A.

Figure 8.3: Left: X-ray light curve presented in the sample by Zhang et al. 2006. More than 50% of the afterglows in the sample have a plateau phase. **Right**: X-ray observations of the afterglow of GRB 100418A (see Chap. 5).

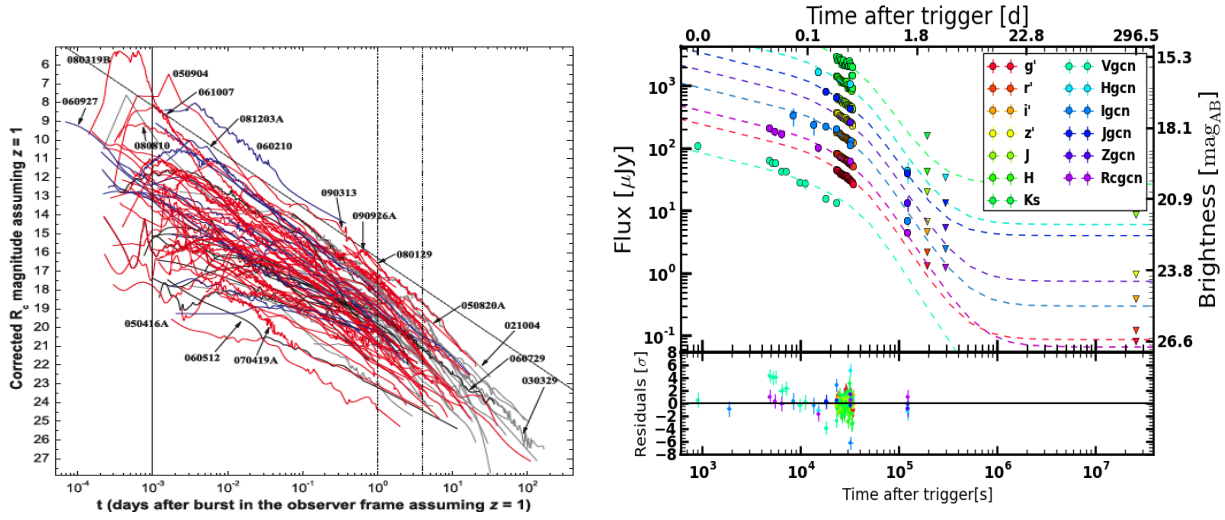

(a) r' light curve. **(b)** Optical/NIR light curve GRB 130418A.

Figure 8.4: Left: Sample of optical r' band light curves presented by Kann et al. (2010). **Right**: Optical/NIR light curve of GRB 130418A (Chap. 7).

A simultaneous detection of the plateau phase at all wave-lenghts, implies a dynamical origin for the change in the temporal evolution of the afterglow emission. A suitable explanation is a strong energy injection phase which can affects the dynamics of the outflow (Rees & Mészáros 1998; Sari & Mészáros 2000). Besides the X-ray and optical plateau phases, prolonged energy injection phases have been detected in sub-mm and radio data (e.g., Jóhannesson et al. 2006; Moin et al. 2013). Broad-band observations of the energy injection phase are important in the analysis. Those broad-band observations assure that other effects, such as flares (e.g., Dai & Lu 1999; Leventis et al. 2014), ISS (e.g., Galama et al. 1998c) or even SSC emission (e.g., Harrison et al. 2001), will not be mis-interpreted and assumed to be an energy injection phase, or vice-versa.

The energy injection mechanism has not been uniquely established yet, but the temporal evolution of the luminosity during prolonged injection is phase by $L(t) = L_0 t^{-q}$, with q the injection parameters and L_0 the initial luminosity. The injection parameter, q, is the inferred parameter during the analysis as in the one that provided the information about the mechanism that might produce the prolonged energy injection. The energy injection mechanism depends on the type of the progenitor and the properties of the central engine. Three main mechanisms have been proposed (Sari & Mészáros 2000; Zhang & Kobayashi 2005):

- A Poynting flux dominated outflow. In this model, the progenitor is associated to a magnetar and a constant luminosity, implying q = 0 (Dai & Lu 1998a, 2000). This model requires a long-lived central engine.

- Mass stratification: it is based on the stratification of the shells in the outflow due to different velocities, i.e., $M(\gamma) \propto \gamma^{-s}$. They will collide between each other causing the additional injection of energy during the afterglow evolution (Rees & Mészáros 1998). The slope s is related to the injection parameter q (Zhang et al. 2006; Pe'er & Wijers 2006). As long as s > 1 the dynamics of the outflow are altered and as a result an energy injection phase could produced. In this scenario a long-lived central engine is not required.

- Relativistic reverse shock: The afterglow phase is associated to dual shock system that is formed during the external shock. This system has a relativistic and dominant forward shock emission and, a negligible reverse shock emission. However, if the reverse shock is strong and relativistic, it could be observed as an energy injections phase (Kobayashi 2000; Laskar et al. 2013; van Eerten 2014).

In this study three of the analysed GRBs have a prolonged energy injection (see Table 8.8). They have plateau phases up to 50-80 ks in the observer's frame. GRB 100418A has plateau phase in both optical and X-ray bands. The slopes of the optical and X-ray plateaus are different, but consistent with each other within a 3σ level. A likely explanation for the slope difference can be associated to an X-ray flare. The available data do not allow to measure the strength of the flare and therefore it is not analysed independently. Due to the lower uncertainty in the slope of the optical plateau phase, I use this value to derive the injection parameter q. GRB 110715A only have an X-ray plateau phase, because the optical observations started after the energy injection phase. GRB 130418A has an optical plateau phase but not X-ray one, however it still can be associated with an energy injection contribution. The X-ray data in not describe by either, the standard model or the energy injection contribution. It can be explained by a strong SSC contribution to the cooling of the electrons, that affects the temporal and SED behaviour. This SSC contribution explains: (1) the fast decay in the LC instead of a plateau phase as in the optical bands. (2) The flat SED slope

($\beta_{XRT} < \beta_{opt}$) in the X-ray wavelength (Sari & Esin 2001). I therefore use the optical temporal and SED slopes to derive the injection parameter[6].

Table 8.8: Temporal slopes α and break times for the four GRBs analysed. (o) : optical, (x) : X-ray bands.

GRB	α_1	α_2	α_3	t_{b_1} [ks]	t_{b_2} [ks]
GRB 121024A	–	0.86 ± 0.05	1.47 ± 0.03	–	49.8 ± 5.1
GRB 100418A	x: 4.16 ± 0.08	x: 0.11 ± 0.05	1.46 ± 0.04	0.62 ± 0.08	76.4 ± 2.7
		o: 0.36 ± 0.04			
GRB 110715A	x: 1.55 ± 0.06	x: 0.33 ± 0.12	1.48 ± 0.05	21.4 ± 1.4	52.7 ± 2.3
GRB 130418A	x: 1.11 ± 0.14	1.11 ± 0.14	2.40 ± 0.19	18.8 ± 3.5	61.7 ± 8.1
	o: 0.31 ± 0.08				

The results for the injection parameters for each afterglow are presented in Table 8.9. The results for the three afterglows are consistent with an $q > 0$ and $s \ll 1$. This values for the injection parameter are consistent with either a mass stratification model or with a long-lived central engine with a relativistic reverse shock. The first scenario is preferred over the relativistic reverse shock based on two main reasons: first, a long-lived central engine, capable to produce a plateau phase of more than a few 10^4 s is difficult to produced by any known astrophysical sources (progenitor). Second, the reverse shock emission is expected to be dominant only in the early stages. Even more, if it is strong enough to change the dynamics of the outflow, a signature of this RS should be observed at low frequencies. Here, however, there is no detection of a RS in the radio data.

Table 8.9: Spectral slopes β , injection parameter q and electron index p for the analysed afterglows. (o) : optical, (x) : X-ray bands. In the case of GRB 100418A and GRB 130418A the final q values corresponds to the optical one. Details on the difference between the optical and X-ray values are given in the text.

GRB	β	q	p
GRB 121024A	0.86±0.02	0.52±0.07	1.73±0.03
GRB 100418A	1.11±0.02	o:0.23±0.04	2.22±0.04
		x:0.00±0.05	
GRB 110715A	1.05±0.01	-0.36±0.15	2.10±0.02
GRB 130418A	x:0.58±0.11	x:0.88±0.16	2.32±0.14
	o:1.16±0.07	o:0.14±0.10	

The Poynting flux dominated outflow mechanisms is discarded for GRB 100418A with a confidence of more than 5.75σ (based on the q value). For GRB 110715A, it is possible within a 3σ level. Though, the magnetar model can, at most, produce a flat slope in the LC (Dai & Lu 1998a, 2000), so the increasing flux in the LC of GRB 110715A makes this model unlikely. The magnetar model would be a possibility with less than 2 σ for GRB 130418A. Based only on the injection parameter q, is difficult to differentiate between the energy injection mechanisms for GRB 130418A. The magnetar model should be able to produce the GRB and the associated SN. So a frequently used argument against a magnetar model is based on the energy restrictions, although the maximum energy depends on the assumptions for the magnetar model (magnetic field, spin-down times). For example, Cano et al. (2016) suggest that the magnetar model under-predict the SN flux by a factor > 7. Lü & Zhang (2014) analysed a large sample of X-ray afterglow and, fixing ε_B= 0.01 and ε_e=0.1, derived an average E_{jet} of about 5×10^{52} erg, which, is just on the upper limit

[6]Table 8.9 have the q values for both, α_{opt} and α_{XRT}, for completeness of the discussion.

for the magnetar energy (e.g., Dai & Lu 2000). Recently, Metzger et al. (2015) shows that the maximum energy from the magnetar model can be about 10^{53} erg. Therefore a strong argument in the case of GRB 130418A for a preferred energy injection mechanism is difficult to be made.

The afterglows presented in the *Cenko sample* do not have an energy injection phase. The three GRBs with broadband observations do not have a plateau phase detection either. Five out of nine afterglow in the sample presented in Panaitescu et al. (2006) could be described including an energy injection phase (only X-ray LC). The values for the q parameter (lower limits) are all in agreement with a stratification of the mass shells as a possible explanation and, are consistent with an in-homogeneous density profile. It is interesting to see that the GRBs with energy injection in my sample and Panaitescu et al. (2006) sample are associated to a stellar wind-like density profile. It is not possible to give an strong statement such as that all the GRBs with a prolonged energy injection phase are evolving into an in-homogeneous density profile, or vice-versa. It would be interesting to do a systematic study with broadband observations to test this correlation. Especially because broad-band data allow to uniquely identify the model for the GRB afterglow emission. For example, in Panaitescu (2005); Panaitescu et al. (2006) each GRB is associated to different models, such as energy injection or jet breaks, and due to the lack of submm and radio data, no final model can be chosen. Here, in the case of GRB 121024A it was shown that without radio and submm data, an energy injection model was a possible explanation to the data. However, when the radio data was included and the parameters derived, the energy injection model was excluded due to the unphysical model parameters, i.e., $\varepsilon_e > 1$.

8.2.4 Jet-break

The measured isotropic energies, in both the GRB and the afterglow phases, are extremely large (up to 10^{54} erg). An association of the GRB with a given progenitor and a central engine, based on known astrophysical objects and processes, is difficult to achieve due to the severe constraints set by the extreme energy requirements (Rhoads 1999). If the outflow associated to the GRB is collimated, these energy requirements will not be too extreme. Indeed, the collimation of the outflow implies a reduction of the observed isotropic energies ($E^{\gamma}_{\rm iso}$, $E_{\rm K,iso}$) by a beaming factor $f_{\rm b} \approx \theta_0{}^2/2$. Therefore, the true energy of the outflow, i.e., $E_{\rm K,jet}$+$E^{\gamma}_{\rm jet}$, is reduced by at least two orders of magnitude (Granot et al. 2006). For example, GRB 971214, GRB 980703 and GRB 990123 (Panaitescu & Kumar 2002) have to be collimated, otherwise the observed energy (up to 10^{53}) is not consistent with being extracted from a massive star (Kumar 1999). The collimated (jet) nature of the outflow is expected to be evident once $\Gamma \propto \theta_0^{-1}$, when the outflow is not ultra-relativistic anymore. When the outflow reaches this condition, two main effects associated with the jet are observed. The geometrical effect, when the edge of the jet becomes visible, but all the energy of the outflow remains contained within the initial half-opening angle θ_0 , i.e., not sideways spreading. And, the sideways spreading of the outflow, where the energy of the jet is not beamed anymore. The dynamics of the jet are unaffected as long as the outflow remains collimated. During this stage, the outflow dynamics can still be treated as in the case of the spherical approximation (Blandford & McKee 1976). A correction to the change in flux due to its faster decrease, by a factor of γ^2, compared to the spherical case is included. The dynamical changes become evident once the jet starts spreading sideways, when the jet becomes sub-relativistic, and later on when the Newtonian phase begins (Granot & Piran 2012).

When the collimated nature of the outflow becomes evident to the observer, there is a change in the observed flux from the afterglow. This change in flux is known as a jet-break. The jet break is expected to be achromatic. The jet-break time, $t_{\rm b}$, is related to the dynamical parameters by $t_{\rm b}\sim(E_{\rm K,iso}{\theta_0}^2/{\rm A})^{1/(3-k)}$ (2.13) (Granot et al. 2005). From an analytical perspective, $t_{\rm b}$ is expected to be sharp, and the sideways spreading is expected to start just at $t_{\rm b}$(Rhoads 1999). However, simulations have that the sideways spreading is delayed respect to the edge effect and the transition is smooth (Dai & Lu 2000; MacFadyen et al. 2001; van Eerten & MacFadyen 2012). The jet break is not easily observed, specially the one associated to the sideways spreading. One of the main reasons is that due to the smoothness of the transition, the break can be confused with other effects, e.g., end of the energy injection phase, or simply the break can be too smooth that is not easy to detect. Kumar & Panaitescu (2000) argue that, the spreading of the jet break, in the case of the edge effect, is about 1 and 2 decades for an ISM and stellar wind-like density profiles, respectively. While for the spreading phase, $t_{\rm b}$can be smeared over 4 decades independent of the CBM density profile.

It is possible to use the closure relations to analyse if there is an evidence of a jet-break. The four GRB afterglows presented here are associated with a uniform non-spreading jet break expanding into a stellar wind-like density profile. The jet-breaks occur in a time interval between 50 ks and 80 ks (Table 8.8) for the four GRBs. Indeed, $t_{\rm b}$ coincides with the time of the end of the energy injection phase (in the case of the three afterglows with energy injection). There is no theoretical correlation between a prolonged energy injection and the opening angle. I assume that measuring the same jet-break and end-of energy injection times, is a result of the smooth transition (2 decades in a stellar wind-like density profile) that overlaps both effects and do not allow to differentiate between the end of one (energy injection) and the start of the other (jet-break edge effect). The measure break time here is earlier than the results from simulations (10^6 s, observers frame e.g., van Eerten & MacFadyen 2012). However, the time from the simulation is highly dependant on the values of $\varepsilon_{\rm B}$, $\varepsilon_{\rm e}$, $E_{\rm K,iso}$ and A_*, and therefore can be shifted by more than two orders of magnitude. Similar values of order 10^4 s have been observed in large sample studies using X-ray observations. Bloom et al. (2003) shows that about 50% of their sample (29 GRBs) have a break time before 1-2 days. Racusin et al. (2009) analysed a large sample of X-ray afterglows (about 230 GRBs) and show that 12% of those GRBs have a clear jet break while other 30% might have a jet break or not. Even more show that at least 60% of the sample can be associated with a jet break between $10^4 - 10^5$ s, but it is usually hidden.

In terms of the actual value for θ_0 , it is expected to be of a few degrees. More than half of the GRBs in the sample presented in Bloom et al. (2003) have θ_0 about 10 deg. Consistent with the observations presented here for three of the GRBs (GRB 130418A have θ_0 about 23 degrees) as seen in Fig. 8.2a. The same results are observed for the GRB sample presented by Berger et al. (2003), where the average value for θ_0 is less than 10 degrees. All this sample are based on X-ray and/or optical data only. The 5 GRBs in the *PK sample* have θ_0 smaller than 10 deg. The *Cenko sample* has three GRB with θ_0 of about 5 degrees and one with θ_0= 22 deg. GRB 000926 has θ_0= 7.8 deg (Harrison et al. 2001), GRB 980703 has $\theta_0\sim$ 15 degrees in both, and ISM and stellar wind-like density profiles (Frail et al. 2003). GRB 030329 has θ_0=6 deg and 23 deg for the narrow and wide jets, in the double jet model (Resmi et al. 2005).

In general, for the 6 to of 7 GRB afterglows in the *group A* θ_0 takes values between 8 to 25 deg, with only 1 out of 7 GRBs with θ_0 about 2.8 deg. In the case of *group B* for 7 out of 9 afterglows θ_0 is between 2 and 8 deg, while for two GRBs θ_0 is bout 23 deg (see Table 8.5). Additionally, there is no evident correlation between the value of θ_0 and the type of the density profile. This is expected based on the fact that the only decisive factor in the dynamics of the outflow should be γ. This is observed in the correlation between θ_0 and $E_{\rm K,iso}$, the more energetic the GRB the smaller θ_0. In general the true energy of the outflow is observed to be about $4 \times 10^{50} - 2 \times 10^{51}$ erg in the sample presented here. Consistent with previous observations, e.g., Fig. 1 (Bloom et al. 2003), but larger than the inferred $E_{\rm jet}$ for the *PK sample* which is of order 10^{49} erg. The study of θ_0 is therefore of vital importance to set the true energy value for the GRBs that allow to set constrains on the progenitor and central engine. Here, our results are consistent with the collapsar model, however, the collimation mechanisms is not possible to distinguish. In the collapsar model the collimation is expected due to neutrino pressure inside the fireball, however, a strong magnetic field could also help in the collimation process. Up to date, this collimation mechanism remains not understood.

8.2.5 Synchrotron-self Compton Scattering - SSC

The contribution from SSC to the cooling of the electrons and therefore to the observed emission is included into the analysis. SSC is expected to be dominant at energies above 10 keV, specially during the early stages of the afterglow evolution (Sari & Esin 2001). In practice this additional cooling effect is usually negligible as the fraction of synchrotron photons that are scattered are low and it is difficult to detect with soft X-ray observations. A direct emission of SSC was observed for GRB 000926 (Harrison et al. 2001). Here 1 out of the 4 afterglows has a direct detection of SSC. As in the case of GRB 000926, $\beta_{\rm opt}$>$\beta_{\rm XRT}$, which in the framework of the synchrotron spectrum is not possible, even if a break frequency between optical and X-ray bands is used. Furthermore, $\beta_{\rm XRT}$ is close to the expected β=1/3 for an SED dominated by SSC and, so does the X-ray temporal slope $\alpha_{\rm XRT}$ = 1.26 that is consistent with an SSC dominated LC when $\nu_{\rm XRT} > \nu_{\rm c}$.

There is a second afterglow, GRB 100418A, in the sample presented here that is expected to have a dominant SSC contribution during the early stages. SSC scattering could be the explanation for the late transition from fast to slow cooling. It lowers the value of the cooling frequency by a factor of $(1+{\rm Y})^{-2}$. Opposite to the expectations, if a strong SSC contribution is included during the fast cooling analysis, the derived $\varepsilon_{\rm B}$ would be larger than 1, which is not possible by physical principles. It is important to mention there is a large uncertainty in the observations during the first two epochs, due to the scattering in the radio observations (ISS effects). This scattering makes it difficult to set strong contraints on $\nu_{\rm sa}$ during this early stages and therefore, on the afterglow parameters during these epochs.

It is then clear that SSC can be a dominant process during the early stages of the afterglow. Even though SSC affects mainly X-ray observations, to set proper limits on the SSC contribution, broad-band observations are required. The reasons for this is that it is necessary to measured $\varepsilon_{\rm B}$ and $\varepsilon_{\rm e}$, and this can only be achieve with multi-wavelength data. It would also be interesting to see the relation between the CBM. Sari & Esin (2001) argue based on the theory of the standard model that a large value of A_* (of order 10 g cm^{-1}) is required to be able to detect the SSC emission directly. This is observed in the case of GRB 130418A which has a A_* of 45 g cm^{-1}. GRB 000926 has also a large magnitude for the density $n_0 = 27$, however the jet is expanding into an ISM density profile.

Late studies f a combined data set of X-ray and LAT data have shown an important contribution of SSC to the obervations. Panaitescu (2017) analysed the data for 24 afterglows monitored by LAT and *Swift* . They conclude that 6 out of 24 GRBs has an evident hard spectra in the energy interval 0.3 - 30 GeV, associated to SSC component. Another 5 our of 24 might also be associated with SSC but the results are not conclusive. Furthermore, he proposed that if the SSC component is strong, the maximum energy of the upscattered photons is above the LAT energy range and therefore Γ can not be calculated. It is an interesting reuslt that 11 our of 24 GRBs can be associated to a strong SSC component. However, they do not distinguished between an ISM or stellar wind-like CBM because $\nu_c$is below the oberving frequency.

8.2.6 Afterglow evolution : Break frequencies

A systematic analysis on the movement of the break frequencies without any additional assumptions is presented here for the first time. The analysis shows that these breaks are evolving as predicted by the model during fast or slow cooling spectral regimes and so do the microphysical and dynamical parameters. These parameters show small deviations from the predicted evolution from the model (or lack of it), but these deviation are no significant within the measured uncertainties. Effects such as ISS contribution to the radio observations are evident and are included in a systematic way when high quality observations over several epochs are taken. Contribution from flares can also affect the observations and give rise to some of the observed deviations (e.g., GRB 110715A) due to the change in the temporal slopes and the flux values. Moreover, it was shown how the use of the broadband observations gives better and stronger constraints on the breaks than when the observations only cover one of the break frequencies. Furthermore, it was evident that the simultaneous fit of the different SEDs of the same GRB afterglow provides even more strong constraints than the individual fits and helps in the fitting when transition between spectral regimes is ongoing. The results for the evolution of the break frequencies ν_c, ν_m and ν_{sa} are presented in Fig. 8.5. The break frequencies are obtained for each one of the SEDs of the individual GRB afterglows using smooth breaks as in Granot & Sari (2002). The error due to the curvature effect are included and as shown in Chap. 2 and are only a few percent of the actual value.

Table 8.10: Temporal evolution of the measured break frequencies for each GRB afterglow. The numbers in the table correspond to the temporal slope (α) using a simple power-law fitting profile $\nu_i(t) \sim t^{-\alpha_i}$, with i = c, m and sa. The subscript T corresponds to the theoretical value, the subscript O corresponds to the observed value.

SED	ν_{cT}	ν_{cO}	ν_{mT}	ν_{mO}	ν_{saT}	ν_{saO}
GRB 100418A	0.5	0.57±0.04	-1.5	-1.72±0.08	-0.6	-0.56±0.06
GRB 110715A	0.5	0.56±0.10	-1.5	-1.34±0.06	-0.6	-0.72±0.10
GRB 130418A	0.5	0.61±0.03	-1.5	-1.45±0.06	-0.6	-0.68±0.08

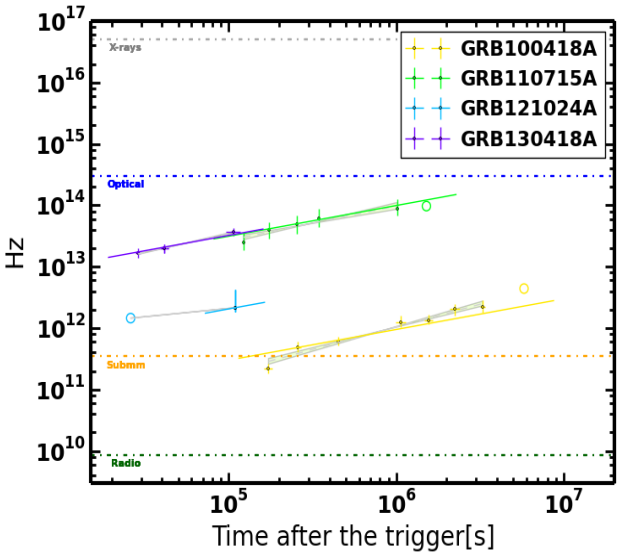

(a) Evolution of ν_c

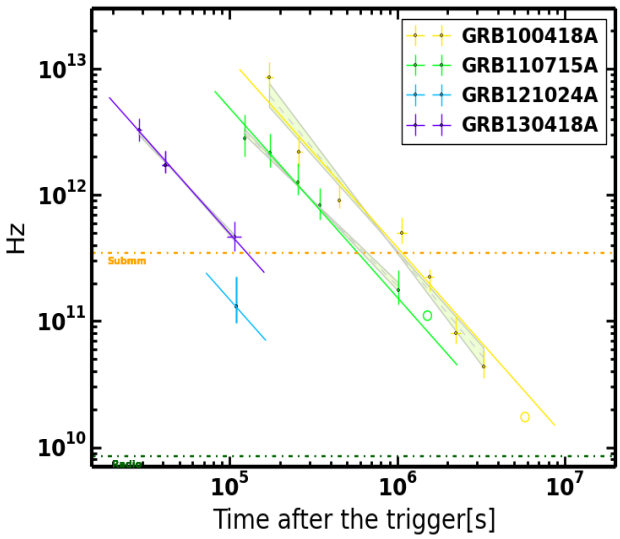

(b) Evolution of ν_m

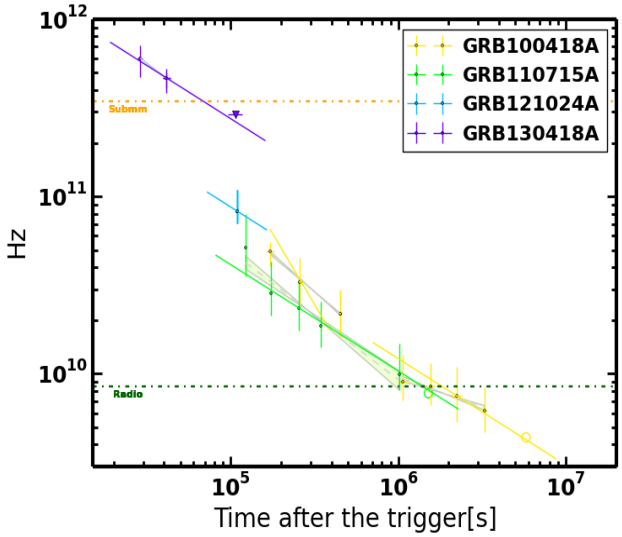

(c) Evolution of ν_{sa}

Figure 8.5: Evolution of the break frequencies for the afterglows of GRB 100418A, GRB 110715A, GRB 121024A and GRB 130418A. The solid lines corresponds to the expected evolution of each frequency from the standard afterglow theory. The dashed lines and the shaded regions are the fits for each frequency. The horizontal dashed lines make the mid frequency for the four main range of the observations, i.e., X-rays, optical, submm and radio.

8.3 Outlook and future

The analysis of the four GRB afterglow presented here shows the importance of a broadband multi-epoch data observations of the afterglows. These multi-wavelength observations allows the determination of the external medium profile without ambiguity and, the determination of all the microphysical and dynamical parameters. It also allows the test of the evolution of the main synchrotron break frequencies. Two important results can be highlighted:

First the CBM profile. Results presented in the literature relying usually only on X-ray and optical observations point toward a large percentage of the GRBs being associated with an ISM density profile. Here, I show that 6 out of 7 GRBs (4 from this study) are uniquely associated to a stellar wind-like density profile. This association is consistent with the collapsar model and, the GRB-SN relation. Furthermore I show that studies based only on X-ray and optical data, probably cannot constrain the CBM and therefore the percentage of GRBs associated with a stellar wind-like density profile is likely even larger than has been previously reported.

The second important result is related to the magnetic field in the shocked region. For the first time, the evolution of the magnetic field strength in the shock is presented. I find the evolution of the magnetic field strength to be in agreement with the predicted one for a magnetic field originating from a shock amplification of the CBM magnetic field. This supports strongly shock compression as a natural and probable origin of the shocked magnetic field. Additionally, based on the values for $\varepsilon_{\rm B}$, the magnetic field in the CBM region is expected to be about 10 mG.

The ground based observations have been improving in quality, quantity and velocity of response to the GRB trigger. The unique sensitivity of ALMA in the submm wavelength range in combination with observing programs at different radio telescopes and the continuation of follow-up optical telescopes is of a vital importance to improve the statistics of broadband observations that allow a systematic study of the GRB physics. Furthermore, studies of the progenitor and central engine of the GRBs are difficult to achieve with only late time afterglow observations.

Bibliography

Achterberg, A., Gallant, Y. A., Kirk, J. G., & Guthmann, A. W. 2001, MNRAS, 328, 393

Aihara, H., Allende Prieto, C., An, D., et al. 2011, ApJS, 193, 29

Aptekar, R. L., Frederiks, D. D., Golenetskii, S. V., et al. 1995, Space Sci. Rev., 71, 265

Arnaud, K. A. 1996, in Astronomical Society of the Pacific Conference Series, Vol. 101, Astronomical Data Analysis Software and Systems V, ed. G. H. Jacoby & J. Barnes, 17

Atteia, J.-L., Boer, M., Hurley, K., et al. 1987, ApJ, 320, L105

Baade, D., Meisenheimer, K., Iwert, O., et al. 1999, The Messenger, 95, 15

Balucinska-Church, M. & McCammon, D. 1992, ApJ, 400, 699

Band, D., Matteson, J., Ford, L., et al. 1993, ApJ, 413, 281

Barthelmy, S. D., Barbier, L. M., Cummings, J. R., et al. 2005, Space Sci. Rev., 120, 143

Beletic, J. W., Gerdes, R., & Duvarney, R. C. 1998, in Astrophysics and Space Science Library, Vol. 228, Optical Detectors for Astronomy, ed. J. Beletic & P. Amico, 103

Berger, E., Kulkarni, S. R., & Frail, D. A. 2003, ApJ, 590, 379

Beuermann, K., Hessman, F. V., Reinsch, K., et al. 1999, A&A, 352, L26

Bhattacharya, D. 2001, Bulletin of the Astronomical Society of India, 29, 107

Bikmaev, I., Khamitov, I., Melnikov, S., et al. 2010, GRB Coordinates Network, 10635

Björnsson, G., Gudmundsson, E. H., & Jóhannesson, G. 2004, ApJ, 615, L77

Blandford, R. D. & McKee, C. F. 1976, Physics of Fluids, 19, 1130

Blandford, R. D. & Ostriker, J. P. 1978, ApJ, 221, L29

Bloom, J. S., Frail, D. A., & Kulkarni, S. R. 2003, ApJ, 594, 674

Boella, G., Butler, R. C., Perola, G. C., et al. 1997, A&AS, 122, 299

Bohlin, J. D., Frost, K. J., Burr, P. T., Guha, A. K., & Withbroe, G. L. 1980, Sol. Phys., 65, 5

Bremer, M., Krichbaum, T. P., Galama, T. J., et al. 1998, A&A, 332, L13

Briggs, M. S., Paciesas, W. S., Pendleton, G. N., et al. 1996, ApJ, 459, 40

Burrows, D. N., Hill, J. E., Nousek, J. A., et al. 2005, Space Sci. Rev., 120, 165

Butler, N., Watson, A. M., Kutyrev, A., et al. 2013, GRB Coordinates Network, 14388

Butler, N. R. & Kocevski, D. 2007, ApJ, 663, 407

Cano, Z., de Ugarte Postigo, A., Pozanenko, A., et al. 2014, A&A, 568, A19

Cano, Z., Johansson Andreas, K. G., & Maeda, K. 2016, MNRAS, 457, 2761

Cenko, S. B., Frail, D. A., Harrison, F. A., et al. 2011, ApJ, 732, 29

Cenko, S. B., Frail, D. A., Harrison, F. A., et al. 2010, ApJ, 711, 641

Chandra, P. & Frail, D. A. 2012, ApJ, 746, 156

Chavan, A. M., Silva, D. R., Boarotto, C., et al. 2000, in Proc. SPIE, Vol. 4010, Observatory Operations to Optimize Scientific Return II, ed. P. J. Quinn, 81–89

Chevalier, R. A. 2000, in American Institute of Physics Conference Series, Vol. 526, Gamma-ray Bursts, 5th Huntsville Symposium, ed. R. M. Kippen, R. S. Mallozzi, & G. J. Fishman, 608–616

Chevalier, R. A. & Li, Z.-Y. 1999, ApJ, 520, L29

Chevalier, R. A. & Li, Z.-Y. 2000, ApJ, 536, 195

Cline, T. L., Desai, U. D., Klebesadel, R. W., & Strong, I. B. 1973, ApJ, 185, L1

Corsi, A., Piro, L., Kuulkers, E., et al. 2005, A&A, 438, 829

Costa, E., Frontera, F., Heise, J., et al. 1997, Nature, 387, 783

Crowther, P. A. 2007, ARA&A, 45, 177

Cucchiara, A., Levan, A. J., Fox, D. B., et al. 2011, ApJ, 736, 7

Curran, P. A., Evans, P. A., de Pasquale, M., Page, M. J., & van der Horst, A. J. 2010, ApJ, 716, L135

Curran, P. A., Starling, R. L. C., van der Horst, A. J., & Wijers, R. A. M. J. 2009, MNRAS, 395, 580

Dai, Z. G. & Cheng, K. S. 2001, ApJ, 558, L109

Dai, Z. G. & Lu, T. 1998a, A&A, 333, L87

Dai, Z. G. & Lu, T. 1998b, Physical Review Letters, 81, 4301

Dai, Z. G. & Lu, T. 1999, ApJ, 519, L155

Dai, Z. G. & Lu, T. 2000, ApJ, 537, 803

Daigne, F. & Mochkovitch, R. 1998, MNRAS, 296, 275

Dainotti, M. G., Cardone, V. F., & Capozziello, S. 2008, MNRAS, 391, L79

Davis, S. P., Norris, J. P., Kouveliotou, C., et al. 1994, in American Institute of Physics Conference Series, Vol. 307, Gamma-Ray Bursts, ed. G. J. Fishman, 182

De Colle, F., Ramirez-Ruiz, E., Granot, J., & Lopez-Camara, D. 2012, ApJ, 751, 57

de Pasquale, M., Baumgartner, W. H., Beardmore, A. P., et al. 2013, GRB Coordinates Network, 14377

de Ugarte Postigo, A., Lundgren, A., Mac-Auliffe, F., et al. 2011, GRB Coordinates Network, 12168

de Ugarte Postigo, A., Lundgren, A., Martín, S., et al. 2012, A&A, 538, A44

Dermer, C. D. & Atoyan, A. 2004, ApJ, 611, L9

Djorgovski, S. G., Metzger, M. R., Kulkarni, S. R., et al. 1997, Nature, 387, 876

Eichler, D., Guetta, D., & Pohl, M. 2010, ApJ, 722, 543

Evans, P. A., Beardmore, A. P., Page, K. L., et al. 2009, MNRAS, 397, 1177

Evans, P. A., Beardmore, A. P., Page, K. L., et al. 2007, A&A, 469, 379

Evans, P. A., Goad, M. R., Osborne, J. P., & Beardmore, A. P. 2011, GRB Coordinates Network, 12161

Fan, Y. & Piran, T. 2006, MNRAS, 369, 197

Fenimore, E. E., Conner, J. P., Epstein, R. I., et al. 1988, ApJ, 335, L71

Fenimore, E. E., Epstein, R. I., Ho, C., et al. 1993, Nature, 366, 40

Fermi, E. 1949, Physical Review, 75, 1169

Filgas, R., Greiner, J., Schady, P., et al. 2012, A&A, 546, A101

Filgas, R., Greiner, J., Schady, P., et al. 2011, A&A, 535, A57

Filgas, R., Schady, P., & Greiner, J. 2010, GRB Coordinates Network, 11091

Fishman, G. J. 1992, BATSE - The burst and transient source experiment on the Gamma Ray Observatory, ed. C. Ho, R. I. Epstein, & E. E. Fenimore, 265–272

Fishman, G. J. & Meegan, C. A. 1995, ARA&A, 33, 415

Frail, D. A., Kulkarni, S. R., Nicastro, L., Feroci, M., & Taylor, G. B. 1997, Nature, 389, 261

Frail, D. A., Kulkarni, S. R., Sari, R., et al. 2001, ApJ, 562, L55

Frail, D. A., Soderberg, A. M., Kulkarni, S. R., et al. 2005, ApJ, 619, 994

Frail, D. A., Yost, S. A., Berger, E., et al. 2003, ApJ, 590, 992

Friis, M., De Cia, A., Krühler, T., et al. 2015, MNRAS, 451, 167

Fruchter, A. S., Levan, A. J., Strolger, L., et al. 2006, Nature, 441, 463

Fruchter, A. S., Pian, E., Thorsett, S. E., et al. 1999, ApJ, 516, 683

Fryer, C. L., Rockefeller, G., & Young, P. A. 2006, ApJ, 647, 1269

Fukugita, M., Ichikawa, T., Gunn, J. E., et al. 1996, AJ, 111, 1748

Galama, T. J., Groot, P. J., van Paradijs, J., et al. 1998a, ApJ, 497, L13

Galama, T. J., Wijers, R. A. M. J., Bremer, M., et al. 1998b, ApJ, 500, L101

Galama, T. J., Wijers, R. A. M. J., Bremer, M., et al. 1998c, ApJ, 500, L97

Gao, H., Lei, W.-H., Zou, Y.-C., Wu, X.-F., & Zhang, B. 2013, New Astronomy Reviews, 57, 141

Garcia, M. R., Callanan, P. J., Moraru, D., et al. 1998, ApJ, 500, L105

Gehrels, N., Chincarini, G., Giommi, P., et al. 2004, ApJ, 611, 1005

Ghirlanda, G., Salvaterra, R., Burlon, D., et al. 2013, MNRAS, 435, 2543

Ghisellini, G., Nardini, M., Tagliaferri, J., G., et al. 2013, MNRAS, 428, 1449

Golenetskii, S. V., Mazets, E. P., Aptekar, R. L., & Ilinskii, V. N. 1983, Nature, 306, 451

Goodman, J. 1986, ApJ, 308, L47

Gorosabel, J., Perez-Hoyos, S., Mendikoa, I., et al. 2013, GRB Coordinates Network, 14378

Granot, J., Königl, A., & Piran, T. 2006, MNRAS, 370, 1946

Granot, J. & Piran, T. 2012, MNRAS, 421, 570

Granot, J., Piran, T., & Sari, R. 2000, ApJ, 534, L163

Granot, J., Ramirez-Ruiz, E., & Loeb, A. 2005, ApJ, 618, 413

Granot, J. & Sari, R. 2002, ApJ, 568, 820

Greiner, J., Bornemann, W., Clemens, C., et al. 2008, PASP, 120, 405

Greiner, J., Krühler, T., Klose, S., et al. 2011, A&A, 526, A30

Greiner, J., Krühler, T., Nardini, M., et al. 2013, A&A, 560, A70

Greiner, J., Mazzali, P. A., Kann, D. A., et al. 2015, Nature, 523, 189

Groot, P. J., Galama, T. J., Vreeswijk, P. M., et al. 1998, ApJ, 502, L123

Guidorzi, C., Mundell, C. G., Harrison, R., et al. 2014, MNRAS, 438, 752

Hakkila, J., Meegan, C. A., Pendleton, G. N., et al. 1994, ApJ, 422, 659

Hancock, P. J., Murphy, T., & Schmidt, B. P. 2011, GRB Coordinates Network, 12171

Harries, T. J., Hillier, D. J., & Howarth, I. D. 1998, MNRAS, 296, 1072

Harrison, F. A., Bloom, J. S., Frail, D. A., et al. 1999, ApJ, 523, L121

Harrison, F. A., Yost, S. A., Sari, R., et al. 2001, ApJ, 559, 123

Hartmann, D., Woosley, S. E., & Epstein, R. I. 1990, ApJ, 348, 625

Hattori, T. & Aoki, K. 2010, GRB Coordinates Network, 10794

Hjorth, J., Sollerman, J., Møller, P., et al. 2003, Nature, 423, 847

Holland, S. T. & Pagani, C. 2012, GRB Coordinates Network, 13901, 1

Hurley, K. 1989, Annals of the New York Academy of Sciences, 571, 442

Jóhannesson, G., Björnsson, G., & Gudmundsson, E. H. 2006, ApJ, 647, 1238

Johnson, H. L. & Morgan, W. W. 1953, ApJ, 117, 313

Kalberla, P. M. W., Burton, W. B., Hartmann, D., et al. 2005, A&A, 440, 775

Kann, D. A., Klose, S., Zhang, B., et al. 2010, ApJ, 720, 1513

Kaufer, A., Stahl, O., Tubbesing, S., et al. 1999, The Messenger, 95, 8

Kirk, J. G., Guthmann, A. W., Gallant, Y. A., & Achterberg, A. 2000, ApJ, 542, 235

Klebesadel, R. W., Strong, I. B., & Olson, R. A. 1973, ApJ, 182, L85

Klotz, A., Gendre, B., Boer, M., et al. 2013, GRB Coordinates Network, 14382

Knust, F., Schady, P., & Greiner, J. 2012, GRB Coordinates Network, 13891, 1

Kobayashi, S. 2000, ApJ, 545, 807

Kobayashi, S., Piran, T., & Sari, R. 1997, ApJ, 490, 92

Kouveliotou, C., Meegan, C. A., Fishman, G. J., et al. 1993, ApJ, 413, L101

Krühler, T., Küpcü Yoldaş, A., Greiner, J., et al. 2008, ApJ, 685, 376

Kuin, N. P. M. & de Paquale, M. 2013, GRB Coordinates Network, 14384

Kuin, N. P. M. & Sonbas, E. 2011, GRB Coordinates Network, 12162

Kulkarni, S. R., Djorgovski, S. G., Odewahn, S. C., et al. 1999, Nature, 398, 389

Kumar, P. 1999, ApJ, 523, L113

Kumar, P. & Barniol Duran, R. 2009, MNRAS, 400, L75

Kumar, P. & Panaitescu, A. 2000, ApJ, 541, L51

Kumar, P. & Piran, T. 2000, ApJ, 535, 152

Kumar, P. & Zhang, B. 2014, ArXiv e-prints

Lamb, D. Q. & Reichart, D. E. 2000, ApJ, 536, 1

Langer, N. 1989, A&A, 220, 135

Laskar, T., Berger, E., Margutti, R., et al. 2015, ApJ, 814, 1

Laskar, T., Berger, E., Zauderer, B. A., et al. 2013, ApJ, 776, 119

Laskar, T., Zauderer, A., & Berger, E. 2012, GRB Coordinates Network, 13903, 1

Lazzati, D. & Perna, R. 2007, MNRAS, 375, L46

Leventis, K., van 2012MNRAS.427.1329L, H. J., Meliani, Z., & Wijers, R. A. M. J. 2012, MNRAS, 427, 1329

Leventis, K., van der Horst, A. J., van Eerten, H. J., & Wijers, R. A. M. J. 2013, MNRAS, 431, 1026

Leventis, K., Wijers, R. A. M. J., & van der Horst, A. J. 2014, MNRAS, 437, 2448

Lü, H.-J. & Zhang, B. 2014, ApJ, 785, 74

Lyubarsky, Y. E. 2003, MNRAS, 345, 153

MacFadyen, A. I., Woosley, S. E., & Heger, A. 2001, ApJ, 550, 410

Mao, S. & Mo, H. J. 1998, A&A, 339, L1

Margutti, R., Zaninoni, E., Bernardini, M. G., et al. 2013, MNRAS, 428, 729

Marshall, F. E., Antonelli, L. A., Burrows, D. N., et al. 2011, ApJ, 727, 132

Marshall, F. E., Beardmore, A. P., Gelbord, J. M., et al. 2010, GRB Coordinates Network, 10612

Marshall, F. E. & Holland, S. T. 2010, GRB Coordinates Network, 10720

Martin, S., de Ugarte Postigo, A., & Petitpas, G. 2013, GRB Coordinates Network, 14400

Martin, S., Petitpas, G., de Ugarte Postigo, A., et al. 2010, GRB Coordinates Network, 10630

Mazets, E. P., Golenetskii, S. V., Aptekar, R. L., Gurian, I. A., & Ilinskii, V. N. 1981, Nature, 290, 378

Medvedev, M. V. 2006, ApJ, 651, L9

Medvedev, M. V., Fiore, M., Fonseca, R. A., Silva, L. O., & Mori, W. B. 2005, ApJ, 618, L75

Medvedev, M. V. & Loeb, A. 1999, ApJ, 526, 697

Meegan, C. A., Fishman, G. J., Wilson, R. B., et al. 1992, Nature, 355, 143

Mészáros, P. 2001, Science, 291, 79

Mészáros, P. 2006, Reports on Progress in Physics, 69, 2259

Meszaros, P., Laguna, P., & Rees, M. J. 1993, ApJ, 415, 181

Meszaros, P. & Rees, M. J. 1993, ApJ, 405, 278

Mészáros, P. & Rees, M. J. 1997, ApJ, 476, 232

Mészáros, P. & Rees, M. J. 1999, MNRAS, 306, L39

Metzger, B. D., Margalit, B., Kasen, D., & Quataert, E. 2015, MNRAS, 454, 3311

Metzger, M. R., Djorgovski, S. G., Kulkarni, S. R., et al. 1997, Nature, 387, 878

Meyer, M., Finger, G., Mehrgan, H., Nicolini, G., & Stegmeier, J. 1998, in Proc. SPIE, Vol. 3354, Infrared Astronomical Instrumentation, ed. A. M. Fowler, 134–138

Michael S. Briggs. 2014, BATSE, http://www.batse.msfc.nasa.gov/batse/grb/skymap/, [Online; accessed 2-Nov-2015]

Milosavljević, M. & Nakar, E. 2006, ApJ, 651, 979

Moin, A., Chandra, P., Miller-Jones, J. C. A., et al. 2013, ApJ, 779, 105

Morsony, B. J., Lazzati, D., & Begelman, M. C. 2007, ApJ, 665, 569

Nardini, M., Greiner, J., Krühler, T., et al. 2011, A&A, 531, A39

Nardini, M., Tanga, M., Kann, D. A., & Greiner, J. 2013, GRB Coordinates Network, 14386

Nelson, P. 2011, GRB Coordinates Network, 12174

Nemiroff, R. J. 1994, Comments on Astrophysics, 17, 189

Nousek, J. A., Kouveliotou, C., Grupe, D., et al. 2006, ApJ, 642, 389

Olivares, E. F., Greiner, J., Schady, P., et al. 2012, in IAU Symposium, Vol. 279, Death of Massive Stars: Supernovae and Gamma-Ray Bursts, ed. P. Roming, N. Kawai, & E. Pian, 375–376

Paczynski, B. 1986, ApJ, 308, L43

Paczynski, B. & Rhoads, J. E. 1993, ApJ, 418, L5

Pagani, C., Barthelmy, S. D., Baumgartner, W. H., et al. 2012, GRB Coordinates Network, 13886, 1

Page, K. L., Maselli, A., Mangano, V., et al. 2012, GRB Coordinates Network, 13892, 1

Panaitescu, A. 2001, ApJ, 556, 1002

Panaitescu, A. 2005, MNRAS, 363, 1409

Panaitescu, A. 2017, ApJ, 837, 13

Panaitescu, A. & Kumar, P. 2000, ApJ, 543, 66

Panaitescu, A. & Kumar, P. 2001, ApJ, 554, 667

Panaitescu, A. & Kumar, P. 2002, ApJ, 571, 779

Panaitescu, A., Mészáros, P., Gehrels, N., Burrows, D., & Nousek, J. 2006, MNRAS, 366, 1357

Pandey, S. B., Sahu, D. K., Resmi, L., et al. 2003, Bulletin of the Astronomical Society of India, 31, 19

Pe'er, A. & Wijers, R. A. M. J. 2006, ApJ, 643, 1036

Pei, Y. C. 1992, ApJ, 395, 130

Perley, D. A. 2013, GRB Coordinates Network, 14387

Piran, T. 2004, Reviews of Modern Physics, 76, 1143

Piran, T. 2005, in American Institute of Physics Conference Series, Vol. 784, Magnetic Fields in the Universe: From Laboratory and Stars to Primordial Structures., ed. E. M. de Gouveia dal Pino, G. Lugones, & A. Lazarian, 164–174

Piro, L., Costa, E., Feroci, M., et al. 1996, IAU Circ., 6480, 1

Price, P. A., Berger, E., Kulkarni, S. R., et al. 2002, ApJ, 573, 85

Quadri, U., Strabla, L., Girelli, R., & Quadri, A. 2013, GRB Coordinates Network, 14379

Racusin, J. L., Liang, E. W., Burrows, D. N., et al. 2009, ApJ, 698, 43

Ramirez-Ruiz, E., Dray, L. M., Madau, P., & Tout, C. A. 2001, MNRAS, 327, 829

Rees, M. J. & Meszaros, P. 1992, MNRAS, 258, 41P

Rees, M. J. & Meszaros, P. 1994, ApJ, 430, L93

Rees, M. J. & Mészáros, P. 1998, ApJ, 496, L1

Resmi, L., Ishwara-Chandra, C. H., Castro-Tirado, A. J., et al. 2005, A&A, 440, 477

Rhoads, J. E. 1999, ApJ, 525, 737

Roming, P. W. A., Kennedy, T. E., Mason, K. O., et al. 2005, Space Sci. Rev., 120, 95

Rybicki, G. B. & Lightman, A. P. 1979, Radiative processes in astrophysics

Sagi, E. & Nakar, E. 2012, ApJ, 749, 80

Santana, R., Barniol Duran, R., & Kumar, P. 2014, ApJ, 785, 29

Sari, R. & Esin, A. A. 2001, ApJ, 548, 787

Sari, R. & Mészáros, P. 2000, ApJ, 535, L33

Sari, R., Narayan, R., & Piran, T. 1996, ApJ, 473, 204

Sari, R. & Piran, T. 1995, ApJ, 455, L143

Sari, R., Piran, T., & Halpern, J. P. 1999, ApJ, 519, L17

Sari, R., Piran, T., & Narayan, R. 1998, ApJ, 497, L17

Schaefer, B. E. & Cline, T. L. 1985, ApJ, 289, 490

Schaefer, B. E., Teegarden, B. J., Fantasia, S. F., et al. 1994, ApJS, 92, 285

Schlafly, E. F. & Finkbeiner, D. P. 2011, ApJ, 737, 103

Schuller, F. 2012, in Society of Photo-Optical Instrumentation Engineers (SPIE) Conference Series, Vol. 8452, Society of Photo-Optical Instrumentation Engineers (SPIE) Conference Series, 1

Schuller, F., Nord, M., Vlahakis, C., et al. 2010, BoA - The Bolometer Data Analysis Software User and Reference Manual, 4th edn., Max-Planck-Institut für Radioastronomie, Argelander-Institut für Astronomie, Auf dem Hügel 69, 53121 Bonn, Germany

Schulze, S., Klose, S., Björnsson, G., et al. 2011, A&A, 526, A23

Siegel, M. H. & Marshall, F. 2010, GRB Coordinates Network, 10625

Siringo, G., Kreysa, E., Kovács, A., et al. 2009, A&A, 497, 945

Sironi, L. & Spitkovsky, A. 2011, ApJ, 741, 39

Skrutskie, M. F., Cutri, R. M., Stiening, R., et al. 2006, AJ, 131, 1163

Soderberg, A. M., Berger, E., Kasliwal, M., et al. 2006, ApJ, 650, 261

Sonbas, E., Palmer, D. M., Krimm, H. A., et al. 2011, GCN Report, 340

Stanek, K. Z., Matheson, T., Garnavich, P. M., et al. 2003, ApJ, 591, L17

Swinbanks, D. 1987, Nature, 326, 322

Tody, D. 1993, in Astronomical Society of the Pacific Conference Series, Vol. 52, Astronomical Data Analysis Software and Systems II, ed. R. J. Hanisch, R. J. V. Brissenden, & J. Barnes, 173

Updike, A., Rau, A., Afonso, P., & Greiner, J. 2010, GRB Coordinates Network, 10577

Usov, V. V. & Chibisov, G. V. 1975, Soviet Ast., 19, 115

van den Bergh, S. 1983, Ap&SS, 97, 385

van der Horst, A. J. 2013, GRB Coordinates Network, 14434

van der Horst, A. J., Kamble, A. P., Wijers, R. A. M. J., et al. 2010, GRB Coordinates Network, 10647

van Eerten, H. 2014, MNRAS, 442, 3495

van Eerten, H., Zhang, W., & MacFadyen, A. 2010, ApJ, 722, 235

van Eerten, H. J. & MacFadyen, A. I. 2012, ApJ, 751, 155

van Eerten, H. J. & Wijers, R. A. M. J. 2009, MNRAS, 394, 2164

van Marle, A. J., Langer, N., Achterberg, A., & García-Segura, G. 2006, A&A, 460, 105

van Marle, A. J., Langer, N., & García-Segura, G. 2007, A&A, 469, 941

van Paradijs, J., Groot, P. J., Galama, T., et al. 1997, Nature, 386, 686

Varela, K., van Eerten, H., Greiner, J., et al. 2016, A&A, 589, A37

Vietri, M. 1997, ApJ, 488, L105

Wang, X. Y., Dai, Z. G., & Lu, T. 2000, MNRAS, 317, 170

Waxman, E. & Draine, B. T. 2000, ApJ, 537, 796

Waxman, E. & Mészáros, P. 2003, ApJ, 584, 390

Weibel, E. S. 1959, Phys. Rev. Lett., 2, 83

Wiersema, K., Covino, S., Toma, K., et al. 2014, Nature, 509, 201

Wijers, R. A. M. J. & Galama, T. J. 1999, ApJ, 523, 177

Wijers, R. A. M. J. & Paczynski, B. 1994, ApJ, 437, L107

Wijers, R. A. M. J., Rees, M. J., & Meszaros, P. 1997, MNRAS, 288, L51

Willingale, R., Osborne, J. P., O'Brien, P. T., et al. 2004, MNRAS, 349, 31

Woosley, S. E. 1993, ApJ, 405, 273

Woosley, S. E. & Heger, A. 2003, ArXiv Astrophysics e-prints

Xu, D., de Ugarte Postigo, A., Leloudas, G., et al. 2013, ApJ, 776, 98

Yoldaş, A. K., Krühler, T., Greiner, J., et al. 2008, in American Institute of Physics Conference Series, Vol. 1000, American Institute of Physics Conference Series, ed. M. Galassi, D. Palmer, & E. Fenimore, 227–231

Yost, S. A., Harrison, F. A., Sari, R., & Frail, D. A. 2003, ApJ, 597, 459

Zauderer, B., Laskar, T., & Berger, E. 2012, GRB Coordinates Network, 13900, 1

Zhang, B., Fan, Y. Z., Dyks, J., et al. 2006, ApJ, 642, 354

Zhang, B. & Kobayashi, S. 2005, ApJ, 628, 315

Zhang, B., Liang, E., Page, K. L., et al. 2007, ApJ, 655, 989

Zhang, B. & Mészáros., P. 2004, International Journal of Modern Physics A, 19, 2385

Zhang, W., MacFadyen, A., & Wang, P. 2009, ApJ, 692, L40

ACKNOWLEDGMENTS

I want to thank all the GROND team, here in Munich and in Tautenburg, for all the help and support during my time at MPE. All the people in La Silla and at MPE who have helped me during this time. I specially want to thank Vlad and Jonny for helping me when I arrived here at the institute and all the patience you had with me. To Julia, Fabian and Phil, it was so nice to work and party with you all, you made this time here in Munich really enjoyable.

I want to say special thanks to Jochen and Patricia for giving me the opportunity to do my PhD here at MPE. I am really happy I got to work under your supervision. I learnt a lot and definitely enjoyed my time here. Thank you for always helping me and cheering me up during the hard times.

To all my friends in Munich and in Bogota, thank you. Chris, Carlos and Santi, I am so happy I got to meet you. Felipe and JuanKimilo thank you for all these years of friendship, I love you both so much.

A mi familia, mil gracias, no se imaginan todo lo que los quiero. Gracias porque a pesar de la distancia siempre estuvieron pendientes de mi. Hmno, gracias porque a su forma siempre esta con mi mamá y porque siempre me apoya. Y mi abuelita y ceci, simplemente gracias por todo, estoy acá gracias a ustedes. Las adoro!

Mamá, no hay persona más importante en el mundo para mi y nadie que me apoye más. Esto es por ti. Te quiero muchísimo.